The use of MRI and MNP to image and track cells *in vivo* for arthritic cell-based therapies

Hareklea Markides

May 2014

School of Postgraduate Medicine

Institute of Science and Technology in Medicine

Abstract

Cell-based therapies have been proposed as novel approaches to treating Osteoarthritis and Rheumatoid Arthritis. A non-invasive means of monitoring cell populations, post implantation could prove valuable in the clinical translation of such therapies. We propose the use of superparamagnetic iron oxide nanoparticles (SPIONs; internalised by cell populations) with magnetic resonance imaging (MRI) to image and track cell populations *in vivo*.

We investigate the potential of commercially available SPIONs (SiMAG, Lumirem, Nanomag and P904) as potential labelling/tracking agents for *in vivo* investigations. Human mesenchymal stem cells (hMSC) and porcine chondrocytes were labelled with SPIONs under passive incubation conditions in either serum free media or serum containing media (24 hrs). SiMAG (10 μgFe/ml) demonstrated greatest potential with highest comparative internalised Fe content (labelled in serum free media) *in vitro*. SPION-labelled cell population maintained viability and proliferative capacity apart from SiMAG-labelled chondrocytes (10 μgFe/ml). Furthermore, SiMAG-labelled hMSC populations demonstrated successful differentiation down mesodermal lineages and retained key cell surface markers.

MRI visibility thresholds were investigated (*in vitro* and *ex vivo*). Dose dependant contrast was generated only by SiMAG-labelled populations *in vitro* when MR imaged. *In vitro* minimum visibility of SiMAG-labelled populations was influenced by various *ex vivo* tissues with similar contrast developing in muscle and fat tissue samples but not for ligament. Finally, an *ex vivo* model of articular cartilage damage confirmed the potential clinical application of SPIONS as cell tracking agents at optimised conditions (cell dosage and SiMAG concentration) using a clinical system.

An AIA murine model (Rheumatoid Arthritis) and a MNX rat model (Osteoarthritis) were implemented to image and track implanted SiMAG-labelled MSCs (murine) *in vivo* for 7 and 29 days, respectively. Additionally, clinically relevant functional outcomes were also monitored. Relevant *in vitro* assessment was performed where mMSCs efficiently internalised SiMAG with no impairment on cell activity. Good contrast was generated in both studies with SiMAG-labelled cell population located within the synovial cavity after 7 days (mouse study) and 29 days (rat study) by MRI. Administration of MSCs significantly reduced joint swelling in the mouse study without influence from the presence of SiMAG. mMSCs significantly influenced weight bearing asymmetry with little influence on paw withdraw threshold indicating potential antinocieotive properties of MSCs. In summary, SiMAG has demonstrated great potential as a labelling and tracking agent to be implemented for imaging and tracking cell populations.

Keywords: Superparamagnetic Iron Oxide Nanoparticles (SPIONs), Magnetic Resonance Imaging (MRI), Mesenchymal stem cells (MSCs), Chondrocytes, Rheumatoid Arthritis (RA), Osteoarthritis (OA).

Table of Contents

List of Figures

Chapter 1

Chapter 2

Chapter 3

Chapter 4

List of Tables

Chapter 1

Chapter 2

Chapter 3

Chapter 4

Chapter 5

Publications and Presentations

Associated research publications

<u>Hareklea Markides</u>, Oksana Kehoe, Robert Morris, Alicia El Haj. *Whole Body Tracking of SPION Labelled Cells – a Rheumatoid Arthritis mouse model,* Stem Cell Research & Therapy. 2013; 4(5):126.

Ian Wimpenny, <u>Hareklea Markides</u>. *Orthopaedic applications of nanoparticle-based stem cell therapies*. (Review) Stem Cells Research and Therapy 2012; 3(2):13.

<u>Hareklea Markides</u>, Michael Rotherham, Alicia J.El Haj. *Biocompatibility and Toxicity of Magnetic Nanoparticles in Regenerative Medicine*. (Review) Journal of Nanomaterials, 2012; 2012:11.

Non-associated research publications

Michael J Sawkins, William Bowen, Paramjeet Dhadda, <u>Hareklea Markides</u>, Laura E Sidney, Adam J Taylor, Felicity R Rose, Stephen F Badylak, Kevin M Shakesheff, Lisa White. *Hydrogels derived from demineralized and decellularized bone extracellular matrix*. Acta Biomaterialia, 2013 8//;9(8):7865-73.

Oral Presentations.

Hareklea Markides, Alicia J El Haj; *Investigating various magnetic nanoparticles for the tagging & imaging of stem cell therapies in orthopaedics* TERMIS EU, Spain June 2011.

Hareklea Markides, Alicia J El Haj; *Ex vivo imaging and tracking of SPION labelled mesenchymal stem cells and chondrocytes in orthopaedic cell based therapies*. TERMIS World Congress, Vienna, September 2012.

Hareklea Markides, Alicia J El Haj; *Ex vivo imaging and tracking of MNP - labelled MSCs in orthopaedic cell based therapies*; BSRT PhD Symposium, Berlin, December 2012.

Hareklea Markides, Alicia J El Haj; *Development of ex vivo and in vivo models for the tagging & imaging of stem cell therapies for orthopaedics.*; DTC cross cadre conference, Nottingham, April 2012.

Hareklea Markides, Alicia J El Haj; *In vivo Imaging and Tracking of MNP - Labelled MSCs in Orthopaedic Cell Based Therapies*; ARUK, May 2013.

Hareklea Markides, Alicia J El Haj; *In vivo Imaging and Tracking of MNP - Labelled MSCs in Arthritic Animal models*; TERMIS Istanbul, June 2013.

Hareklea Markides, Alicia J El Haj; *In vivo Imaging and Tracking of MNP - Labelled MSCs in Arthritic Animal models; Nanoparticle Tracking Symposium*, Liverpool, July 2013.

Poster Presentations

Hareklea Markides, Alicia J El Haj, *Development of Magnetic Nanoparticle Strategies for use in Tagging & Imaging Stem Cell Therapies for Orthopaedics*; TCES July 2011

Hareklea Markides, Alicia J El Haj, *Development of Magnetic Nanoparticle Strategies for use in Tagging & Imaging Stem Cell Therapies for Orthopaedics*; ARUK October 2011

Hareklea Markides, Alicia J El Haj, *Development of Magnetic Nanoparticle Strategies for use in Tagging & Imaging Stem Cell Therapies for Orthopaedics*; November 2011

Hareklea Markides, Alicia J El Haj, *Development of Ex vivo and In vivo Models for the Tagging & Imaging of Stem Cell Therapies for Orthopaedics*; ARUK October 2012

Acknowledgments.

I am sincerely grateful to my supervisor Professor Alicia El Haj whose constant support and guidance throughout the years has made this project a reality. I feel very privileged to have worked so closely with Alicia, learning so much along the way. I am particularly thankful to Alicia for all the opportunities to travel and present my work, to meet and interact with so many influential people and to expand my skill set and personal network. Alicia is a great leader, constantly pushing me beyond boundaries I never imagined I could reach, especially this past year. The El Haj research group is a group to be a proud of – friends before colleagues. In addition to all the support during my PhD, I`d like to also thank Alicia for giving Dave, Alex and I the opportunity to establish and run the FIRM symposium, a task I thoroughly enjoyed. I look forward to working with her in the future.

Dr Oksana Kehoe has been a massive pillar of strength, an excellent supervisor and above all a great friend, always going above and beyond to check up on me. There was ever a task too big or a question too many - Thank you.

A massive thank you to Dr Robert Morris for his guidance and patience during the long MRI hours enduring my many **MANY** MRI questions. Rob is a fantastic teacher from whom I have learnt so much from. I am sincerely grateful for all his input in this project.

To my advisors, Prof Sally Robert and Prof James Richardson for including me in all ARUK activities and offering unlimited resources of the Robert Jones and Agnes Hunt Orthopaedic Hospital I am very thankful.

A special thank you to Dr Deepak Kumar who has dragged me through this PhD with a constant smile on his face. **I definitely would not have managed without him**. I am particularly grateful for the proof reading of this thesis.

Working with such great people at the Guy Hilton has made coming into work every day so enjoyable. I am so proud of the dynamics of the students at the Guy Hilton, it not often you find yourself working with people who have your best interest at heart. In particular, a big thank you to Tina Dale, Michael Rotherham, Abigail Rutter, Eva Cespedes, Maria Kyriakou and Rupert Wright, for services above the call of duty.

Finally, I would like to acknowledge the support of the EPSRC and the ARUK for funding sources.

Abbreviations

ACI	Autologous Chondrocytes Implantation
ADAMTS	A Disintegrin And Metalloproteinase with Thrombospondin Motifs
BLI	Bioluminescence Imaging
BSA	Bovine Serum Albumin
CD	cluster of differentiation
CT	computed tomography
DAPI	4',6-diamidino-2-phenylindole
DMARDS	Disease Modifying Antirheumatic drugs
DMEM	Dulbecco's Modified Eagle Medium
DMSO	Dimethyl sulfoxide
DNAse	Deoxyribonuclease
ECM	Extracellular Matrix
EGF	Epidermal growth factor
FACS	Fluorescence-activated cell sorting
FBS	Fetal Bovine Serum
FDA	Food and Drug Administration
Fe	Iron
FGF	Fibroblast growth factors
FISP	Fast Imaging With Steady State Precession
FITC	Fluorescein isothiocyanate
FLASH	Fat Low Angle Shot
FLS	Fibroblast like synoviocytes
FSE	Fast Spin Echo
GAG	Glyosaminoglycans
GEFI	Gradient-echo Fast Imaging
ICP - OAS	Inductively Coupled Plasma-Optical Emission Spectrometry
IL	Interlukin
ISCT	International Society for Cell Therapy
MIA	Monosodium Iodoacetate
MMP	Metalloproteinases
mMSC	Murine mesenchymal stem cells
MNP	Magnetic Nanoparticles
MPION	Micron- Sized particles
MRI	Magnetic Resonance Imaging
MRS	Magnetic Resonance Spectroscopy
MSC	Mesenchymal stem cells
MSME	Multi Slice Multi Spin Echo
MTT	3-(4,5-dimethylthiazol-2-yl)-2,5-diphenyltetrazolium bromide
MXN	Meniscal Transection
NC3R	National Centre for the Replacement Refinement and Reduction of Animals in Research

NSAID	Non-Steroidal Anti-Inflammatory
OA	Osteoarthritis
OD	Optical Density
PBS	Phosphate buffered saline
PET	Positron Emission Tomography
PI	Propidium Iodine
RA	Rheumatoid Arthritis
RARE	Rapid Acquisition with Relaxation Enhancement
SCM	Serum Containing Media
SFM	Serum Free Media
SPECT	Single Photon Emission Computed Tomography
SPIONs	Superparamagentic Iron Oxide Nanoparticles
T	Tesla
T_1	Longitudinal relaxation
T_2	Transverse relaxation
T_2^{eff}	Transverse relaxation effective
TA	Transfection Agent
TE	Tissue engineering
TGF	Transforming Growth Factor
TIMP	Tissue Inhibitors of Matrix Metalloproteinase
TNF	Tumour Necrosis Factor
USPION	Ultra small Superparamagentic Iron Oxide Nanoparticles

Chapter 1

Literature Review

1.1. The Promise of Regenerative Medicine and Stem Cell Therapies

Regenerative medicine (RM) is a pioneering field which aims to develop strategies to replace and regenerate human cells, tissues and organs in order to restore normal function (1). The field thrives on the cross collaboration of multiple disciplines to develop tissue engineering approaches to achieve these goals. It harnesses the tools and knowledge developed by material scientists, molecular biologists, engineers and clinicians for the design and development of cellular therapies to treat a broad range of diseases and conditions. RM primarily employs the use of stem cells as the fundamental component of most therapies. The field of RM has experienced several exciting breakthroughs over the years; for example, the development of induced pluripotent stem cells which saw Yamanaka receive the Nobel Prize for this discovery (2). In addition, Macchiarini and his colleagues succeeded in implanting the first functioning human tissue engineered trachea (3). Popular avenues of research currently include; Parkinson's, Alzheimer's, spinal cord injury, diabetes and arthritis (1). Due to the successful progress by Brittberg and his team (4), cartilage restoration approaches are currently in clinical use today and primarily focus on targeting osteoarthritis. Nonetheless arthritis still remains to be a burden on healthcare systems worldwide.

This thesis will therefore focus on the contributions regenerative medicine has made in tackling rheumatoid arthritis (RA) and osteoarthritis (OA) of the knee and how multidisciplinary approaches can contribute to the further understanding and enhancement of these therapies.

1.2 Arthritis

Arthritis is used to describe a set of musculoskeletal disorders affecting one or more joints within the body. Examples include, Rheumatoid Arthritis (RA; a type of inflammatory arthritis) and osteoarthritis (OA; classified as degenerative arthritis), (5). The mechanisms by which these diseases progress are significantly different with RA being a systemic autoimmune disorder whereas OA is a non-systemic degenerative, mechanical disorder (6, 7). Both forms of arthritis however result in pain and inflammation of the joint and are accompanied by joint destruction resulting in an eventual loss of function (6). The knee joint is the largest, most common joint affected by arthritis and is the focus of much research combating this disease. For this reason the knee joint will be the main joint of focus of this thesis. To fully understand arthritis of the knee, it is important to first grasp the key anatomical and physiological components making up the knee joint.

1.2.1 The Biology of the Knee

Characterised as the largest joint in the human body (8, 9) the knee plays a vital role in the mobility and movement of the lower body. It is a prime example of a synovial hinge joint due to the presence of the synovial lining and the single plane of joint movement. In basic anatomy terms, the knee is made up of 3 bones, the femur, the tibia and finally the patella (10). The movement of the joint is dependent on the shape of the bones, the characteristics of the ligaments and the surrounding soft tissue (11). Figure 1.1 illustrates the general anatomy of the knee highlighting the main components.
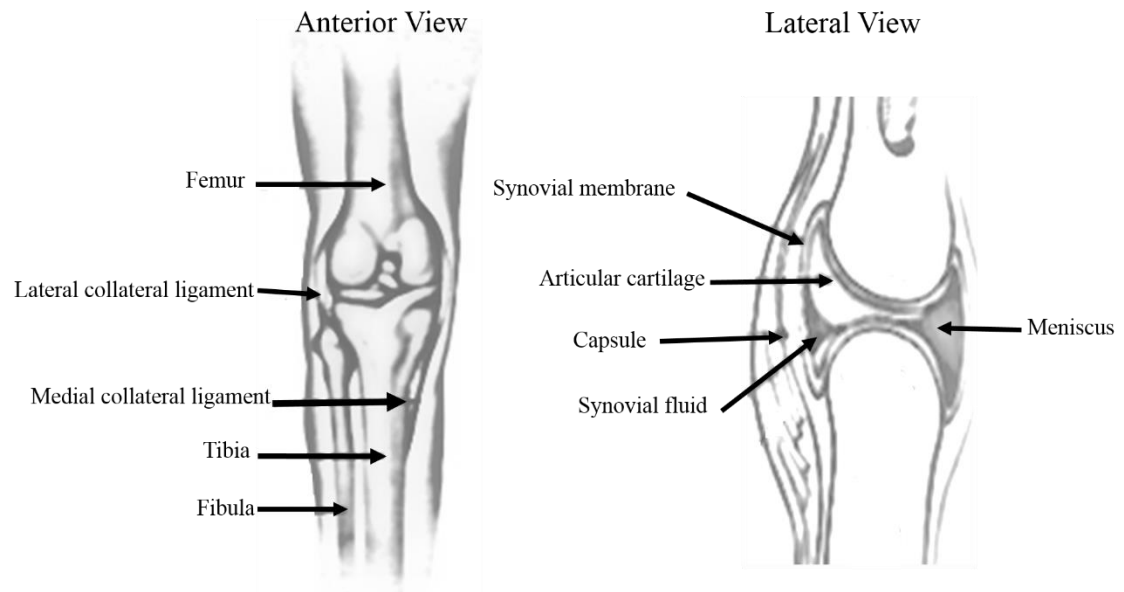
Figure 1.1 Basic anatomy of the human knee. Adapted from Gillian *et al*. 2000 (12).

The distal ends of the femur progress into two condyles (9). The surface of these condyles are lined with articular hyaline cartilage, a highly load bearing tissue effectively allowing for the smooth, almost frictionless movement of one bone over the other and is critical to the function of the joint (10, 13). The function of hyaline cartilage is aided by the production of synovial fluid which not only nourishes the cartilage but also keeps the coefficient of friction low. This fluid is produced by the surrounding membrane (the synovium), and has a tough outer layer (the capsule), which essentially prevents excessive movement of the bone. Excessive movement of bones is further restricted by the ligaments, which run either within or just outside the capsule and hold the three bones mentioned above, together (8). The main stabilizing ligaments are the anterior cruciate ligament (ACL), posterior cruciate ligament (PCL), medial collateral ligament (MCL) and the lateral collateral ligament (LCL), which provide combined stability throughout a range of motions characteristic to the knee (9). Furthermore, two "C" shaped pieces of cartilage (meniscus) are located between the cartilage layers of the femur and tibia (8). Unlike the cartilage found at the surface of the condyles, the meniscus is fibrocartilage in nature and effectively resists compression of weight bearing

loads and also allows for the correct alignment of the femoral condyle to the tibial condyles (9). Finally, tendons function to attach the muscles to bone (8), and act in an antagonistic manner to provide appropriate joint movement. Finally, the patella tendon attaches with the patella (kneecap) acting to protect the tendon at the back of the knee (11).

Major considerations in the efficient functioning of the knee are: a) the geometry of the bone and articulating surfaces, b) the functional and anatomical integrity of the surrounding supportive structures such as ligaments, tendons and muscles, and c) the mechanical properties of the articular cartilage and subchondral bone. Any short comings of these pre-requisites can ultimately result in a broad range of disorders such as articular cartilage damage (14).

1.2.2 Cartilage

Cartilage is a specialised connective tissue found in various forms and in numerous sites within the body playing a key structural and supportive role (15, 16). Cartilage located within different areas of the body are subjected to various site specific mechanical stresses (tensile, shear and compressive) and therefore have different physical properties to account for such site specific biomechanical properties (13, 17). For example, **Hyaline cartilage** is found at the surface of synovial joints functioning to resist compression during joint movement whilst also facilitating the smooth and frictionless movement of joint. Furthermore, hyaline cartilage makes up the rings of the trachea and the plates in the bronchi providing the necessary structural support required by the respiratory system. **Fibrocartilage** on the other hand is found within the intervertebral disks and the meniscus on the knee where its main role is to resist tensile loads under stresses. Finally, **Elastic** cartilage makes up the outer part of the ear and is adapted to providing flexible support (16).

In general, cartilage is a complex structure made up of collagen fibres, proteoglycans, and water, which collectively make up the extracellular matrix (ECM) (9, 17). The ECM is maintained by chondrocytes which is the only cell type that sparsely resides within this tissue. The specific ratio of these biochemical components effectively dictates the type of cartilage present (17).

Collagen is a highly abundant fibrous protein found within the human body playing a significant role in contributing to the strength, structure and 3D shape of cartilage (14) . The general structure of collagen can be described as being a triple helix made up of three helical α chains twisted around each other to form a superhelix (9). Variations in this structure results in alternative forms of collagen such as collagen type I, II, IX and XI, with the various types having specific roles in the overall structure of cartilage (14). Collagen type I is primarily found in fibrocartilage whereas collagen type II makes up 80-90 % of hyaline cartilage and elastin (9, 16). Attached to the collagen fibrils, are proteoglycan aggregates which contribute to the formation of ECM. **Proteoglycans** are complex macromolecules comprising of a protein core covalently attached to glycosaminoglycan side chains linked with a variety of sulphated polysaccharides (chondroitin 4, 6 and keratin sulphate) (9, 14). Proteoglycans play an important role in maintaining cartilage function by promoting lubrication, providing a structural element within the connective tissue, mediating the adhesion of cells to the ECM and providing binding factors that effectively stimulate cell proliferation (13, 14). The **water** content in cartilage varies according to cartilage type, age and specific location in the body and is an essential part of maintaining tissue integrity, supporting loads and nourishing chondrocytes (7, 9).

The specific ratios of these biochemical components (collagen and proteoglycans) effectively dictate the type of cartilage present (17). Orientation of the collagen fibres further impacts the biomechanical properties of cartilage tissue. Longitudinal fibre orientation, (type

I collagen) has greater tensional strength in comparison to transverse collagen fibre orientation (type II collagen) which are more adapted to resist compressive forces (18). The relative quantities of collagen and proteoglycans making up hyaline and fibrocartilage are shown in Table 1.1. Therefore, the function of hyaline cartilage is aided by the presence of type II collagen and the high proteoglycan quantity, whereas type I and type II collagen content of fibrocartilage allow for resistance to both compression and tension forces. It is important at this point to note that fibrocartilage does not have the same biochemical composition or structural organisation to provide the mechanical function demanded by the knee thus resulting in faster degradation over time due to insufficient load bearing capabilities (13, 19). This is an important consideration in tissue engineering of cartilage.

Table 1.1 The relative proportions of the three major components in hyaline and fibrocartilage (19)

Tissue Type	Type I collagen	Type II collagen	Proteoglycan
Fibrocartilage	++	+	+
Hyaline cartilage	0	+++	+++

Healthy cartilage is maintained by a dynamic equilibrium between the production and degradation of cartilage matrix over time in a process referred to as "cartilage homeostasis" (7, 9, 13). This process is regulated by chondrocytes residing within the cartilage tissue and is governed by a variety of soluble catabolic (degrading), anabolic (pro-synthesis), inflammatory and apoptotic mediators derived from chondrocytes and the synovium (7, 9). Normal homeostasis is dependent on the ability of chondrocytes to detect changes in the matrix composition and consequently respond by triggering the degradation of ECM via the secretion of matrix degrading enzymes to allow for the deposition of newly synthesised ECM specific molecules (collagen, proteoglycans and glyosaminoglycans) (16). It is vital to have

a firm understanding of the factors involved in cartilage homeostasis in order to better understand disease pathology. A detailed overview of factors involved in cartilage homeostasis are stated in Table 1.2. Furthermore, homeostasis is partially driven by mechanical stimulation (mechanotransduction) of chondrocytes where the loading of the joint creates mechanical, electrical and chemical signals which are transduced through the cartilage matrix effectively directing chondrocytes towards anabolic activities (16). However, with age, cells are less able to respond to these signals resulting in a disruption in the homeostasis balance (13, 16). In fact, any event (such as trauma, disease and age) causing a disruption in this balance may result in excessive catabolic events over anabolic events. This ultimately causes the overall breakdown of the matrix subsequently causing cartilage damage, pain and reduced mobility (7, 13). Given the limited proliferative capacity of mature chondrocytes, these cells are not able to compensate for this damage, resulting in disease progression (7).

Table 1.2 Catabolic and anabolic factors of normal cartilage homeostasis (9)

Catabolic Factors	Anabolic Factors
Cytokines: Interleukin (IL-1) and Tumour necrosis factor (TNFα).	**Cytokine inhibitors**: Interleukin antagonist (IL-1RA) and human cytokine synthesis inhibitory factor (IL-10)
Proteinases: a) Cysteine and serine proteinases b) Metalloproteinases (MMP). E.g. MMP-1 (interstitial collagenase), MMP-2 (gelatinases), MMP-3 (Stromelysin), MMP-13 (Collagenase-3), ADAMTS 4 &5 (A Disintegrin And Metalloproteinase with Thrombospondin Motifs) Aggrecanase -1 &2	**Proteinase Inhibitors:** Tissue inhibitors of matrix metalloproteinase (TIMP)
	Growth Factors: FGF (Fibroblast growth factors), EGF (Epidermal growth factor), TGFβ (Transforming growth factor)
	Mechanical Loading: Mechanotransduction

1.2.2.1 Articular Hyaline Cartilage

From the Greek word, "hyalos", meaning glass, articular hyaline cartilage is identified as the smooth, glistening white, glass-like tissue found covering the surface of articulating joints (13, 16). Hyaline cartilage is a metabolically active tissue whose function lies in the ability to provide resistance to compressive, shear and tensile forces occurring during normal joint motion. This is made possible by distributing applied forces to the underlying bone in the knee without sustaining wear (16, 20). Although hyaline cartilage is considered to be a fairly tough and robust tissue, recovery from damage to the articular surface is not easily overcome

(16). This is attributed to the avascular nature and consequent lack of blood supply accounting for the limited healing capacity and regeneration of the articular cartilage (13, 16, 21, 22).

The mechanical properties of articular cartilage are attributed to the arrangement of the macromolecules making up cartilage ECM, as mentioned in section 1.1.2 (16). The relative quantities of each constituent making up hyaline cartilage are shown in Figure 1.2. Collagen is the major matrix protein found in hyaline cartilage ECM with type II collagen being the most abundant and prominent of all collagen types present. Type IX, XI, X and VI are also present and work to facilitate interactions with proteoglycans and cells, regulate fibril size and organize collagen into 3D structures (13, 16). The arrangement of collagen fibres not only provide the tensile strength for cartilage but can also respond to swelling pressures of proteoglycans (15).

Proteoglycans are made up of: glyosaminoglycans (GAGs), hyaluronan, chondroitin sulphate and keratin sulfate. The attachment of GAGs to a protein core essentially creates a proteoglycan monomer. Aggrecan is the most abundant proteoglycan found in hyaline cartilage, comprising of a protein core with keratin sulfate and chondroitin sulfate side chains. These molecules are stabilized by link proteins and are attached to hyaluronic acid molecules within the ECM. Up to 200 aggrecan molecules can attach to one hyaluronan molecule, forming a macromolecular aggregate, which is shown in Figure 1.2. Negatively charged side chains that repel each other encourage the adsorption of water and providing the tissue with swelling properties. This is a key aspect in resisting compression and contributing to the mechanical properties of the tissue (13, 16). Other proteoglycans (decorin, biglycan and lumican) can also be found within hyaline cartilage. The collaborative effect of all proteoglycans contributes to the function of cartilage (capacity to resist excessive loads and provide frictionless movement of joints) (15, 16). Furthermore, multi-adhesive proteins

(non-collagenous and non-proteoglycan linked proteins) found within the matrix are present to encourage and facilitate interactions with chondrocytes and cartilage matrix molecules, by playing roles in cell anchoring (16).

Hydration of cartilage matrix is a particularly important aspect of maintaining cartilage health and function. Water molecules residing within the pores of ECM not only facilitate the diffusion of nutrients and waste to and from the chondrocytes and the synovial fluid, but also act to maintain tissue integrity when the joint is in motion. This is significantly important given the avascular and alymphatic nature of cartilage (13, 16, 22). During motion, cartilage can respond to varying pressure loads resulting in the rapid pressurisation of the fluid inside the tissue resulting in the ability to withstand the load (9, 13, 16).

Chondrocytes reside within the lacunae of ECM and become attached to the ECM via integrins (specialised cell surface proteins mediating bidirectional signalling between the intracellular and extracellular regions of the cell). This is essential in the maintenance of homeostasis, viability and morphology (23).
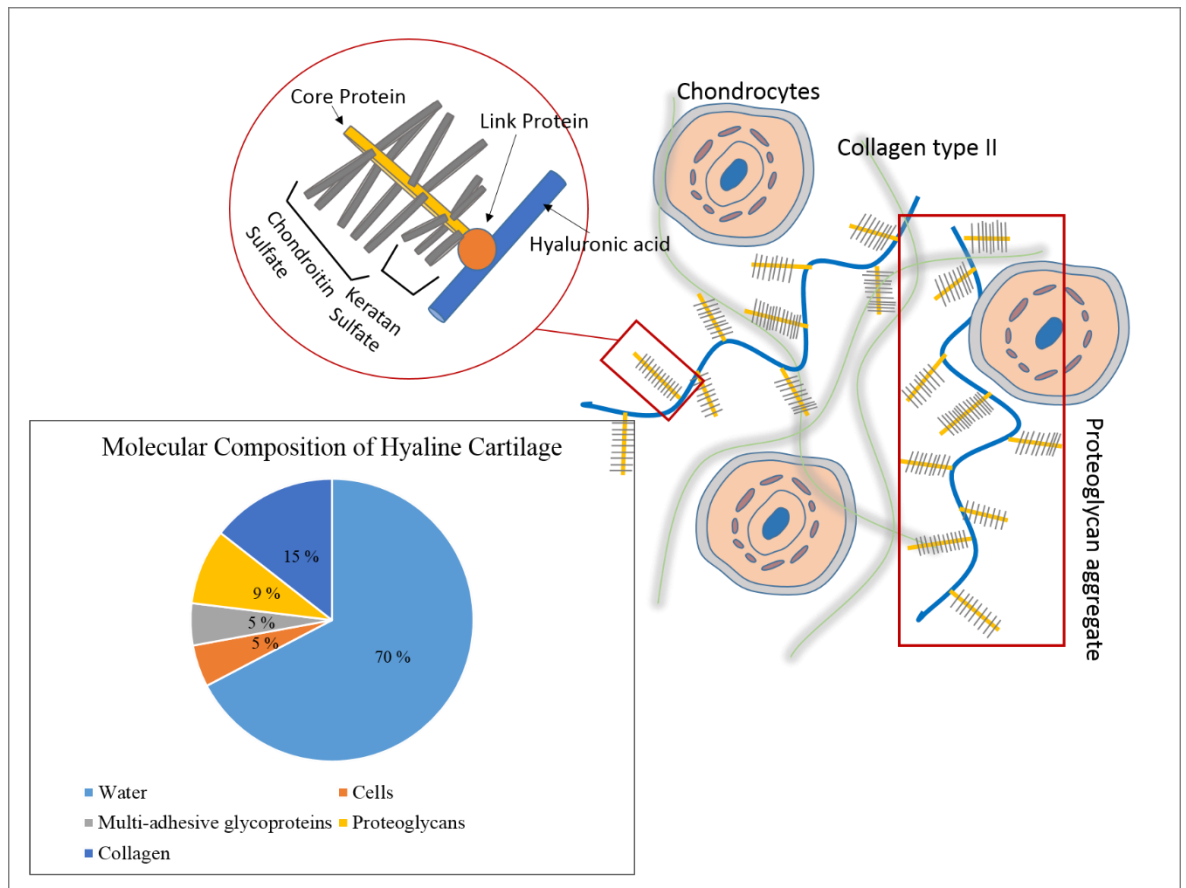
Figure 1.2. Structure and molecular composition of hyaline cartilage, adapted from (13, 16)

Hyaline cartilage is divided into zones classified by collagen fibre orientation and chondrocyte morphology (Figure 1.3). The composition of each zone varies from top to bottom i.e. from the surface of the tissue down to the subchondral bone. These regions are known as; **superficial, middle/intermediate and deep regions**. Chondrocyte morphology, size, collagen fibre orientation and biochemical composition vary throughout these zones and for this reason are identified accordingly (9, 13).

- The **superficial zone** forms approximately 10-20 % of the tissue and is characterised by; a) densely packed collagen fibres orientated parallel to the cartilage surface, b) relatively low proteoglycan content and c) few densely packed and flattened chondrocytes, aligned along the neighbouring collagen fibres (9, 13).

- The **middle zone** comprises of about 40-60 % of the tissue thickness. This zone is characterised by: a) collagen fibres arranged in an oblique manner, b) high proteoglycan content and c) low chondrocyte density with cells more spherical in shape (9, 13).

- Finally, the **deep zone** is characterised by: a) large collagen bundles orientated vertically to the articular surface and fixed to the underlying bone, b) low proteoglycan content and c) very low cell density. The chondrocytes in this area are elongated and grouped together in a columnar manner (9, 13).
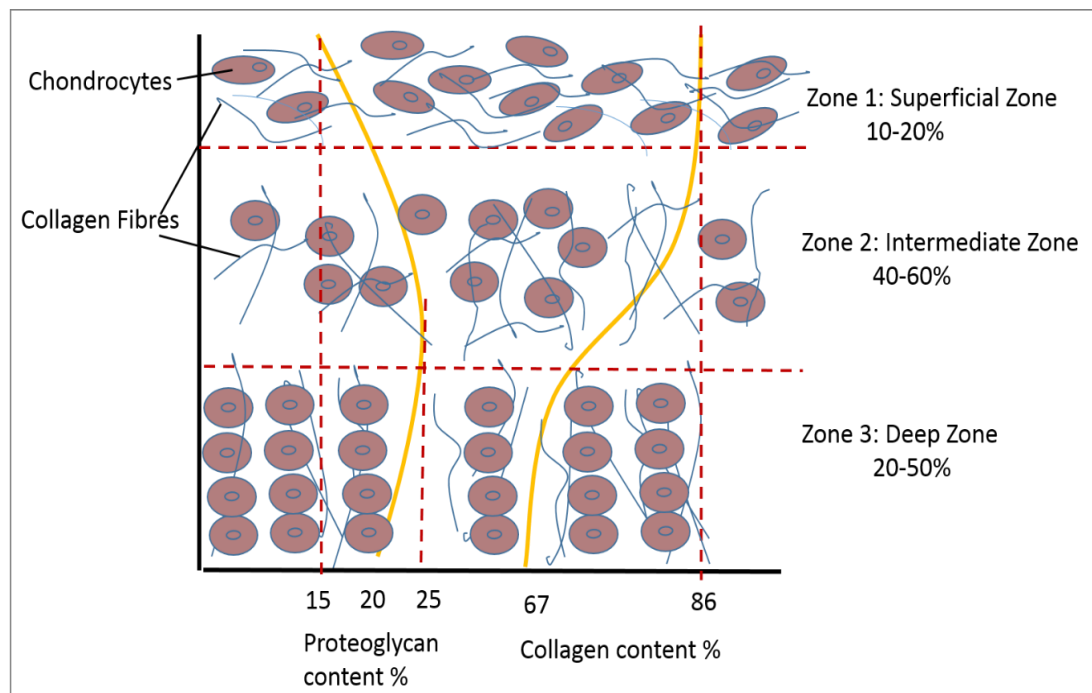
Figure 1.3. Zonal classification of hyaline cartilage highlighting the composition and structure in terms of cell morphology and collagen fiber orientation at every level. Adapted from (9, 13)

1.2.3 Arthritis Pathology.

1.2.3.1 Osteoarthritis

Osteoarthritis (OA) of the knee is considered to be one of the most prevalent forms of joint diseases affecting approximately 8.5 million people in the UK (8, 24). It is a chronic disorder characterised by the degeneration of articular cartilage ultimately resulting in the destruction of the synovial joint (24-26). This consequently causes pain, stiffness and inflammation of the diseased joint resulting in a loss of joint function and significantly impacting the quality of life of the patient. In fact, OA is considered to be the third leading cause of disease burden accounting for a sizeable contribution to morbidity and disability (particularly among the elderly) within a population (24, 27, 28).

OA primarily affects those at risk of developing cartilage damage such as those possessing various risk factors. Risk factors (described in Figure 1.4) can be categorised as either general susceptibility risk factors or specific biomechanical risk factors. Increasing age and obesity for example, significantly enhance a person's chances of developing OA. These are considered general susceptibility risk factors describing those with a predisposition for developing OA. Various activities demanding strenuous repetitive activities (such as, sports and occupations) place a person at high risk of developing OA. These are considered as biomechanical risk factors where everyday activities play a role in OA incidence. It is important to appreciate the interplay between risk factors (4, 9, 27).
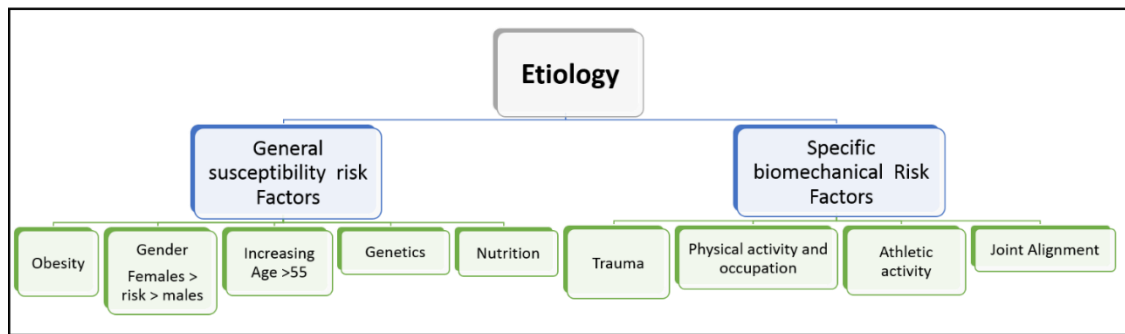
Figure 1.4 Risk factors associated with the development of OA. Adapted from (9, 13, 26, 29)

OA is initiated by damage to the articular cartilage surface creating a delicate balance of homeostasis. This is governed by the release of various catabolic factors by chondrocytes and synovial fibroblasts in response to a traumatic event (stress response). IL-1β and TNF-α are key mediators in this process effectively up regulating the expression of various proteinases (such as MMP) enzymes working to degrade components of ECM matrix (collagen and proteoglycans) (7). The overall breakdown of ECM matrix consequently leads to articular cartilage loss (24, 27). Various intrinsic repair mechanisms efficiently secrete anti-inflammatory and anabolic factors to restore the degraded ECM by inhibiting cytokine induced MMPs and blocking chondrocyte apoptotic pathways. (7). However, due to the notoriously limited healing capacity of articular cartilage, small injuries can progress into full degeneration (4, 26). In such cases, damage becomes so severe that the subchondral bone becomes exposed, triggering the production of bone and cartilage in the form of osteophytes (this response is thought to be a repair mechanism of the joint). This consequently causes the misalignments and instability of the joint relying on the stabilising ligaments to work to stabilise the joint. These structures therefore become thicker and tougher further limiting movement (16, 24-26, 30). Figure 1.5 highlights the key structural changes occurring within

an osteoarthritic knee. It can be summarised that OA is not a disease affecting only the articular cartilage but in fact a number of components related to the knee (30, 31).

1.2.3.2 Rheumatoid Arthritis

RA (a systemic autoimmune disease) is characterised by chronic inflammation of the synovial joint ultimately leading to joint destruction and subsequent disability or morbidity (32-34). It commonly affects multiple symmetrical joints such as the knee, finger and ankle in parallel, causing severe pain, inflammation and stiffness (33). RA is considered to be the most common autoimmune disease affecting approximately 1 % of the global population (32-34) and 400 000 people in the UK (30). Similar to OA, it bares significant economic burden (33) with an annual cost of £8 billion to the NHS in the UK (30). Further disability and morbidity is attributed to infection and inflammation of extra-articular organs over time. Issues related to pericarditis, pulmonary fibrosis, vasculitis are all examples of complications associated with RA (33, 34) further contributing to economic burden and reduced quality of life (33, 34).

People of all ages may be affected by RA, however, it is more prevalent with increasing age primarily affecting those over the age of 50. It is also 2-3 times more common in woman than in men (33, 34). Within 10 years of diagnosis approximately 40 % present with severe disability to the extent that they cannot work (34). The causes of RA are believed to be attributed to a combination of genetic and environmental factors (33-36). Genetic factors only account for approximately 30 % of the total number of diagnosed cases of RA whilst additional risk factors such as smoking, alcohol, stress, diet and infection are also believed to further contribute to the onset of RA (33, 34).

It is thought that these genetic and environmental factors can trigger the immune system to initiate the inflammatory process. This involves the infiltration of inflammatory cells such as; neutrophils, macrophages, lymphocytes and monocytes into the synovium causing inflammation, pain and swelling (5, 35-38). The subsequent activation of inflammatory cells causes a cascade of events whereby pro-inflammatory factors such as TNF –α and IL-B are secreted further causing the up regulation of other catabolic factors such as MMPs. This consequently causes disruption in cartilage homeostasis resulting in the destruction of the articular cartilage (34-38). Furthermore, the diseased, inflamed synovium of the knee is characterised by the presence of fibroblast-like synoviocytes (FLS). These cells grow in mass resulting in the development of the pannus. This process is fairly invasive resulting in continued erosion of bone and cartilage (6, 38). As a result, the patient experiences pain and disability.

A. Healthy Joint

Femur
Ligaments (Capsule)
Synovium
Meniscus
Articular Cartilage
Tibia

B. OA Joint

Swollen and
inflamed synovium
Exposed subchondral bone
Thinning of articular cartilage
Osteophytes
Tight thickening capsule

C. RA Joint

Swollen and inflamed
synovium
Thinning Articular Cartilage
Bone Erosion
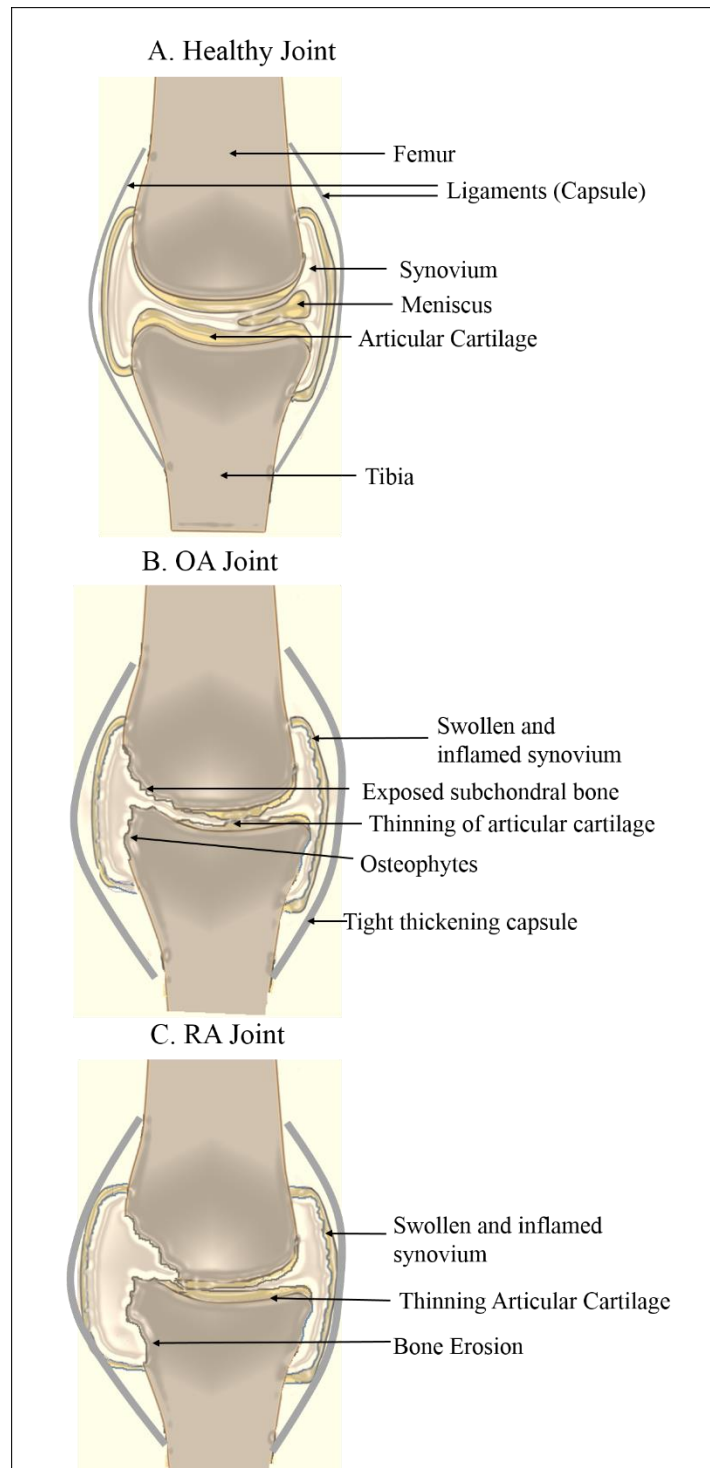
Figure 1.5. Lateral view of: A) healthy, B) OA, C) RA joint highlighting the destruction of the synovial joint adapted from Arthritis Research UK (ARUK); (8, 30).

The physical changes in the OA and RA joint are easily diagnosed by X-Ray or magnetic resonance imaging (MRI), by evaluating changes in the joint space causing the narrowing of

the cartilage and changes in bone thickness. In general, MRI is far more informative of the stages and the degree of disease (28, 33).

1.2.3.3 Treating OA and RA

There are no known cures for either forms of arthritis discussed in this document. Treatment regimens are focused on relieving painful symptoms, minimising disability and maintaining quality of life. These range from simple non - pharmacological approaches, to invasive surgical techniques (34, 39). Non-pharmacological options such as education, exercise and weight loss regiments are implemented in the early stages of the diseases and are aimed at improving general wellbeing, reducing stress, whilst increasing the strength of muscles local to the knee in order to improve joint alignment (9, 24). These approaches however are not effective at tackling the pain and inflammation associated with the disease and thus require pharmacological interventions (9). Basic pharmacological approaches implemented in early stages of the disease aim to address symptoms such as pain and inflammation by prescribing pain killers (analgesia) or anti-inflammatories. In fact, pain is considered to be the worst symptom of these diseases affecting even the most basic activities and increasing in intensity with disease progression. In extreme cases, pain may even persist at rest (24, 40). Treatments for pain have limited efficacy encouraging researchers to find better, more effective means of tackling this symptom. Nonetheless, these approaches do not impact disease progression (40). Whilst pharmacological interventions are the primary form of treatment for RA (34), they are also implemented to address pain and inflammation in early cases of OA forming the basic core treatments for OA (24). Nonetheless, these approaches do not impact disease progression and so alternative means of tackling these diseases are currently under investigation.

Osteoarthritis

When core treatments have failed, and the disease still bares significant burden on the patient; surgical approaches become necessary. In these cases, the diseased joint can be replaced with an artificial implant (arthroplasty) (13). Joint replacement techniques however are not suitable for patients under the age of 50 due to the limited life span of the prosthesis (5-10 years) (4, 24). This has motivated research into developing a means of restoring damaged hyaline cartilage through cartilage replacement techniques (4, 24, 39, 41). Examples of surgical techniques targeting the regeneration and restoration of damaged cartilage mainly include microfracture, debridement, ACI (Autologous Chondrocyte Implantation) and mosaicplasty.

- **Microfracture** involves the release of mesenchymal stem cells (MSC) from the underlying bone marrow by arthroscopically drilling into the subchondral bone within the defect area (21, 39). This initiates the flow of blood containing mesenchymal stem cells (MSCs) and cartilage progenitor cells to enter and clot within the micro fractures (20). Although this technique has received some positive results, the regenerated cartilage tends to be fibrocartilage in nature, which does not compare in terms of mechanical properties (strength) to hyaline cartilage therefore undergoing severe degradation within two years (42). Further to this, this technique has proved ineffective for elderly patients, overweight patients and for patients with lesions larger than 2.5 cm. The success of this approach is heavily dependent on the quality and health of native mesenchymal stem cell population and may account for the conflicting clinical outcomes (39).

- **Mosaicplasty** involves the isolation of osteochondral grafts from non-weight bearing regions of the knee to be subsequently transplanted within the defect area (20, 43). Practical limitation associated with this technique involves the mismatching of

surface shapes resulting in gaps between grafts in addition to damage to the donor site. Therefore, this technique is only suitable for smaller lesions (20, 21, 44).

Issue with these techniques has driven the development of cell therapy strategies to treat articular cartilage damage. This involves the administration of cells to the body for therapeutic purposes (45). The first articular cartilage focused cell based therapy was introduced by Brittberg *et al* in 1984, in a technique known as Autologous Chondrocytes Implantation (ACI). After a series of clinical successes it was later commercialised in 1994 by Genzyme (4, 42, 46). Multiple hospitals in the UK and worldwide provide ACI in routine clinical practices with good manufacturing practise (GMP) laboratories to provide cell culture services.

Autologous Chondrocyte Implantation is a surgical technique whereby samples of the patients' healthy cartilage are harvested from non-load bearing areas of the knee, digested to extract chondrocytes, expanded in culture ($\pm$ 6 weeks) in order to obtain adequate cell numbers ($5\text{-}10\text{x}10^6$) and then re-implanted into the area of cartilage damage (Figure 1.6). In early versions of this technique, the periosteal flap was sutured over the defect (4). Within three months, the defect had closed and was occupied by cartilaginous tissue. Further to this, patients experienced a reduction in pain and swelling (47). The actual mechanism of cartilage repair in ACI is unknown, however, three theories have been proposed. These include;

1) Repopulation of the defect site by implanted chondrocytes. This causes the synthesis of specific cartilage ECM components with the periosteum acting as a physical support in localising the cells in place.

2) Repopulation of the defect site by implanted chondrocytes through the synthesis of specific cartilage ECM components stimulated by the periosteum.

3) The periosteum and transplanted cells act to stimulate chondrocytes in the surrounding cartilage to enter the defected area, divide and regenerate damaged cartilage (4).
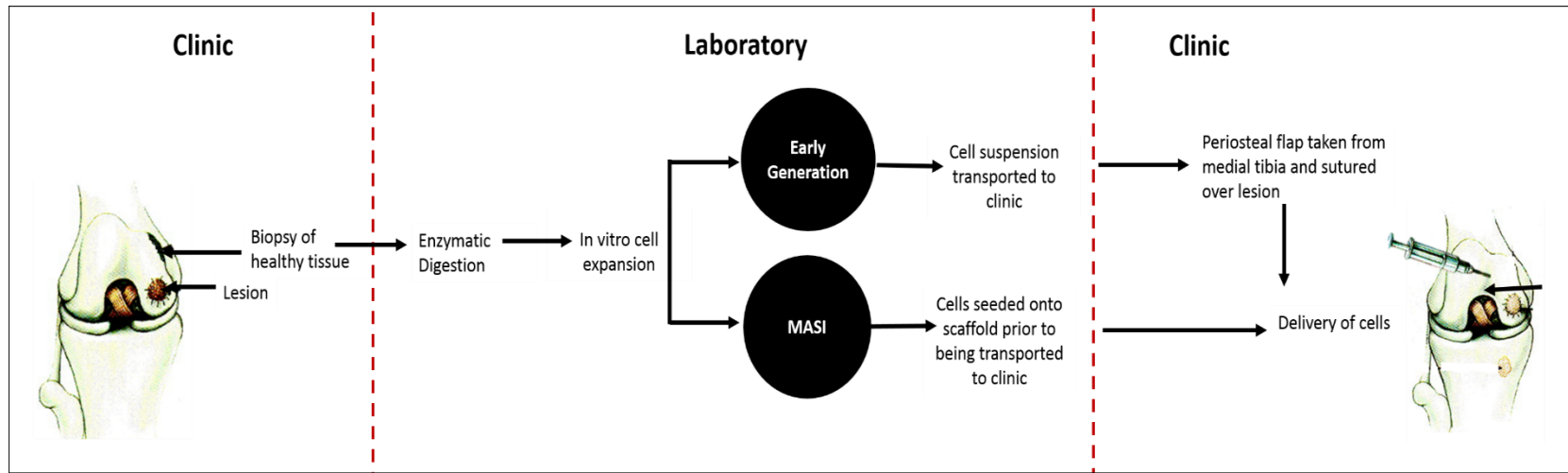
Figure 1.6. Flow chart highlighting critical steps in performing first generation ACI and MASI (matrix associated chondrocyte implantation).

Although the formation of hyaline cartilage is the ultimate clinical goal of ACI, this is often not the case and results in the formation of fibrocartilage instead in certain cases (21, 48). In a study with 23 patients, it was found that success was very much dependant on the site of the defect (49). Nonetheless, ACI has since undergone various iterations and has evolved to enhance its therapeutic potential. Iterations have focused on the replacement of the periosteal flap with natural polymers such as collagen, fibrin, and hyaluronic acid (to minimise surgery time and donor site morbidity) (50); the use of biocompatible scaffolds in matrix-associated chondrocyte implantation (MACI) approaches where scaffold have been implemented to support chondrocytes during the remodelling process (42). Little is actually known about the fate of cells in the defect. This is a topic of much interest and of vital importance. A better knowledge of cell fate post implantation can contribute to the understanding of mechanism of repair and with this, enable therapies to be optimised for maximal therapeutic output.

Rheumatoid arthritis

RA is primarily managed with drugs aimed at either treating the symptoms of the disease (pain and inflammation) or by disease modifying agents aimed at preventing further disease progression (34). These include:

- **Anti-inflammatory agents:** typically referred to as "non-steroidal anti-inflammatory (NSAID) drugs". These are primarily prescribed to address the inflammation of the knee whilst also offering some pain relief to the patient. Unfortunately, such recommendations are limited in their ability to prevent or suppress joint damage with various formulations varying in efficacy. Low doses of corticosteroids are also thought to effectively tackle pain and inflammation of the diseased joint, however these are limited to offering only short term relief (33, 34).

- **Disease Modifying Anti-rheumatic drugs (DMARDS)** are aimed at reducing or preventing further joint damage, hence preserving joint function. Unfortunately, DMARDS are limited in their ability to control pain, taking from weeks, up to months, to have an effect (33, 34)

- **Cytokine antagonists** work to inhibit the activity of cytokines (e.g.TNF-α) participating in the onset and progression of inflammation in RA. However, these are very expensive requiring intravenous administration and are associated with unpleasant toxic effects (51).

For optimal results, a combination of these drugs is prescribed to address disease symptoms in addition to disease progression. However, such drug regiments are particularly unpleasant to the patient causing significant side effects whilst also being very expensive. Additionally, these drugs have varying effects and results are highly patient dependant. In some cases, patients may even become resistant to these drugs, thus continuing to cause significant disability (51, 52). In certain extreme cases, minor operations may become necessary to either correct deformities or replace the damaged joint in the case of the hip and knee (53).

The chronic inflammatory environment of the rheumatic arthritic joint renders cartilage regeneration techniques (implemented in OA) ineffective, as similarly to the original native cartilage, newly formed cartilage undergoes destruction within the hostile environment (6). This highlights the growing need for more effective means of restoring damaged cartilage in RA patients (42).

1.3 Motivation for Cell Therapies.

Pain and inflammation can be effectively treated offering some relief for OA and RA sufferers. Although some progress has been made in the restoration of damaged cartilage, these techniques (mosaicplasty and microfracture) are not always successful in offering the OA patient full function of their joint and are not suitable for RA sufferers (6). Cell therapies based on ACI are believed to hold most promise in treating full cartilage defects, even though long term follow up studies have not conclusively demonstrated the clinical advantage of implementing ACI over microfracture (49) and moisacplasty (54).

A number of limitations have been attributed to ACI:

1. The dedifferentiation of chondrocytes when cultured in monolayer encouraging the formation of fibrocartilage as opposed to hyaline cartilage when replaced in the joint (50).

2. Quality of isolated chondrocytes is highly donor dependant (age and degree of disease progression) leading to impaired cartilage repair (50).

3. The need to isolate healthy cartilage from a non-weight bearing region in the knee placing further burden on the patient, donor site morbidity and increased risk of developing OA in the future (50).

4. The use of the periosteum to localise cells to the defect increases surgery time and donor site morbidity. Although commercial product such as Chondroguide have reduced this issue (50).

5. The unpredictable and non-reproducible variability in tissue quality (50).

ACI forms a solid foundation to develop alternative cell based therapies for OA and RA. In ACI, the cartilage defect is used to trigger the production of cartilage. This environment has all the necessary physical and chemical factors required for cartilage regeneration (55). This has encouraged the development of approaches mimicking this *in vivo* environment whereby the implanted cells can either repopulate the damaged area or stimulate the surrounding cartilage cells to divide and repopulate defected areas (6). ACI is only effective in those suffering from OA but not RA. The hostile environment of the rheumatic joint renders this approach ineffective as similar to native cartilage the newly synthesised cartilage will also undergo destruction. However, by diversifying this approach to include alternative cell types such as mesenchymal stem cells, novel and plausible approaches to tackling RA can be developed based on the traditional ACI approach. The application of stem cell-based therapies therefore has the potential to develop a reproducible means of promoting high quality tissue (comparable to that of native cartilage in terms of biochemical and mechanical properties). The therapy would aim to replace and/or repair damaged cartilage and provide the opportunity for full recovery along with total joint function. This would ultimately hold promise to fully eliminating diseases such as OA and RA (21, 24).

1.3.1 Cell Therapies

The newly established Cell Therapy Catapult in the UK, defines a cell therapy as: "Any treatment for a medical condition that employs at its core one or more types of viable human cells" (56). Cell therapy is a platform technology employed in many fields of medicine including regenerative medicine (57). Cell types employed in the development of such therapies include the use of the patient's own cells (autologous), donor derived (allogeneic) cells, stem cells (adult stem cell, embryonic stem cells and induced pluripotent stem cells)

and immune cells. Examples of cell therapies include; bone marrow transplantation (earliest stem cell-based therapy dating back to 1968), the application of chondrocytes in treating cartilage lesions as described previously for ACI (56, 58), the autologous transplantation of limbal stem cells for corneal disorders and finally the implementation of T cell in autoimmune therapies (59). In the context of regenerative medicine, cell therapy approaches are implemented to replace, regenerate and restore the function of damaged or injured tissues/organs, primarily using stem cells (1, 57)

Tissue Engineering (TE) is one particular branch in the cell therapy industry (57) and involves the combined use of cells, engineering materials and biochemical factors to develop *ex vivo* living tissues and organs that can be implanted within the body to repair injury or replace the function of a failing organ (42, 45, 60). TE skin grafts were some of the earliest TE strategies developed dating back to 1981 (42). Since then, TE strategies have extended to the development of the first bio-artificial neo bladder by Atala and colleagues (61). In fact, the possibilities of TE has extended to the engineering of whole organs such as livers, pancreases, and cartilage (62).

Cell therapies are believed to significantly impact the way OA and RA are treated in the future. The precedent for developing cell therapies in treating debilitating diseases such as OA and RA lie with ACI (58). The ultimate clinical goal of ACI is to restore and repair damaged articular cartilage offering the patient complete function of the joint resulting in the improvement of quality of life (63). The choice of cells is vital in the success of such therapies. Tissue specific cells, (chondrocytes) and stem cells (MSCs) are ideal candidates in the development of cell-based therapies for OA and RA. Reasons will be discussed below.

1.3.2 Cell Types

1.3.2.1 Mature Chondrocytes

Chondrocytes isolated from articular hyaline cartilage possess the desired phenotype and are pre-conditioned to synthesise the correct components required to repair damaged cartilage. This makes them potentially the ideal cell source for cartilage regeneration (12)(13). Chondrocytes may be isolated from a host, and used either for the same host defining an autologous cell therapy or for a different host (of the same species) defining an allogeneic cell therapy (45). The standard argument for use of autologous cells versus allogeneic cells apply here, where the major disadvantage of using allogeneic cells concerns immune rejection and the risk of disease transmission (10). While, isolating autologous chondrocytes from healthy tissue limits the amount of cells that can be sourced due to the risk of donor site morbidity. This makes it particularly difficult to meet specific patient needs and requires the *in vitro* expansion of isolated chondrocytes to obtain clinically relevant numbers (13, 42, 62, 64). This introduces the problem of dedifferentiation. Chondrocytes are known to dedifferentiate rapidly when cultured in monolayer becoming more fibroblastic like (64). Under these conditions, chondrocytes have been known to lose their phenotypic markers rapidly subsequently causing the loss in their characteristic expression and instead promoting the synthesis of collagen type 1 (characteristic of fibrocartilage). Hence, newly synthesised cartilage will lack the mechanical properties required to withstand loads in the knee (7, 13, 23). These issues are overcome by applying various culture techniques including; a 3D culturing environment, hypoxic conditions, mechanical stimulation and growth factors (64). Finally, the quality of isolated chondrocytes is highly donor dependant (age and degree of disease progression) further limiting the application of chondrocytes in cell therapy application (50). Hence, alternative cell sources are desired for better cartilage regeneration

such as stem cells which are potential candidates to be incorporated into cartilage tissue engineering strategies. (24, 64).

1.3.2.2 Stem Cells

Stem cells are defined by: a) their ability to self-renew via symmetrical cell divisions to maintain the pool of undifferentiated stem cells and b) the ability to undergo asymmetric cell division giving rise to daughter progenitor cells capable of differentiation (45, 65). These properties are particularly important *in vivo* to reconstitute any given tissue as a repair mechanism (66). Stem cells are found within specialised 3D micro environments also referred to as niches. Stem cell niches are responsible for controlling the properties, activities and gene expression through signalling molecules, cell-cell interactions and interaction with the ECM. Stem cells are further categorised by their plasticity or their flexibility to differentiate into mature cell types and are defined as being either totipotent (giving rise to all embryonic and extra embryonic cell types e.g. Zygote), pluripotent (giving rise to all cell types of the embryo apart from the placental cells e.g. Embryonic Stem Cells) or multipotent (giving rise to few specialised cell lineages e.g. Adult Stem Cells)(42, 66).

Although embryonic stem cells may have a greater differentiation capacity than adult stem cells, their clinical application is limited by ethical concerns linked to their isolation and potential teratoma formation (*in vivo*) (1, 42, 62). In comparison, adult stem cells are easily sourced from a range of tissues including, bone marrow, blood, brain, liver, muscle, and skin potentially forming the basis of a number of therapies such as diabetes, neural degeneration and ischemia (62). Table 1.3 highlights the various adult stem cells available. For these reasons adult stem cells are the preferred choice in tissue engineering purposes.

Table 1.3. Examples of adult stem cells, their location *in vivo* and their differentiation capacity (67).

Cell Type	Tissue Specific Location	Differentiation Capacity
Hematopoietic stem cells	Bone marrow Peripheral blood	Bone marrow and blood lymphohematopoietic cells
Mesenchymal stem cells	Bone marrow Peripheral blood	Bone, cartilage, tendon, adipose tissue, muscle, marrow stroma, neural cells
Neural stem cells	Ependymal cells, astrocytes (subventricular zone) of the central nervous system	Neurons, astrocytes, oligodendrocytes
Skeletal-muscle stem cells or satellite cells	Muscle fibres	Skeletal muscle fibres

Bone marrow derived MSCs are considered to be the ideal candidate in the development of stem cell-based therapies. This is attributed to the well-established, optimised and characterised isolation and expansion protocols with proven therapeutic potential associates with this cell source (6, 68).

Mesenchymal Stem cells (MSCs)

MSCs (also known as bone marrow stem cells and bone marrow stromal cells) are multipotent cells with the ability to differentiate towards tissues of the mesenchymal lineage to form osteocytes, chondrocytes and adipocytes both *in vitro* and *in vivo* (69-71). More recently it has been discovered that MSCs may potentially have greater plasticity than originally thought, as demonstrated by their differentiation into neurons, hepatocytes, fibroblasts, tenocytes and cardiomyocytes (72, 73). MSCs reside within specialized 3D micro environments (niches) of connective tissues within various tissues (e.g. bone marrow, synovium, adipose tissue and umbilical cord) (24, 31, 46, 69). The bone marrow stroma is a complex structure housing a variety of cell populations creating the niche for haematopoietic stem cells; synergistically the haematopoietic stem cells also create the required niche for the bone marrow stromal population (74). Within the bone marrow cell populations,

approximately 0.001-0.01% are known to be multipotent MSCs (68). However, similar to chondrocytes, donor variability may play a significant role in impacting quality and therapeutic potential of cells.

MSCs do not possess a unique panel of markers that can be reliably and accurately used for characterisation purposes, consequently relying on a combination of techniques to successfully identify these cells (46, 68, 69, 75). The following criteria have been set by The Mesenchymal and Tissue Stem Cell Committee of the International Society for Cellular Therapy. These include;

- Ability to adhere to plastic when maintained under standard culture conditions (75).

- Positive expression of: CD (cluster of differentiation) 73, CD90, and CD105

- Negative expression of haematopoietic markers: CD11b, CD14, CD19, CD34, CD45, CD79a, and HLA-DR (24, 75)

- Ability to differentiate to osteoblasts, adipocytes, and chondroblasts (75)

MSCs have had a significant impact in the field of regenerative medicine as demonstrated by the extensive and impressive portfolio of therapies in research today. Examples include the use of MSCs to treat myocardium infarction (76), spinal cord injuries and osteogenesis imperfecta, with successes being demonstrated in a range of animal studies (68).

The therapeutic potential and consequent clinical application of MSCs are further governed by the release of soluble factors (such as growth factors and chemokines) by MSCs, generating a regenerative environment by mediating anti-apoptosis, cell proliferation, differentiation of stem cells, mitosis and angiogenesis, immunomodulation, anti-scarring and chemo-attractant properties (6, 70). This potential is known as trophic activity (6). The factors involved in each of these activities are shown in Figure 1.7.
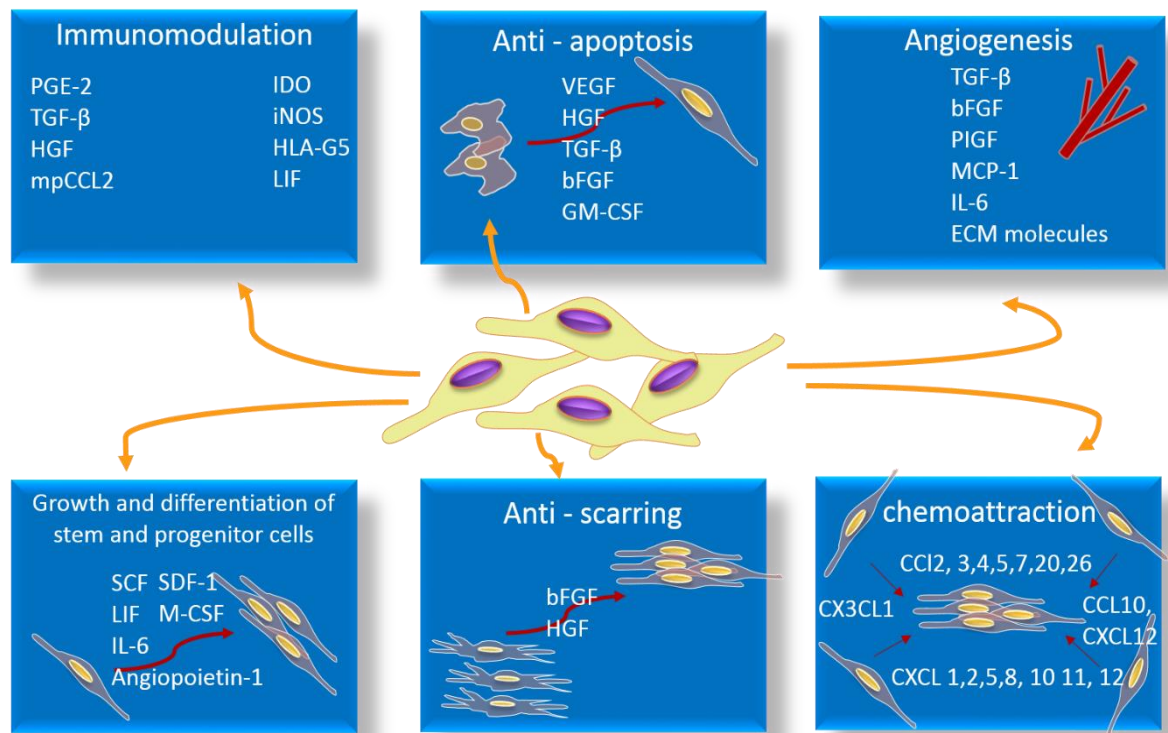
Figure 1.7. Paracrine effects of MSCs highlighting key bioactive molecules secreted defining the theraputic properties of MSCs; Immunomodulation, Anti-apoptosis, Angiogenesis, Chemoattraction, Antiscarring, Growth and differation (70).

It has been suggested that cell therapies focused on treating cartilage defects should not ignore other components of the knee such as bone and ligament, as these are also affected by the disease. MSCs can therefore not only address the structural issues (attributed to their ability to differentiate towards bone, cartilage and adipose tissues - the tissues of interest) (6) but their immunosuppressive and anti-inflammatory properties enable the inflammation and autoimmune aspects of the disease to also be addressed (24). The release of cytokines and growth factors such as interleukins (IL)-10, (IL)-6, (IL)-11 and TGF-β (transforming growth factor – β) act to inhibit T cells and dendritic cells (77, 78) whilst the secretion of soluble antigens such as HLA-g (human leukocyte antigen G) effectively disable natural killers and moderate dendritic cell and T cell activity. In addition, secreted immunosuppressive enzymes such as IDO (Indoleamin 2, 3-dioxygenase), suppress

leukocytes such as B cells (77, 78). The combined secretion of these factors, their role in tissue homeostasis and repair (governed by signalling mechanism) (79) and the cartilage forming ability of MSCs, provide a trophic regenerative environment, stimulating the proliferation and differentiation of tissues to achieve intrinsic repair whilst protecting the neo tissue in a localised immunosuppressive manner (6, 77, 78). The immunomodulation effects have been shown *in vivo* in animal models where MSCs have shown success in treating grafts versus hosts disease (24, 69, 70). This supports the use of MSCs in cartilage tissue engineering as a means of treating OA and RA (6).

1.4. Imaging and Tracking – The Need

The clinical adoption of any cell-based therapy demands the systematic and regulated progression from bench to bedside to evaluate and demonstrate the safety and efficacy of the proposed therapy before ultimately receiving clinical approval (80). Animal models are in place to not only address safety concerns, but also to assess the efficacy of the therapy. Issues related to the extent of tissue integration, migratory patterns post transplantation, dosage schemes and optimal delivery route, are primarily addressed with the implementation of relevant animal models (19, 36). These questions are central to a wide range of cell based therapies, the answers to which are vital in the assessment of the risks and success rates of the therapy whilst optimising the therapy's potential and are of key importance to the regulatory bodies (such as the Food and Drug Administration; FDA)(80). These studies can fundamentally offer an insight into the short and long term survival of the cells, rate of repair, and the number of cells remaining or migrating to/from the desired location (bio-distribution). With this data, physiological repair mechanisms can be better understood

which allows for delivery methods and dosage schemes to be fully optimised (81), therefore enhancing therapeutic potential (82).

Traditionally, gathering such data has been performed by carrying out histological and immuno-histochemical tests (83-85). This is highly invasive, as a biopsy of the tissues of interest needs to be taken (86) and often demands the euthanization of animals to collect tissue samples for assessment. Furthermore, continuous and repetitive long term follow up of animals is impossible, therefore high numbers of animals are required to thoroughly investigate all parameters to make statistically significant conclusions (83, 86, 87). The initiative in place by NC3Rs aims to reduce, refine and replace the number of animals used in research. This highlights the need for a non-invasive means of accurately and reproducibly evaluating *in vivo* events occurring post-implantation to evaluate the success and risks of the given therapy (86, 88, 89).

A range of non-invasive clinical imaging modalities are currently available and possible candidates to image and track stem cell populations *in vivo*. These include, Magnetic Resonance Imaging (MRI), Magnetic Resonance Spectroscopy (MRS), Positron Emission Tomography (PET), Single Photon Emission Computed Tomography (SPECT), Bioluminescence Imaging (BLI) and X-ray based computed tomography (CT). However, there are pros and cons associated with each of the mentioned imaging modalities for cell tracking applications. MRI for example, suffers from low sensitivity but benefits from high resolution, i.e. 25-100 μm (90). On the other hand, SPECT, PET and BLI have higher sensitivity but unfortunately much lower resolution when compared to MRI (1-2 mm) (90). Furthermore, MRI is traditionally linked to the use of FDA approved iron based magnetic nanoparticles (SPIONs) contrast agents, which endeavour to improve the sensitivity of the technique without the exposure of ionizing radiation (as is the case for SPECT, CT and PET) (91). Its non-invasive nature, coupled with the rapid and repetitive acquisition of images (92)

and the ability to distinguish between soft and hard tissues at high contrast, makes MRI a very powerful clinical diagnostic tool (93) and a highly suitable candidate for the imaging and tracking of implanted cell populations *in vivo*. (84).

It is thought that superparamagnetic iron oxide nanoparticles (SPION) can be employed in conjunction with the use of magnetic resonance imaging (MRI) to track implanted cells *in vivo* (94, 95). In essence, stem cells are encouraged to internalise SPION; in this way, implanted cells can be distinguished against host cells/tissues when MR imaged, facilitating the identification and tracking of cells *in vivo* when imaged by MRI (Figure 1.8) (96). The non-invasive imaging and tracking of implanted cells *in vivo* requires the labelling of cell populations with suitable SPIONs at significant quantities to allow implanted cells to be distinguished against host cells/tissues (97). It is essential to select biocompatible label e.g SPIONs that do not interfere with the basic function of the cell and in turn also not affect any aspects of stem cell differentiation (95). With this a great deal of *in vivo* information can be gathered and therapies optimised, not only for arthritic cases but for a large portfolio of cell based therapies (89).
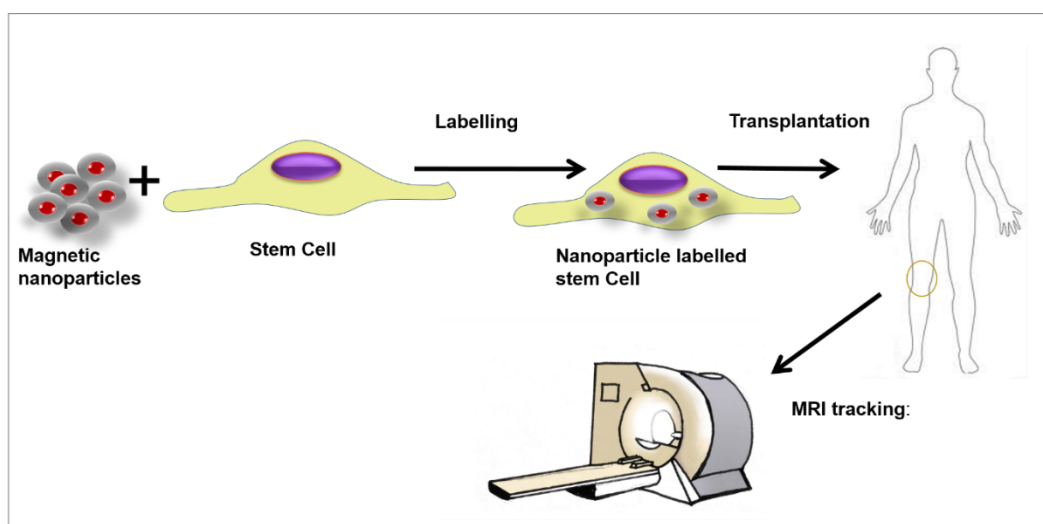
Figure 1.8. Schematic highlighting the principle of *in vivo* cell imaging and tracking with the application of MRI and SPIONs, image modified and adapted from (86).

Early SPION-based tracking studies involved the intravenous administration of SPIONs which were subsequently taken up by various cells such as macrophages. The migratory patterns and location of labelled macrophages were easily identified as hypointense regions of signal loss on MRI images (98)(97). This proved particularly useful in the *in vivo* evaluation of inflammatory disease models. For example, areas of liver damage were identified by the lack of hypointense regions on MR images, implying that the damaged structure of the liver prevented the infiltration of labelled Kupffer cells (specialised macrophages) (98)(97). Other examples include the monitoring, biodistribution and activity of macrophages in rat and mouse models of autoimmune encephalomyelitis as well as models of ischemia renal damage. Beckmann *et al* demonstrated using SPION and MRI technologies, the ability to monitor the infiltration of macrophages into a rat knee of antigen induced arthritis (99). Finally, this technology has also been implemented in the visualisation of organ engraftment or rejection where a good correlation was found with hypointense signal (signifying macrophage infiltration) and graft rejection (100). The practicality and usefulness of these studies encouraged the utilisation of MRI and SPION based *in vivo*

molecular imaging in regenerative medicine and tissue engineering applications in order to evaluate aspects of cell migration and tissue integration. Stem cell-based therapies primarily involve the implantation of stem cell populations within the body, which in contrast to the above studies require the labelling of cell populations *in vitro* as opposed to *in vivo* (97). Since the development of *in vivo* labelling strategies, small animal *in vivo* tracking studies have been developed (101). Table 1.4 summarises some of the recent SPION and MRI based tracking studies in tissue engineering and regenerative medicine.

Table 1.4: Recent SPION and MRI based Studies.

Study	Tracking system	Cell Type	Particles	Size of particle	Concentration	MRI	Results	Ref
Tracking the delivery and engraftment of MSCs in tumours	*In vivo*; Rat	MSC	FluidMag	200 nm	0.5 mg/ml	9.4 T	Efficient uptake of particles. MSC characteristics maintained. Proliferation not affected, 1000 cells visualised at 28 days	(102)
Tracking autologous MSC in knee for ACI	*In vivo*; Rabbit	MSC	Endorem	150 nm	25 µg/ml	1.5 T	Labelled cells can be visualised by MRI Autologous MSC not located within defect MSC characteristics maintained, Proliferation not affected	(83)
Tracking autologous MSC in knee for ACI with microsized iron oxide particles; Defect size 5mm x 9 mm	*Ex vivo*; Bovine knee	MSC	Unknown	1630 nm	2.8 µg/ml	3 T	Efficient uptake of particle by cells MSC characteristics maintained, Proliferation not affected MPIO visualised in the defect Effect of MPIOs in chondrogenic differentiation showed that pellet did form but aggregation of Fe in pellet hinders ECM visualisation	(103)
Tracking MSC injected into the heart	*In vivo*; Mini pigs	MSC	Resovist	60 nm	25-400 µg/ml	1.5 T	Cell growth and viability not affected by Fe concentration	(104)
Detectability of labelled MSC and gene expression	*In vitro*; Agarose gel	MSC	Resovist vs Endorem + transfection agent	60 nm and 150 nm	12.5 µg/ml	1.5 T	More efficient uptake of particles with Feridex than Resovist Feridex had greater signal loss implying better detectability by MRI. Proliferation not affected by either particle. Particles lost one week after loading due to dilution effect Change in expression of Oct -3/4 and CD 45 of labelled cells	(105)
Investigating the detectability of chondrocytes	*In vitro*; Hollow	Chondrocytes	Endorem + transfection agent	150 nm	25 µg/ml bioreactor	9.4 T	Chondrocytes can be labelled efficiently and imaged No negative effect on chondrogeneic genes.	(96)

within tissue engineered scaffold	fibre bioreactor, Hydrogel				67 µg/ml Hydrogel			
Tracking MSC in liver cirrhosis model	*In vivo*; Rats	MSC	Ferrite core Silica shell and fluorescent material (name unknown) vs Feridex	Information not available	100 µg/ml	3 T	Labelled cells could be seen in the liver No significant difference between Feridex and Silica labelling	(106)
Assess the effect of SPIO labelling on adult human chondrocytes behaviour	*In vitro*; Alginate	Chondrocytes	Endorem	150 nm	168 µg/ml	*Ex vivo* 3 T Cells suspended in alginate	Inserting 1000 cells in a defect 4mm in size, could not be detected. However, when 10 000 and 100 000 cells were implanted, clear signals were observed and easily distinguishable from surrounding cartilage This shows how MRI can be used to investigate the number of cells required for a successful therapy.	(107)

1.5. Nanoparticles

In recent years, nanoscale materials have been the focus of much research in regenerative medicine and tissue engineering. Nanoscale materials in the forms of nanoparticles, nanofibers, and nanotubes have been fabricated and specifically tailored to suite their role and function in the development of cell based therapies and tissue engineering strategies (108).

Of particular interest are nanoparticles due to their unique, electronic, optical, and magnet properties. Nanoparticles are organic or inorganic materials with three external dimensions at equal nanoscale (109). Their specific size and dimensions allow them to be accurately manoeuvred and targeted to a specific biological entity or biological component (110) and interact on a cellular (10-100 μm), subcellular (20-250 nm), protein (3-50 nm) or genetic scale (10-100 nm) (111, 112). This facilitates a broad range of applications in the biomedical field in terms of cell isolation, drug delivery, diagnostics (MRI), cellular imaging and magnetic hyperthermia (111, 112). Examples of nanoparticles include liposomes, quantum dots, polyplexes, magnetic nanoparticles (MNPs) (86, 113) and carbon-based nanoparticles (114). MNPs in particular have a multifunctional role within the field of regenerative medicine and tissue engineering where they can be used in the tagging, tracking (115) and activation of stem cells with significant implications in cartilage tissue engineering (116-118).

1.5.1 Magnetic Nanoparticles (MNPs)

Magnetic nanoparticles are principally magnetic materials with three dimensions of equal nanoscale. Various materials can be used to convey the magnetic properties of MNPs such as nickel, cobalt and iron. It has been found that cobalt and nickel are toxic to biological entities effectively eliminating their biomedical application while iron based particles are considered safer for biomedical use (119, 120). Figure 1.9 illustrates the structure of a magnetic nanoparticles. Improved biocompatibility and handling is achieved by coating the magnetic core with a variety of organic (fibronectin, polysaccharides) and inorganic (silica and gold) polymers (119). The biocompatibility minimises the risk of toxicity as a result of being in indirect contact with the metal core, whilst offering a platform to further customise the particle for specific applications (121, 122). Surface coating can be functionalised in terms of; charge, protein binding capacity and biomolecules (118). This encourages enhanced interaction with biological entities with minimal toxic effects (111, 123). The nature of the polymer coating and the consequent modifications determine the ultimate physical and biological properties of the particles such as the size, charge, toxicity and degradability (91). This dictates the success of the chosen application demonstrating how important particle characteristic choice is. The versatility of MNP means that they can be tailored to specific purposes and so this opens up an enormous range of potential applications. In the field of nano-medicine, MNPs have been utilised for applications such as targeted gene/drug delivery, hyperthermia treatment of tumours, or stem cell tracking by MRI (124).
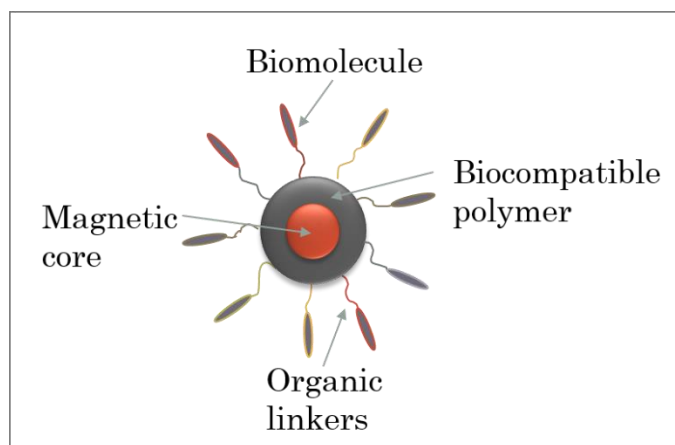
Figure 1.9. Structure of a magnetic nanoparticle.

The behaviour of a MNP within an applied magnetic field is governed by the magnetic properties of the particles and can be categorised according to their susceptibility to the application of an external magnetic field (125). In general, magnetism observed in nature is categorised by the orientation of the magnetic moments and can be defined as: a) diamagnetic, b) paramagnetic, c) ferromagnetic, d) antiferromagnetic and e) ferrimagnetic. Diamagnetism is considered a very weak type of magnetism displayed by all materials (126) while paramagnetic substances are only magnetised when exposed to a magnetic field. On the other hand, ferromagnetic or ferrimagnetic materials remain magnetised even after the magnetic field has been removed (119). Importantly, ferromagnetic materials develop paramagnetic properties as they decrease in size to approximately 20 nm in diameter (110, 127). This implies that once the magnetic field has been removed, the particles are no longer magnetic but still maintain a high magnetic saturation magnetism. This is known as superparamagnetism. For the biomedical application of MNPs, particles exhibiting superparamagnetic properties are preferred as this implies that the particles will not be attracted to each other and so the risk of agglomeration in a medical setting is minimised (128, 129).

1.5.2 Superparamagnetic Iron Oxide Nanoparticles (SPIONs)

SPIONs are a specific class of magnetic nanoparticle, which are well known for their application as a T_2 weighted MRI contrast agent (130). They are typically composed of either a magnetite (Fe_3O_4) or maghemite (γ-Fe_2O_3) core (125, 131), both of which are ferrimagnetic in nature. However, as they decrease in size below 30 nm, they lose their permanent magnetism and become superparamagnetic (109). These cores can then either be coated with a biocompatible polymer as described previously (121, 132), or precipitated through a larger porous polymer hence generating overall larger particles (greater than 30 nm in diameter) whilst maintaining superparamagnetic properties (Figure 1.10) (125, 133). Alternatively, the larger nanoparticles may be generated by controllably aggregating nanoparticles. SPIONs can be further categorised by size although there is no clear consensus as to the specific size range making up each class. However, as a general indication, ultrasmall superparamagnetic iron oxide nanoparticles (USPION) are below 50 nm in diameter; SPIONs are hundreds of nanometers in diameter and micron-sized MNPs are (MPIO) >1 µm (134). For the purpose of this thesis, the term SPION will be used to refer to iron oxide nanoparticles with superparamagnetic properties of all sizes. SPIONs are particularly suited in their application as MRI contrast agents given their biocompatible nature and ability to generate significant contrast with little risk of *in vivo* agglomeration (97, 120, 129, 135). This highlights the potential use of SPIONs to image and track stem cell population *in vivo* using MRI technologies.
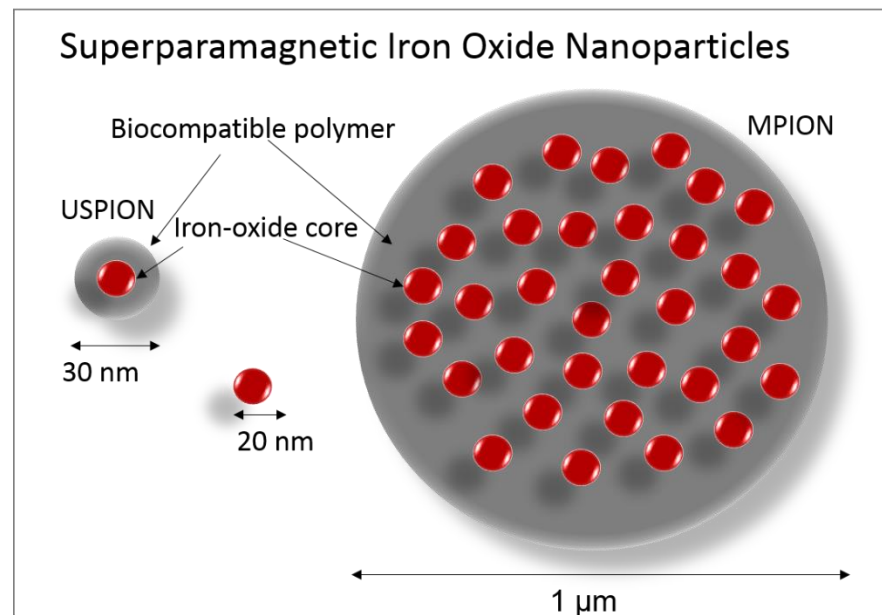
Figure 1.10. SPIONs demonstrating the size and distribution of superparamagentic iron cores within biocompatible polymers to generate UPSIONs and MPIOs.

The use of FDA approved SPIONs are particularly attractive in the implementation of MRI based tracking protocols. Endorem (also referred to as Feridex) and Resovist are all examples of FDA approved, iron-based MRI contrast agents which have been used to image and track cells by MRI in recent years (125, 136). However, these particles have recently been removed from the market (125, 137) and alternative particles have been investigated for biomedical application such as cell tracking purposes. Based on the intended application of these particles, a list has been devised stating the properties that a SPION should have, before being considered for cell tracking purposes. The commercial market for SPIONs is both large and extensive (119) and therefore, commercially available particles may also be suitable for biomedical applications as long as the particles comply with the below list.

PROPERTIES OF SPIONS FOR BIOMEDICAL APPLICATIONS (133)

1. Low toxicity

2. Biocompatible

3. Chemically stable in physiological conditions

4. Biodegradable

1.6. SPION labelling of cell populations

SPION labelling of cell populations is a necessary prerequisite in the imaging and tracking of cell populations by MRI. Intracellular and extracellular approaches have been suggested as a means of SPION cell labelling (82, 138, 139) (Figure 1.11). The ability to functionalise the surface of SPIONs with various ligands (such as; small molecules, antibodies or specific proteins) allows for SPIONs to be specifically targeted to various cell surface receptors or ion channels and encourage extracellular labelling (118, 124). Alternatively, cells can actively internalise SPIONs within the cell cavity resulting in intracellular labelling. The general mechanism of internalisation in non-phagocytic cells (such as stem cells) is believed to be endocytosis with this specifically been divided into the following categories; clathrin-mediated endocytosis, caveolaemediated endocytosis, macropinocytosis, phagocytosis and receptor mediated endocytosis (86, 91). This technique results in the intracellular accumulation of SPION and is shown in Figure 1.11.

Internalisation is more suited for *in vivo* tracking as this approach results in increased iron concentrations improving the detectability of detecting implanted cells *in vivo* whilst also increasing the resolution of the image (86, 95). Furthermore, SPION internalisation

facilitates long term monitoring of implanted cell populations as SPIONs are less likely to be dissociated from the cells in the early stages of labelling and tracking (103, 123). However, internalisation is limited by the dilution of the SPION label during the proliferation and cell division of cells or via the physical removal of the particle by exocytosis. The rate of internalisation depends on a number of factors including, cell type, particle size, hydrophobicity, surface charge of particle polymer and the rate of cell proliferation (118). This method tends to be time consuming and is limited to cells that have a high degree of phagocytosis (140). Cells exhibiting a low degree of phagocytosis may require prolonged incubation for the efficient internalisation of SPIONs. This may be undesirable, as extended culture could impair the potency of the cells or redirect differentiation towards an unwanted lineage (141). The use of transfection agents (TA) can be employed to increase labelling efficiency in a shorter period of time, as they can form complexes with SPIONs, therefore increasing uptake by phagocytosis (98, 123). Examples include poly–L-lysine, protamine and cationic liposomes (140). In a study by Kostura *et al* it was found that Feridex- poly-L–lysine inhibited chondrogenesis; however, this was not found with Feridex – protamine (142, 143). Thus the effect of the TA must be investigated further as it could interfere with the activities of the cell (144). To overcome these limitations incurred by internalisation and the use of TA, a technique known as ''magnet electroporation'' has been introduced (137). Essentially, a magnetic field is used to induce the accumulation of the contrast agent in the cytoplasm of the cell by increasing membrane permeability (140). This eliminates the need for transfection agents (TA) but unfortunately this is considered somewhat damaging to cells (137). Past studies demonstrated the ability of SPIONs to be taken up by a wide variety of cells by simple incubation, these included; fibroblasts, lung cells, liver cells, stem cells, kidney cells, macrophages, nerve cells, endothelial cells and various cancer cells lines (109).
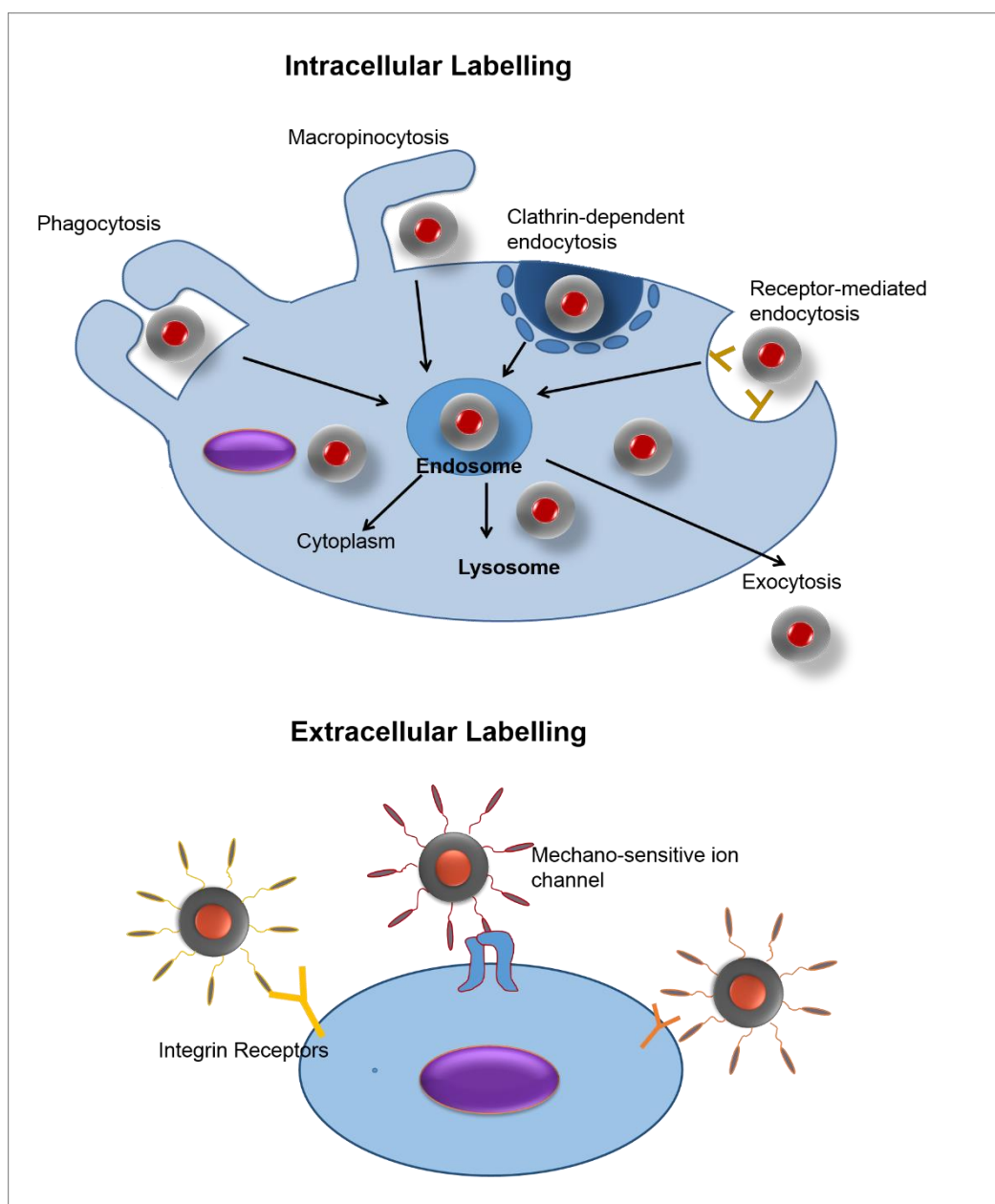
Figure 1.11. Schematic highlighting intracellular and extracellular cell labelling. Intracellular labelling involved the internalisation of SPION via various endocytic mechanisms; clathrin-mediated endocytosis, macropinocytosis, phagocytosis and receptor mediated endocytosis. Extracellular labelling involves the attachment of SPION to various integrin receptors or ion channels aided by the functionalization of particles with specific biomolecules.

1.7. Toxicity

When considering SPION for any biomedical application, the toxic nature of the particles must be considered (145). SPIONs are considered to be inert and biocompatible given the nature of iron (146). Iron is a naturally occurring element in the human body (ferritin) playing an important role in cellular metabolic processes such as DNA synthesis, oxygen transport, and redox reactions (117, 147). The body is therefore adapted for iron metabolism and thus labelling cells with SPIONs is not likely to affect biological properties of cells (147). However, in high quantities and in various oxidation states, Fe can possibly impair cell viability by damaging cell membranes, causing morphological changes in proteins and DNA (105, 147). This can have adverse effects on cell viability, proliferation, metabolic activity and impair the therapeutic efficiency of the therapy (148, 149). Iron is found in two main oxidation states; Fe (II) and Fe (III). Fe (II) is thought to be the main source of cellular damage as a direct consequence of free radical generation (150). At the cellular level, oxidative stress is thought to be the main cause of toxicity by MNPs. Oxidative stress arises when there is an imbalance between damaging oxidants also referred to as reactive oxygen species (ROS) such as hydrogen peroxide, hydroxyl radicals, and the protective antioxidants of which vitamin C and glutathione are examples. ROS are primarily formed by the incomplete reduction of oxygen. The accumulation of oxidants eventually leads to destruction of cellular proteins, enzymes, lipids, and nucleic acids, and as a consequence the normal cellular processes become impaired leading to the development of diseases and cell apoptosis and necrosis (117). Therefore, it is important to obtain a balance between Fe incorporation for the required role and cell function (105). Labelling stem cells for this application, therefore demands the preservation of physiological cellular properties and the retention of SPIONs over prolonged periods (140).

The toxicity of SPIONs on biological entities is highly dependent on a range and combination of factors related to the properties of the SPION itself as well as structural properties, dosage and the intended use are also among dominating factors (148, 151). The chemical composition of the particles themselves can be naturally toxic. Additionally, the location of SPIONs in relation to the cells is an extremely important consideration (148). For instance SPIONs could invoke a cytotoxic response when internalised by potentially interfering with the biological function of the cells but not when attached to the cell membrane (123, 148). However, in other cases, SPIONs attached to the surface of cells, may interfere with cell surface interaction (123). Furthermore, the physical properties such as the particle size, shape and surface coating can also evoke a toxic response by aggregating and coagulating according to size and shape (148, 151). When addressing the possible *in vivo* application of SPION, it is equally important to consider the fate of the SPION after they have been released by the cells. Further issues arise when considering the degradation of the SPION and the outcome of accumulated SPION or SPION by-products in various tissues and organs (109). Degradation products are thought to possibly react with various components of the body or cells. Therefore, the effects of the breakdown products on the surrounding tissue should be fully investigated (98, 109).

Many investigations have assessed the effect of labelling cells with SPIONs on the viability, proliferation and differentiation of stem cells (138). Majority of the studies have reported that SPIONs are frequently non-toxic to stem cells and do not affect differentiation (142, 152). Balakumaran *et al* reported that the use of SPIONs as tracking agents for MSCs in no way interfered with their multi-lineage differentiation potential towards adipogenic, chondrogenic and osteogenic lineages (153). Table 1.5 highlights the range of studies and the finding on SPION toxicity.

Table 1.5 Summary of *in vitro* studies performed in recent years highlighting commonly used assays aimed at investigating toxicity of SPIONs on stem cells and the findings.

Particle	Coating	Size	Cells	Concentration	Toxicity Assay	Result	Ref
Feridex	Dextran	80-150 nm	MSC (human, rat, mouse) ESC (Embryonic stem cells)	25-250 µg/ml	Live/dead (7 days post labelling) Comet assay FACS to evaluate cell death Trypan Blue	No loss of cell viability observed after 7 days with or without either TA	(136) (106) (92) (154)
Non commercial	Silica	110 nm	hMSCs	200 µg/ml	MTT (1 hr and 24 hrs) Trypan Blue	No reduction in viability after 1 hour. No reduction in cell proliferation.	(148)
Iron fluorescent particle	Polystyrene	900 nm	Porcine MSC	Unknown	Trypan Blue, MTT Morphological observations	Cells maintained viability and retained label for up to 3 months. Differentiation capacity not altered.	(155)
Manganese oxide nanoparticles	Mesoporous silica	65 nm	mMSCs	Unknown	MTT	75 % cell viability Limited cell differentiation in the osteogenic lineage.	(156)
Unknown	HEDP (hydroxyethylide bisphosphonic acid)	n/a	rMSC	25, 50, 100 µg/ml	MTS	Cell viability not affected at lower concentrations but viability decreased to 70 % at 100 µg/ml	(157)

1.8. MRI

Magnetic Resonance Imaging (MRI) is a clinically relevant imaging modality capable of distinguishing between healthy and diseased tissues aiding in the diagnosis of a wide range of diseases (130, 158). MRI has rapidly revolutionised the medical diagnostics field with its conception dating back to the early 1970`s. The system rapidly developed through the 1980s with the first 0.15 T clinical scanner being installed at the Hammersmith Hospital, London. By 1996, there were over 10 000 scanners worldwide (130). Today, it is not uncommon to find 1.5 and 3 T (tesla) MRI scanners in every hospital (159) whilst 4.7, 7.4, 9 and 11 T (160) are being used throughout research labs. MRI permits tracking of implanted cell population, whilst still monitoring the surrounding anatomical structures. This is particularly useful for the clinician as information on the pathology of the surrounding tissue is a major issue when assessing the success of the therapy (82). MRI scanner strength significantly influences resolution and contrast, not only defining MRI detection thresholds but also defining the quality of images and the extent to which information can be gathered. In general, higher strength scanners (similar to those used in research; 4.7, 7, 11.7 T) offer better contrast, resolution and specificity (130). These are all highly attractive qualities in the evaluation of cellular therapies *in vivo* (161). Such resolution however is difficult to achieve in clinical grade scanners (1.5 T). Therefore, scanner strength must be carefully considered when devising tracking protocols for clinical therapies as it is unlikely that resolution achieved in research (4.7, 7, 11.7 T) will be maintained clinically (1.5, 3 T). It must also be noted that in addition to scanner strength, SPION properties and total intracellular Fe content also impact the detection threshold of implanted cells *in vivo*.

1.8.1 Equipment

An MRI scanner consists of the follows components (Figure 1.12);

a) **Magnet**: produces a strong constant magnetic field. In standard clinical MRI grade scanners, superconducting magnets are primarily used with the magnet field present at all times. The strength of an MR system is expressed in terms of its magnetic strength for example 1.5 T and 3 T where T (tesla) is a unit of magnetic flux (130).

b) **Radio frequency (RF) transmitter coil**. This generates the RF pulses that excite protons, therefore producing a signal, which can be detected. These are commonly built into the magnet although organ specific coils such as knee and head coils are also available (130).

c) **RF receiver coil**. This detects the MR signal produced by the body in response to the RF pulse (130).

d) **Gradient coils**. Localisation of the MR signal in the body to produce images and controls the pulse sequence in all three directions (x, y and z) to produce a gradient field (130).
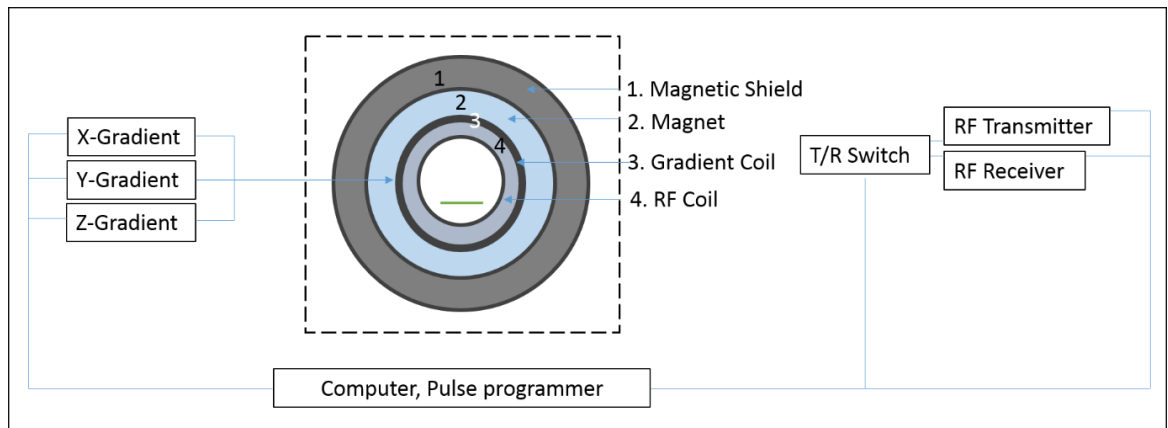
Figure 1.12. Components of an MRI scanner. 1) Magnetic Shield, 2) Magnet (commonly superconducting in clinical grade scanners), 3) Gradient Coil and 4) RF coil.

1.8.2 Theory

It is important to understand that MRI is a technique primarily sensitive to protons associated primarily within the hydrogen atom of the water and fat molecules. These protons are positively charged and are in a constant spin motion spinning about their axis effectively generating a small magnetic field Figure 1.13 a. In the presence of an external magnetic field, the protons align themselves either with (parallel) or against (antiparallel) the direction of the applied magnetic field with opposing moments cancelling out resulting in a net magnetic moment Figure 1.13 b. While protons are in alignment, they precess, (following a similar motion to a spinning top) Figure 1.13 c with the speed of precession known as the precession frequency (Lamor frequency) and is dependent on the strength of the magnetic field. The stronger the magnetic field, the faster the precession rate (130, 157)
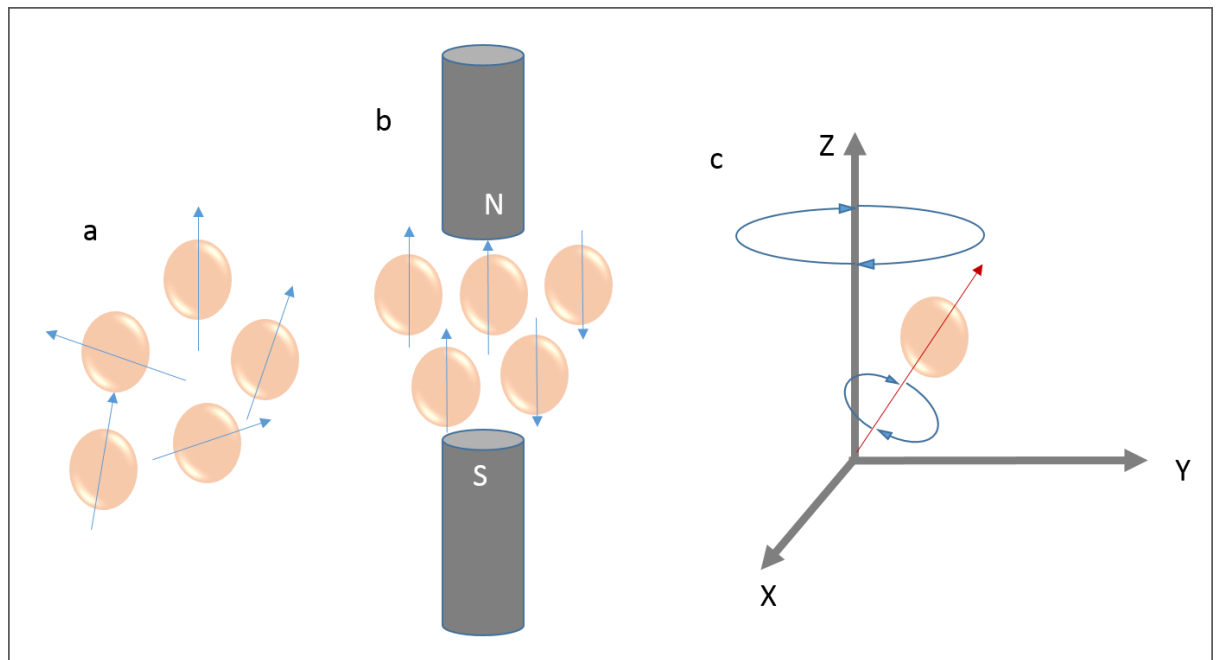
Figure 1.13. Behaviour of protons. A) Proton alignment in a random fashion in the absence of a magnetic field. B) Alignment of protons either parallel or anti-parallel to the external magnetic field. C) Precession of protons within a strong magnetic field. Adapted from Schild *et al*, 1990 (158)

A person develops a net magnetic charge when placed into the MRI scanner. The magnetic moments of the body are aligned with the main field of the MRI scanner (permanent magnet) typically the longitudinal or z axis. During scanning, a RF pulse is applied to disrupt the alignment of the protons causing the protons to move from the z axis (longitudinal axis) to the y axis (transverse axis). This allows for the magnetization of the body to be measured (130, 158) and as a result, a signal is created. Once the RF pulse is removed, the magnetization reverts back to its equilibrium or relaxes either via spin lattice or spin-spin relaxation. Spin lattice relaxation controls the growth of magnetization along the z axis and is known as T_1 or longitudinal relaxation (Figure 1.14 Aii). Spin- Spin relaxation, controls the decay of the signal in the transverse plane and is known as T_2 relaxation (Figure 1.14 Ai) and is attributed to the dephasing of protons in the transverse plane. Each tissue will have its

own characteristic proton density, T_1 and T_2 values, which all contribute to the image (Figure 1.14 B). However, by controlling various parameters the contrast of the image can be altered to be dependant of just one of the parameters, i.e T_1 or T_2 weighted contrast where contrast is dependant mainly on T_1 or T_2 relaxation respectively. All MRI images are produced using pulse sequences. These sequences are made up of radiofrequency pulses and gradient pulses which all have very specific durations, timing and flip angles. These parameters can be altered depending on the imaging required. The simplest MRI sequences begins with the 90º pulse which knocks the magnetization from the z-axis to the y-axis. There are a great deal of MRI sequences available and are most commonly referred to by acronyms. Table 1.6 highlights some of these acronyms (130).
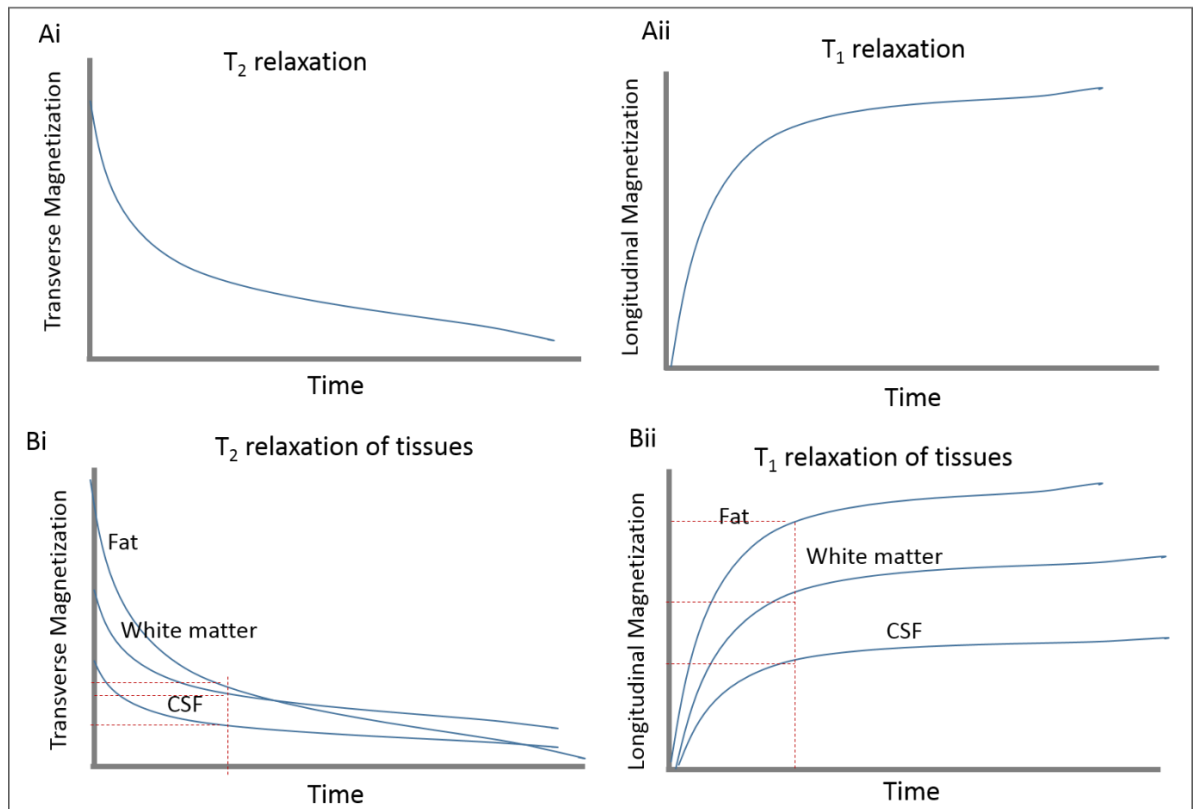
Figure 1.14. T₁ and T₂ relaxation profiles. A) General relaxation profiles demonstrating i) decay curve significant of T₂ relaxation and ii) build up curve significant of T₁ relaxation. B) Comparative i) T₂ and ii) T₁ and relaxation profiles for various tissues where white matter refers to the white matter in the brain and the CSF, the cerebrospinal fluid. Adapted from (130, 157, 160). Red dashed line demonstrates the variation of T₁ and T₂ values for the different tissue types at a time (t).

Table 1.6. Commonly used MRI Pulse sequence acronyms (130)

FSE	**F**ast **S**pin **E**cho
RARE	**R**apid **A**cquisition with **R**elaxation **E**nhancement
GE	**G**radient **E**cho
FLASH	**F**at **L**ow **A**ngle **S**hot
FISP	**F**ast **I**maging **W**ith **S**teady **S**tate **P**recession

1.8.3 Contrast Agents

Contrast agents are applied to aid in the diagnosis of several pathologies where contrast is defined as the relative difference in the signal intensities between two adjacent regions. Therefore, contrast agents work to enhance the differences between normal and diseased tissues by modifying the intrinsic parameters of the tissue. It must be noted that it is the effect of contrast agents on the surrounding tissues that we primarily see, not the contrast agent itself. Contrast agents improve the visibility of internal structures by modifying relaxation time of protons in the tissue where they accumulate, causing changes in the MR signal intensity and consequently imaging contrast. Contrast agents induce shortening of relaxation time in either T_1 (longitudinal) or T_2 (transverse) and exhibited by the shift in the relaxation curves (Figure 1.15; denoted by the arrow) (162). Contrast agents are further classified as either positive contrast agent or negative contrast agents. Positive contrast agents are paramagnetic compounds such as Gadolinium and are used in the clinic as extracellular hepatobiliary or blood pool agents by shortening T_1. Therefore, tissue/organs incorporating these agents appear bright in T_1 weighted sequences (159). Negative contrast agents are superparamagnetic iron oxide compounds and are applied clinically in order to be used as blood pool agents for the diagnosis and imaging of organs such as the liver. T_2 contrast agents work by influencing the relaxation of the protons in the water molecules in the near vicinity of the agent. These compounds therefore cause a shortening of T_2 causing tissues to appear dark in T_2 weighted sequences. The magnetic field of the contrast agent effectively perturbs the nuclear spin relaxation process of the protons leading to shortening of T_2 of the protons affected (163). Contrast is dependent on the combination of a variety factors; these include intrinsic factors such as proton density and extrinsic factors such as; the type of pulse sequence, timing parameters, and the strength of the magnetic field (159).

Superparamagnetic iron oxides agent are generally preferred over Gadolinium based contrast agents as labelling agents due to their overall better T_1 and T_2 relaxivity properties, implying that contrast can be created at lower concentrations. (97, 130, 134, 164).
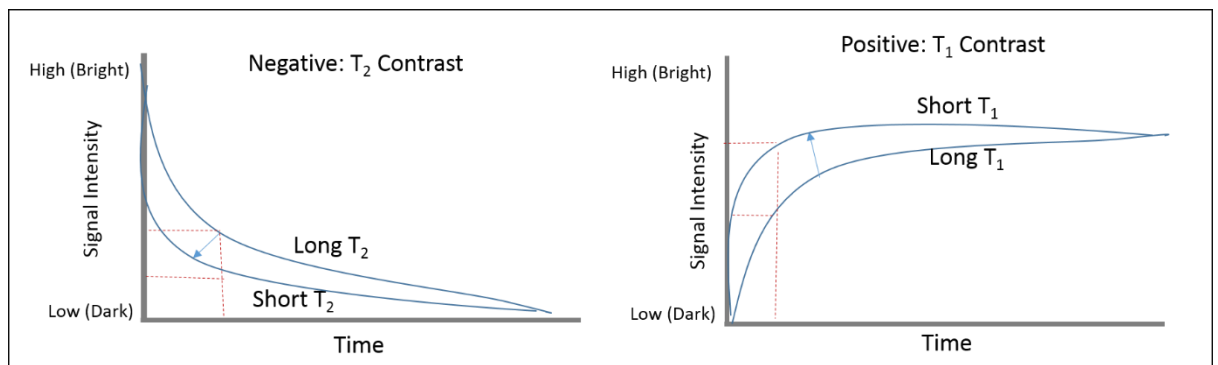
Figure 1.15. Schematic illustration demonstrating the effect of MRI contrast agent on T_1 and T_2 weighted MRI scans. The presence of a MRI contrast agents cause the shortening of T_1 and T_2 (shown by the arrow) resulting in decreasing signal for T_2 and increase in signal for T_1 weighted scans.

1.9. Multifunctional Application of SPIONs in Regenerative Medicine

The use of SPIONs has a multifunctional role in regenerative medicine and can be used for the tracking, targeting and activation of stem cells both *in vitro* and *in vivo* and these aspects are explored in greater detail.

1.9.1 Targeting of Magnetically Labelled Stem Cells

Incorporating SPIONs into cells allows for non-contact manipulation of cells using an external magnetic field gradient. This can be used to precisely position or target the cells to the site for regeneration or repair (165, 166), which is a powerful, non-invasive tool in stem cell therapy (167, 168). This technology has been applied in the vascularisation of various tissues by endothelial progenitor cells (EPC). Attaching magnetic particles to these cells displayed no affect on differentiation or proliferation of the cells, and also did not alter the membrane proteins which are essential for vascularisation (169). It is thought that attaching magnetic particles to EPCs can help in localised cell based therapies as vascularisation is essential for tissue formation. Thus, directing these cells from a distance with an external magnetic field to areas that require vascularisation can enhance the regeneration/repair of damaged tissues. Therefore, the targeting of cells to a specific site and monitoring their behaviour in a model system can be examined and translated to *in vivo* studies (167).

1.9.2 Guided Differentiation of Stem Cells using SPIONs

Mechanical stimulation can be used to facilitate cell proliferation, differentiation and migration of stem cells (170). Physical forces include; fluid flow, axial compression, tension, and magnetism (116). Biological responses are achieved through the process of mechanotransduction, whereby cells convert physiological mechanical stimuli into biochemical signals to activate the biological response (171). Using SPIONs functionalised with antibodies or peptides, it is possible to attach SPIONS to specific mechano-sensitive cell surface receptors and ion channels. This has been shown to result in membrane polarisation, receptor activation and subsequent downstream second messenger signals in hMSC (172). Using this technology it has been possible to promote an osteochondral phenotype of hMSC and human osteoblasts in response to magnetic activation using an external oscillating magnetic field (173, 174).

1.10 Thesis Aims and Objectives

The overall aim of this project is to develop and implement a non-invasive means of imaging and tracking implanted cell populations *in vivo* with arthritis as the main focus. This imaging and tracking modality relies on the combined use of (SPIONs) and magnetic resonance imaging (MRI). Through this work it is anticipated that cellular bio-distribution, integration and tissue regeneration can potentially be evaluated.

The specific aims of this thesis are to:

- Identify a suitable SPION that can be used to label MSC and chondrocytes populations

- Establish and optimise a SPION based labelling protocol

- Evaluate cellular functions as a result of SPION labelling

- Investigate MRI visibility threshold in both *in vitro* and *ex vivo* environments

- Apply the developed labelling protocol to animal tracking study.

Chapter 2

Materials and Methods

2.1 General Cell Culture

Human mesenchymal stem cells (hMSCs), murine mesenchymal stem cells (mMSCs) and porcine chondrocytes were cultured and expanded under standard cell culturing practice with cells receiving total media changes with their relevant media every 2-3 days and passaged when 80-90 % confluent. Incubation conditions were as follows; 5% CO_2 and at 37 ^{o}C. All activities took place within a class II Biological Safety Cabinet under sterile conditions.

2.1.1 Cell Isolation

2.1.1.1 Human Bone Marrow Derived Mesenchymal Stem Cells.

Human MSCs were directly isolated from human bone marrow aspirate (Donor Details; 20 year old Caucasian male) (Lonza, UK). Flasks (T^{75}) were coated with fibronectin (Sigma-Aldrich, UK, cat # F0895; 10 ng/ml; prepared in PBS) and incubated at room temperature for 1 hr. Bone marrow aspirate was then seeded (mononuclear cell density of 1.5 x10^3 cell/cm^2) in 15 ml isolation media comprising of low glucose (1 mg/ml) DMEM (Lonza Biowhittaker, UK Cat # BE12-614) supplemented with 10 % Fetal Bovine Serum (FBS; Lonza Biowhittaker, UK Cat # DE14-801F), 1 % L-Glutamine (Sigma-Aldrich, UK Cat # G7513) and 1 % Penicillin/Streptomycin (Sigma-Aldrich, UK Cat# P4333). Cells were then cultured in hMSC isolation media for one week. After this period, a 50 % media change with hMSC isolation media was performed followed by a 100 % media change one week later to hMSC proliferation media (high glucose (4.5 mg/ml) DMEM (Lonza Biowhittaker, UK Cat # BE12614F) supplemented with 10 % FBS, 1 % L-Glutamine and 1 % Penicillin/Streptomycin). hMSCs were identified as those which had adhered to the tissue culture vessel after 14 days in culture. Adherent hMSCs were then cryopreserved using

freezing down media (90 % FBS; 10 % DMSO) at approximately $5x10^5$ cells/ml or expanded up until passage 3 for subsequent experiments.

2.1.1.2 Murine Bone Marrow Derived Mesenchymal Stem Cells.

Murine mesenchymal stem cells (mMSCs) were isolated from BALB/c mice as described by Chamberlain *et al* (175). Femurs and tibia's were flushed to remove and isolate bone marrow cells. Cells were subsequently plated and cultured in mMSCs isolation media consisting of RPMI-1640 (Lonza, UK Cat # BE12-702F) media supplemented with 9 % FBS, 9 % horse serum (Gibco, Life technologies, UK) Cat # 26050088), 1 % L-Glutamine and 1 % Penicillin/Streptomycin and incubated in standard conditions 5 % CO_2 and at 37 °C for 24 hrs. Non-adherent cells were then removed and adherent cells cultured for a further 4 weeks at which point cells were re-plated at a seeding density of 100 cells per cm^2 in proliferation media (IMDM media (Gibco, Life technologies Cat # 211786) supplemented with 9 % FBS, 9 % horse serum 1% L-Glutamine and 1 % Penicillin/Streptomycin for mMSC expansion.

2.1.1.3 Porcine Chondrocytes

Chondrocytes were isolated from porcine articular knee cartilage (Staffordshire Meat Packers, Stoke-on-Trent, UK) two hours post slaughtering based on a technique adapted from Hayman *et al* (23). Cartilage was carefully removed from the upper condyles of the knee, finely diced, weighed and then rinsed three times in a solution of phosphate buffer solution (PBS) and 2 % Penicillin/Streptomycin. The extracellular matrix (ECM) of the cartilage was digested overnight in chondrocyte isolation media consisting of DMEM HAMS F12 (Lonza Biowhittaker, UK Cat # BE12-719F), 2 % Penicillin/Streptomycin, 50 µg/ml sterilised ascorbate (Sigma-Aldrich, UK, Cat # A4544), 1 mg/ml clostridal

collagenase (Sigma-Aldrich, UK, Cat # C6885) and 0.1 mg/ ml DNAse (Deoxyribonuclease) (Sigma-Aldrich, UK, Cat # D4263) while being continuously agitated using a magnetic stirrer at 37 $^{\circ}$C and 5 % CO_2. Digested cartilage suspension was filtered to remove tissue debris through 100 μm cell strainer. Supernatant containing chondrocytes was collected and centrifuged at 600G for 10 mins. Trypan blue (Sigma-Aldrich, UK, Cat # T8154) exclusion test was carried out at this point in order to determine cell viability (%). Chondrocytes were then re-suspended, seeded at $2x10^4$ cells/cm^2 and cultured under standard cell culturing conditions (5 % CO_2 and 37 $^{\circ}$C in chondrocytes proliferation media; DMEM HAMS F12 supplemented with 10 % FBS, 1 % L-Glutamine and 1 % Penicillin/Streptomycin) up to a maximum passage number of 3.

2.2. Cell Characterisation

Cell (hMSCs, mMSCs and chondrocytes) were characterised upon isolation prior to the establishment of cells banks. Cell banks were continuously maintained by cryopreserving (90 % FBS; 10 % DMSO) a minimum of $5x10^5$ cells at each passage (P1-3).

2.2.1 Multi-lineage Differentiation of MSC.

MSCs (human and murine) were tested for their ability to undergo differentiation into osteocytes, adipocytes and chondrocytes. Cells ($2.5x10^3$) were seeded into 24 well plates (n=3) and cultured in the relevant differentiation media (Table 2.1) or standard proliferation media (control samples) for 21 days. Media change was performed every three days. Cells were fixed using 95 % methanol (Fisher Scientific UK, Cat # M395021) (15 mins) for both osteogenic and chondrogenic samples and in 4 % formalin (15 mins) for adipogenesis at all

time point samples (Day, 0, 7, 14, 21). Fixed cells were then stained with the relevant

histology staining (section 2.5). In brief, osteogeneisis was confirmed by Alizarin red

staining (section 2.5.1.1), adipogenesis by oil red "O" staining (section 2.5.1.3) and finally

chondrogensis by alcian blue staining (2.5.1.2).

Table 2.1. Relevant differentiation media compositions to drive the chondrogenic, adipogenic and osteogenic differentiation of hMSCs and mMSCs.

Reagent	hMSCs	mMSCs
CHONDROGENESIS (176)		
ITS (Insulin, Transferin, Sellenium Prefix) (Sigma-Aldrich, UK, Cat # I3146)	1 % v/v	1 % v/v
Dexamethasone (Sigma-Aldrich, UK, Cat # D2915)	0.1μM	0.1 μM
Ascorbic Acid (Analar, BDH, UK, Cat # 103033E)	50 μM	50 μM
L-proline (Sigma-Aldrich, UK, Ca t# P5607)	40 μg/ml	40 μg/ml
Sodium Pyruvate (Sigma-Aldrich, UK, Cat# S8636)	1 % v/v	1 % v/v
TGF-β3 (Peprotech, UK, Cat # 120-14E)	10 ng/ml	10 ng/ml
FBS	1 % v/v	1 % v/v
ADIPOGENESIS	**hMSCs (71)**	**mMSCs (175)**
3-Isobutyl-1-methylxanthine (Sigma-Aldrich, UK, Cat# I5879)	0.5 mM	0.5 μM
Dexamethasone	0.5 μM	1 μM
Insulin (Sigma-Aldrich, UK, Cat # 19278)	10 μg/ml	0
Indomethecin (Sigma-Aldrich, UK, Cat # 17378)	100 μM	100 μM
ITS	0	1% v/v
OSTEOGENESIS	**hMSCs (177)**	**mMSCs (175)**
Dexamethasone	0.1μM	0.01μM
Ascorbic Acid	50 μM	88 ng/ml
B-Glycerophosphate (Sigma-Aldrich, UK, Cat# G9422)	50 mM	10 mM

2.2.2 Flow Cytometry

Flow cytometry (Fluorescence-Activated Cell Sorting; FACS) was implemetnted to evaluate

cell surface markers for hMSCs and mMSCs. hMSCs (P1) and mMSCs (P12) were expanded,

trypsinised, and re-suspended at a cell dose of 10^6 cells/ml in blocking solution (hMSCs; 10 %

Human IgG (Flebogamma), mMSCs; 2 % BSA (Bovine Serum Albumin) in PBS).

Following an incubation period of 1 hr at 4 °C, cells were centrifuged at 400 g for 4 min at 4 °C and the supernatant discarded. Cells were then re-suspended in 2 % BSA/PBS solution resulting in a cell density of $1x10^6$/ml and dispensed at a cell density of $8x10^4$ per 5 ml Falcon tube. The directly conjugated antibody or the respective isotype control was then re-suspended in 2 % BSA/PBS and added to cells for a further incubation period of 30 min at 4 °C on a rocker in the dark. Cells were centrifuged twice (400g, 5 mins) before being re-suspended in a final volume of 200 µl 2 % BSA/PBS to be analysed.

2.2.2.1 Antibodies

hMSCs

Directly conjugated antibodies and their corresponding dilutions (made up in 2 % BSA) used in this study were as follows: CD 14 (1:50), CD 19 (1:50), CD 34 (1:100), CD 31 (1:50) CD 45 (1:200), CD 105 (1:50), (Immunotools, Germany) CD 73 (1:20), CD 90 (1:200) (BD Biosciences, UK). Isotype control antibodies used in this study were HLA – DR (1:200), IgG1 (1:50), IgG2a (1:50) (Immunotools, Germany). In this study, propidium iodide staining was not included.

mMSCs

Antibodies used in this study were as follows: anti-mouse CD 31 (PECAM-1) PE (5 µg/ml), anti-human/mouse CD 44 PE (5 µg/ml), anti-mouse CD 11d PE (5 µg/ml), anti-mouse CD 45 PE (5 µg/ml), anti-mouse Ly-6A (Sca-1) PE (5 µg/ml), anti-mouse CD 105 PE (12,5 µg/m1). Isotype control antibodies used in this study were: rat IgG2a-PE (5 µg/ml) and rat IgG2b-PE (5 µg/ml) (eBioscience). Propidium iodide staining was included in the immunophenotyping to evaluate the viability of the cells.

2.2.2.2 Flow Cytometric Analysis

The samples were analysed on a Becton Dickinson FACScan flow cytometer. Fluorescein isothiocyanate (FITC) fluorescence was detected using the FL-1 channel, while R-phycoerythrin (PE) fluorescence was detected in the FL-2 channel. FITC has maximum absorbance at 494 nm and maximum emission at 518 nm; R-PE has maximum absorbance at 490 and 565 nm and maximum emission at 578 nm. Excitation was achieved at 488 nm with an Argon laser. Data gated to exclude dead cells and select the required cell population on the basis of forward scatter versus side scatter profiles. Mean fluorescence intensity (MFI) and percentage positive cells were measured. Data were collected and displayed in dot plot and histogram format using CellQuestPro software (Becton Dickinson, Oxford, UK).

2.2.3 Histological Evaluation of Chondrocytes

Chondrocytes (P3) were tested for their ability to secrete sulphates glyosaminoglycans. Cells ($12x10^3$) were seeded into 96 well plates (n=6) and cultured in the chondrogenic differentiation media (Table 2.1) or standard proliferation media (control samples) for 21 days. Media change was performed every 3 days. Cells were fixed using 95 % methanol (15 mins) and stained for the secretion of GAG (glycosaminoglycans) using Alcian blue staining (section 2.5.1.2).

2.3 Particle Labelling

2.3.1 Superparamagentic Iron Oxide Nanoparticles (SPIONs)

SPIONs (SiMAG, Lumirem, Nanomag, P904) ranging in size from 25 nm to 1000 nm in diameter were selected and assessed as potential labelling agents. The specific properties of these particles are listed for comparative purposes in Table 2.2.

Table 2.2. Properties of the four SPIONs selected for this study.

	SiMAG	Lumirem	Nanomag	P904
Iron Core	Maghemite (Fe_2O_3)	Maghemite (Fe_2O_3) and Magnetite (Fe_3O_4)	Magnetite (Fe_3O_4)	Maghemite (Fe_3O_4) (178)
Size	1000 nm	300 nm	50-75 nm	25-30 nm
Polymer Coating	Silica non porous	Siloxane	Dextran	Glucose derivative
Iron (Fe) contents	15000 µgFe/ml	175 µgFe/ml	2400 µgFe/ml	22000 µgFe/ml
FDA approval	No	Yes	No	Pre-clinical
Magnetisation	Superparamagnetic	Superparamagnetic	Superparamagnetic	Superparamagnetic
Application	Purification of DNA	MRI contrast agent	Magneto-immuno assay	MRI contrast agent
Functional group	Silanol	None	None	unknown
Supplier	Chemicell, Germany (Cat# 1101)	Guebert, France (Cat# 211786)	Micromod, Germany (Cat# 79-00-501)	Guebert, France (Cat# G00904.016)

2.3.2 SPION labelling of cells

Cells (hMSCs and porcine chondrocytes, P2 or P3; mMSCs, P12 or P13) were labelled with SPIONs. Cells were trypsinised (1% Trypsin and EDTA (Lonza Biowhittaker, UK Cat # BE02007E) solution in PBS; 5 mins incubated at 37°C) and then plated at the desired seeding density per specific experiment. Cells were allowed to attach for 24 hrs in standard proliferation media at 37 °C before aspirating media and washing once with PBS to remove

any residual FBS. SPIONs were re-suspended in SF (serum free) proliferation media at the desired Fe concentration (Equation 2.1 Appendix) and vortexed well before adding to cells. Cells were then incubated with the particle solution for 24 hours at 37 °C. A ratio of 1 ml of particle suspension at the desired Fe concentration per 2×10^5 cells was maintained for all particles across all experiments. Following incubation, cells were thoroughly washed with PBS (3 times) to remove excess particles attached to the surface of the cells, trypsinised, collected and counted for subsequent experiments.

2.3.3 Characterisation of cell populations post SiMAG labelling

SiMAG-labelled cells (hMSCs, mMSCs and chondrocytes) were characterised to ensure that the presence of SiMAG had not affected cell properties. hMSCs were characterised by evaluating their multi-lineage differentiation abilities as described in section 2.2.1 and the expression of key cell surface markers (section 2.2.2). Characterisation of chondrocytes was performed by evaluating sulphated GAG secretion (Section 2.2.3). In each case, cells were seeded at the required cell density (as described section 2.2.1, 2.2.2 and 2.2.3) and labelled according to the particle-cell labelling protocol described in section 2.3.2. Briefly, cells were allowed to attach for a period of 24 hrs in standard proliferation media prior to the addition of SiMAG solution (10 µgFe/ml; SFM) and allowed to incubate for 24 hrs. The particle solution was then removed, cells thoroughly rinsed in PBS (three times) and characterised accordingly.

2.4 Particle Characterisation

2.4.1 Particle Size

Hydrodynamic particle size was measured using a Malvern ZetaSizer 3000 HSa. This operates on the principal of dynamic light scattering and is an important indicator of particle behaviour and size distribution within a colloidal suspension. Working concentrations were initially assessed by re-suspending a range of volumes (5 μl – 100 μl) of each particle stock solutions (SiMAG, Lumirem, Nanomag and P904) in 3 ml (the total holding volume of the cuvette) of dH_2O, vortexed and analysed using the ZetaSizer. Working volumes were chosen based on the volume that resulted in a KCps (count rate) ranging from 50 – 200 counts as this was recommended for accurate particle size measurements. Therefore 10 μl volumes (SiMAG and P904) and 100 μl volumes of (Nanomag and Lumirem) were used in all subsequent zeta-size measurements. Accurate reflection of particle properties relevant to the cells was performed at 37 ºC in either serum free or serum containing DMEM to obtain actual measurements (146). Measurements were taken at 0 and 24 hr incubation periods. Three individual samples were prepared with 10 measurements taken for each sample. Statistical analysis was performed with two way Anova with Bonferrioni post-test using GraphPad.

2.4.2 Particle Surface Charge

Surface charge of each particle was measured also using the Malvern Zetasizer 3000 HSa with the settings being changed from size mode to the zeta potential mode. This is an important indication of particle stability and colloidal suspension. Contrary to the size measurements, analysis was carried out in dH_2O and not in labelling media so as to negate

the charge of the particles in the labelling media, (n=5) (179). Here, 10 µl (SiMAG and P904) or 100 µl (Nanomag and Lumirem) were re-suspended in 10 ml dH_2O and passed through the system using a syringe (10 ml) taking care not to allow any air bubbles through the system.

2.4.3 Fe Content

Fe content of each particle was measured using ICP-OES (Inductively Coupled Plasma – Optical Emission Spectrometry). A serial dilution in dH_2O was used to achieve concentrations ranging from 0.01, 0.1, 0.5, 1, 5, 10 µgFe/ml of each particle (SiMAG, Lumirem, Nanomag, P904). Each sample was then digested by adding 1 ml concentrated analytical grade nitric acid (Fisher Scientific, UK, Cat #: N/23001PB17) and heated to 60 ^{o}C overnight in a chemistry oven. Samples were diluted with dH_2O to achieve a final acid concentration of less than 10 % prior to scanning using ICP at 3 wavelengths (239.563, 259.940, and 238.204 nm). Samples were measured against a selection of Fe ICP standards (0.1, 1, 5, 10 ppm (parts per million)) made from a Fe stock of 1000 ppm in ddH_2O.

2.4.4 Particle Relaxivity

The relaxivity (R2) of each particle was measured by MR imaging varying concentrations of particles and applying T_2 specific sequences on the Brucker 2.3 T animal scanner. Through serial dilution, 40, 20, 10, 5, 2, 1, 0.5, 0.1, 0.01 µgFe/ml of each particle were prepared in water and 100 µl of each sample was then aliquoted in a customised 96 well plate and MR imaged using MSME sequences. The inverse of the T_2 values for each particle were then plotted against particle concentration and the slop of the curve taken as the R2 values.

2.5 Histological Staining

2.5.1 *In vitro* Histological Staining

2.5.1.1 Alizarin Red

Characterisation of osteogenic differentiation of MSCs was confirmed by staining with Alizarin Red (Sigma-Aldrich, UK Cat# A5533) prepared at 1% in dH_2O and syringe filtered using a 2 μm filter. Samples were washed in PBS and treated with 500 μl of alizarin red for 5 min at room temperature. The stain was then removed and washed 3 times with dH_2O. Calcium ions secreted into the extra cellular matrix were stained red (positive) and imaged using a bright field microscope AMG-EVOS x1 CORE.

2.5.1.2 Alcian Blue

Alcian Blue stain (Sigma-Aldrich, UK Cat# A3157; 0.1%) was prepared at pH 1.5 using 3 % acetic acid made using dH_2O and syringe filtered (0.2μm filter). Fixed samples were immersed in the stain overnight at room temperature. Upon removal of the stain, samples were washed 3 times in dH_2O. The presence of GAGs secreted by chondrocytes was identified as by areas stained as blue. Stained samples were imaged using a bright field microscope Olympus CKX41.

2.5.1.3 Oil Red O

Oil-Red-O (Sigma-Aldrich, UK, Cat # O-0625) stain was prepared at 0.18 % in 60 % isopropyl alcohol (IPA) and syringe filtered (0.2 μm filter). Samples were first washed in dH$_2$0 followed by 60 % isopropyl alcohol. The stain was then added to wells and allowed to stain the samples for 15 min at room temperature. Following the incubation period, the stain was removed and rinsed 3 times. Lipids secreted by differentiated MSCs into adipocytes appeared as small red droplets. Samples were imaged using a bright field Olympus CKX41 microscope.

Representative images for each stain were taken of various samples at x4, x10 and x20 magnifications in at least 3 different areas of each sample.

2.5.2 *In vivo* Histological Assessment.

2.5.2.1 Knee Joint Processing

Once all the animals (mice and rats) had been MR imaged, animals were culled and joints were collected for histology. Joints were fixed in neutral buffered formal saline, and transported to Robert Jones and Agnes Hunt Orthopaedics Hospital Histopathology labs to be further processed. Briefly, fixed joint were decalcified with formic acid at 4 $^{\circ}$C before embedding in paraffin. Mid-sagittal serial sections (4 μm thickness) were obtained using a Buehler Isomet low speed saw with a diamond tipped blade (Buehler, An ITW Company, Germany).

Joint sections were prepared for subsequent staining by initially de-waxing sections in 100 % Xylene (Sigma-Aldrich, UK Cat# 534056) for 5 mins. Samples were then rehydrated in

100 % ethanol for a further 2 min followed by washes in PBS for 5 min prior to subsequent staining.

2.5.2.2 Hematoxylin and Eosin (H&E) Staining

H&E staining was carried out by the Histopathology Department at the Robert Jones and Agnes Hunt Orthopaedic Hospital.

2.5.2.3 DAPI

The fluorescent dye DAPI (1:200 dilution prepared in PBS; Sigma-Aldrich, UK, Cat# D9542) was added (1 ml) over joint sections using a pasture pipette. Hydromount (Analar, UK, Cat# 360294 H) mounting solution was then used to mount the glass cover slip and allowed to dry overnight before imaging using a UV fluorescent microscope (Nikon Eclipse Ti-S).

2.5.2.4 Toluidine Blue

Joint sections were stained using 0.25 % solution of Toluidine blue with a final pH ranging from 3.7-4.1 prepared in buffer (0.63 g citric acid, 0.3 g disodium phosphate and 400 ml H_2O). Samples were treated with 500 μl of toluidine for 20 sec at room temperature. The stain was then removed and washed 3 times with dH_2O. Toluidine blue stained GAGs purple whilst nuclear material was stained blue. Stained joint sections were imaged using a bright field microscope AMG-EVOS x l CORE.

2.5.2.5 Prussian Blue

A 20 % Aqueous (aq) solution of hydrochloric acid (HCL; Analar, UK, Cat #10307) was prepared and added to 10 % aq solution of potassium ferrocyanide (Sigma-Aldrich, UK Cat # P3289) in equal parts, immediately prior to use. This involved the reaction of ferrocyanide with Fe particles to effectively stain any Fe particles bright blue. 1ml of this solution was added to each joint section and left for 20 mins at room temperature. Joint Sections were subsequently washed with PBS prior to having coverslips mounted. Sections were imaged with a light electron microscope (Nikon Eclipse TS100) equipped with a Canon Eos 400D digital SLR camera.

2.6 Particle Uptake Assessment

2.6.1 Inductively Coupled Plasma Optical Emission Spectrometry (ICP-OES)

ICP-OEAS was performed to quantify the uptake of all particles (SiMAG, Lumirem, Nanomag and P904) by hMSCs, mMSCs (SiMAG only) and chondrocytes. This technique allows for the accurate evaluation of Fe within a sample therefore allowing the quantification of particle uptake by cells. 6-well plates were seeded with $1x10^5$ cells per well and allowed to attach overnight. 10 µgFe/ml of each particle (SiMAG, Lumirem, Nanomag and P904) solutions were prepared (Section 2.3.2) in either serum free or serum containing media relevant for each cell type. 2 ml of each particle suspension was added to each well (n=3). Control plates were set up as follows: Cell control; cells treated with no particles; (n=3) and

B) Particle controls: 2 ml of each particle solution added to empty wells to serve as a reference to the total amount of particles and subsequent total Fe added to each well.

Following the incubation period, media was removed from each well and collected into individual 15 ml centrifuge tubes. Cells were washed twice in PBS with PBS washes also collected into the same tubes. After trypsinisation (1 ml), detached cells were then removed and collected in a separate tube and washed once with PBS to ensure all cells had been collected. 1 ml concentrated analytical grade nitric acid was then added to each tube and heated to 60 ^{o}C overnight using a chemistry oven to digest the particles thus releasing Fe. Finally, samples were diluted with dH_20 to achieve a final acid concentration of less than 10 % prior to being analysed using ICP at 3 wavelengths (239.563, 259.940, and 238.204 nm) vista-mpx. During each experiment, an ICP standard (1 PPM) was prepared and analysed to ensure correct calibration of the instrument.

Data Analysis

The total Fe content (PPM) within a given sample was calculated by averaging the Fe (PPM) detected at each of the 3 wavelengths and subtracting the cell control to find the total net Fe content associated with the cells. This value is then adjusted to account for the dilution of the sample pre ICP analysis. Finally, the amount of Fe per cell was calculated by dividing for all cells in the sample (initial seeding density). Two way Anova followed by Bonferroni post test, statistical analysis was applied using Graphpad prism.

2.6.2 Prussian Blue

Prussian blue stain was carried out as a visual assessment of particle uptake. Here, 10^5 cells (hMSCs, mMSCs and chondrocytes) were seeded within 6-well plates and labelled with each particle at 0, 1, 5, 10 and 100 µgFe/ml as described previously in Section 2.3.2. Labelled cells were fixed and permealised using 95 % methanol for 15 mins at room temperature. 20 % (aq) solution of HCL was prepared and added to 10 % (aq) solution of potassium ferrocyanide in equal parts immediately prior to use. 1 ml of this solution was added to each well and left for 20 mins for the reaction to occur. Potassium ferrocyanide solution was removed and samples washed with dH_2O three times. Cells were imaged using bright field inverted Nikon TI eclipse.

2.6.3 Particle Retention

The ability of hMSCs and chondrocytes to retain internalised SiMAG over a 28 day period was assessed by ICP-OES and Prussian blue staining. Experiments were set up according to Sections 2.6.1 and 2.6.2 using hMSCs and chondrocytes labelled with 10 µgFe/ml SiMAG. Samples were then either collected to be analysed by ICP-OES or fixed to be stained by Prussian blue at various time points (1, 7, 14, 21 and 28 days) with all samples receiving a full media change every two days for the duration of this experiment. Standard students t test was performed using Excel.

2.7 Cell Viability and Proliferation

2.7.1 MTT Assay

To determine the effect of particle labelling on the viability and proliferation rate of hMSCs, mMSCs and chondrocytes, a tetrazolium salt (MTT; Sigma-Aldrich, UK, Cat #M5655) assay was applied. Cells were seeded at 10^5 cells per well of a 6-well plate and labelled under serum free conditions with each particle (SiMAG, Lumirem, Nanomag and P904) at 0, 10 and 100 μgFe/ml (Section 2.3.2) (n=6). Samples were analysed 24 hrs and 7 days post-labelling. A negative control mimicking toxic events was induced at each time point by exposing healthy unlabeled cells to 1 ml DMSO (Dimethyl sulfoxide; Sigma-Aldrich, UK, Cat# D8418) for 5 mins. At the relevant time points, 0.5 mg/ml MTT working solution (prepared in SFM) was added to each well and allowed to incubate for 4 hours at 37 °C. Following incubation period, MTT solution was carefully removed and 1ml of DMSO added for a further 10 mins to solubilise the crystals. Finally, 200 μl aliquots of this solution were then transferred to 96 well plates and read using the plate reader (Synergy 2, Biotek) at a wavelength of 570 and 690 nm (excitation/emission). Data was analysed by subtracting the blank (DMSO) from each value at the given OD and then subsequently subtracting OD value at the 690 nm wavelength from the 570 nm wavelength. All data was then normalised to the 24 hr untreated samples.

2.7.2 Live Dead Staining

A live dead assay was implemented to further investigate the toxicity of particle labelling on hMSCs, mMSCs and chondrocytes using the LIVE/DEAD® Viability/Cytotoxicity Kit (Invitrogen, UK, Cat# L3224). This assay consists of Calcein-AM and Propidium Iodide (PI)

solutions, respectively staining viable cells green and dead cells red. Here, 2 x 10^4 cells were seeded per well of a 24 well plate and labelled with 0, 10 and 100 µgFe/ml of each particle (SiMAG, Lumirm, Nanomag and P904) under serum free conditions (Section 2.3.2). Live dead staining was applied directly after the labelling period (24 hrs and after 7 days of culture). In both cases, the particle media solution was removed after the initial 24 hours of culture and cells thoroughly washed with PBS. Fresh proliferation media was added to samples continuing in culture for a further 7 days. At the relevant time points (24 hrs and 7 days) 1 % Calcein AM and 2 % Propidium Iodide solutions prepared in PBS as per manufacturer's instructions and 200 µl added to each well. Following, 45 minutes of incubation (37 ℃; complete darkness) samples were immediately imaged using a UV fluorescent microscope (Nikon Eclipse Ti-S) where live cells appeared green (FITCI filter), whilst dead cells appeared red (TRITC filter).

2.7.3 Trypan Blue Exclusion Assay

Trypan blue exclusion assay was applied to assess cell viability during cell culture. In brief, a 10 µL volume of cell suspension was mixed with 10 µL of trypan blue solution. 10µL of the mixed solution was then pipetted onto a disposable haemocytometer and cells counted. Live cells appeared clear in the centre with a blue outer membrane whilst dead cells appeared totally blue. Viable and non-viable cells were counted separately and an overall average and percentage viability gained.

2.8 Magnetic Resonance Imaging

2.8.1 MRI Scanners

2.8.1.1 Bruker 2.35 T Small Animal Scanner

A research grade Bruker 2.35 T animal scanner was used for all experiments unless otherwise stated. This scanner was operated by Dr Robert Morris of Nottingham Trent University. In general samples were placed within the scanner (within the RF (radio frequency) coil) (Figure 2.1 Aii) and adjusted to ensure that the samples were placed within the centre of the coils and the magnet for best results (approximately 933 mm from the front plate, Figure 2.2). A tripilot (3 orthogonal reference image) scan was always performed to ensure that the samples were placed in the optimal location to adjust scanning parameters accordingly.
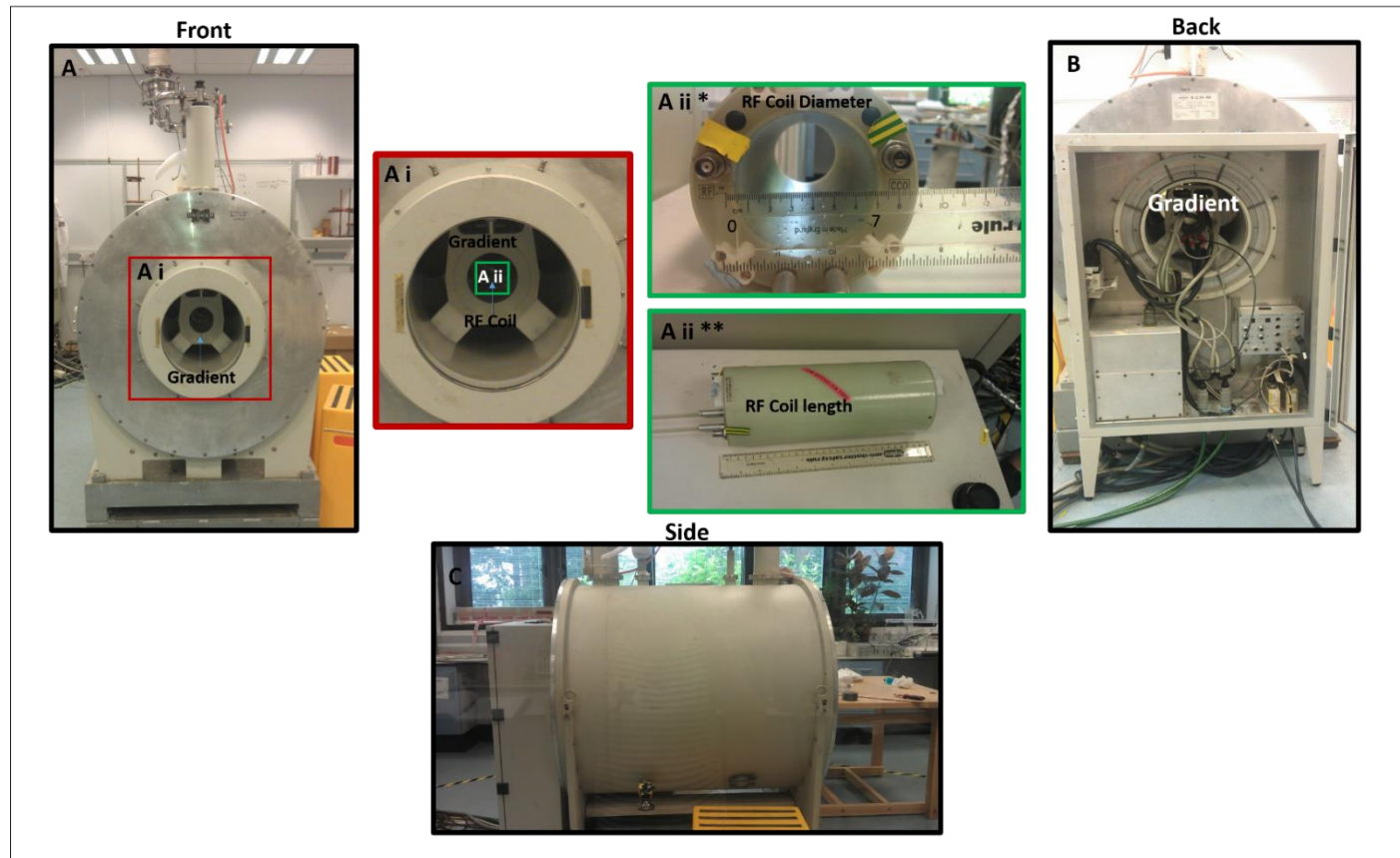
Figure 2.1. The Bruker 2.35 T animal scanner where: (A) is the front of the scanner, (B) the back of the scanner and (C) the side view of the scanner. (Ai) highlights the entrance of the scanner with the gradient visible. The RF coil is positioned within the gradient coil highlighted by the green box (Aii). The dimensions of this coil are clearly shown in Aii * and Aii ** when the inner diameter of the RF coil is 7 cm and the total length of the coil 29 cm
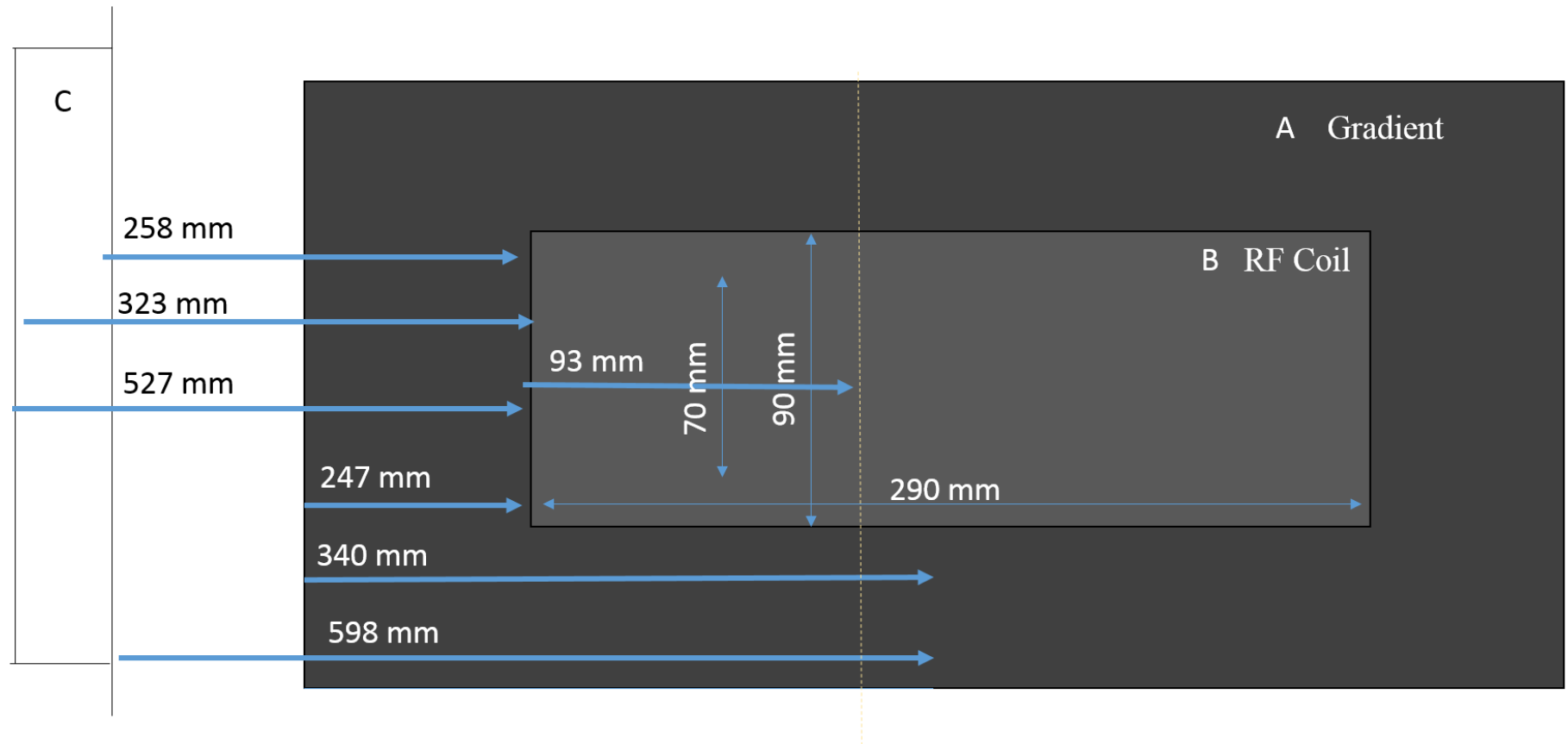
Figure 2.2. Cross sectional dimensions of the Bruker 2.35 T animal scanner highlighting key features of the scanner: (A) Gradient coil (B) Radio frequency coil (C) Front entrance.

2.8.1.2 Siemens Symphony 1.5 T Clinical Grade Scanners

Experiments involving the use of porcine knee specimens (Section 2.8.5.2) were performed at the MARIARC centre part of Liverpool University using a clinical grade 1.5 T scanner (Figure 2.3). The equipment was operated by Miss Valerie Adams.

Figure 2.3. Siemens Symphony 1.5 T MRI scanner. Image courtesy of Miss Valerie Adams (University of Liverpool).

2.8.2 MRI Sequences and Parameters

2.8.2.1 Bruker 2.35 T Animal Scanner

Table 2. 3 Sequences and corresponding parameters for each MRI experiment performed using the Bruker 2.35T animal scanner.

Experiment		Section	Sequence	Repetition time (ms)	Echo time (ms)	Number of echoes	Matrix size	Spatial resolution (mm)
In vitro dose response	Gel optimisation T_2	2.8.4.1	MSME	1000	10.25	8	256 x 192	0.469 x 0.625
	Gel optimisation T_1	2.8.4.1	MSME	100 - 5000	10.25	8	256 x 192	0.469 x 0.625
	Collagen Gels	2.8.4.2	MSME	1000	10.25	8	256 x 192	0.469 x 0.625
Ex vivo dose response	Orthopaedic tissues – (Muscle, Fat, Ligament)	2.8.5.1	MSME	1000	10.25	8	256 x192	0.391 x 0.365
In vivo dose response	Mouse model	2.8.6.1	RARE	4000	10.25	4	256 x 192	0.469 x 0.417
	Rat model	2.8.6.1	RARE	4000	10.25	4	256 x192	0.312 x 0.260
Tracking studies	Mouse model	2.8.6.2	RARE day 3	4000	10.25	4	256 x192	0.312 x 0.260
			FLASH day 3	1000	3.35	4	256 x 256	0.45 x 0.29
			RARE day 7	4000	10.25	4	256 x192	0.312 x 0.260
			GEFI day 7	500	4.7	8	256 x 256	0.47 x 0.47
	Rat model	2.8.6.2	MSME day 29	200	11	1	128 x128	1.172 x 1.172

2.8.2.2 Siemens Symphony 1.5 T Clinical Grade Scanner

The following scanning parameters (table 2.4) were implemented in the *ex vivo* cadaveric porcine model experiment. These sequences are considered highly appropriate as these are applied in routine MR diagnosis of knee pathology

Table 2. 4 Sequences and corresponding parameters for the set of *ex vivo* porcine model performed using the Siemens Symphony 1.5 T Clinical Grade Scanner.

Experiment	Section	Sequence	Repetition time (ms)	Echo time (ms)	Number of echoes	Matrix size	Spatial resolution (mm)
Ex vivo cadaveric porcine model study	2.8.5.2 & 2.8.5.3	DESS	3500	15-240 (30 ms intervals)	16	256 x 256	0.6 x 0.6 x 3

2.8.3. MRI Data Analysis

2.8.3.1 Bruker 2.35T Animal Scanner

Data generated by each scan is received by standard ParaVision 4 software. Data managed by this software is then saved in the Bruker format, a format that cannot be opened on a standard laptop or PC without specialist software. Therefore, data in this format is processed using a purpose written Matlab programme (Dr Robert Morris). This programme is capable of extracting representative T_2^{eff} values from the Bruker data files and fitting these values exponentially to the envelope of the echoes thus generating T_2^{eff} maps. All gel MRI data (section 2.8.4) was processed in this manner. Alternatively, Bruker folders were converted to a different format; "Analyze" using a Bruker- to- Analyze converter (Br2Anz) allowing for these files to be processed by the MRIcron programme, effectively allowing for all MRI images to be opened and analysed on simple windows operating system but not allowing for relaxation measurements to be obtained. All animal and tissue work were processed in this way.

2.8.4 *In vitro* MRI.

2.8.4.1. Optimisation

2.8.4.1.1 Plate Layout

The high cost of performing MRI scans limits the number of samples that can be imaged and analysed. It thus became necessary to devise a means of increasing throughput to increase the number of samples that can be imaged at one time. Early plate layouts (Figure 2.4 i) involved the fabrication of an eppendorf holder aligned with the inner dimensions of the scanner allowing for 6 x 1.5 ml eppendorf tubes to be places and MRI imaged. This set up

limits the number of samples to 6 per scan and also requires a relatively high volume of collagen (0.5 ml) per sample. The modification of a standard 96 well plate (Figure 2.4 ii) allows for the number of samples capable of being imaged at one time to increase from 6 to 24. Note, not every well of the modified 96 well could be used due to the restricted field of view of this particular MRI scanner, this area is clearly marked (Figure 2.4 ii). Furthermore, the very shallow depth of the plate allows for 2 plates to be imaged at the same time, by placing one plate over the other further increasing the number of samples to be scanned from 6 – 48 samples per scan. In this instance, the number of slices are simply increased to account for 2 plates with no extra time being added to the overall scan time. Further to this, the use of a 96 well plate, reduces the amount of collagen required to be used from 500 µl to 100 µl.
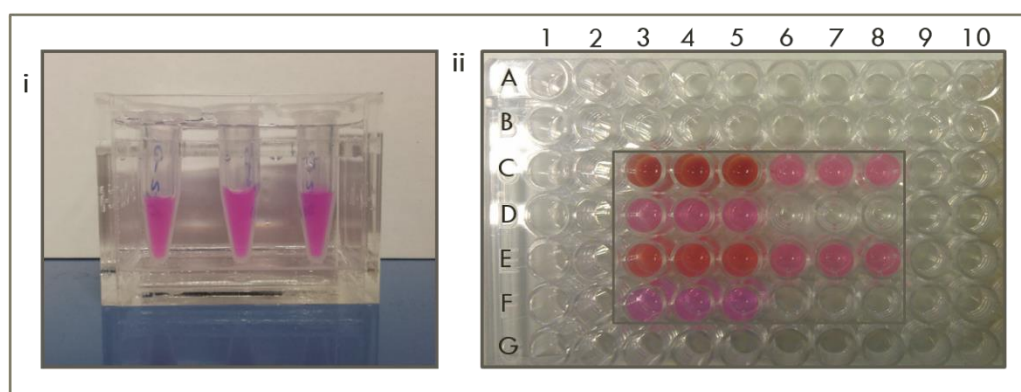
Figure 2.4. Plate layouts. i) Early plate layout facilitating the imaging of 6 samples within 1.5ml eppendorf tubes ii) Optimised plate layout facilitating the imaging of 18 samples within a 96 well plate format.

2.8.4.1.2 Collagen gels concentration optimisation

Type I collagen gels were prepared at various concentrations (0.5, 2, 5 and 9 mg/ml) by combining 10 x DMEM, NaOH (Sigma-Aldrich, UK, Cat # S8045), stock collagen gel (BD Biosciences, UK Cat # 354249) and water in certain ratios where the amount of each component are worked out according to the following set of equations (Equation 2.2

Appendix). All gel components were mixed and stored on ice until use to prevent gelation. Standard students t- test was performed using Excel.

Gels were produced by forming a solution of 10 X DMEM, NaOH, and water with the addition of stock collagen solution at the end in order to prevent premature gelation. Gel solutions were homogeneously mixed creating a uniform colour solution taking care to not create any air bubbles. 100 µl of each gel solution was carefully pipetted into the customised 96 well plates (n=6) and allowed to set for 1 hr at 37 $^{\circ}$C. Plates were then MR imaged using Bruker 2.35 T animal scanner applying MSME sequences as described in Table 2.3.

2.8.4.1.3 MRI sequences;

T_1 and T_2^{eff} weighted MRI sequences were investigated by re-suspending hMSCs labelled with varying concentrations of SiMAG (0, 1, 5 and 10 µgFe/ml) at various cell densities (10^3, 10^4, 10^5, 3×10^5, 5×10^5) in 2 mg/ml rat tail type I collagen (optimised gel concentration) (made up according to equation 2.2). 100 µl of each sample was carefully aliquotted within the wells of a customised 96 well plate. Samples were MR imaged and relaxation parameters T_1 and T_2^{eff} estimated for each of the samples using a MSME imaging (Table 2.3).

T_1 relaxation. This involves the realignment of moments with the main magnetic field or longitudinal axis (z axis) and is defined as the time taken for magnetization to revert back to 63% of its full longitudinal magnetization (130, 164).

T_2 relaxation: This involves the loss of transverse magnetization due to the dephasing of protons in the transverse plane. Once the RF pulse is removed, the protons start to dephase. Although moments are still precessing, each of the magnetic moments is also generating its own magnetic field which will affect the neighbouring moments (spin spin interactions). This will mean that over time a given magnetic moment will drift out of phase with its

neighbours. Dephasing protons are therefore cancelled out with this resulting in a loss of magnetization in the transverse plane. We are effectively measuring the number of magnetic moments which are in phase with each other at a given time. Therefore T_2 can be defined as the time taken for the magnetization to decay to 37% of its full value in the transverse plane (all moments in phase). T_2^{eff} (effective) is measured by applying a series of pulses which act to reverse the effect of protons dephasing seen in T_2 decay. This results in a significantly slower decay which can be measured more easily when the decay times in question are very short.

2.8.4.2 *In vitro* MRI Dose Response Investigation

The *in vitro* minimum visibility threshold for particle-labelled cells was investigated by re-suspending varying cell doses of labelled cell populations in a 2 mg/ml rat tail type I collagen gel, 100 µl samples were then aliquoted into the customised 96 well plates and the gels allowed to set for 1 hr (37 ºC) prior to MR imaging (MSME Table 2.3)

2.8.4.2.1 hMSCs and Chondrocytes

hMSCs and porcine chondrocytes were labelled in serum free media with 0, 1, 5, 10 and 100 µgFe/ml of each particle (SiMAG, Lumirem, Nanomag and P904) and subsequently re-suspended at varying cell doses, (5×10^5, 10^5 and 10^4) within a 2 mg/ml collagen gel suspension, prior MR imaging (MSME Table 2.3).

2.8.4.2.2 mMSCs

Murine MSCs were labelled with 0, 1, 5 and 10 µgFe/ml of SiMAG in serum free media and re-suspended into the following cell densities; 5×10^5, 3×10^5, 10^5, 10^4 and 10^3 within a 2 mg/ml collagen gel suspension, prior MR imaging (MSME Table 2.3)

2.8.5 *Ex Vivo* MRI.

2.8.5.1 Orthopaedic Tissues.

The effects of various tissue structures on *in vitro* MRI visibility thresholds were investigated by re-suspending SiMAG labelled cells (hMSCs and chondrocytes) at different concentrations (0, 1, 5 and 10 µgFe/ml) in serum free media and injected (50 µl) at various cell densities (5×10^5, 1×10^5, 10^4) using a 21 G needle within key tissues associated with the knee (muscle, ligaments and patellar fat pad). Porcine legs were purchased from Staffordshire meat packers on the day of the experiments to prevent the need for freezing. The knee was identified and dissected from the rest of the leg using a surgical scalpel (21 Blade). Once the knee had been isolated, the medial and collateral ligaments were identified and removed from the structure using a surgical scalpel and all the connective tissue carefully removed. The ligament tissue and patella fat tissues were then dissected into equal sized pieces and placed within a 24 well plate (n=3), as shown in figure 2.5. Similarly, 1 x 1 cm pieces of muscle were extracted from the quadricep femoris muscle and placed within a 24 well plate (n=3), as shown in figure 2.5. Each well was fully submerged in water before injecting cells to prevent any air bubbles from being injected within the tissues. Plates were then MR imaged on Brucker 2.3 T animal scanner using MSME sequences stated in Table 2.3.
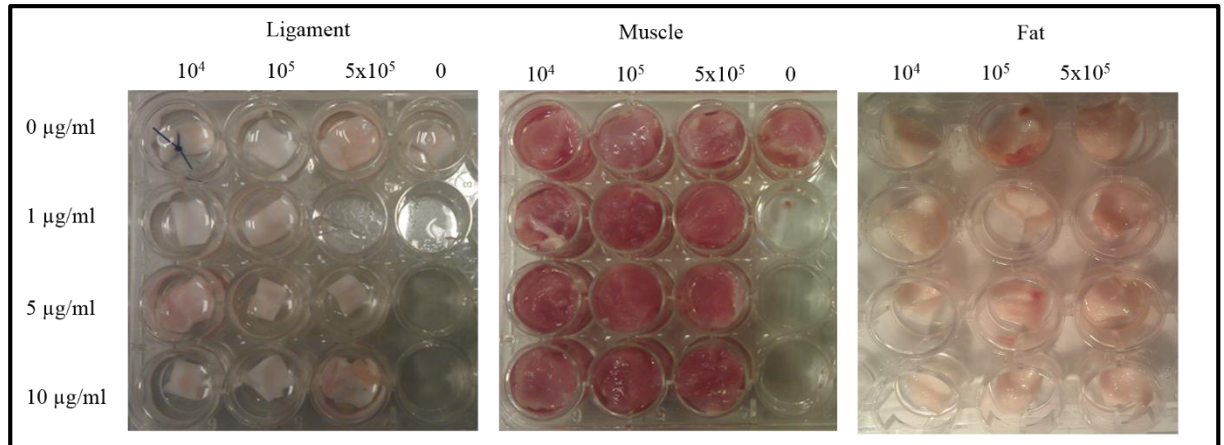
Figure 2.5. Plate layout for ligament, muscle and fat prepared for MR imaging when injected with SiMAG labelled hMSCs and chondrocytes and prepared for ex vivo visibility threshold evaluation

2.8.5.2 Porcine Knee Model

A cadaveric porcine knee model of articular cartilage damage was created to assess the visibility threshold of SiMAG-labelled cells within a clinical relevant model. All MR imaging related to this model were carried out at the MARIARC centre part of Liverpool University using the Siemens Symphony 1.5 T scanner. Pig's legs were purchased from Staffordshire meat packers (Staffordshire, UK) and processed to remove all surrounding tissue using a surgical scalpel (21 Blade). Once the knee had been isolated, the patella tendon was sliced and the patella pulled back revealing the articulating ends of the femur and tibia with the articular cartilage being clearly visible as shown in Figure 2.6. The knee was then bent to fully expose the upper condyles, and cartilage flaps were created (1.5 cm x 0.5 cm x 1.5 cm) at various locations across the upper condyles of the knee. A maximum of two defects were created on each condyle (left and right) ensuring that defect were at least 0.5 cm apart. In all experiments (sections 2.8.5.2.1, 2.8.5.2.2, 2.8.5.2.3) SiMAG-labelled chondrocytes were suspended in collagen type 1 gel (4.5 mg/ml) and injected within the defect while the knee was in the bent upright position. Care was taken to ensure that no

bubbles were created and that none of the collagen and cell suspension had leaked out. Once the gels had set (1 hr 37 ^{o}C) the leg was then straightened, the patella replaced and securely bandaged, to prevent excess movement. The leg was then stored at-20°C until MR imaged. The joint was defrosted 1 day prior to MR imaging. On the day of imaging, knees were transported to the MARIARC centre for scanning. During imaging knees were placed within a circularly polarised extremity coil and placed hip first into the scanner and Double Echo Steady State (DESS) sequences were applied (Table 2.4). These are common MRI scanning conditions implemented in the MR imaging and diagnosis of human knee pathologies.
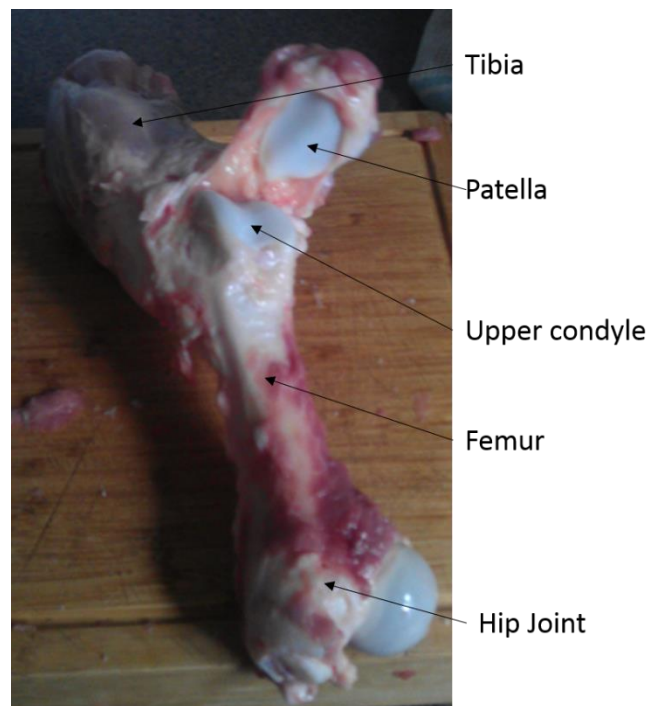
Figure 2.6. Dissected pigs knee with the patella pulled back exposing the upper condyle articulating the femur.

2.8.5.2.1 Porcine Knee Model Optimisation

Optimisation experiment included the use of two cadaveric pig knee joints. In the first knee (Figure 2.7 A), two defects were created in each of the upper condyle; left condyle: cartilage flap was created and injected with 100 μl volume of type 1 collagen gel (4.5 mg/ml), right condyle: the piece of cartilage was completely removed to expose the subchondral bone. The purpose of this was too evaluate defect appearances on an MRI image. It is important to establish that the defect created on the left condyle is suitable for further SPION-labelled cell experiments i.e the creation of the defect to not result in hypointenties when MR imaged that could encourage false positives with the implantation of SPION-labelled cells. In the second knee (Figure 2.7 B), only one defect was created in the upper left condyle and injected with 100 μl of $3x10^6$ SiMAG-labelled chondrocytes in excess (concentration > 100 μg Fe/ml) suspended collagen type 1 gel (4.5 mg/ml collagen gel). The purpose of this was assess if SPION-labelled cells could be detected within the defect with standard pulse sequences while still evaluating knee anatomy.
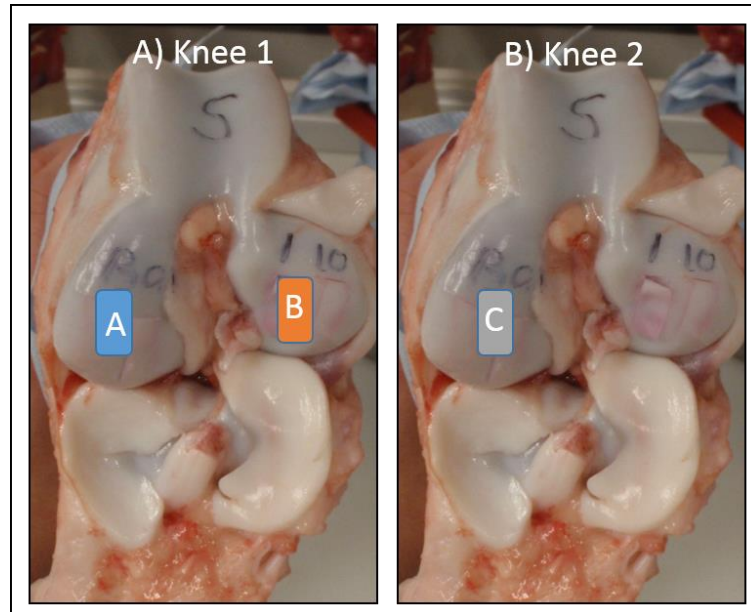
Figure 2.7. Image highlighting the sites of artificially induced cartilage defects across the upper left and right condyle of 2 separate knee. (A) Knee 1; Cartilage flap filled with collagen (4.5 mg/ml), (B) Knee 2; Cartilage completely removed C) Cartilage flap injected with 3x10^6 SiMAG-labelled chondrocytes (excess) re-suspended in 4.5 mg/ml collagen gel.

2.8.5.2.2 Particle Concentration Investigation

The effect of particle concentration on the visibility threshold within the clinically relevant model was assessed by implanting 5x10^5 chondrocytes labelled with SiMAG (0.1, 1, 10 µgFe/ml) into the porcine model (Figure 2.8) and MR imaged as described in section 2.8.5.2 .
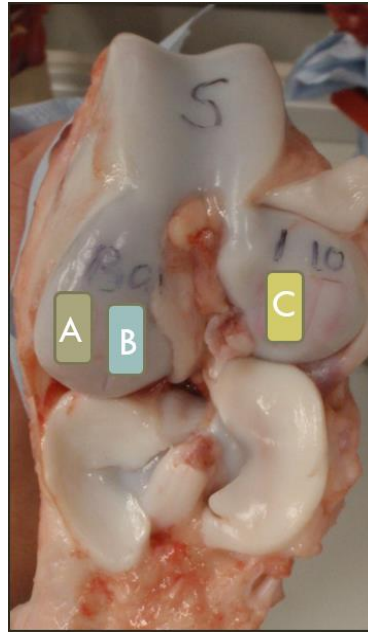
Figure 2.8. Particle concentration investigation. Schematic highlighting the implantation sites of $5x10^5$ SiMAG-labelled chondrocytes: (A) 0.1 µgFe/ml, (B) 1 µgFe/ml and (C) 10 µgFe/ml.

2.8.5.2.3 Cell Dose Investigation

Finally, the effect of cell densities on the visibility threshold was determined by implanting varying cell doses (10^4, 10^5 and $5x10^{6)}$ of SiMAG-labelled chondrocytes (5 µgFe/ml and 10 µgFe/ml) into the porcine model (Figure 2.9 i and ii) and MR imaged as described in section 2.8.5.
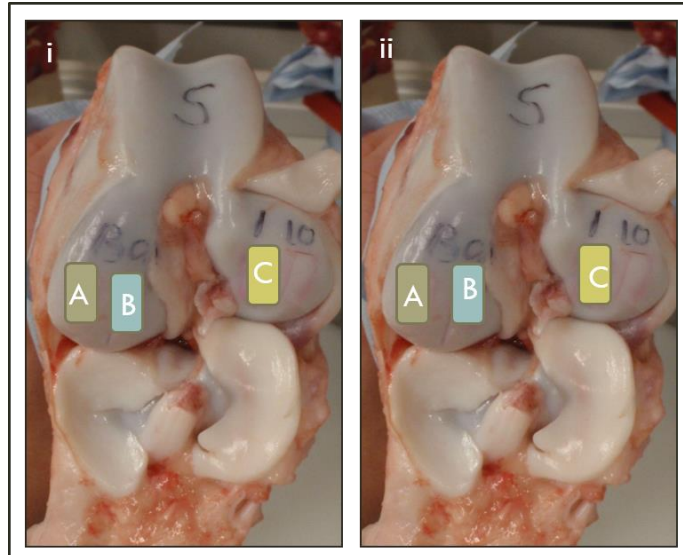
Figure 2.9. Cell dose investigation. Schematic highlighting the implantation sites of varying cell densities: (A) 10^4, (B) 10^5, (C) 5×10^5 of chondrocytes labelled with; (i) 10 µgFe/ml and (ii) 5 µgFe/ml SiMAG.

2.8.6 *In vivo* MRI

2.8.6.1 Visibility Threshold: Animal Models

The *in vivo* visibility threshold for both animal models (mouse and rat) was determined by injecting a 10 µl volume of cell suspension intra-articularly into each joint of healthy (non-arthritic) mice (10 week old BALB/c mice) and rats (18 week old Wistar rats). SiMAG-labelled mMSCs (1, 5 and 10 µgFe/ml) were re-suspended at the relevant cell dose (mouse; 3×10^5, rat; 1×10^6 & 2×10^6) in serum free media prior to injection.

Mice were placed face down into a purpose built holder (Figure 2.10) and inserted head first into the scanner. Rats were also positioned head first into the scanner, however, due to significantly larger size of the rats no holder was necessary. Mice were then MR imaged on Brucker 2.3 T animal scanner where whole body coronal slices were achieved for the mouse

while only sagittal knee focused imaged were possible for the rat. (MRI sequence; RARE Table 2.3).

Figure 2.10. Mouse positioned in the customised holder prior to MR imaging thus ensuring that the knees were a suitable distance apart and positioned on an even plane.

Data Analysis- Signal loss profiles

Bruker files were first converted to Analyze files using Bru2Anz converter and subsequently processed using MRIcron. MRIcron allows for relative signal intensities of every point within the whole image to be obtained. Once the files were loaded, the slices were assessed to identify 3 slices where all the anatomical structures of the knee were in full form (Figure 2.11; slice number 8, 9 and 10). The signal intensity (SI) at 10 points of equal intervals across each knee of the mouse and 20 points of the rats were then measured. At all times the coordinates between slices were maintained. The average SI of the 3 slices were then averaged, plotted and compared.
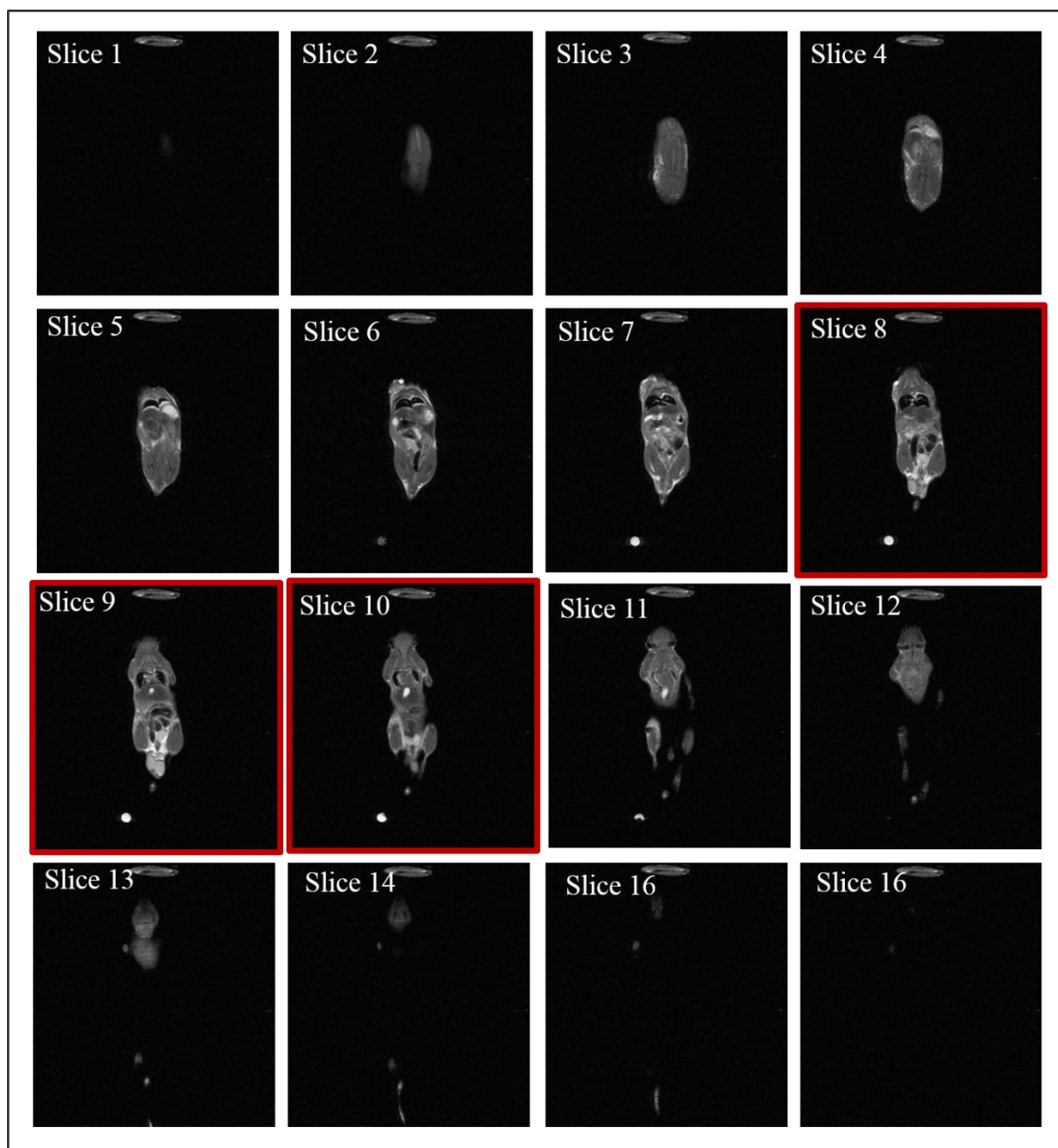
Figure 2.11. Slice 1-16 of mouse MR imaged using Bruker 2.35T animal scanner using GEFI T$_2$ weighted MR sequences and analysed using MRIcron. Slices outlined in red highlight slices whereby signal intensities (SI) profiles were taken.

2.8.6.2 *In vivo* MRI Tracking Studies.

Once sacrificed (mice; days 3 & 7, rats at day 29) animals were transported to Nottingham Trent University to be MR imaged using Bruker 2.3 T animal scanner. Animals were positioned within the scanner as described in Section 2.8.6.1. Whole body coronal FLASH & RARE sequences (Table 2.3) were applied to image mice at the day 3 time point while GEFI & RARE sequences were used for day 7 (Table 2.3). Finally sagittal knee focused slices were implemented to MR image rats using MSME sequences day 29. Signal profiles were obtained as described in section 2.8.6.1.

2.9. Animal Models

2.9.1 CM-DiI Labelling

Stock solution of the fluorescent cell-tracer CM-DiI (Molecular Probes, UK, Cat # C7000) was prepared in dimethyl sulfoxide (DMSO) at a concentration of 1 mg/ml. Cells were trypsinised, suspended in the CM-Dil working solution (2.5 µl of stock per 1 ml of PBS) and incubated for 5 mins at $37\,^{\circ}C$, and then for an additional 15 min at $4^{\circ}C$, in the dark. Unbound dye was removed by centrifugation at 300 g for 5 mins and washed twice using PBS. Finally, cells were resuspended in serum free media and maintained at $4\,^{0}C$ prior to injection

2.9.2 Rheumatoid Arthritis Model

2.9.2.1 Animals

Procedures were performed in accordance with Home Office-approved project licence. PPL 40/3594 were approved by the Ethical Review Committee at Liverpool John Moores University UK, February 2012. Experiments were conducted in 10 week old male C57Bl/6 mice (Harlan, Bicester UK) and carried out by Dr Oksana Kehoe.

2.9.2.2 Induction of Murine Antigen-induced Arthritis (AIA)

Murine AIA was induced as described by Nowell *et al* (180). Mice were subcutaneously immunised with 100 µl of 1 mg/ml of methylated BSA/PBS emulsified with an equal volume of Freund's complete adjuvant into the right knee using 29 G insulin syringe (BD microfine 0.5ml). 100 µl heat-inactivated *Bordetella pertussis* toxin (Sigma-Aldrich, Poole, UK) was then injected intraperitoneally. The immune response was boosted 1 week later by subcutaneously injecting 1 mg/ml of methylated BSA/PBS emulsified with an equal volume of Freund's complete adjuvant. 21 days after the initial immunisation, murine AIA was induced (day 0) by intra-articular (IA) injection of 10 µl of 10 mg/ml BSA/PBS in the right knee joint. A left knee joint was treated as control by receiving 10 µl of PBS. 20 hours post arthritis induction, 10 µl of serum free media, containing 3×10^5 CM-DiL labelled mMSCs (either labelled with or without SiMAG (10 µgFe/ml)) were injected intra-articularly into the right knee joint (day 1) and monitored for either 3 or 7 days. Experimental groups are descried in Table 2.5. Control animals were injected with only serum free CEM. Upon experiment termination, animals were sacrificed, MR imaged and joints were also collected for histological assessment (section 2.5.2).

Table 2.5. Explanations of experimental groups.

Group	Description	Tracking period	Study
1 (n=6)	SiMAG-labelled mMSCs	3 days	MRI tracking study
2 (n=5)	SiMAG-labelled mMSCs	7 days	MRI tracking study
3 (n=6)	Unlabelled mMSCs	3 days	MRI tracking study
4 (n=5)	Unlabelled mMSCs	7 days	Pilot mMSCs study
5 (n=6)	Serum Free Media	3 days	Pilot mMSCs study
6 (n=5)	Serum Free Media	7 days	MRI tracking study

2.9.2.3 Joint Swelling Measurements.

Animals were inspected daily for arthritic development by measuring knee joint diameters on days 0, 1, 2, 3, 5 and 7 using a digital micrometer (Kroeplin GmbH, Schlüchtern, Germany). The difference in joint diameter between the arthritic (right) and non-arthritic control (left) in each animal gave a quantitative measure of swelling (in mm). Statistical analysis was performed using unpaired t-test.

2.9.3 Osteoarthritis Model

2.9.3.1 Animals

This study was carried out in accordance with UK Home Office Animals (Scientific Procedures Act 1986) and the guidelines of the International Association for the Study of Pain. Experiments were performed in 6 week old male Sprague Dawley Rats ranging in weight from 160-200 g obtained from Nottingham University animal house. Surgery was carried out by Dr Devi Sagar and Dr James Burston.

2.9.3.2 Induction of Osteoarthritis- Meniscal Transection Model (MNX)

OA was induced by transecting the medial collateral ligament of the left knee of each anaesthetised rat and a full thickness cut made through the meniscus (day 0). Incisions were then closed using surgical staples. Weight gain, posture and behaviour were carefully monitored throughout the post-injury period. 14 days post-surgery, rats were stratified into groups (n=4) (Table 2.6) according to pain behavioural responses and prepared for cell implantation. Unfortunately, 1 rat did not survive the surgery and for this reason, only 3 rats were placed within the SiMAG-labelled group. A 10 µl solution containing 1.5×10^6 CM-DiL labelled mMSCs (either labelled with or without SiMAG (10 µgFe/ml) re-suspended in serum free media were then injected intra-articular through the infrapatellar ligament of the diseased knee.

Table 2.6. Explanations of experimental groups.

Group	Description	Tracking period
1 (n=3)	SiMAG-labelled mMSCs	29 days
2 (n=4)	Unlabelled mMSCs	29 days
3 (n=4)	Serum Free Media	29 days

2.9.3.3 Pain Perception

Behavioural tests assessing changes in weight-distribution and sensitivity to mechanical stimuli were performed for up to 42 days post-surgery by Dr Devi Sagar and Dr James Burston. Baseline measurements were taken immediately prior to intra-articular injection (day 0) and then from day 3 onwards.

2.9.3.3.1 Weight Bearing Asymmetry

The effects of MNX surgery on the weight-distribution through the left and right knee was assessed using an incapacitance tester (Linton Instrumentation, UK) (Figure 2.12) and was assessed between post-operative days 3 to 42. The two hind-paws were placed on separate sensors and the force (in grams) exerted by each hind limb was calculated and averaged over a period of 3 seconds as described previously by Clayton *et al* and Elmes *et al* (181, 182). Each data point was taken as the mean of three 3 second readings and the weight bearing asymmetry calculated by applying the below equation 2.3. Statistical analysis performed by two way Anova with Bonferrioni post-test using GraphPad.

Equation 2. 1 Equation used to calculate the weight bearing asymmetry of rats. This is the ratio of the forces placed on the treated (left) and untreated (right) hind legs.

$$\text{Weight bearing asymmetry} = \frac{\text{Weight on Right Limb (g)} - \text{Weight on Left Limb (g)}}{\text{Total weight on Hind Limbs (g)}} \times 100$$

Figure 2.12. Incapacitance tester used to evaluate weight bearing asymmetry of rats. Rats are placed within a transparent box with hind legs placed on the sensor pads.

2.9.3.3.2 Mechanical Allodynia

The development of allodynia is commonly assessed using von Frey monofilaments (Semmes-Weinstein monofilaments) of bending forces 1, 1.4, 2, 4, 6, 8, 10 and 15 g (40)

(Figure 2.13). Rats were placed in transparent plastic cubicles placed on a mesh floored table and allowed to acclimatize prior to testing. Von Frey monofilaments were then applied, in ascending order of bending force, to the plantar surface of both hind-paws. Each von Frey was applied for a 3 sec period. Once a withdrawal reflex was established, the paw was re-tested with the next descending von Frey monofilament until no response occurred. The lowest weight of monofilament which elicited a withdrawal reflex was noted as the paw withdrawal threshold. Statistical analysis performed by two way Anova with Bonferrioni post-test using GraphPad.
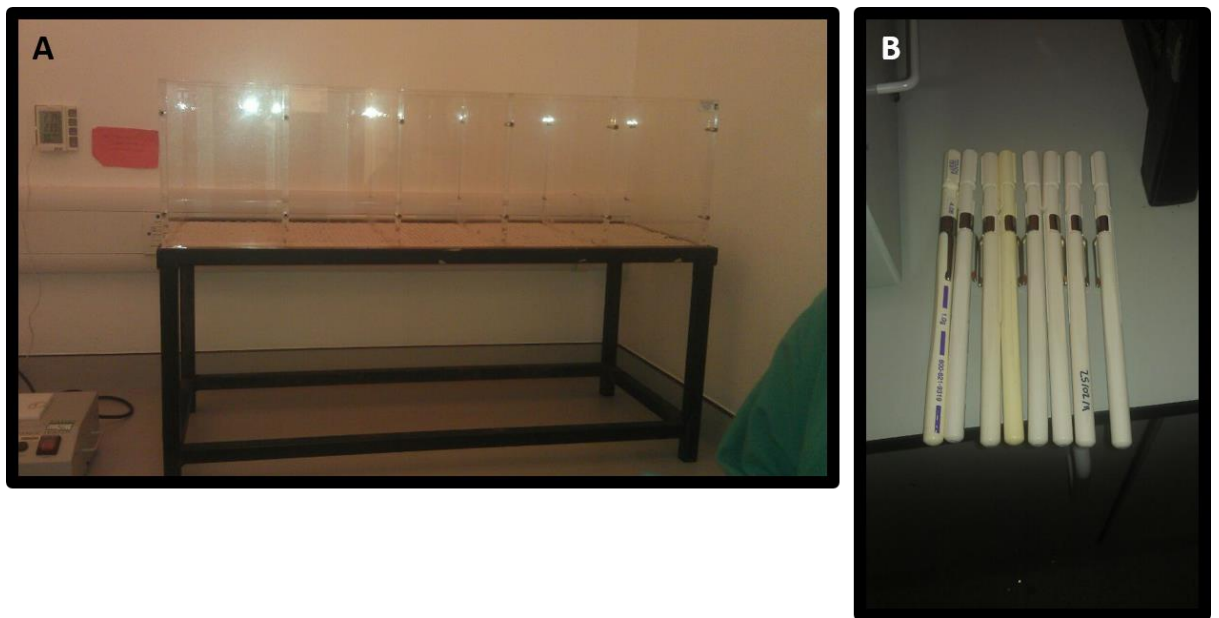
Figure 2.13. Equipment used to measure paw withdrawal threshold. Rats are placed within the transparent cubicle shown in A) allowed to settle before assessing pain using a range of von Frey monofilaments shown in B.

Chapter 3

Labelling of Cell Populations with SPIONs

3.1 Introduction

The imaging and tracking of stem cell population *in vivo* requires the application of a contrast agent with the complementing imaging modality to distinguish the implanted cells against the biological tissue (84, 93, 183). MR imaging is a highly powerful, non-invasive technique benefiting from high spatial resolution, high tissue contrast and importantly, is available in most clinics today (93). Furthermore, the use of contrast agents in MR imaging improves the diagnostic power of this technique by enhancing the contrast between healthy and diseased tissues/organs and also improves image specificity. Of notable importance are the group of FDA approved SPION-based MRI contrast agents (119, 128). These are accepted T_2 weighted contrast agents (119, 128) and are commonly used to image the liver and spleen (130). Table 3.1 describes the range of commercially available T_2 weighted MRI contrast agents, specifically focusing on their size and coating characteristics. Noticeably, dextran is the preferred coating of choice with a hydrodynamic diameter commonly ranging from 20 – 150 nm in size.

Table 3. 1. Commercial FDA approved T_2-Weighted Contrast Agents.

Brand Name	Generic Name	Target	Hydrodynamic diameter (nm)	Coating	Reference
Endorem (EU), Feridex (USA)	Ferumoxide	Reticulo-endothelia system, Liver	80-150	Dextran	(184, 185) (186) (91)
Rienso (EU), Feraheme (USA)	Ferumoxytol	Fe replacement	20-30	Carboxyl - methyldextran	(91, 187)
Resovist (EU, USA)	Ferucarbotran	Blood Pool	20	Carboxydextran	(91, 188)
Sinerem (EU) Combidex (USA)	Ferumoxytol	Blood Pool	15-30	Dextran	(91, 189) (186)
Lumirem (EU) Gastromark (USA)	Ferumoxsil	Liver, Blood pool	300	Silica	(91)

The clinical approval of this range of contrast agents (Table 3.1) has encouraged the adoption of these particles by research communities working to image and track cells *in vivo* (83, 184,

187). Whilst still in seldom use, Endorem, Resovist and Sinerem have officially been off the commercial market since 2009 and are no longer available for purchase (91). Therefore, extensive efforts have been devoted to the development of novel SPIONs as imaging and tracking agents (91, 134). A commercial and literature search has revealed a vast and extensive range of SPIONs currently available, ranging in size, coating and functionalities.

In general terms SPIONs are composed of either a magnetite (Fe_3O_4) or maghemite (γ-Fe_2O_3) core (125, 131) coated with a biocompatible polymer (121, 132); together defining the hydrodynamic diameter of the particle. Both maghemite and magnetite are ferrimagnetic in nature; however as their size decreases below 30 nm they lose their permanent magnetism and become superparamagnetic in nature (109). This has significant implications in the biological context as the superparamagnetic nature of the particles implies that the particles do not retain their magnetisation after the removal of the magnetic field. Therefore, will not be magnetically attracted to each other and so the risk of agglomeration in a medical setting is minimised (120, 129). The biocompatibility of the particle is attributed to the addition of the polymer coating preventing the biological entity from adverse effects as a result of being in direct contact with the iron core (121, 122). Silica, fibronectin and dextran are all examples of biocompatible polymer coatings, all of which can be further surface functionalised to enhance cell–SPION interactions (111,118,123). The nature of the polymer coating and the consequent modifications determine the ultimate physical and biological properties of the particles such as the size, charge, toxicity and degradability (91).

SPION internalisation is a necessary prerequisite for the successful imaging and tracking of stem cell populations *in vivo* by MRI. Essentially, cells are encouraged to internalise SPIONs via various uptake mechanisms in order to accumulate within the cell cavity. When MR imaged, the SPIONs effectively alter the transverse relaxation properties of the water protons thus producing dark negative contrast providing an effective, simple and non-invasive means

of visualising cells against the background of a tissue as hypointense signal voids on MRI scans (91).

Each of the particle characteristics (size, polymer coating and functionalities) have been reported to impact the rate and efficiency of SPION internalisation. In addition to the physical properties of the particle, cell type and rate of proliferation have also been known to affect this process (91, 118). Transfection agents (TA) can be implemented to promote SPION uptake (91, 106). A downfall of using TA is associated with unwanted toxic effects and impaired biological properties of the cells thus limiting the therapeutic potential of cells (91).

There is no clear consensus as to the ideal set of SPION characteristic that would yield the greatest uptake while producing the best contrast. Figure 3.1 lists the criteria defining the ideal labelling agent. This includes efficient particle uptake, the ability to create T_2 weighted contrast, biocompatible and the long term retention of particles to facilitate long term tracking.

Pre-requisites for *in vivo* cell tracking agent

1. Efficient stem cell labelling
2. Significant T_2 relaxivity
3. Long term retention of SPIONs
4. Biocompatible
5. No impaired biological activity

Figure 3.1. Basic criteria defining the ideal labelling agent for the *in vivo* imaging and tracking of implanted cells.

3.2 Aims and Objectives

This chapter aims to investigate four commercially available SPIONs, namely SiMAG, Lumirem, Nanomag and P904 and their potential as tracking agents in arthritic stem cell based therapies. The criteria listed in Figure 3.1 will form the basic acceptance criteria according to which each particle will be assessed. However, this list has been modified (Figure 3.2) to increase the likeliness of clinical adoption.

> **Specific Pre-requisites for *in vivo* cell tracking agent**
> 1. Efficient stem cell labelling with SPIONs **without the use of transfection agents.**
> 2. Significant T_2 relaxivity at **minimal particle concentrations on clinically relevant systems (1.5T – 3T)**
> 3. Long term retention of SPIONs with cells
> 4. Biocompatible of SPIONs
> 5. No impaired biological activity

Figure 3.2. Modification of basic criteria defining the ideal labelling agent to increase likelihood of clinical adoption.

Therefore, this chapter aims to assess a range of commercially available SPIONs on their potential application as *in vivo* tracking agents based on Figure 3.2. SPION internalisation will be assessed and subsequent effects on cell viability, proliferation and biological function of hMSCs and porcine chondrocytes will be further evaluated.

3.3 Materials and Methods

The flow chart summarises key experimental aims of this chapter in dark blue with specific experimental parameters in light blue (Figure 3.3). Further details can be found in Chapter 2; Materials and Methods.

Isolation & characterisation of cells
hMSC ; multi-lineage differentiation & cell surface markers using flow cytometry (facs) **Chondrocytes**; Alcian blue staining

Selection and characterisation of labelling agents
SPIONs ranging in size: 20 nm; P904, 50 nm; Nanomag, 300 nm; Lumirem & 1000 nm; SiMAG characterised in terms of size, charge, Fe & MRI relaxivity.

Development of Labelling protocol - *In vitro* assessment of particle uptake.
Selection of labelling conditions; particle concentration (1, 5, 10, 100 µgFe/ml) and labelling media (SFM or SCM). **Assessment**: Prussian blue staining and ICP-OES

In vitro assessment of cell viability & proliferation
SiMAG, Lumirem, Nanomag & P904; 10 and 100 µgFe/ml over 24 hrs and 7 days. **Assessment:** Live dead and MTT assay;

Characterisation of cells post SiMAG-labelling (10 µgFe/ml)
hMSC ; tri-lineage differentiation, cell surface markers using FACS **Chondrocytes**; histology

Particle retention
SiMAG-labelled hMSCs and Chondrocytes; 1, 7, 14, 21 & 28 days. **Assessment**: Prussian blue staining and ICP-OES

Figure 3.3. Experimental plan for the selection of a labelling agent and the development of a labelling protocol for the use of SPIONs to track cell populations using MRI.

3.4 Results

3.4.1 Cell Characterisation

Bone marrow derived hMSCs reside within a heterogeneous population of cells within the bone marrow. It is therefore essential to validate the specific characteristics of the isolated cells and confirm their identity as multipotent MSCs. hMSCs were characterised by applying the minimal criteria, set by the International Society for Cell Therapy (ISCT) (75).

Similarly, it is necessary to characterise the porcine primary chondrocytes isolated from fresh articular knee cartilage. Primary chondrocytes can be characterised by their ability to secrete sulphated glycosaminoglycans (50).

3.4.1.1 Human Mesenchymal Stem Cells (hMSCs)

3.4.1.1.1 Plastic Adherence

hMSCs were identified as those which after two weeks in culture had adhered to tissue culture plastic with a spindle shaped fibroblastic like appearance, as shown in Figure 3.4.
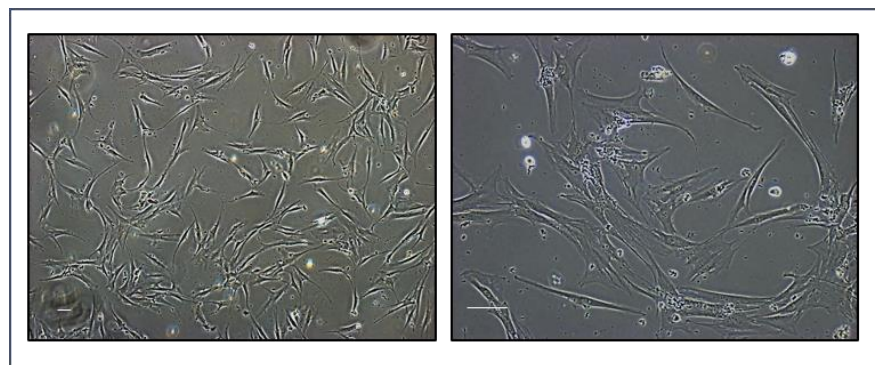
Figure 3.4. hMSCs attached to tissue culture plastic at passage 1. Scale Bar = 100µm.

3.4.1.1.2 Cell Surface Marker Expression

Flow cytometry was implemented to investigate the expression of cell surface markers typical to hMSCs and to validate the lack of hematopoietic markers as defined by Dominici *et al* (75). Flow cytometry analysis (Figure 3.5) demonstrated the positive expression of the MSC markers: CD 73, CD 90 and CD 105 while proving negative for the expression of CD14, CD 19, CD 31, CD 34, CD 45 and HLA-DR although the expression for CD14 was higher than expected. Percentage of positive expression of each of these cell markers are stated in Table 3.2.

Table 3. 2. Positive expression of typical MSC Surface Markers.

Cell Surface Marker	% Positive
CD14	13.50
CD19	4.25
CD31	5.60
CD34	4.89
CD45	4.66
CD73	62.13
CD90	74.57
CD105	65.91
HLA-DR	4.77
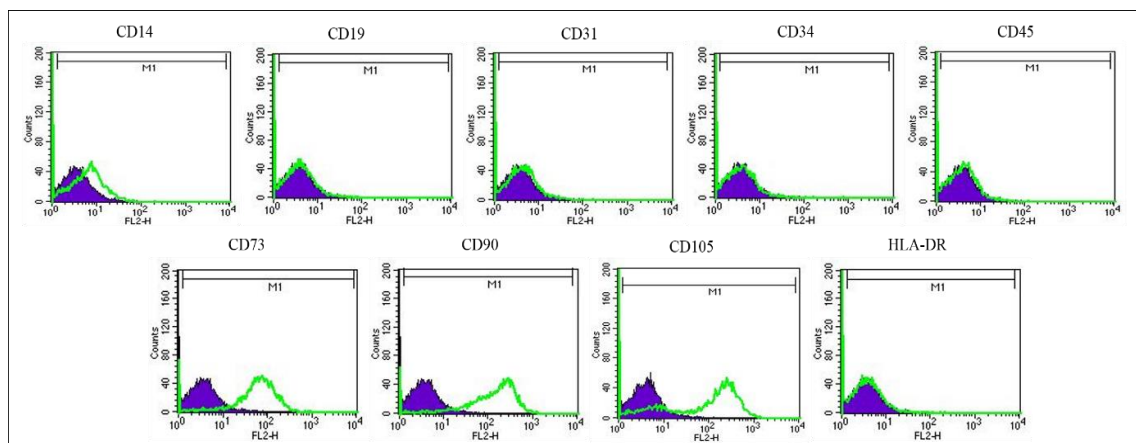
Figure 3.5. Characterisation of the expression profile of typical hMSC surface markers (CD 105, CD 73, CD 90) and demonstrating the lack of hematopoietic markers (CD34, CD 45, CD 14, CD 19, CD 31 and HLA-DR) using flow cytometry.

3.4.1.1.3 Multi-lineage Differentiation of hMSCs

The multipotent differentiation capacity of bone marrow derived hMSCs was investigated by inducing differentiation towards osteogenic, adipogenic and chondrogenic lineages. hMSCs underwent successful differentiation towards all three lineages (adipogenic, chondrogenic and osteogenic) after 21 days in culture with relevant differentiation media. Adipogenesis was confirmed by the presence of lipid and triglyceride droplets stained positive with oil red O after 21 days cultured with adipogenic differentiation media (Figure 3.6 A). Calcium deposition was stained positive by alizarin red for samples receiving osteogenic differentiation media, thus confirming osteogenesis (Figure 3.6 B). Alcian Blue stain was used to identify the secretion of sulphated gycosaminoglycans by cells which had undergone chondrogenic differentiation (Figure 3.6 C). No positive staining was observed in control groups receiving basic proliferation media for all cases nor at day 0 (image not shown). This study confirms the multipotency of isolated hMSCs as well as their differentiation capacity.
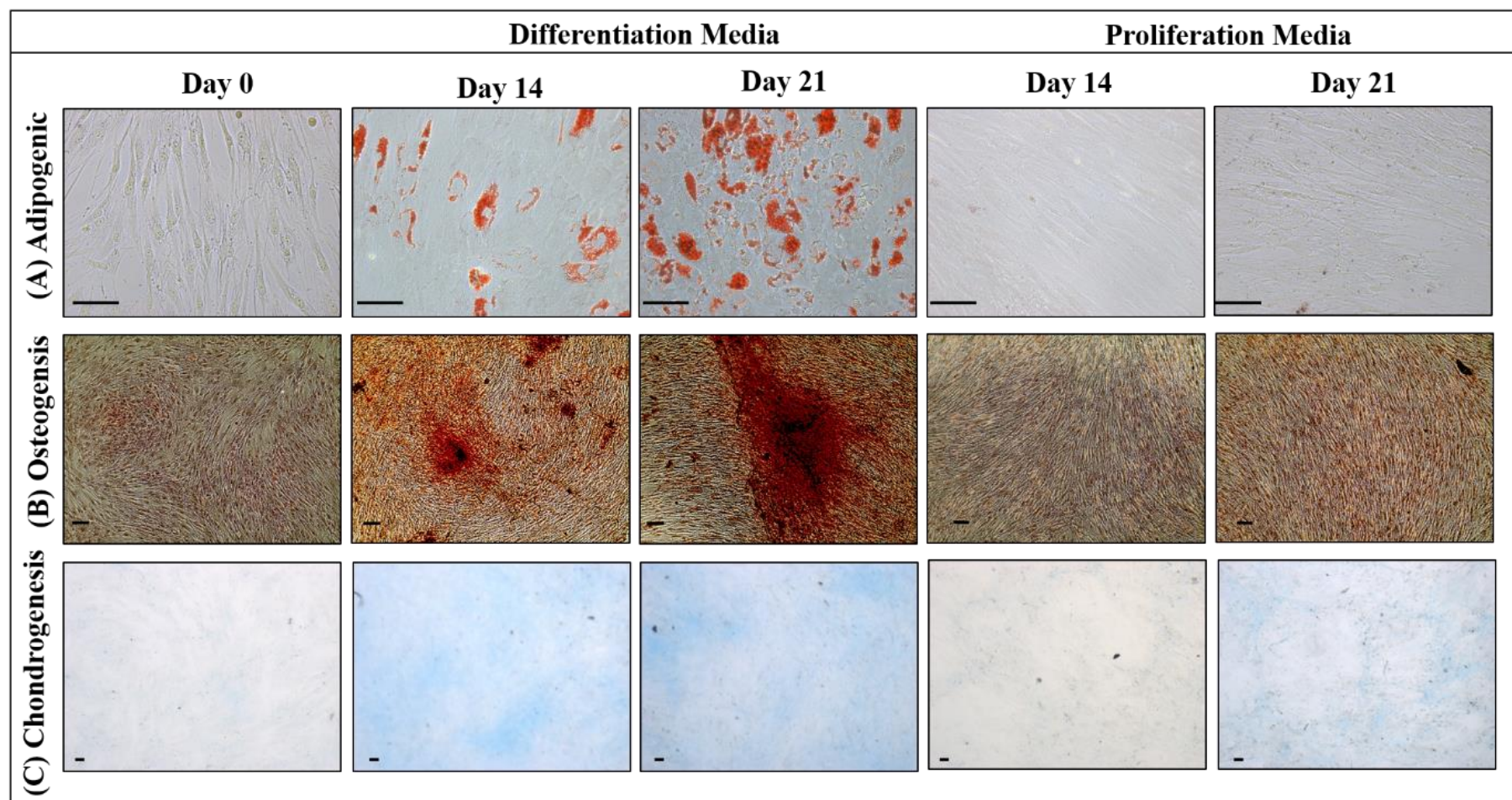
Figure 3.6. Multi-lineage differentiation of hMSCs. Images represent differentiation of hMSCs towards (A) Adipogeneic, (B) Osteogenic and (C) Chondrogenic lineages with time at days 14 and 21 days. Scale Bar = 100 µm.

3.4.1.2 Chondrocytes

Chondrocyte morphology appeared rounded upon isolation at Passage 0 while at P1, chondrocytes appeared to be flatter and more spread out (Figure 3.7).
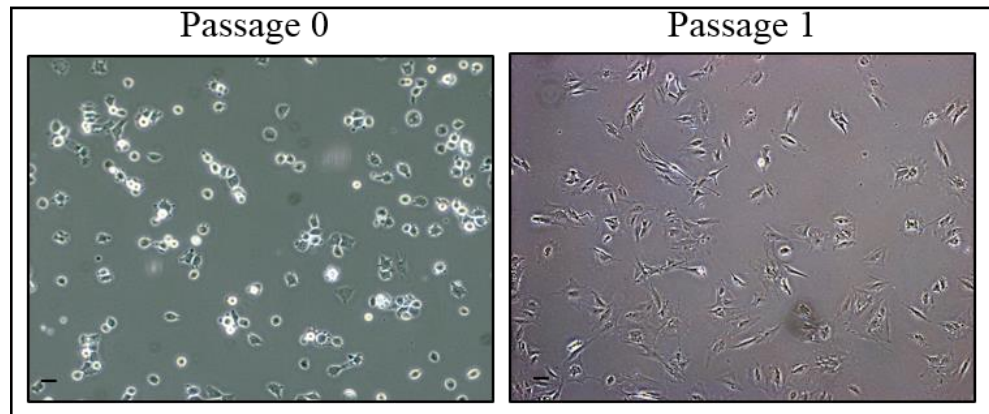
Figure 3.7. Chondrocyte morphology at passages 0 and 1. Scale Bar = 100 µm

3.4.1.2.1 Alcian Blue Staining

Porcine chondrocytes (P3) were characterised by their ability to secrete sulphated glyosaminoglycans (GAGs) when cultured in monolayer in either standard proliferation media or in chondrogenic differentiation media. Alicia blue staining highlights secreted sulphated GAGs as blue. Secreted GAGs were detected for chondrocytes cultured in both proliferation media and chondrogenic media while the use of chondrogenic media resulted in the increased secretion of sulphated GAGS over a 21 day culturing period (Figure 3.8). This confirms the identity of chondrocytes.
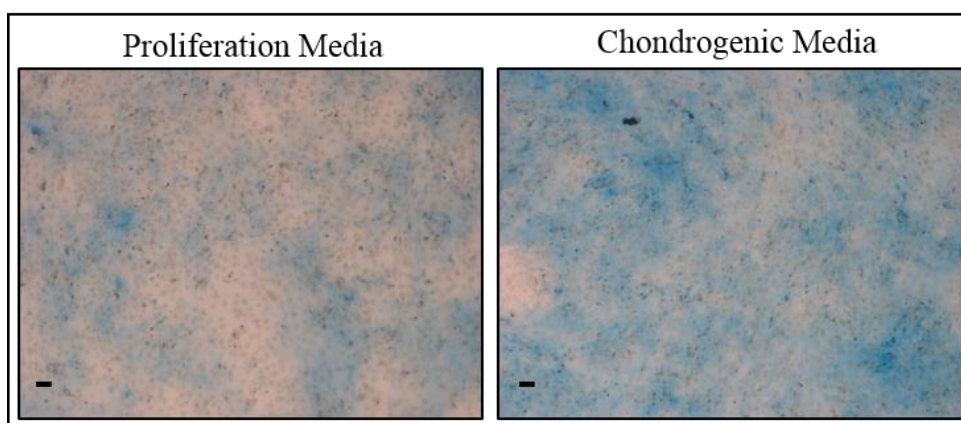
Figure 3.8. Alcian Blue staining of chondrocytes highlighting the secretion of sulphated GAGs as blue areas when cultured in chondrogenic media or basic proliferation media at day 21. Secreted sulphated GAGS are depicted by blue s. Scale Bar= 100 μm

3.4.2 Particle Characterisation

The physiochemical properties of the each particle (SiMAG, Lumirem Nanomag and P904) were assessed in terms of particle size, particle charge and Fe content. Nanoparticle fabrication can be a highly variable process. It is therefore essential to validate the information given by the manufacturers, as these parameters can affect the uptake of particles by the cells.

3.4.2.1 Size

The principal of dynamic light scattering was applied to measure and validate the reported hydrodynamic diameter (HD) of each particle (SiMAG, Lumirem, Nanomag and P904). Particles were characterised under standard cell culturing conditions. Nanoparticles were re-suspended in either serum free media (SFM) or serum containing media (SCM) and incubated for 24 hrs at 37 °C and 5 % CO_2 in order to mimic cell labelling conditions.

The HD of SiMAG as reported by Chemicell is 1000 nm. The addition of serum to culture media (SCM) resulted in a statistically significant decrease in the HD of SiMAG when compared to SFM at the same time point (0 hrs) (SFM; 1.23 $\pm$ 0.103 μm vs SCM: 0.97 $\pm$ 0.041 μm with P < 0.001). This difference became insignificant over the 24 hr incubation period time where similar HD sizes were measured for SiMAG when incubated in SFM and SM for 24 hrs (SFM 1.19 $\pm$ 0.228 μm vs SCM, 1.09 $\pm$ 0.178 μm). The effect of incubation time on the HD of SiMAG when incubated in either SFM or SCM resulted in a non-statistically significant difference in HD over the 24 hr period (SFM: 0 hrs; 1.23 $\pm$ 0.103 μm vs 24 hrs; 1.19 $\pm$ 0.228 μm; SCM: 0 hrs 0.97 $\pm$ 0.041 μm; vs 24 hrs, 1.09 $\pm$ 0.178 μm). In all cases, the HD of SiMAG falls approximately within the 1 μm range roughly validating the manufacture`s report (Figure 3.9 A).

The incubation of Lumirem with either SCM or SFM resulted in a marked increase in HD at either of the two time points (0 hrs and 24 hrs) when compared to the reported value of 300 nm. Further to this, the addition of serum and the effect of incubation time had no significant impact on the HD of Lumirem (SFM: 0 hrs; 1271$\pm$ 221 nm, 24 hrs; 1208$\pm$ 216 nm; SCM: 0hrs; 1329 $\pm$ 168 nm, 24 hrs; 1401 $\pm$ 152). (Figure 3.9 B).

A HD ranging between 50-75 nm has been reported for Nanomag. In this case, the effect of serum had a significant effect on the HD of Nanomag whilst the effect of incubation time had no effect on this parameter. The addition of serum resulted in a significant (*P<0.0001*) decrease in the HD of Nanomag when compared to SFM at both time points (0 hrs: SFM; 76.4 $\pm$ 2.9 nm vs SCM 48.3 $\pm$ 2.8 nm and 24 hrs: SFM 78.5 $\pm$ 2.6 nm vs SCM 49.2 $\pm$ 1.48 nm). Both sets of values fall within the reported range highlighting the effect of serum on the HD of Nanomag (Figure 3.9 C).

Finally, the addition of serum and the effect of incubation time had no statistically significant impact on the HD of P904 with values falling in very close to the reported value of 22 nm (SFM: 0 hrs; 23.9 ± 1.68 nm, 24 hrs; 24.7 ± 1.01 nm, SCM: 0 hrs; 22.3 ± 1.44 nm, and 24 hrs 22.1 $\pm$1.21 nm) (Figure 3.9 D).
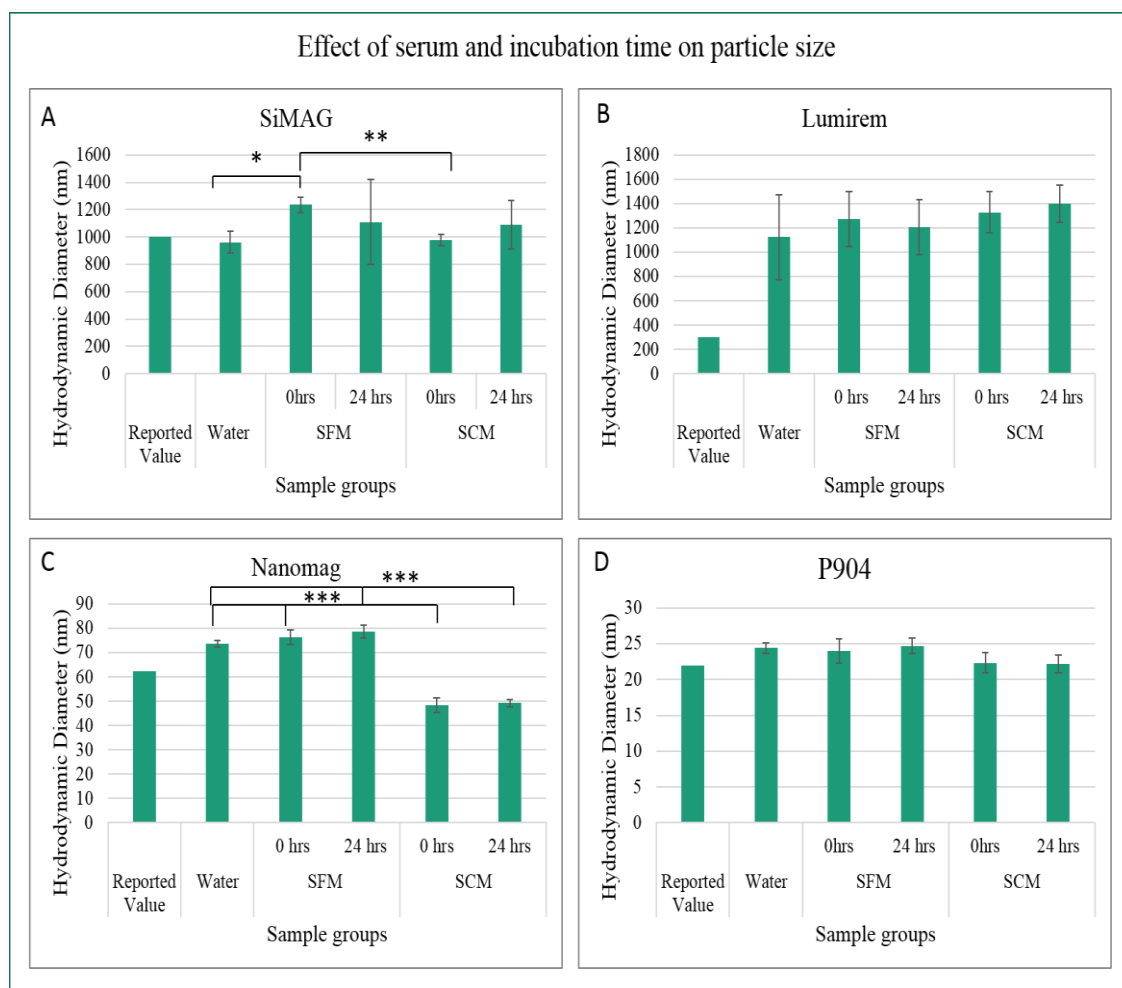
Figure 3.9. Dynamic light scattering analysis of particle size to investigate the effect of SCM (serum containing media), SFM (serum free media) and incubation time on the hydrodynamic diameter (HD) of each particle: (A) SiMAG, (B) Lumirem, (C) Nanomag and (D) P904 when compared to the equivalent particles in water and the reported manufactures value. Data = mean HD $\pm$ SD, n=3. Statistical significance levels represented by * where p < 0.05, ** is p < 0.01 and *** is p<0.001.

A poly dispersity value is produced by the Malvern H3000 zetasizer to complement the DLS data. This is a measure of the size distribution of particles within a suspension. This is a dimensionless value ranging from 0-1 and scaled such that the lower range of values are representative of monodispersed solutions. Values greater than 0.7 are indicative of a particle solution with a highly broad size distribution. Table 3.3 highlights the polydispersity values at each condition (SFM or SCM) and time point (0 hrs and 24 hrs) for each particle (SiMAG, Nanomag, Lumirem, P904) when measuring HD by DLS. The maximum polydispersity value of 1 was reported for Lumirem at all conditions and is thus characterised as being a solution with a highly broad size distribution of particles. SiMAG is considered the next broadly dispersed solution amongst the group of particles with polydispersity values of 0.51 ± 0.11 and 0.53 ± 0.28 reported at 0 hrs for both SFM and SCM respectively. This value then increases to 0.75 ± 0.28 and 0.78 ± 0.23 for SFM and SCM respectively after the 24 hr incubation period. This is followed by Nanomag. A lower polydispersity index is noticed for Nanomag incubated in SFM at either time point (SFM 0 hrs; 0.29 ± 0.004, 24 hrs; 0.33 ± 0.004). However, the polydispersity index for Nanomag appeared to increase to 0.7 ± 0.006 and 0.74 ± 0.007 when incubated in SCM at either 0 hrs or 24 hrs respectively. The lowest range of polydispersity values was observed for P904 with a noticeable trend similar to Nanomag. The polydispersity of P904 was higher when incubated with SCM than in SFM at either time point (SFM: 0 hrs; 0.19 ± 0.03, 24 hrs; 0.2 ± 0.06, SCM: 0 hrs; 0.4 ± 0.007, 24 hrs; 0.36 ± 0.02). Polydispersity values for all particles (SiMAG, Lumirem, Nanomag and P904) in different conditions (SFM vs SCM) are summarised in Table 3.3. Furthermore, a schematic diagram illustrating the relative size differences between all four particles and the cells used in this study (hMSCs and chondrocytes) under different conditions and time points (Figure 3.10). This set of results imply that SiMAG, Nanomag

and P904 do not cluster and aggregate in the presence of either SFM or SCM media with the measured HD values hovering closely similar to the reported value.

Table 3.3. Polydispersity values of SiMAG, Lumirem, Nanomag and P904 when incubated in serum free and serum containing media at either 0 hrs or 24 hrs. Values are expressed as mean $\pm$ SD (n=3)

Particle	Serum Free Media		Serum Containing Media	
	0 hrs	24 hrs	0 hrs	24 hrs
SiMAG	0.51 ± 0.11	0.75 ± 0.28	0.53 ± 0.17	0.78 ± 0.23
Lumirem	1 ± 0	1 ± 0	1 ± 0	1 ± 0
Nanomag	0.29 ± 0.04	0.33 ± 0.04	0.70 ± 0.06	0.74 ± 0.07
P904	0.19 ± 0.03	0.2 ± 0.06	0.40 ± 0.07	0.36 ± 0.02
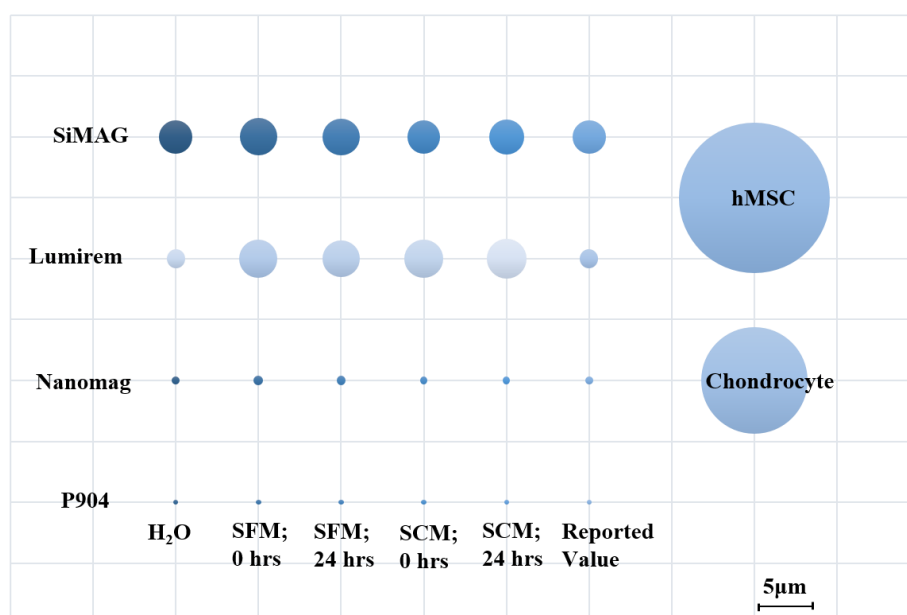
Figure 3.10. Schematic representing the relative size difference between the four selected particles: SiMAG, Lumirem, Nanomag and P904 under various incubation conditions (SFM, SCM, for either 0 hrs or 24 hrs) in comparison to the manufactures reported value and to a hypothetical hMSCs (20 µm) and Chondrocytes (10 µm) size. Scale bar = 5µm

3.4.2.2 Charge – Zeta Potential

The zeta potential (ζ) is defined as the degree of electrostatic repulsion or attraction between particles and is an essential parameter dictating stability of a particle suspension (colloidal suspension) (179). SiMAG and Lumirem were discovered to be negatively charged but stable (-34.6 $\pm$ 0.4 and -61.4 $\pm$ 0.8 mV respectively), whilst P904 and Nanomag were both found to be positively charged with a lower degree of stability (1.8 $\pm$ 3.4 and 2.7$\pm$ 0.4 mV respectively) in comparison to SiMAG and Lumerim, as shown in Table 3.4.

Table 3.4. Zeta potential values for each particle. Values are expressed as a mean $\pm$ SD (n=5). kCPs refers to the count rate; Mob refers to the electrophoretic mobility.

Particle	kCPs	Mob	Zeta Potential ζ (mV)
SiMAG	6765 $\pm$ 217	-2.74 $\pm$ 0.03	-34.6 $\pm$ 0.4
Lumirem	2980 $\pm$ 105	-5.09 $\pm$ 0.065	-61.4 $\pm$ 0.8
Nanomag	2383 $\pm$ 3.8	0.24 $\pm$ 0.031	2.7 $\pm$ 0.4
P904	2380 $\pm$ 15	0.14 $\pm$ 0.27	1.8 $\pm$ 3.4

3.4.2.3 Particle Relaxivity

The relaxivity of a given particle is a measure of its ability to form contrast when MR imaged. Figure 3.11 demonstrates the comparative R_2 relaxivity of each particle (SiMAG, Lumirem, Nanomag and P904) with R_2 being defined by the gradient of the slope. Under these imaging conditions, Lumirem appears to have the greatest potential to form contrast with an R2 value of 0.019 ms^{-1} in comparison to SiMAG (0.011 ms^{-1}) Lumirem (0.007 ms^{-1}) and finally P904 (0.0005 ms^{-1}).
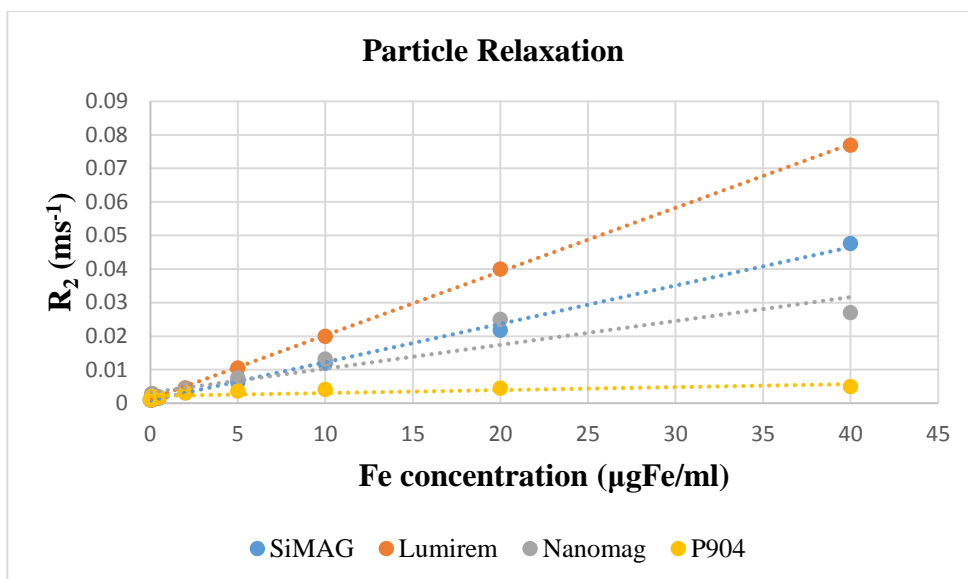
Figure 3.11. Particle relaxivity (R_2) of SiMAG, Lumirem, Nanomag and P904. MR imaging of each particle at varying concentrations (5-40 μg Fe/ml; T_2 weighted MSME sequences) used to determine R_2 measurements. Data shown represents the inverse of T_2 measurements at each concentration with the slope signifying the R_2 value.

3.4.3 Assessing Particle Uptake

3.4.3.1 Prussian Blue Staining

The visual assessment of particle internalisation following a passive incubation period of 24 hrs was assessed by Prussian blue staining (Figure 3.12 & 3.13). hMSCs and chondrocytes were labelled with SiMAG, Lumirem, Nanomag and P904 ranging in Fe concentration 0, 1, 5, 0 and 100 μgFe/ml. The hydrochloric acid component of the stain was used to degrade the particle thus exposing the iron core which then reacts with the potassium ferrocyanide component. The reaction results in the formation of a blue stain of the iron particles when visualized by light microscopy. Prussian blue staining revealed the presence of SiMAG within the cell membrane of hMSCs and chondrocytes when labelled with 1, 5, and 10 μgFe/ml. Particle content was noticed to increase within increasing SiMAG concentration 1-10 μgFe/ml for both hMSCs and chondrocytes (Figure 3.12 & 3.13). It is obvious that the

addition of 100 µgFe/ml of SiMAG is in significant excess, as SiMAG particles are observed to almost completely cover the bottom of the well and appear to sit on top of the cells (hMSCs and chondrocytes) (Figure 3.12 & 3.13). Further to this, considerably fewer stained particles could be detected within hMSCs when labelled with 5, 10 and 100 µgFe/ml Lumirem, shown by white arrow in Figure 3.12. No Lumirem particles could be detected at either concentration (1, 5, 10 and 100 µgFe/ml) for chondrocytes (Figure 3.13). Furthermore no particles could be detected in either cell type when labelled with Lumirem (1 µgFe/ml), Nanomag (1, 5, 10 and 100 µgFe/ml), P904 (1, 5, 10 and 100 µgFe/ml) appearing similar to unlabelled cells.
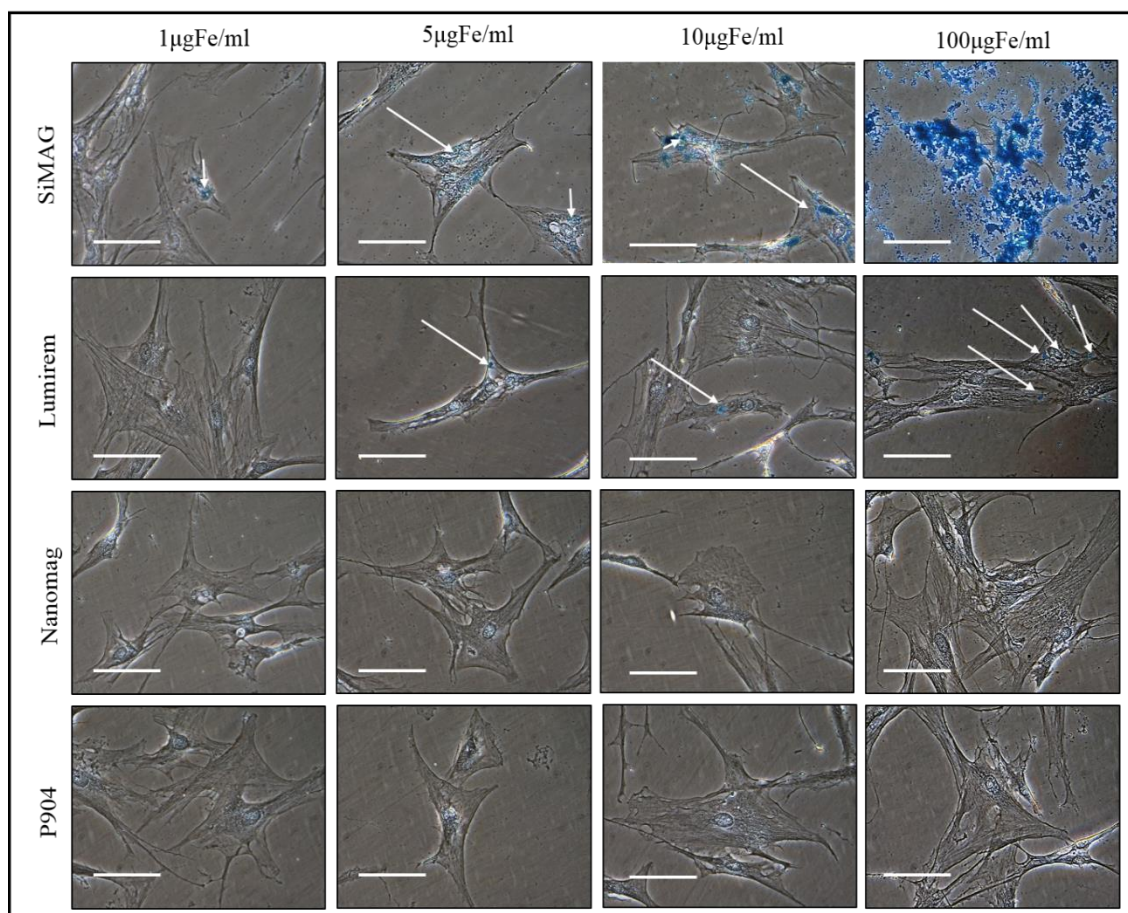
Figure 3.12. hMSCs stained with Prussian Blue. Light microscopy images (24 hrs post labelling) of Prussian blue stained SPION-labelled hMSCs (SiMAG, Lumirem, Nanomag & P904; 1, 5, 10, 100 µgFe/ml). SPION are stained blue and shown by white arrow Scale bar = 100 µm.
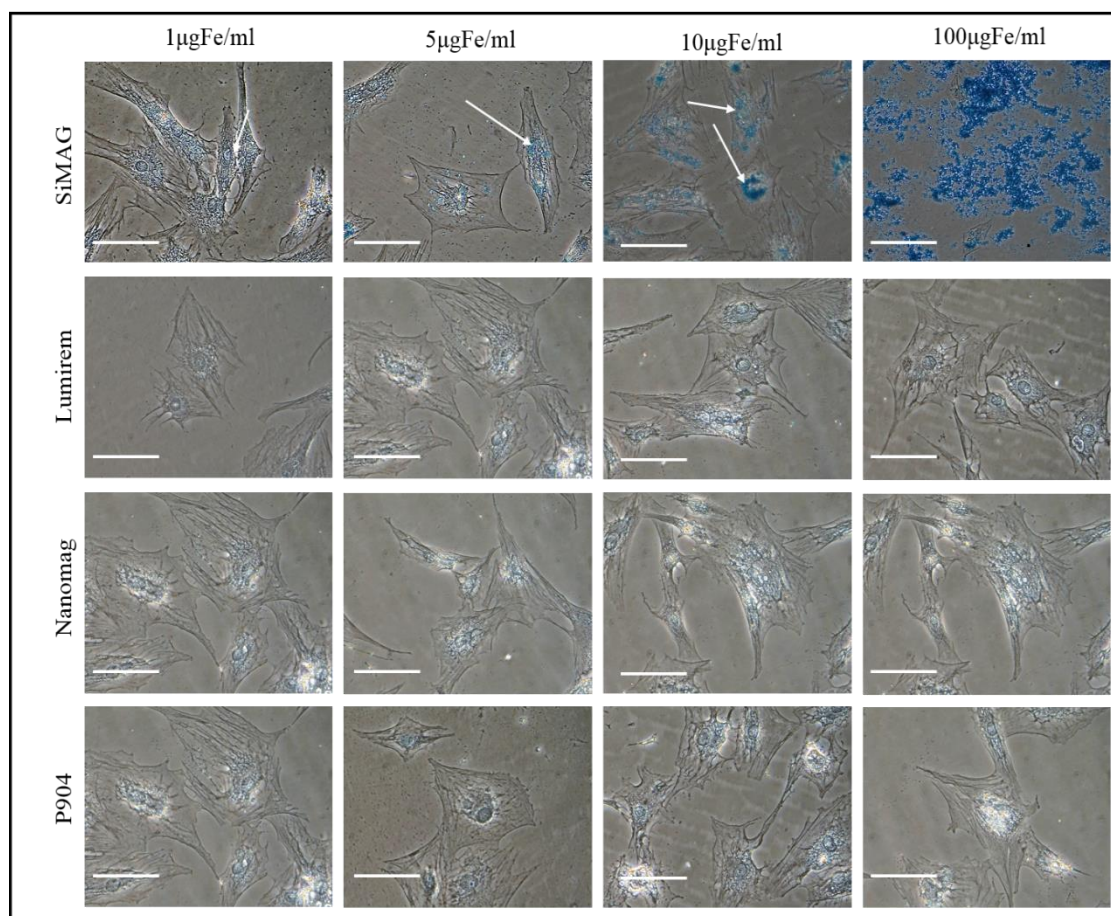
Figure 3.13. Porcine chondrocytes stained with Prussian Blue. Light microscopy images (24 hrs post labelling) of Prussian blue stained SPION-labelled chondrocytes (SiMAG, Lumirem, Nanomag & P904; 1, 5, 10, 100 µgFe/ml). SPION are stained blue shown by the white arrows. Scale bar = 100 µm 24hrs

3.4.3.2 ICP–OES

ICP-OES was used to determine the intracellular Fe content of hMSCs and chondrocytes when labelled with 10 µgFe/ml of SiMAG, Lumirem, Nanomag, and P904 in either serum free (SFM) or serum containing media (SCM). In general, the use of serum free labelling media facilitated improved uptake efficiencies for both hMSCs and chondrocytes when compared to the use of serum containing labelling media for all particles apart from P904 and Lumirem labelled chondrocytes. Furthermore, SiMAG was most efficiently internalised

by both hMSCs and chondrocytes, corroborating Prussian blue results. Similar uptake trends were obtained for hMSCs and chondrocytes when labelled with either SiMAG, Nanomag or P904, this however was not the case for Lumirem. (Figure 3.14 & 3.15 E).

The use of SCM resulted in very similar uptake efficiencies for hMSCs (58 % $\pm$ 3.29) and for chondrocytes (55 % $\pm$ 6.08) (Figure 3.15 A) when labelled with 10 µgFe/ml SiMAG resulting in 16$\pm$0.7 pgFe/hMSC and 14 $\pm$0.9 pgFe/chondrocyte (Figure 3.14 A). The labelling of hMSCs and chondrocytes in SFM resulted in a significant increase in the uptake of SiMAG by both hMSCs (p<0.001) and chondrocytes (p<0.01) when compared to SCM media, equating to 22 $\pm$ 0.41 pgFe/hMSC and 20 $\pm$ 0.46 pgFe/chondrocyte (Figure 3.14 A).

Lumirem labelling (Figure 3.14 and 3.15 B) resulted in significantly greater amount of Fe uptake in hMSCs when compared to chondrocytes in both media types (SFM and SCM). The labelling of hMSCs with Lumirem in SCM resulted in approximately 11 % of the Lumirem being taken up with this equating to 2.4 $\pm$ 0.46 pgFe/hMSC. This is a significant (p<0.001) increase over chondrocytes where only 0.63 % uptake being detected under similar conditions (SCM) equating to 10 times less Fe per cell (0.2 $\pm$ 0.13 pgFe/chondrocyte). Furthermore, there was an insignificant increase in the uptake of Lumirem in SFM over SCM for chondrocytes resulting in 1.39 $\pm$ 0.35 pgFe/chondrocyte. In comparison, there was a statistically significant increase in the uptake of Lumirem in the presence of SFM over SCM for hMSCs resulting in 4.8 $\pm$ 0.5 pgFe/hMSC (p<0.0001) which is also a significant increase over chondrocytes under the same conditions (SFM) (0.45$\pm$0.34 pgFe/chondrocyte p<0.0001).

Nanomag (Figure 3.14 & 3.15 C) did not demonstrate the ability to be significantly taken up for either of the cell types (hMSCs and chondrocytes) with only 0.8 % of the Fe being internalised by hMSCs and 1.19 % for chondrocytes when labelled with SCM translating to

0.2 $\pm$ 0.3 pgFe/hMSC and 0.34 $\pm$ 0.2 pgFe/chondrocyte. The uptake efficiency then significantly increased in SFM to 4 % for hMSCs (p<0.05) and 4.23 % for chondrocytes (p<0.001) which was equivalent to 1 $\pm$ 0.3 pgFe/hMSC and 1.3 $\pm$ 0.35 pgFe/chondrocyte. Over 95 % of the Fe associated with Nanomag was detected in the media (SFM and SCM). No significant differences were observed between cell types while the presence of SFM resulted in a significant increase in particle uptake over SCM for both cell types.

Overall, the labelling of chondrocytes with P904 resulted in significantly greater levels of Fe per cell than for hMSCs in both types of labelling media (Figure 3.14 & 3.15 E). Furthermore, choice of labelling media did not appear to influence uptake. Under SCM 2.3$\pm$0.34 pgFe/chondrocyte were detected. This was just over double the amount found in hMSCs under the same conditions (1.3 $\pm$ 0.35 pgFe/hMSC; p<0.0001). Significantly greater Fe levels were also detected under SFM for chondrocytes (1.7 $\pm$ 0.07 pgFe/cell) than hMSCs (0.65 $\pm$ 0.16 pgFe/cell; p<0.0001).
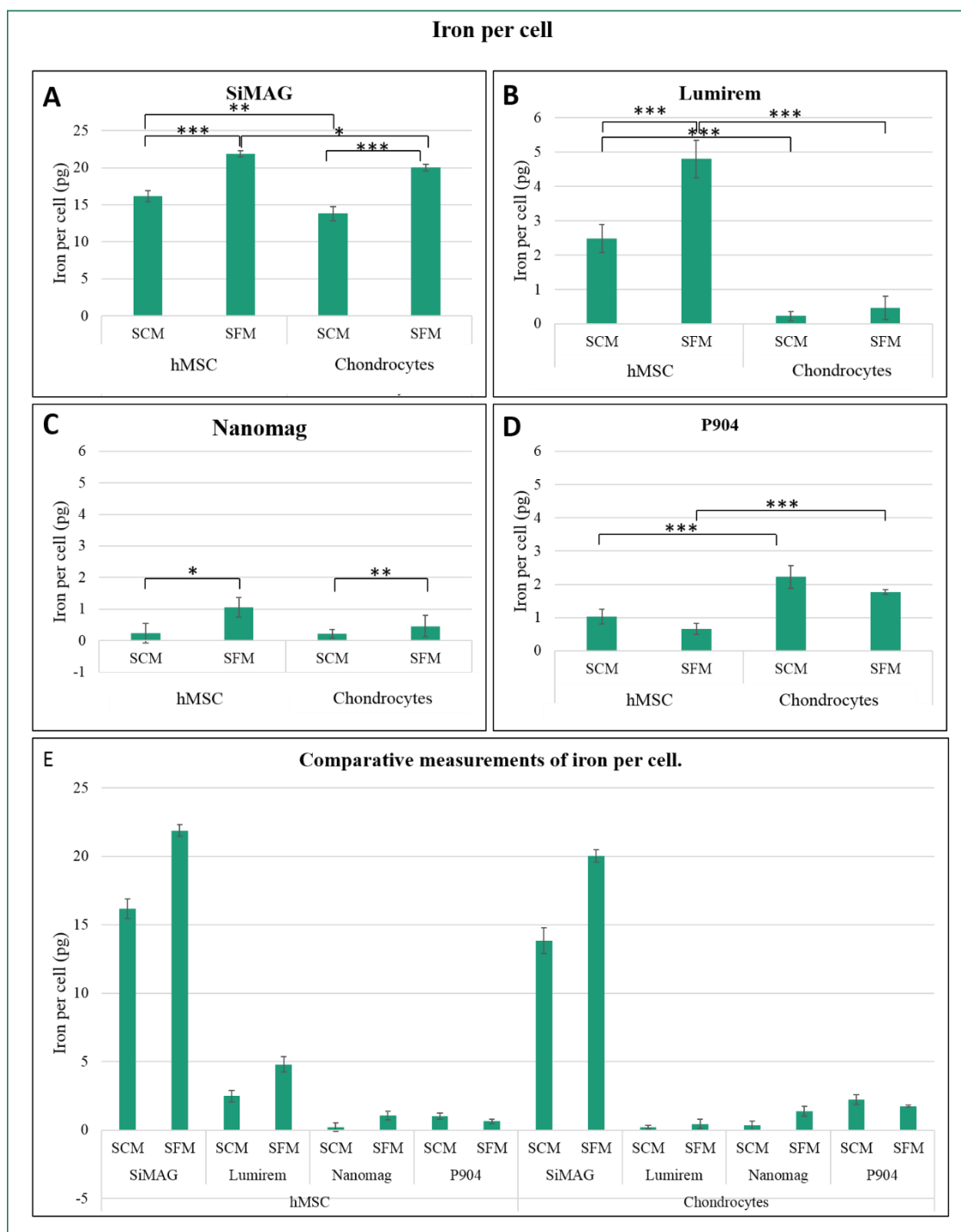
Figure 3.14. ICP-OES quantification and comparison of total Fe content per cell (hMSCs and chondrocytes) post particle labelling in either serum free media (SFM) or serum containing media (SCM) for: (A) SiMAG, (B) Lumirem, (C) Nanomag and (D) P904 labelled with 10µgFe/ml. (E) Shows a comparative graph comparing the total iron content for each particle per cell type and media condition. Data = mean Fe $\pm$ SD, n=3.
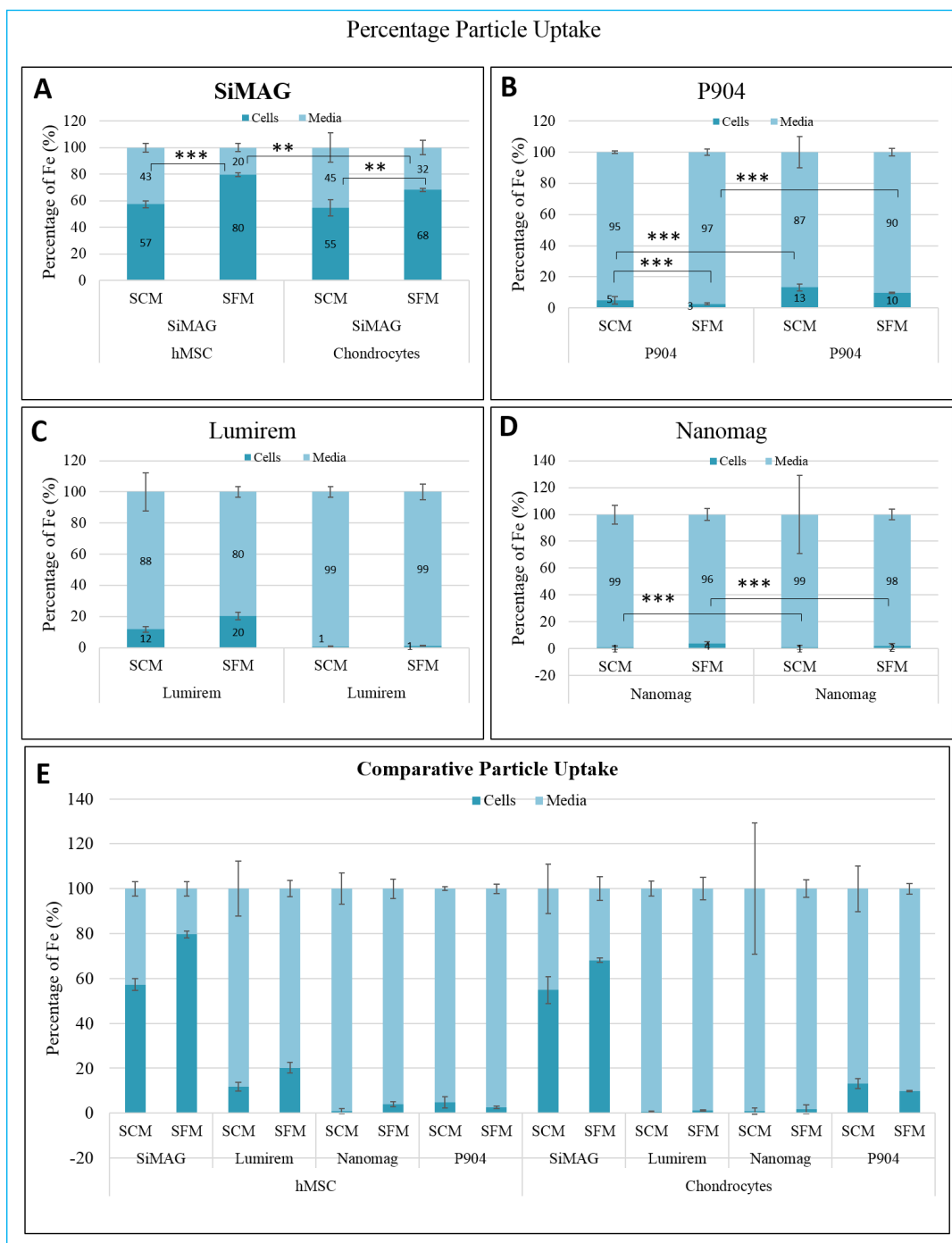
Figure 3.15. Percentage Fe uptake and comparison of Fe in media and cells (hMSCs and chondrocytes) post particle labelling in either serum free media (SFM) or serum containing media (SCM) for: (A) SiMAG, (B) Lumirem, (C) Nanomag and (D) P904. E) Shows a comparative graph comparing the total iron content for each particle per cell type and media condition. Data = mean $\pm$ SD (n=3).

3.4.4.3 Particle uptake efficiency

Prussian blue staining and ICP-OES analysis confirmed the efficient internalisation of SiMAG by both hMSCs and chondrocytes. The labelling efficiency was then investigated at varying SiMAG concentrations (1, 5 and 10 μgFe/ml) in SFM. Prussian blue staining revealed approximately 95% of cells to have internalised SiMAG when labelled with 5 (hMSC; 94±2% & chondrocytes 94±5%) and 10 μgFe/ml (hMSC; 95±3% & chondrocytes 95±2%) while fewer cells appeared to be labelled with 1 μgFe/ml (hMSC; 10±1.5% & chondrocytes 14±4%) SiMAG (Figure 3.16). As expected, the amount of Fe per cell significantly increased ($p<0.0001$) with increasing SiMAG concentration between each condition for both cell types hMSCs; (1 μgFe/ml; 0.22 ± 0.09 pgFe/cell, 5 μgFe/ml; 14.29 ± 0.59 pgFe/cell and 10 μgFe/ml; 21.88 ± 0.4 pgFe/cell) and chondrocytes; (1 μgFe/ml; 0.33 ± 0.36 pgFe/cell, 5 μgFe/ml; 13 ± 0.54 pgFe/cell and 10 μgFe/ml; 20 ± 0.3 pg Fe/cell) (Figure 3.17).
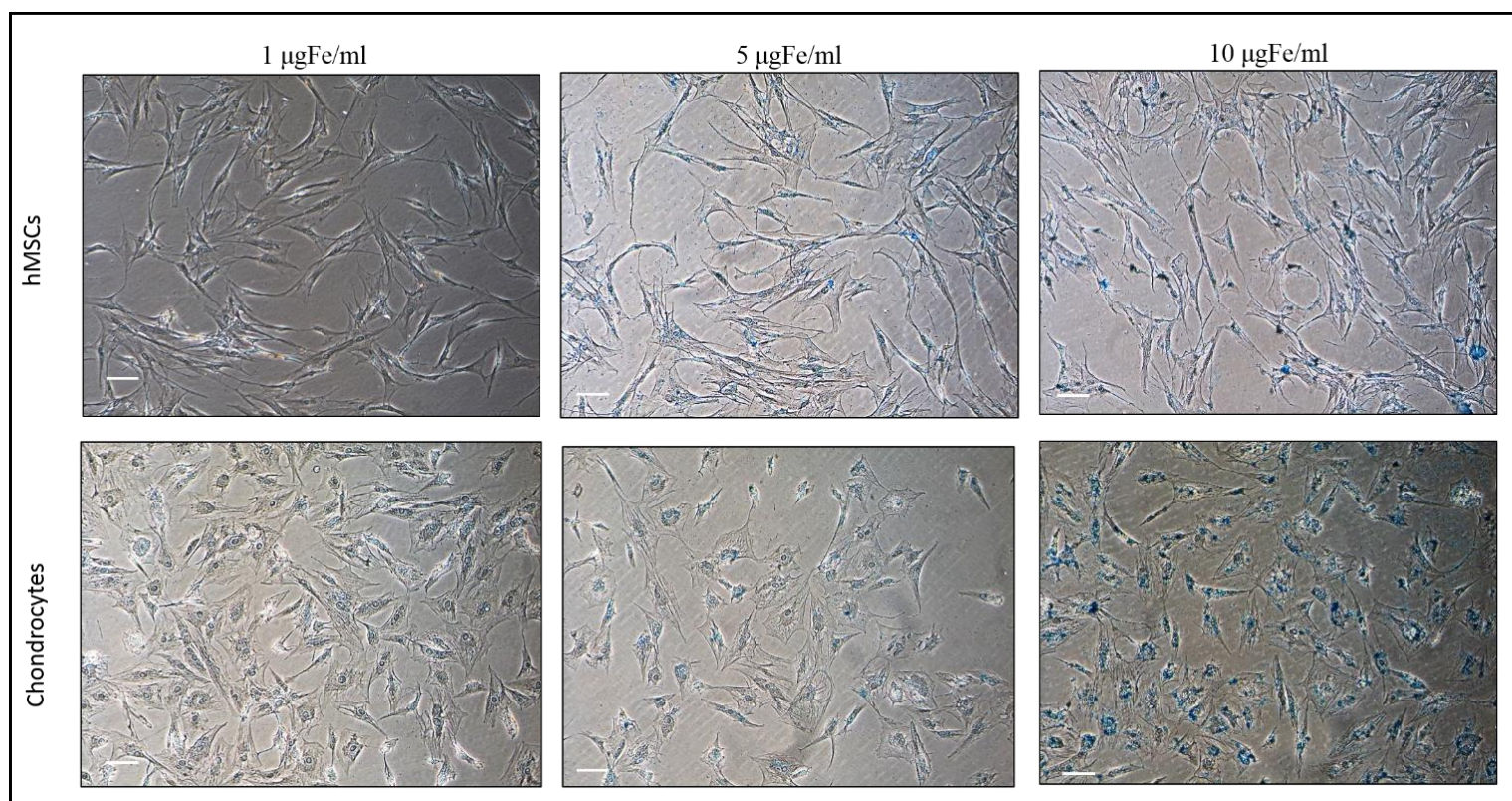
Figure 3.16. Prussian blue staining to investigate particle uptake efficiency 24 hrs post labelling. Light microscopy images of Prussian blue stained SiMAG-labelled hMSCs (1, 5, & 10 µgFe/ml). SPION are stained blue. Scale bar = 100 µm
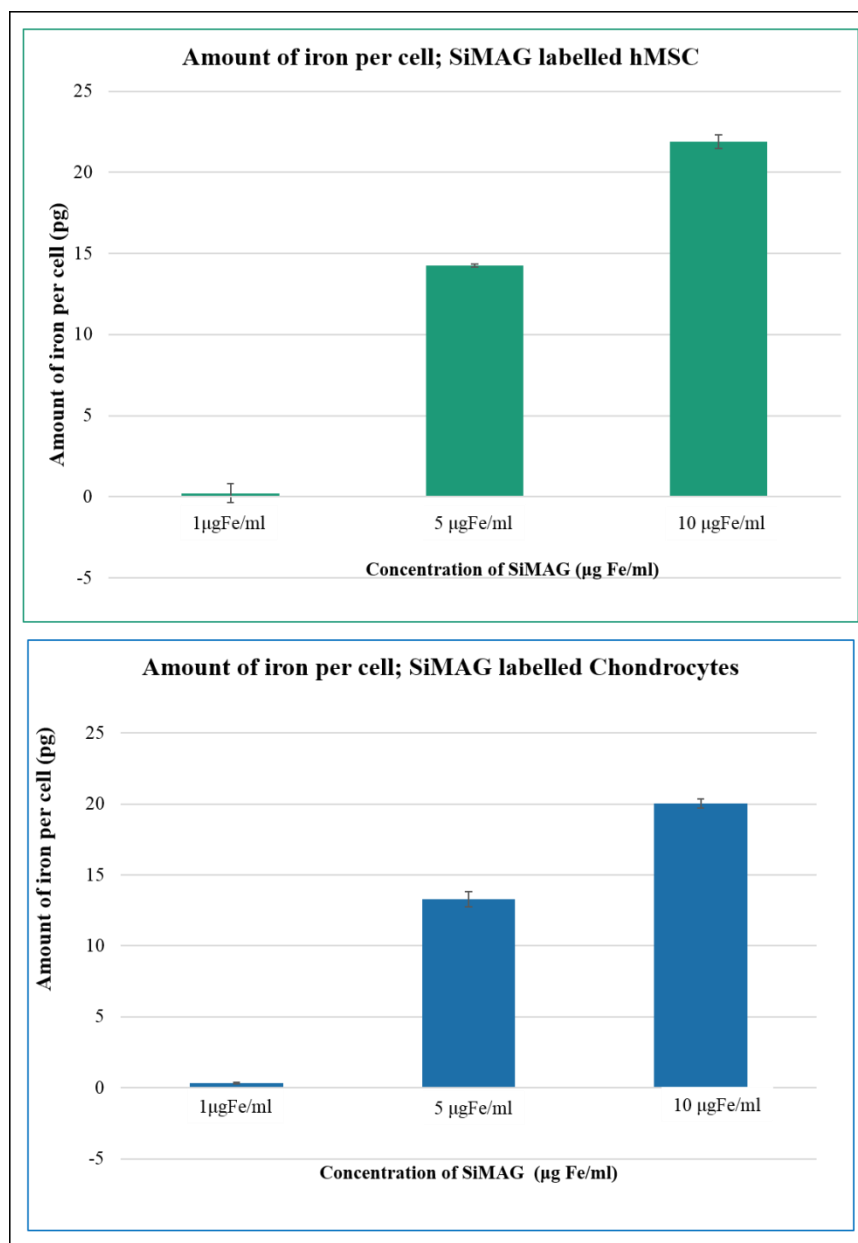
Figure 3.17. ICP-OES quantification of internalised Fe as a result of increasing SiMAG concentration (1, 5, & 10 μgFe/ml) (n=3). Data = mean *Fe* ±SD. Statistical significance levels represented by *** where is p<0.001 unless otherwise stated

3.4.4 Cell Viability and Proliferation Assessment

The effect of particle labelling (SiMAG, Lumirem, Nanomag and P904) on the viability and proliferative capacity of hMSCs and chondrocytes was investigated at 24 hrs and 7 days when labelled with 10 and 100 μgFe/ml of each particle. This investigated the effect of

particle dose and exposure time on the viability of cells. An MTT assay and a double staining live dead assay were implemented in this study.

3.4.4.1 MTT Assay

This a measure of mitochondrial activity and is a standard means of assessing cell viability and proliferation (109). Normalised MTT data allows for comparisons between the two cell types to be made. MTT analysis revealed no diminished viability for either cell type (hMSCs and chondrocytes) when labelled with 10 μgFe/ml of the relevant particle (SiMAG, Lumirem, Nanomag and P904) after a 24 hr incubation period when compared to untreated cells (Figure 3.18 A & B). A marked increase in optical density (OD) was observed between all groups incubated with 10 μgFe/ml of each particle (apart from chondrocytes labelled with 10 μgFe/ml SiMAG) from 24 hours with those tested at 7 days. When compared to untreated cells, no impaired viability could be detected in hMSCs incubated with 10 μgFe/ml of either particle type after 7 days exposure. This represents the proliferative abilities of labelled cells with results indicating that labelled hMSCs populations retain their ability to proliferate. Conversely, there is a significant reduction in OD for chondrocytes labelled with 10 μgFe/ml SiMAG after 7 days exposure. This signifies a reduction in metabolic activity (Figure 3.18 B).

As demonstrated in Figure 3.18 the effect of a higher particle dose (100 μgFe/ml) did not appear to affect viability and proliferation of hMSCs (Figure 3.18 A) and chondrocytes (Figure 3.18 B) labelled with Lumirem, Nanomag and P904 at either time point (24 hrs and 7 days) when compared to untreated groups. However, for hMSCs and chondrocytes labelled with 100 μgFe/ml SiMAG a significantly low OD is measured similar to the negative control

(dead cells) and is thus indicative of cell death or reduced metabolic activity at both time points.
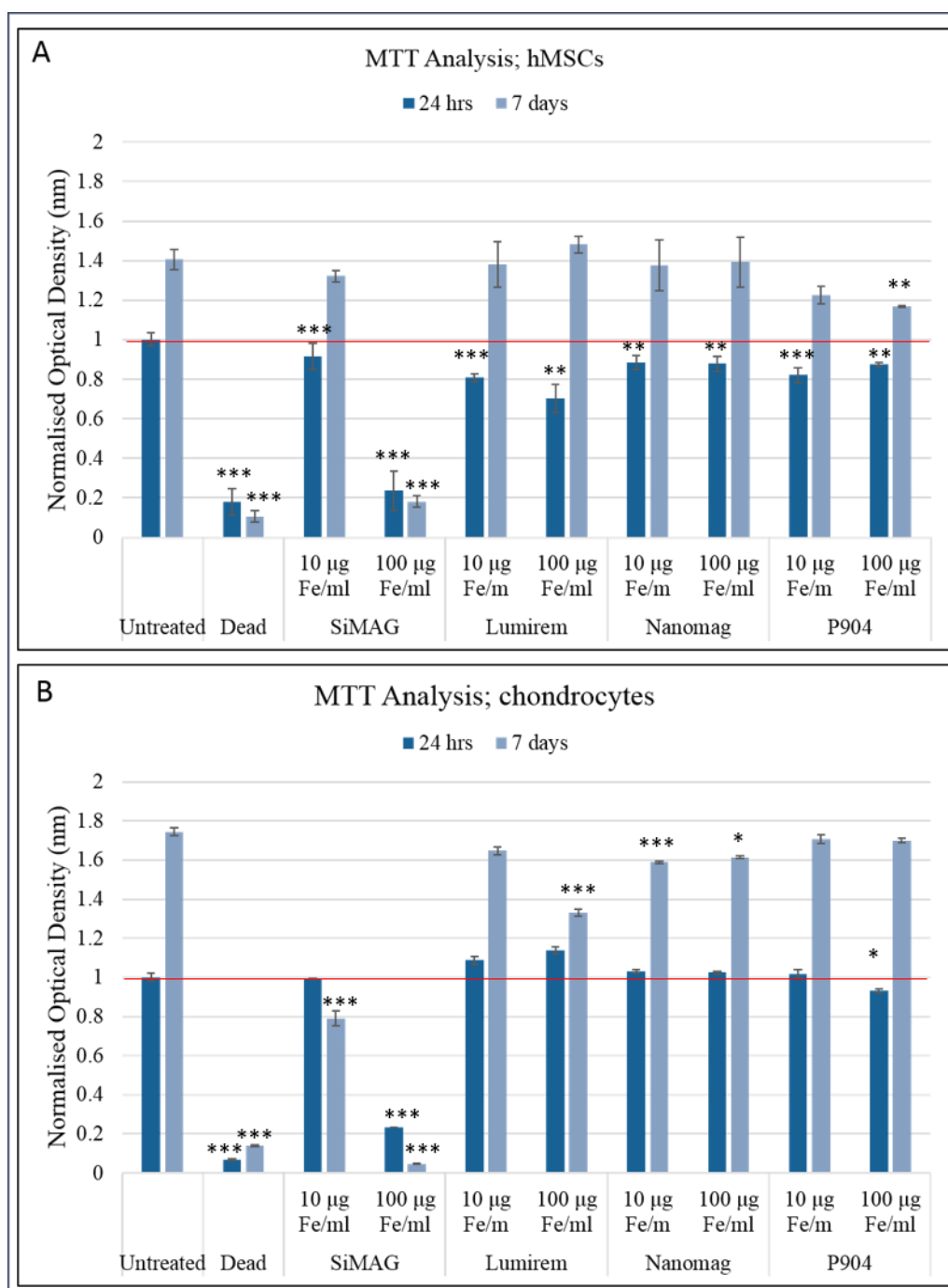
Figure 3.18. Normalised MTT analysis (A) hMSCs and (B) chondrocytes labelled with 10 and 100 µgFe/ml and left to culture for 24 hrs and 7 days. Data = mean OD $\pm$ SD, n=3; Statistical significance levels represented by * where p < 0.05, ** is p < 0.01 and * is p<0.001**

3.4.4.2 Live Dead Assay

This is a simple and visual means of assessing cell viability and is based on a double staining protocol where live cells, showing intact cell membranes are stained fluorescent green while cells with impaired viability and compromised cell membranes are stained fluorescent red.

A greater number of viable cells (hMSCs and chondrocytes), appearing in green were observed in all groups (SiMAG, Lumirem, Nanomag and P904) treated with 10 µgFe/ml in comparison to dead cells (red) and displaying similar patterns to the untreated controls (Figure 3.19 - 3.21). Furthermore, it was also revealed that there was an increase in the overall number of cells (hMSCs and chondrocytes) in these groups after 7 days in culture similar to the untreated controls (Figure 3.19-3.21). This demonstrates the proliferative abilities of these groups apart from SiMAG-labelled chondrocytes where the proliferation activity is clearly demonstrated to be limited as can be seen by the insignificant increase in the number of green cells.

A higher dose (100 µgFe/ml) did not seem to affect the viability and proliferation of hMSCs and chondrocytes labelled with Lumirem, Nanomag and P904 at either time point (24 hrs and 7 days) when compared to untreated groups, as shown in Figure 3.19 and 3.20. However, only a few stained cells (hMSCs and chondrocytes) were visible when exposed to 100 µg Fe/ml SiMAG over 24 hrs and 7 days. This is likely due to the excessive amount of particles (as depicted by Prussian blue staining (Figure 3.12 & 3.13) preventing the dyes from penetrating the majority of the cells.
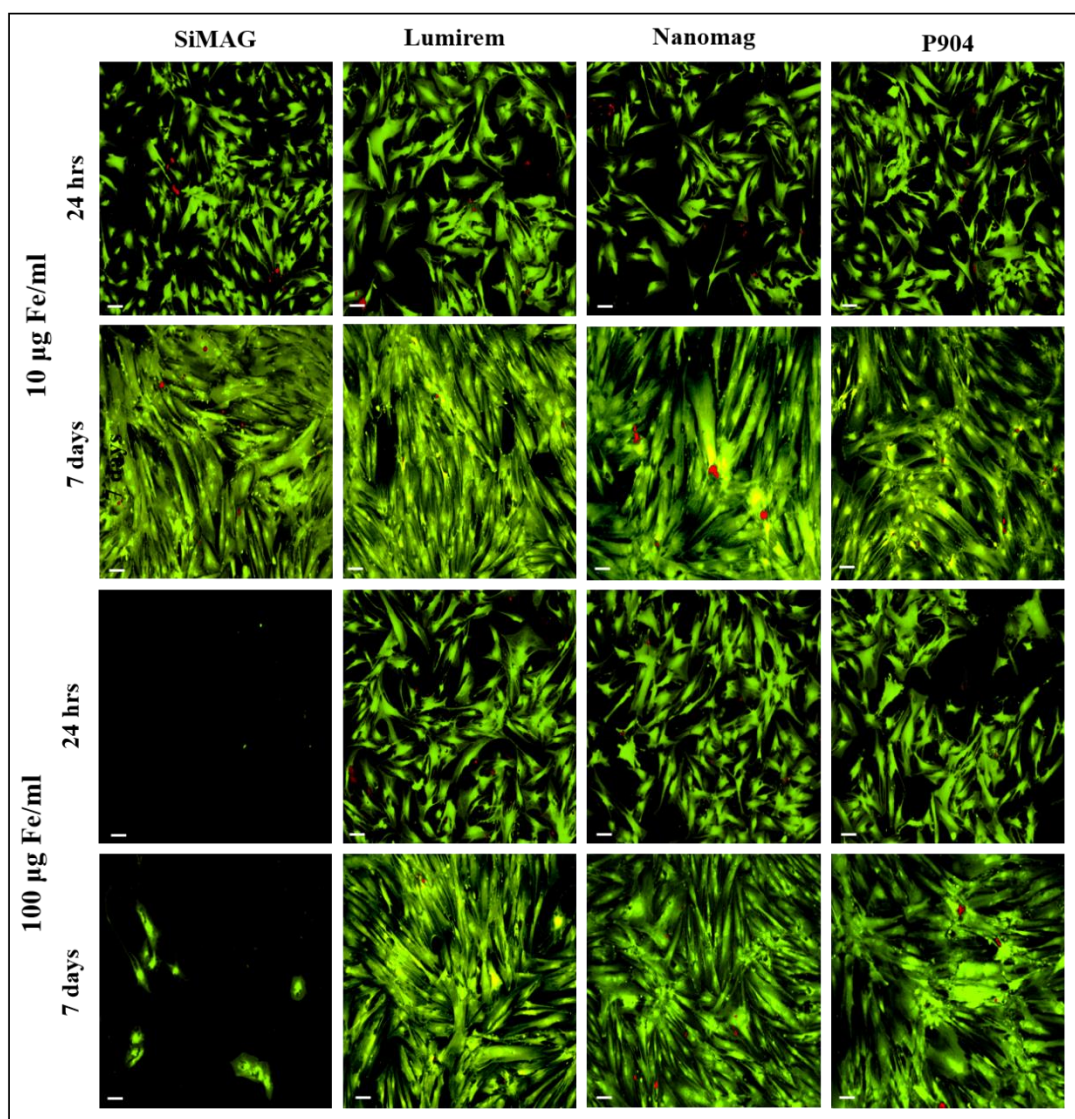
Figure 3.19. Live Dead staining of hMSCs labelled with 10 µgFe/ml and 100 µgFe/ml SiMAG, Lumirem, Nanimag and P904 cultured for 24 hrs and 7 days. Green stained cells represent live, viable cells whereas red stained cells represent dead, non-viable cells. Scale bar = 100 µm.
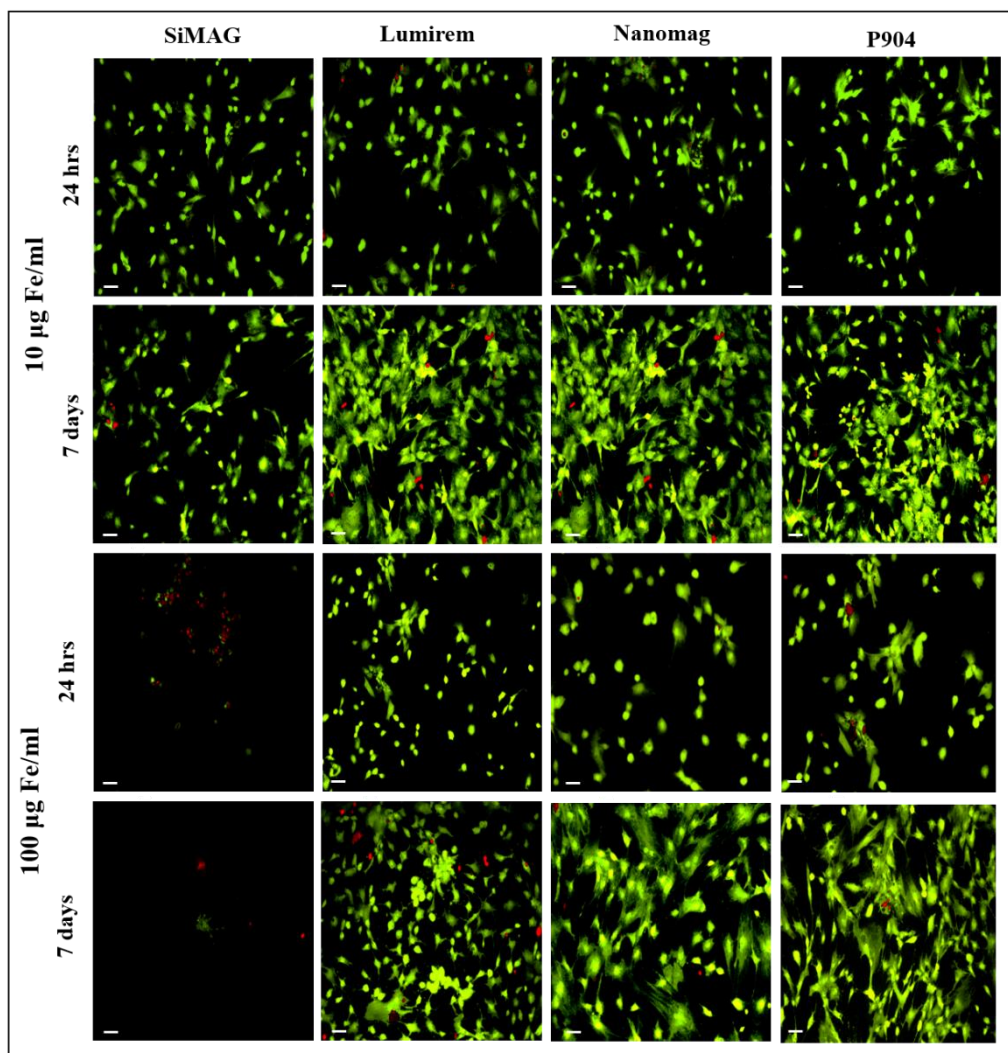
Figure 3.20. Live Dead staining of chondrocytes labelled with 10 μgFe/ml and 100 μgFe/ml SiMAG, Lumirem, Nanimag and P904 cultured for 24 hrs and 7 days. Green stained cells represent live, viable cells whereas red stained cells highlight dead, non-viable cells. Scale bar = 100 μm.
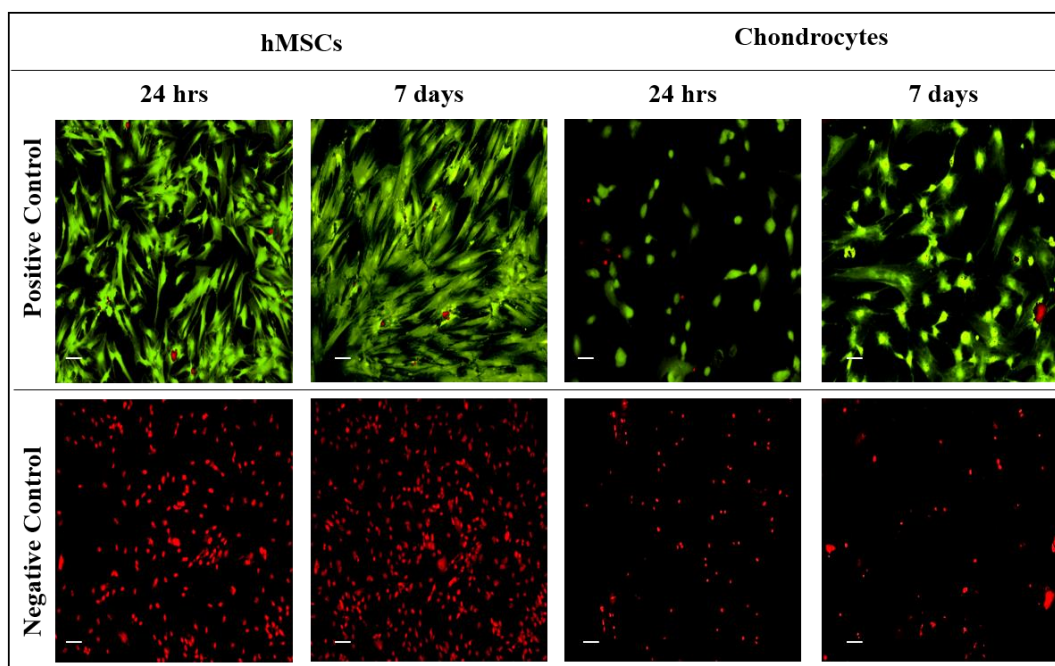
Figure 3.21. Live Dead stain controls. Untreated positive control and DMSO treated negative control hMSCs and chondrocytes after 24 hrs and 7 days in culture. Scale bar= 100 μm.

3.4.5 Cell Characterisation Post SiMAG labelling.

The relatively high doses of Fe found in SiMAG-labelled cells (hMSCs and chondrocytes) encouraged further investigation into the influence of SiMAG labelling on cell function and characteristics. Therefore cells were characterised to ensure cell populations remained robust in culture after particle uptake and that biological properties remained intact (75).

3.4.5.1 hMSCs

3.4.5.1.1 Cell Surface Marker Expression

Flow cytometry was implemented to investigate the effect of SiMAG labelling (10 μgFe/ml) on the expression of standard cell surface markers typical to hMSCs. It demonstrates the positive expression of typical mesenchymal markers: CD 73, CD 90 and CD 105 while

proving negative for the expression of CD 14, CD 19, CD 31, CD 34, CD 45 and HLA-DR as expected (Figure 3.22). Positive expression (%) of each of these cell markers are stated in Table 3.7. These values appear similar to values seen in section 3.4.1.1.2 for unlabelled hMSCs and can thus be deduced that SiMAG labelling does not influence marker expression.

Table 3 5. Positive expression of typical mesenchymal cell surface markers in hMSCs treated with SiMAG (10 µgFe/ml).

Cell Surface Marker	%Positive
CD14	22.22
CD19	5.91
CD31	6.97
CD34	4.53
CD45	5.72
CD73	77.1
CD90	80.93
CD105	73.54
HLA-DR	5.40
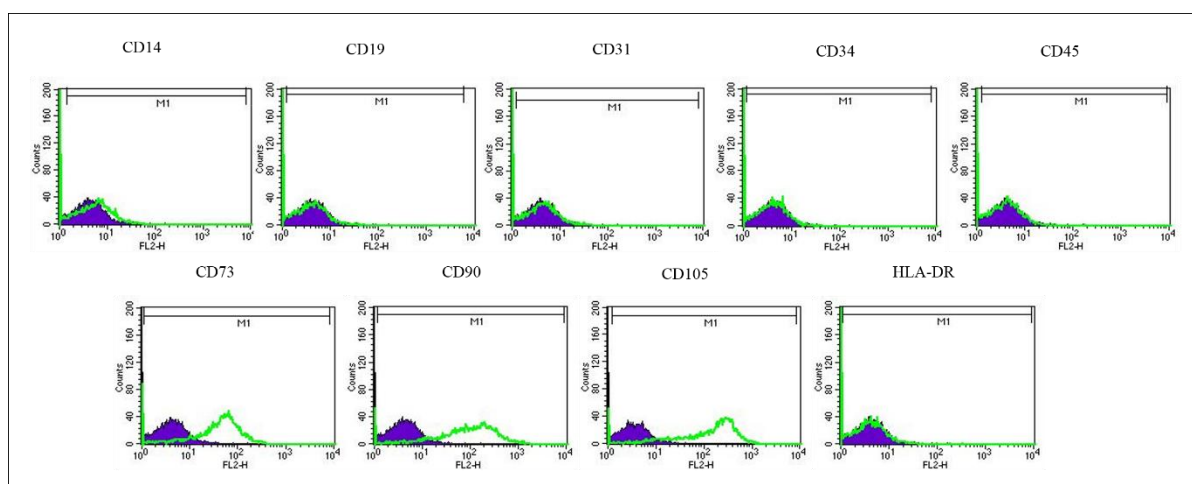
Figure 3.22. Characterisation of hMSC surface markers using FACS. hMSCs labelled with SiMAG at 10 µgFe/ml for 24 hrs in serum-free conditions.

3.4.5.1.2 Multi-lineage Differentiation

SiMAG-labelled hMSCs (10 µgFe/ml) were tested for their differentiation capacity into adipocytes, chondrocytes and osteocytes. Labelled cells were incubated for a period of 21 days in the relevant differentiation medias. Similar to unlabelled hMSCs (Figure 3.6) SiMAG-labelled hMSCs underwent successful differentiation towards all three lineages (adipogenic, chondrogenic and osteogenic) after 21 days in culture. Adipogenesis was confirmed by the presence of lipid and triglyceride droplets stained positive with oil red O after 21 days in samples treated with adipogenic differentiation media (Figure 3.23 A). Calcium deposition was stained positive by alizarin red for samples cultured in osteogenic differentiation media confirming osteogenesis (Figure 3.23 B). Alcian Blue stain was used to identify the secretion of GAGs by cells which had undergone chondrogenic differentiation (Figure 3.23 C). No staining was observed in control groups cultured under basic proliferation media for all cases (Adipogenesis, Chondrogensis and Osteogenesis) and to the day 0 control.
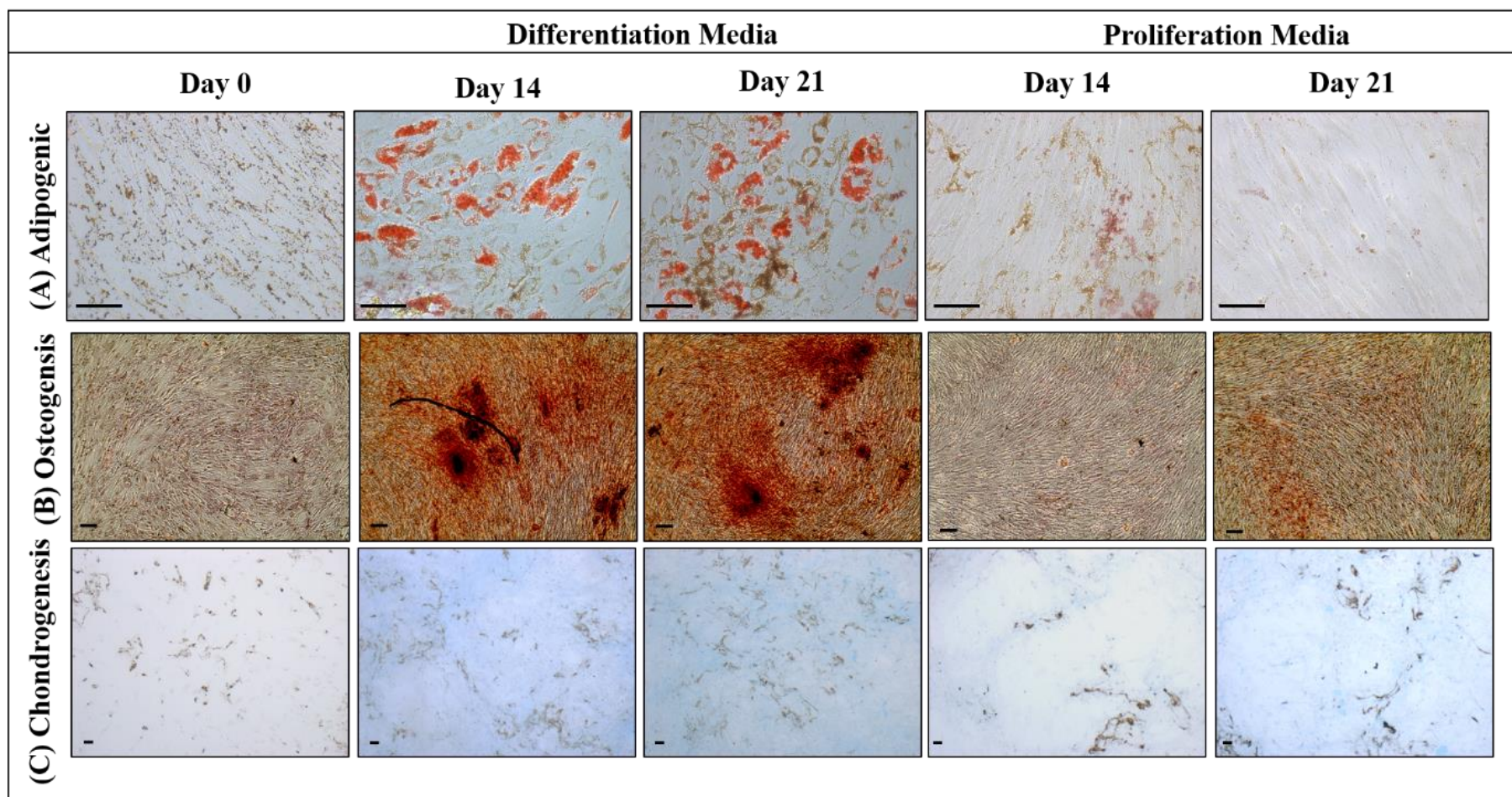
Figure 3.23. Multi-lineage differentiation of SiMAG-labelled hMSCs. Multi-lineage differentiation of hMSCs. Images represent differentiation of hMSCs towards (A) Adipogeneic, (B) Osteogenic and (C) Chondrogenic lineages with time at days 14 and 21 days. Scale Bar = 100 μm.

3.4.5.2 Chondrocytes

SiMAG-labelled chondrocytes (10 µgFe/ml) maintained the ability to secrete sulphated GAGs when cultured under standard proliferation media for 21 days. In comparison to day 0, increased levels of secreted GAGs can be noticed (Figure 3.24)
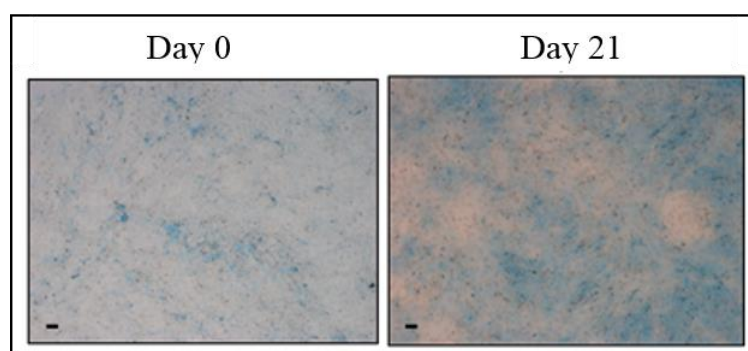
Figure 3.24. Alician Blue staining of SiMAG-labelled chondrocytes at day 0 and day 21. Secreted GAGs are shown by blue staining. Scale Bar = 100 µm.

3.4.6 Particle retention

hMSCs and chondrocytes were labelled with 10 µgFe/ml SiMAG and the retention of SiMAG within the cells was monitored over 28 days. Analysis was performed quantitatively using ICP-OES and visually using Prussian blue staining on days 1, 7, 14, 21 and 28.

The amount of Fe associated with SiMAG-labelled hMSCs and chondrocytes over 28 days was quantified by ICP-OES. Fe content remained largely stable from day 1 until day 21 for both hMSCs and chondrocytes at approximately 20 pgFe/ cell up until day 21. This value was seen to significantly decrease to 12 ± 2.8 pgFe/hMSC at day 28 in comparison to days 1 ($p < 0.008$), days 7 ($p < 0.008$), day 14 ($p < 0.0116$) and day 21 ($p < 0.0018$) (Figure 3.25 A). Similarly, the value for SiMAG-labelled chondrocyte was also seen to significantly decrease to 6 ± 4.6 pgFe/chondrocytes at day 28 in comparison to day 1 ($p < 0.0129$), days 7 ($p < 0.0037$), day 14 ($p < 0.0032$) and day 21 ($p < 0.005$) (Figure 3.25 B).

Prussian blue staining confirmed the retention of internalised SiMAG by chondrocytes (Figure 3.26) for the duration of the study. However, hMSC in comparison a network of particles appeared to have developed and it is unclear whether this network was interacting with the network of cells (Figure 3.26).
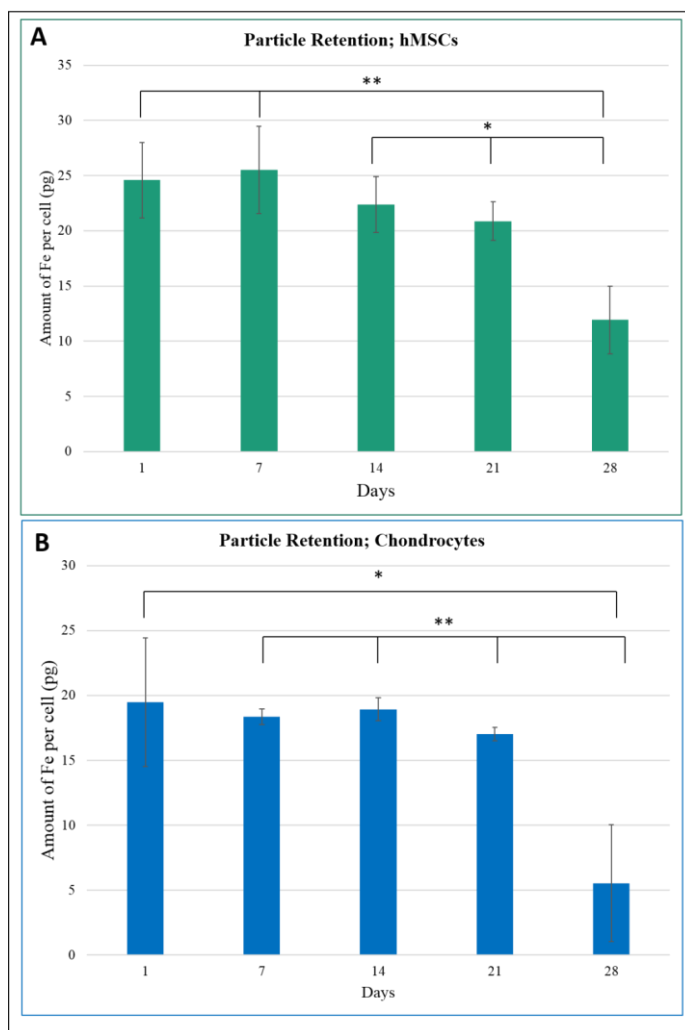
Figure 3.25. ICP-OES quantification of Fe content: (A) hMSC and (B) chondrocytes labelled with 10 µgFe/ml SiMAG and cultured for 1, 7, 14, 21 and 28 days post labelling. Data point = mean ±SD (n=3); where*p < 0.05, **p < 0.01, ***p < 0.001.
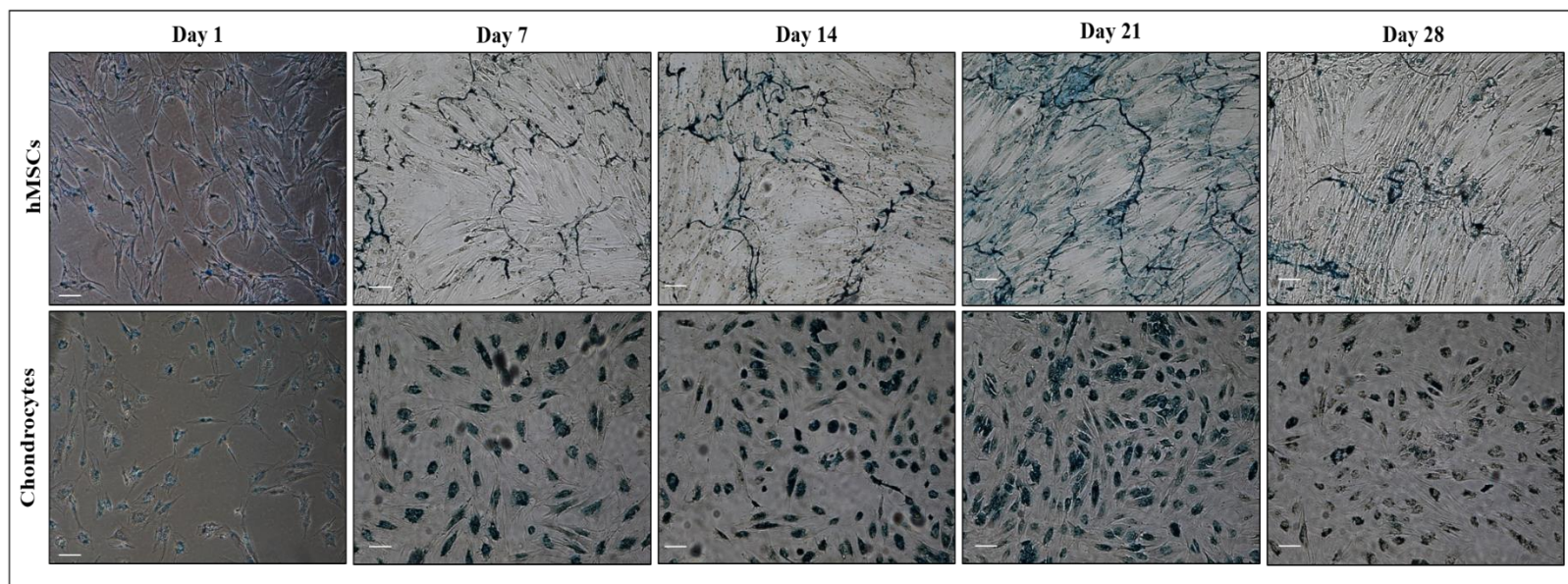
Figure 3.26. Prussian blue staining of SiMAG-labelled hMSCs and chondrocytes for 1, 7, 14, 21 and 28 days post labelling.

3.5 Discussion

Studies by Clift *et al* and Mairano *et al* have shown that the exposure of SPIONs to a solution containing serum can significantly impact the rate and efficiencies of particle uptake. The presence of various proteins in FBS may account for this effect by either causing the aggregation of particle or the development of the protein corona (190-192). This theory was validated here, where ICP-OES analysis revealed enhanced uptake efficiencies for both hMSCs and chondrocytes when labelled with SIMAG, Lumirem and Nanomag in the presence of serum free media (SFM) over serum containing media (SCM). The dynamic light scattering data (measuring hydrodynamic diameter) did not account for any significant SPIONs aggregation with regards to SiMAG, Nanomag and P904 when incubated in either SFM or SCM. Although variations in the HD of Nanomag were observed between SFM and SCM this is not believed to be a result aggregation but rather an effect of the dextran coating and is expected. The measurements of Lumirem (± 1200 nm) however resulted in HD values far greater than the reported manufacturer's value (300 nm). This is potentially due to the overall application of Lumirem as an oral contrast agent requiring the addition of various additives and preservative (and even orange flavouring) to enable its use. Lumirem is therefore not a pure SPION solution but has extra additions prohibiting accurate measurement of the actual particle size. Unfortunately, statistical comparison of the measured HD of each particle could not be made with the manufacturer's value due to the lack of reported errors. However the measured values are similar to the manufacturers reported value and thus assuming a realistic error for all SPIONs, these values can be considered acceptable.

It is unlikely that the lower uptake levels in SCM media are a result of particle aggregating. The theory of the development of the protein corona may better account for these results. This theory takes the interaction of the protein in the media as well as the surface of the SPION. It is thought that proteins interact with the particle to form a complex layer of molecules over the SPION. This biological layer is termed as "corona" (190, 193). The physical and chemical properties of SPION (size, surface coating and functionalization) dictates the binding of molecules to the particles resulting in either a hard or weak corona which is significantly different to that of the surface of the particle (190, 193). This affects the initial interaction of the cell with the particle as the cell`s first point of contact is with the corona and not the surface of the particle (193). In turn, this dictates subsequent cellular and tissue responses, thus the presence of the protein corona may impede particle uptake in serum containing conditions (190).

The greatest amount of Fe was detected in cells (hMSCs and chondrocytes) labelled with SiMAG, where approximately 20 pgFe/cell was detected in serum free conditions. Less Fe was detected in cells labelled with Lumirem and in particular Nanomag and P904 under the same conditions. Detected levels, are however comparable to other studies where internal Fe content ranged from 1-30 pg of Fe/cell in comparison to a value of 0.1 pg of Fe/cell for unlabelled cells (146, 152). However, it cannot be assumed that the increased Fe content detected in SiMAG-labelled cells is a result of enhanced uptake efficiency when compared to the other three particles but rather as a result of its size. In general, larger SPIONs have a greater Fe content per particle than smaller SPIONs, therefore, fewer larger SPIONs need to be internalised to result in significant Fe measurements (194, 195). To compare SiMAG and Nanomag for example; SiMAG is 20 times larger than Nanomag, assuming each SiMAG particle has 20 times more Fe than a single Nanomag particle; then cells would need to internalise 20 times more Nanomag particles to achieve similar values to SiMAG. Therefore,

without counting individual particle within each cell, conclusions of the comparative uptake efficiency between the four particles cannot be made. This observation has significant implications for non-phagocytic cells being labelled without the use of TA with intended MRI applications implying that the application of micron-sized SPIONs may be beneficial for non-phagocytic cells such as stem cells, as each cell would need to internalise fewer particles than it would if smaller SPIONs were applied to create contrast. This also implies that smaller particles may be required at higher concentrations to facilitate sufficient uptake (194). No conclusive comments could be made about the uptake efficiency between SPIONs of varying sizes in this study.

The significantly higher levels of Fe (measured by ICP and visually confirmed using Prussian blue staining) for Lumirem between hMSCs and chondrocytes can be explained by the concept of "cell vision" presented by Laurent *et al*, (196). This refers to the contact point between a particle and the cell membrane, which is characterised by surface molecules i.e. proteins, sugars and phospholipid composition. The binding of particles to these structures may be different for different cell types and explains how individual cell types ''see'' the particle. As a result, the binding of exogenous objects like SPIONs to these structures may cause different responses and influence uptake and metabolism depending on the cell type (196, 197). The fact that these results are only seen for Lumirem and not for other particles may be accounted for by the variations in polymer coatings between the other SPIONs. Alternatively, residual Lumirem solution may have not been washed off properly, as Lumirem is a viscous solution which has proved to be difficult to handle.

A particular limitation associated with ICP-OES is the inability to distinguish between intracellular and extracellular Fe. Multiple wash steps were performed to try and mitigate this issue by removing all extracellular SPIONs. Histological Prussian blue staining is a more conclusive method of establishing SPION and cell association. Although, there are increased

levels of difficulty in seeing smaller particles which may account for the lack of visual evidence for Nanomag and P904.

Ideally, to strategically determine the effect of any one physiochemical parameter (hydrodynamic diameter, polymer coating, surface charge and functionalisation) on internalisation of particles, all parameter will need to be maintained while varying the parameter in question. This is no easy task as physiochemical properties of SPIONs are strongly interconnected thus altering one parameter may subsequently have effects on other parameters (198).

A vast number of studies have reported stem cells tagged with SPIONs to have little or no effect on the proliferation and viability of cells (91, 146, 152, 199). It is still necessary however to address the issue of toxicity in a case by case fashion. Laurent *et al* demonstrated the same concentration of SPIONs caused significant toxicity on neuronal and glial cells whilst displaying little toxicity on other cell types like heart and kidney cells (196, 197). In general, a combination of factors can influence SPION toxicity. These factors include; particle core material, SPION size, polymer coating and also the immediate *in vitro* (culture media) environment (91, 198). Toxicity may arise from the leaching of ions from metal core and the biodegradation polymer coating; processes that are heavily reliant on the physical environment of the particles (198). At the cellular level, oxidative stress is thought to be the main cause of toxicity by SPIONs (156). Oxidative stress arises when there is an imbalance between damaging oxidants also referred to as reactive oxygen species (ROS) such as; hydrogen peroxide, hydroxyl radicals and the protective anti-oxidants of which vitamin C and glutathione are examples. ROS are primarily formed by the incomplete reduction of oxygen (200). The accumulation of oxidants eventually leads to the destruction of cellular proteins, enzymes, lipids and nucleic acids and as a consequence the normal cellular processes become impaired (121, 129, 156, 200). ROS can be generated from the surface of

SPIONs, the leaching of metal ions from the core or release of oxidants by enzymatic degradation of the SPIONs (109). It has been reported that dissociated iron oxide can promote the formation of ROS and hydroxyl radicals and as a result may lead to cellular toxicity along with impaired cell metabolism and increases in apoptosis (123).

Even though Fe is a naturally occurring element in the human body with the body adapted to metabolise Fe (88, 98, 105, 120, 136, 147), the potential risk of toxicity associated with iron based particles is low but does still need to be assessed. It is important to further remember that in high quantities, Fe can possibly impair cell viability by damaging cell membranes, proteins and DNA, impeding normal cell function (91, 105, 147). Therefore, it is important to obtain a balance between Fe incorporation (concentration) for the required role and cell function (105). Particle concentration ranging from 2.8- 400 µg/ml have been reportedly used in *in vivo* tracking (83, 104-107). The particle concentration chosen for this study were purposely chosen to primarily lie within the lower range of this range. However, the problem lies with studies not generally offering enough information of their labelling protocols and generally being vague in terms of concentration specifics. For example, it is unclear as to what 50 µg/ml of a certain particle refers too; e.g the level of Fe or cell/SPION ratio. There is a significant difference between the addition of 50 µg/ml to 10^5 cells and to 10^6 cells. Therefore, although a concentration of 400 µg/ml seems high, it really does depend on the number of cells that are being labelled to properly put this into perspective. For this reason the labelling protocol in this study clearly stipulated all of these parameters. In this study, SPION concentration (in terms of Fe) ranging from 1-100 µgFe/ml has been investigated. The exposure of hMSCs and chondrocytes to 10 µgFe/ml to either of the particles (SIMAG Lumirem, Nanomag and P904 had no significant implication on the viability of these cell. A slight reduction in metabolic activity however is observed for hMSCs labelled with either of the 4 particles (SiMAG, Lumirem, Nanomag and P904)

during the first 24 hrs of labelling. This is most likely attributed to resources being directed to physically endocytosing SPIONs therefore resulting in reduced cell metabolism. 7 days post labelling metabolic activity restored to levels observed by untreated cells. The exposure of hMSCs and chondrocytes to 100 μgFe/ml SIMAG appeared to significantly impact the cell viability of both cells. This was not the case for Lumirem, Nanomag and P904. The SiMAG result may not be true, however; based on the Prussian blue staining highlighting the obvious excess of particle and the inability of the live dead stain to reach the cells, it may be possible that the MTT reagent was not able to come into contact with the cell. In any case, further investigation of this needs to be explored. Impaired proliferation capacity was only identified for SiMAG-labelled chondrocytes labelled with 10 μgFe/ml SiMAG. This may be attributed to the development of ROS which have shown to impair biological activities.

The ability to potentially track cells over time in *in vivo* is unfortunately limited by the dilution of SPIONs with the proliferation of the cell and exocytosis of the particles by the cells. It has been reported that exocytosis is size dependent and smaller particles are exocytosed at a faster rate than larger particles. Chondrocytes appeared to fully retain SiMAG after 28 days in culture whilst this was not as obvious in the case of hMSCs. Furthermore, it became obvious that chondrocyte morphology remained consistent throughout the 28 day culture period while hMSCs became elongated with confluency with hMSCs appearing to be closely packed from day 7 onwards. Prussian blue staining revealed the presence of Fe amongst this cell population. Contrary to chondrocytes (where particles are clearly observed within the cell), the particles linked to hMSCs formed chains throughout this network of cells. This may indicate that the arrangement of the particles within hMSCs is altered with cell shape with particles therefore appearing to form network. The conflicting hMSCs and chondrocyte results may be explained by referring to the high proliferation rate

of hMSCs in comparison to chondrocytes where proliferative rates of chondrocytes were found to be impaired with SiMAG labelling.

3.6 Conclusion

This chapter investigated the potential of 4 commercially available SPIONs (SiMAG, Lumirem, Nanomag, and P904) as possible cell tracking agents when used in conjunction with MRI. Labelling condition revealed optimal uptake in serum free media. A range of particle doses were further investigated (1-100 μgFe/ml) revealing the greatest measure of intracellular Fe content by SiMAG (for both cell types). Furthermore, at optimal concentrations (10 μgFe/ml) no diminished viability or proliferative capacity was demonstrated by SiMAG, Lumirem, Nanomag and P904 labelled cell population, although the presence of SiMAG appeared to impair the proliferation of labelled chondrocytes (10 μgFe/ml). SiMAG-labelled hMSCs (10 μgFe/ml) successfully underwent differentiation down mesodermal lineages whilst maintaining immunophenotypical profiles post labelling.

The findings from this chapter highlight the potential application of the investigated SPIONs (SiMAG, Lumirem, Nanomag and P904) as possible contrast agents given the observation of Fe present within both cell types with no impaired cellular function. It can be concluded that these SPIONs largely meet the prerequisites presented in Figure 3.2 defining the ideal *in vivo* cell tracking agent. This chapter however failed to assess the contrast forming ability of these particles therefore to make a definitive decision regarding these particles this will need to be evaluated. With this, chapter 4 has been design to assess the MRI contrast forming potential of SPION-labelled cell population.

Chapter 4

MR-Imaging of SPION-labelled Cell Populations

4.1 Introduction

SPION and MRI based technologies have been identified as a practical and non-invasive means of generating data linked cell fate *in vivo*. The internalisation of SPIONs by cells allows for the location of SPION-labelled cell populations to be identified *in vivo* by MR imaging as hypointense areas of signal loss. The successful imaging and tracking of implanted cell populations *in vivo* using SPIONs and MRI based technologies requires the synergistic and optimised relationship between cell labelling (SPIONs) and subsequent *in vivo* cell imaging (MRI). Chapter 3 describes the investigation of SPION-labelling protocols for four commercially available SPIONs (SiMAG, Lumirem, Nanomag and P904) by hMSCs and chondrocytes. This chapter therefore aims to evaluate the MR imaging component of this strategy and assess the ability of SPION-labelled cells to create contrast using clinically relevant MRI scanners.

It is important to have a firm understanding of the MRI detection limits of the system to be able to fully exploit the technology in gathering data for stem cell therapy evaluation. Furthermore, understanding key parameters affecting visibility threshold is useful in optimising the labelling and tracking strategy for maximum results. The MRI detection limits of SPION-labelled cells is dependent on a range of factors including;

a) The total SPION concentration for a population of cells. This is governed by the SPION uptake efficiency and the total number of labelled cells.

b) The relaxivity properties of the labelling SPION (91).

c) MRI parameters e.g sequence choice and magnet strength (134, 159).

The ability for a contrast agent to successfully create contrast depends on longitudinal (R1) and transverse relaxivities (R2) properties of agent itself. Relaxivities can be defined as the inverse of the relevant relaxation times; $R1 = \frac{1}{T1}$ and $R2 = \frac{1}{T2}$ (159). Table 4.1 highlights the relaxivities of some of the commercially available FDA approved contrast agents.

Table 4.1 Relaxivity measurements for various positive and negative contrast agents when assessed at 1.5T and 37 ºC.

Brand Name	Type of contrast agent	Magnetic material	Relaxivity R1 (s⁻¹mM⁻¹)	Relaxivity R2 (s⁻¹mM⁻¹)	Reference
Endorem	Negative	Fe	10.1	120	(159)
Resovist	Negative	Fe	9.7	189	(159)
Magnevist	Positive	Gd	3.3	3.9	(159)
Dotarem	Positive	Gd	2.9	3.2	(159)

SPIONs have generally been the preferred contrast agent for cell labelling and tracking purposes. Gadolinium contrast agents tend to be extracellular compounds and unlike SPIONs are not easily internalised by cells. This not only limits the amount of contrast agent that can be associated with the cell but the significantly lower particle relaxivity of gadolinium compounds in comparison to SPION compounds (Table 4.1) implies that much higher concentrations of the gadolinium compound are required to achieve the same level of contrast for cell detection (130). In addition, gadolinium is not biocompatible and has been associated with toxic outcomes when used to label cells *in vitro* (97). SPIONs on the other hand have improved biocompatibility as they are composed of biodegradable iron which can be incorporated into normal iron metabolism in addition to having increased contrast potential.

Understanding the relaxivity characteristics of SPIONs used in cell labelling and tracking is highly advantageous. Selecting particles with high relaxivities implies that contrast can be created in at low particle concentration. This is particularly beneficial to cells with low

degree of phagocytosis as fewer particles need to be internalised. Furthermore risk of toxicities are minimised with lower particle concentration (186)

Investigating MRI detection limits or visibility thresholds is a necessary step in the development of all cell based therapies and is primarily investigated *in vitro* by re-suspending labelled cell populations (varying in cell doses and particle concentrations) within a gel e.g collagen, agarose and agar to be MR imaged.

To our knowledge, no studies have taken this further to investigate the detection limits of labelled cell populations in various tissues. Given the varying T_1 and T_2 properties of tissues we hypothesise the visibility threshold or detection limits to be influenced by the host tissue. We believe this to be an important consideration in tracking cell *in vivo* in particularly for stem cell based therapies reliant on the ability of cells to migrate towards the injured tissue and integrate with the tissue. It is important to be able to recognise the implanted cells at the given doses against your tissue of interest in order to investigate parameters such as cell integration and migration. This is especially important in the knee where there are a number of tissues with which cells can integrate in addition to cartilage. These include the patella fat pad, patella tendons and the various stabilising ligaments.

4.2 Aims and Objectives

- To investigate the contrast forming potential and consequent MRI visibility threshold of SPION (SiMAG, Lumirem, Nanomag and P904) labelled hMSCs and chondrocytes with relation to particle concentration and cell dosage when visualised *in vitro*.

- Investigate how the minimum *in vitro* visibility thresholds are affected by various orthopaedic tissue adipose tissue, ligament and muscle

- Establish an *ex vivo* model of articular cartilage damage to investigate the minimum visibility threshold in a clinically relevant animal model and MRI scanner.

4.3 Materials and Methods

4.3.1 Chapter Experimental Plan

To address the specific chapter aims and objectives, a series of experiments shown in Figure 4.1 were implemented. More elaborate details of experimental procedures can be found in chapter 2; Materials and Methods.

In vitro assessment of minimal MRI visibility threshold - optimisation

MRI sequences; hMSCs labelled with 1, 5, 10, µgFe/ml SiMAG re-suspended at varying cell doses (10^3 , 10^4, 10^5, $3x10^5$, $5x10^5$) within collagen (2mg/ml) and MR imaged using T_1 and T_2 weighted sequences.
Collagen concentration; Acellular collagen gels fabricated (0, 0.5, 2, 9 mg/ml) and MR imaged using T_2 weighted sequences

In vitro assessment of minimal MRI visibility threshold

MR Imaging of hMSCS and Chondrocytes labelled with SiMAG, Lumirem, Nanomag & P904 (0, 1, 5, 10, 100 µgFe/ml) re-suspended at varying cell doses (10^4, 10^5, $5x10^5$) within 2mg/ml type I collagen.

Effect of tissue type on minimal visibility thresholds.

MRI Imaging of hMSCs and Chondrocytes labelled with SiMAG (0, 1, 5, 10, µgFe/ml) and varying cell doses (10^4, 10^5, $5x10^5$) when implanted within muscle, fat and ligament and MR imaged using Bruker 2.35T scanner.

Validation of detection threshold in knee model of articular cartilage damage on clinically relevant scanner

SiMAG-labelled Chondrocytes implanted within cartilage defects in a cadaveric porcine model of articular cartilage damage to investigate particle concentration (0.1, 1, 5, 10 µgFe/ml) and cell dose (10^4, 10^5, $5x10^5$) when MR imaged Siemens Symphony 1.5T scanner.

Figure 4.1. Experimental plan for MR-imaging of SPION-labelled cell populations

4.3.2 Interpretation of MRI data.

The presence of SPIONs results in a decrease in signal or a shortening of T_2 and is portrayed visually by an increase in hypointensity (progression from high signal to low signal). The colours are such that blue areas (on colour images) and black areas (on grey scale images) are significant of low signal conditions and are referred to as hypointense regions or areas of short T_2 (Figure 4.2). Areas of high signal are seen as lighter, brighter areas with red areas representing areas of the highest signal or longest T_2 (Figure 4.2). A decrease in signal implies that the likeness of that particular set of conditions to create contrast is improved (0-1000 ms). The colours produced by the signal offer an indication as to the signal intensity range. The specific T_2 value can differ within this range. For this reason, the T_2^{eff} is quantified as a more accurate means of comparing various conditions and how these could possibly affect the visibility threshold. For short values of T_2 the signal rapidly decays into the noise level. We therefore define the visibility threshold of this particular system as any condition (particle concentration and cell dose) which produces a T_2^{eff} value below 75 ms as below this value signal cannot be significantly differentiated from the noise thus making it highly likely that contrast will be generated within a tissue at those conditions. T_2^{eff} values are taken from the periphery of each well as the SI in the center of each well (where the gel dips) presents with greater hypointensity.
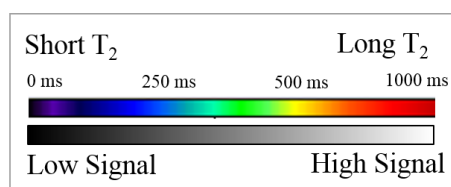
Figure 4.2. Signal map. Colour range related to signal strength. High signal (red or white) representing a long T_2 while blue or black areas are significant of low signal and short T_2 implying that these areas will create contrast.

4.4 Results

4.4.1 *In vitro* MRI visibility threshold.

4.4.1.1 *In vitro* MRI dose response optimisation.

4.4.1.1.1 MRI sequences

A selection of MRI sequences were investigated and optimised in order to establish a set of conditions that will accurately and reproducibly allow for variations in contrast to be detected. In this study, hMSCs were labelled with 1, 5 and 10 μgFe/ml SiMAG and re-suspended within a collagen gel (2mg/ml) at varying cell doses (10^3, 10^4, 10^5, $3x10^5$, $5x10^5$).

In this set of experiments T_2 MSME (Multi Slice Multi Spin Echo) imaging sequences were applied in the first instance. Using standard T_2 weighted sequences, signal was seen to decay rapidly thus making it difficult to obtain values. For this reason it was decided to apply a refocusing pulse to delay signal decay allowing for signal to be detected easier. Therefore T_2^{eff} was measured in all cases. T_1 and T_2^{eff} relaxation parameters were obtained by varying repetition times from 100-5000 ms. Figure 4.3 is a graphical interpretation of the effect of SiMAG concentration and hMSC cell dose on T_1 and T_2^{eff} measurements. As expected T_1 is not affected by the presence of SiMAG with just a slight variation observed around 1 s at each condition (Figure 4.3 B). On the other hand, T_2^{eff} is seen to be greatly affected by SiMAG (Figure 4.3 A). T_2^{eff} was found to decrease for increasing numbers of labelled cells (from 10^3 to $5x10^5$) with this further decreasing with increasing SiMAG concentration from 1 μgFe/ml to 10 μgFe/ml. The T_2^{eff} at 1000 cells labelled with 1 μgFe\ml resulted in a lower value than anticipated (0.175 ms). This is likely due to poor distribution of the small number of cells. With this, it was decided to limit MRI scans to MSEM T_2^{eff} weighted imaging sequences with a repetition time 1000 ms.
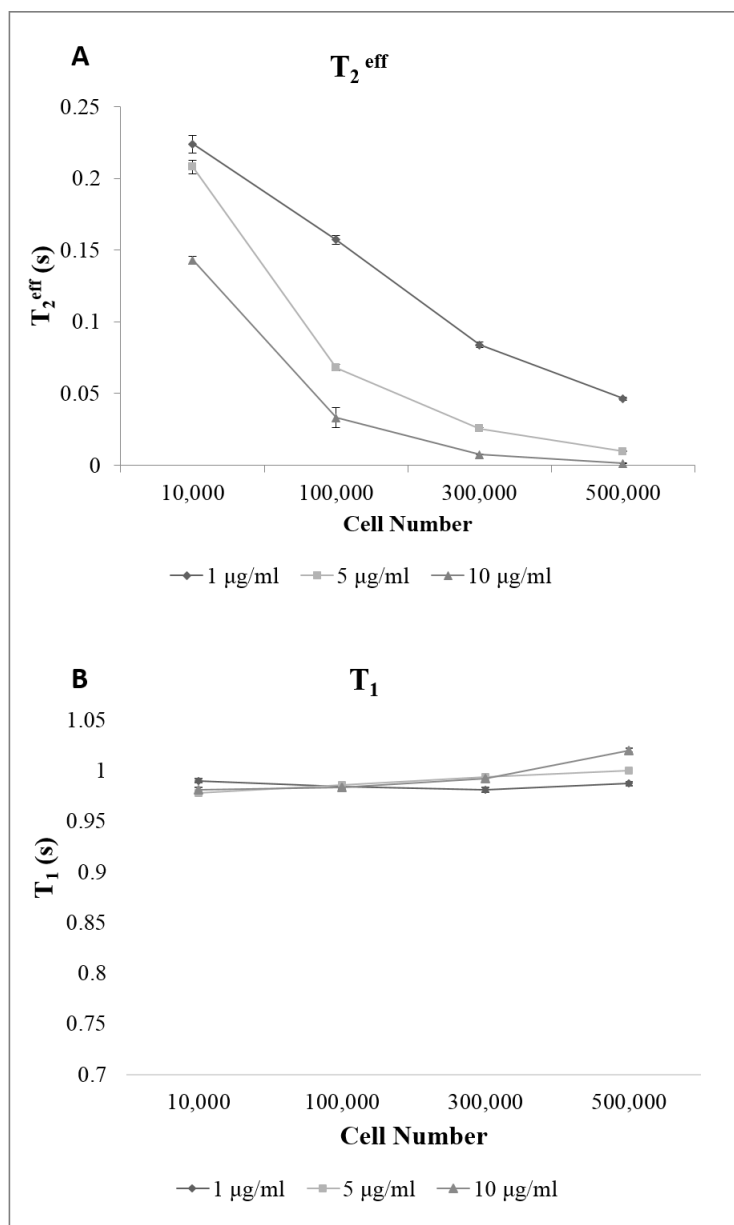
Figure 4.3. Relationship between SiMAG concentration (1, 5 and 10 µgFe/ml) and cell dose (10^4, 10^5, $3x10^5$, $5x10^5$) on A) T_2^{eff} and B) T_1.

4.4.1.1.2 Collagen Gel Concentration.

SPION-labelled cells will be re-suspended within a collagen gel when investigating the effect of cell dose and SPION concentration on the *in vitro* MRI visibility threshold. The collagen gel serves as a means of providing a physiologically relevant environment while retaining cells in suspension and preventing SPION-labelled cells from settling during imaging. In this study, varying collagen concentrations (0.5, 2, 5 and 9 mg/ml) were MR imaged using the established T_2^{eff} MSME imaging sequence (section 4.4.2.1.1). These values were then compared to the T_2^{eff} of water (Figure 4.4 A). Little variation in the T_2^{eff} is observed between water and 0.5 mg/ml and 2 mg/ml gels while a significant drop ($p<0.000053$) in T_2^{eff} is observed between water and 5 mg/ml and 9 mg/ml gels. The corresponding T_2^{eff} maps (Figure 4.4 B) appears to be similar in appearance across all concentration ranges being bright red/yellow in appearance significant of high signal apart from the 9 mg/ml sample where the presence of an air bubble is noticed (arrow Figure 4.4). From this experiment, it was decided that 2 mg/ml gel would be used in subsequent experiments. This implies that a concentration of 2 mg/ml will not influence the T_2^{eff} measurement of SPION-labelled cell populations in subsequent *in vitro* experiments while still preventing the settling of particles during imaging.
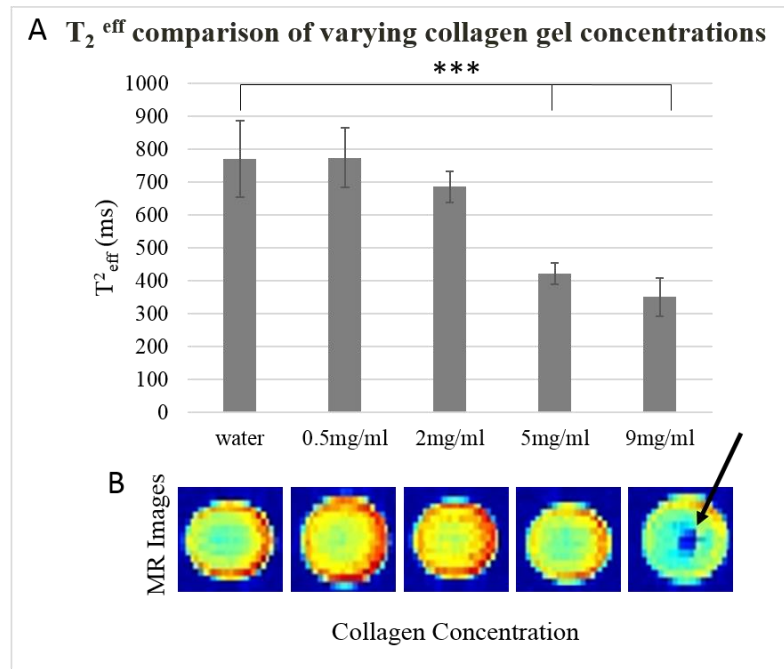
Figure 4.4. T_2^{eff} comparison of varying collagen gel concentration and corresponding T_2^{eff} map. Arrow represents air bubble shown as hypointense (blue). Data=mean$\pm$SD (n=6) where *** is significant of p<0.005.

4.4.1.2 *In vitro* MRI visibility threshold assessment.

To investigate the minimum visibility threshold, hMSCs and chondrocytes were labelled with varying concentrations (1, 5, 10, 100 µgFe/ml) of each particle (SIMAG, Lumirem, Nanomag and P904), re-suspended at varying cell density (10^4, 10^5 and 5×10^5) within 2 mg/ml of a type 1 collagen gel and MR imaged using the Bruker 2.3T MRI scanner with optimised MSME T_2^{eff} weighted sequences (section 4.4.2.1.1). For each particle, a T_2^{eff} map was produced comprising of the T_2^{eff} image at each condition (particle concentration and cell dose) with the corresponding T_2^{eff} value building the T_2^{eff} plot (n=3). This was carried out for each cell type (hMSC and chondrocyte) in addition to an acellular control. Together this set of results offers a qualitative and quantitative means of determining the minimum visibility threshold. The acellular control represents a scenario whereby 100 % of the

particles would hypothetically be taken up by each cell type and how this would set the visibility threshold.

a) Unlabelled cells

T_2^{eff} images (Figure 4.5 A) appear to be bright (yellow/red) in colour across all cell doses for both cell types similar to that exhibited by water. The bright colours (Figure 4.5 A) are representative of long T_2 values and can be verified by the high T_2^{eff} values in Figure 4.5 B.
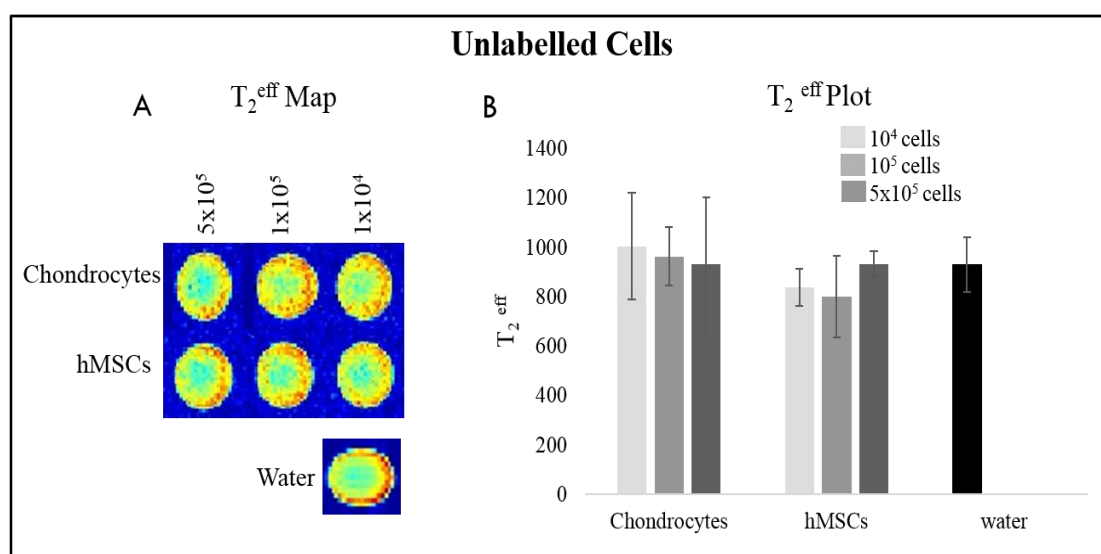
Figure 4.5. A) T_2^{eff} map and B) corresponding T_2^{eff} plot of unlabelled hMSCs and chondrocytes at varying cell doses ($5x10^5$, 10^4, 10^3)

b) SiMAG

Hypointense regions of signal voids (blue areas) highlight the presence of SiMAG-labelled cells. Hypointensity is seen to increase with increasing SiMAG concentrations (from 1 μgFe/ml to 100 μgFe/ml) and increasing cell dose ($10^4 – 5x10^5$). This is significant of signal loss while progressing from low concentrations of SiMAG (1 μgFe/ml) towards the higher concentrations (100 μgFe/ml) and from lower cell densities (10^4) towards high cells densities ($5x10^5$). This trend is clearly observed in the T_2^{eff} plots where a clear relationship is observed between the number of labelled cells at each concentration and T_2^{eff} (Figure 4.6)

A complete loss of signal is experienced when 5×10^5 and 10^5 cells are labelled with 100 µgFe/ml while the colour is seen to transform to a lighter blue (representing increasing signal) when 10^4 cells are labelled with 100 µgFe/ml (Figure 4.6 Ai and Bi). This effect becomes less pronounced with decreasing SiMAG concentration where a complete loss in signal is experienced only when 5×10^5 cells are labelled with 10 µgFe/ml while 10^4 and 10^5 are represented by a lighter blue area again significant of increasing signal. Continuing with this trend, relatively dark blue area seen when 5×10^5 cells are labelled with 5 µgFe/ml while 1×10^4 labelled with 5 µgFe/ml is represented by bright yellow/red areas significant of high signal. Similar trends are observed for hMSCs and chondrocytes alike (Figure 4.6 B). In this case, the minimum visibility threshold for SiMAG-labelled hMSCs and chondrocytes will be set at 5 µgFe/ml (5×10^5 labelled cells) (hMSCs; $T_2^{eff} = 41.92$ ms and chondrocytes; $T_2^{eff} = 41.66$ ms) in terms of minimum particle concentration and 10^4 cells (100 µgFe/ml) (hMSCs; $T_2^{eff} = 73.66$ ms and chondrocytes; $T_2^{eff} = 65.32$ ms).

The acellular control represents a scenario whereby 100% of the particles would hypothetically be taken up by each cell type and how this would set the visibility threshold (Figure 4.6 C). Under these conditions, the minimum visibility threshold for SiMAG-labelled hMSCs and Chondrocytes assuming that all the particles were internalised increased to 1 µgFe/ml (5×10^5 labelled cells)($T_2^{eff} = 22.3$ ms) and 10^4 labelled cells (10 µgFe/ml)($T_2^{eff} = 50$ ms). Noticeably, the T_2^{eff} for 10^4 labelled with 5 µgFe/ml and 10^4 and 10^5 (1 µgFe/ml) is measured to be longer (Figure 4.6 C ii) than those measured for hMSC and chondrocytes (Figure 4.6 A and B ii).

Figure 4.6. *In vitro* **dose response; SiMAG. Investigating the relationship between SiMAG concentration (1, 5, 10 and 100 µgFe/ml) and cell dose (10^4, 10^5, 5×10^5) on the MR visibility threshold for 2 cell types A) hMSCs and B) Chondrocytes while C) represents the acellular control. Data is presented as i) T_2^{eff} map and ii) corresponding T_2^{eff} plot. Red line indicated visibility threshold 75 ms.**

c) *Lumirem*

Greatest signal loss is noticed for hMSCs labelled with 100 µgFe/ml of Lumirem with T_2^{eff} increasing with decreasing cell doses from when 5×10^5 to 10^4 at this concentration (100 µgFe/ml). However, only 5×10^5 hMSCs labelled with 100 µgFe/ml Lumirem created enough contrast to fall below the minimal visibility threshold (75 ms) ($T_2^{eff} = 56.43$ms) (Figure 4.7 A ii). Further trends are evident where T_2^{eff} is seen to increase with decreasing Lumirem concentration, however, this was only significant of 5×10^5 Lumirem-labelled hMSCs across all concentrations. All other conditions appeared to be bright and yellow in appearance with high T_2^{eff} values. (Figure 4.7 A)

Lumirem-labelled chondrocytes did not appear to follow the trends displayed by Lumirem-labelled hMSCs. Despite this, 5×10^5 chondrocytes labelled with 100 µgFe/ml of Lumirem still appeared to cause the greatest loss of signal (similar to hMSCs). Although this drop was not as intense as that of hMSCs and did not fall below the visibility threshold. All other conditions resulted in bright red/yellow areas and supported by the long T_2^{eff} values (Figure 4.7 Bi & ii). Therefore, the visibility threshold for Lumirem can bet set at 5×10^5 chondrocytes labelled with 100 µgFe/ml and 10^5 hMSCs labelled with 100 µgFe/ml.

The acellular control demonstrating the potential signal profiles when total internalisation of Lumirem is achieved, sets the minimal visibility threshold at a minimal particle concentration of 5 µgFe/ml (5×10^5) ($T_2^{eff} = 74.33$ ms) and a minimal cell dose of 10^4 cells labelled with 100 µgFe/ml ($T_2^{eff} = 74.89$ ms) (Figure 4.7 C)
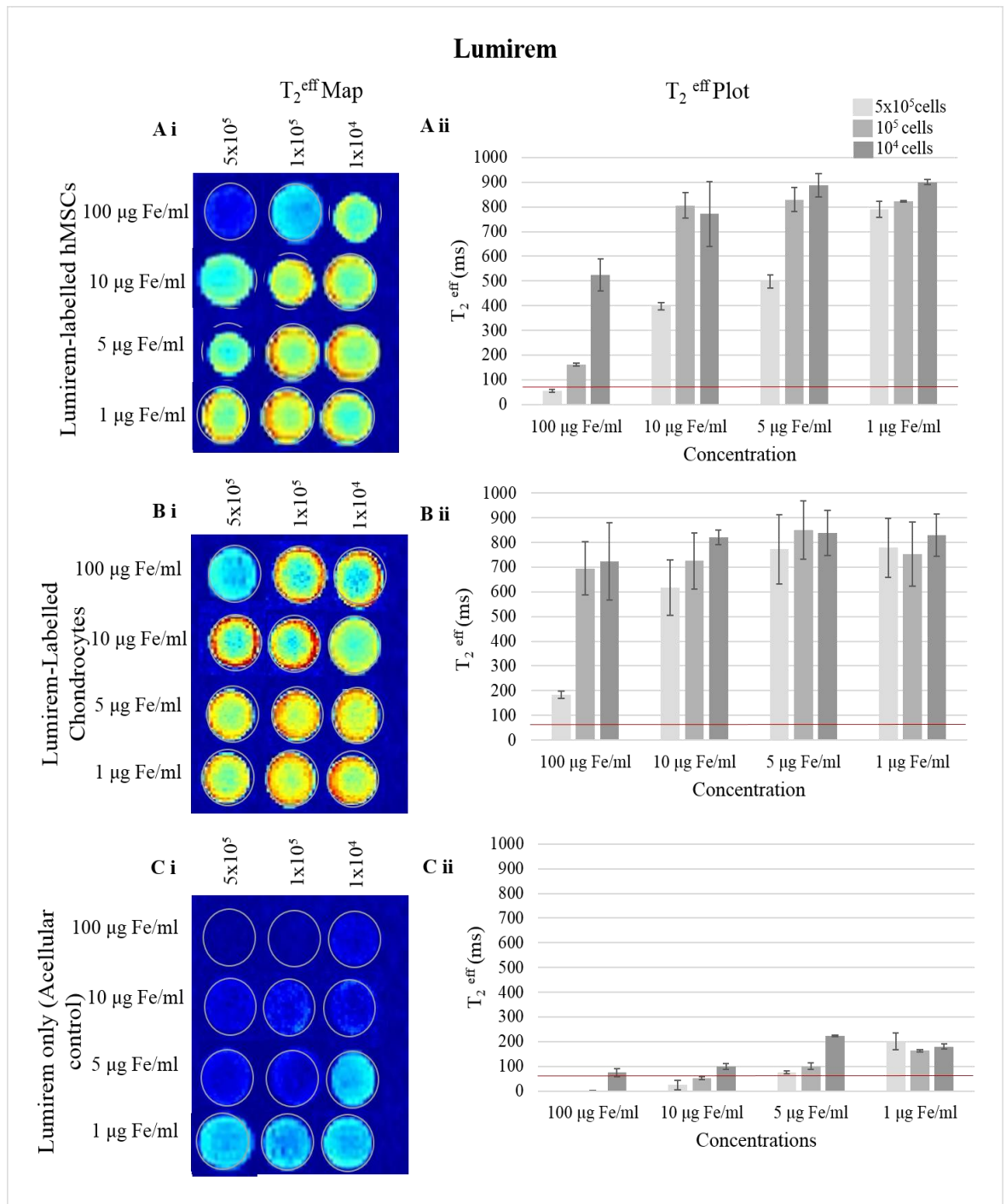
Figure 4.7. *In vitro* **dose response; Lumirem. Investigating the relationship between SiMAG concentration (1, 5, 10 and 100 µgFe/ml) and cell dose (10^4, 10^5, 5×10^5) on the MR visibility threshold for 2 cell types A) hMSCs and B) Chondrocytes while C) represents the acellular control. Data is presented as i) T_2^{eff} map and ii) corresponding T_2^{eff} plot. Red line indicated visibility threshold 75 ms.**

d) *Nanomag*

The labelling of hMSCs and chondrocytes by Nanomag did not result in significant contrast with long T_2^{eff} values being measured for all conditions (1, 5, 10 and 100 μgFe/ml; 10^4, 10^5 and 5×10^5 cells) for both hMSCs and chondrocytes (Figure 4.8 Aii and Bii) with no condition resulting in a T_2^{eff} below 75 ms. Corresponding T_2^{eff} maps (Figures 4.8 Ai and Bi) were all bright and red/yellow in appearance corroborating high T_2^{eff} signal intensities.

Significant signal loss was demonstrated by the acellular control with areas of hypointensity seen to increase with increasing Nanomag concentrations (from 1 μgFe/ml to 100 μgFe/ml) and increasing cell dose (10^4–5×10^5). Under conditions facilitating 100% internalisation of Nanomag by either hMSCs or chondrocytes, the visibility threshold would be set to a minimum of 1 μgFe/ml (labelled with 10^5) (T_2^{eff} = 75.33 ms) in terms of minimum particle concentration and 10^4 cells when labelled with 10 μgFe/ml (T_2^{eff} = 72.83 ms) in terms of minimal cell dose (Figure 4.8 C).
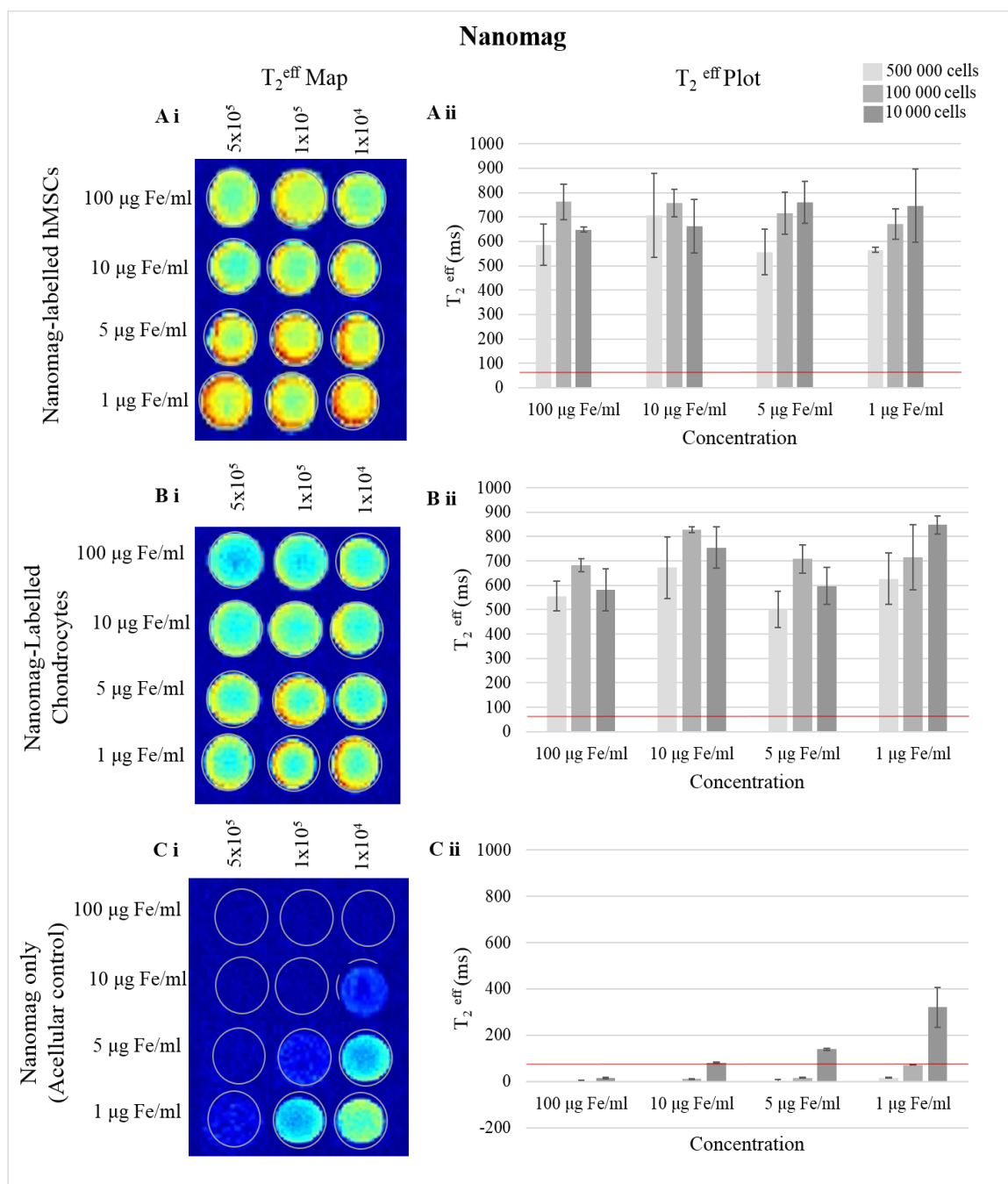
Figure 4.8. *In vitro* **dose response; Nanomag. Investigating the relationship between SiMAG concentration (1, 5, 10 and 100 µgFe/ml) and cell dose (10^4, 10^5, $5x10^5$) on the MR visibility threshold for 2 cell types A) hMSCs and B) Chondrocytes while C) represents the acellular control. Data is presented as i) T_2^{eff} map and ii) corresponding T_2^{eff} plot. Red line indicated visibility threshold 75 ms.**

e) *P904*

Similar to Nanomag neither hMSCs nor chondrocytes resulted in significant hypointensity when labelled by P904. Bright, yellow/red areas are noticed at every condition in the P904 T_2^{eff} map (Figure 4.9A and B i). This is further confirmed by the T_2^{eff} plots highlighting long T_2^{eff} values at each condition. (Figure 4.9A and B ii)

Shortening of T_2^{eff} was demonstrated by the acellular control with areas of hypointensity seen to increase with increasing P904 concentrations (from 1 µgFe/ml to 100 µgFe/ml) and increasing cell dose (10^4–$5x10^5$). Under these conditions the visibility threshold would be set to a minimum of $5x10^5$ cells labelled with 1 µgFe/ml ($T_2^{eff} = 16.30$ms) or 10^4 cells when labelled with 10 µgFe/ml in terms of minimal cell dose ($T_2^{eff} = 40.00$ms) (Figure 4.9 C)
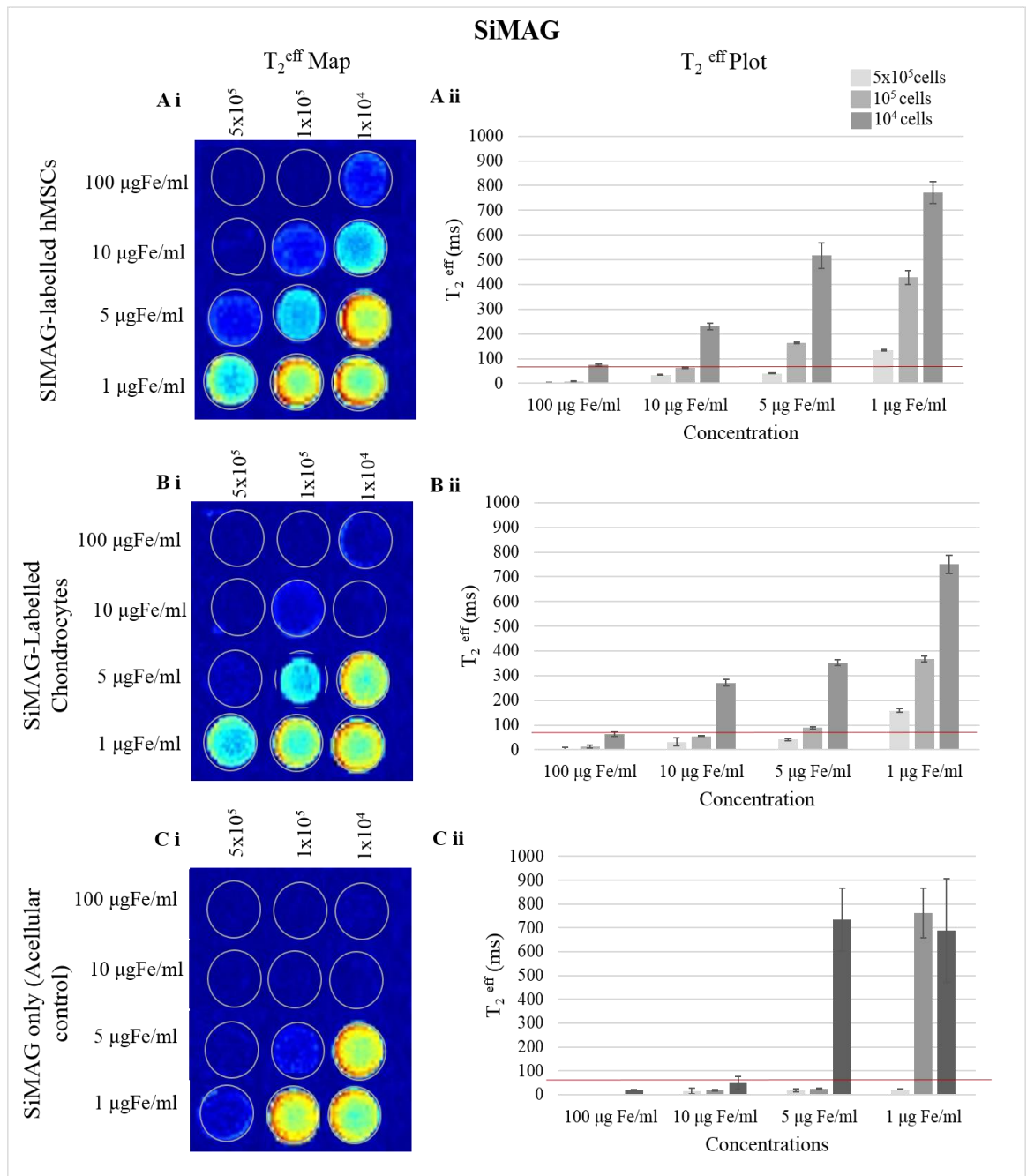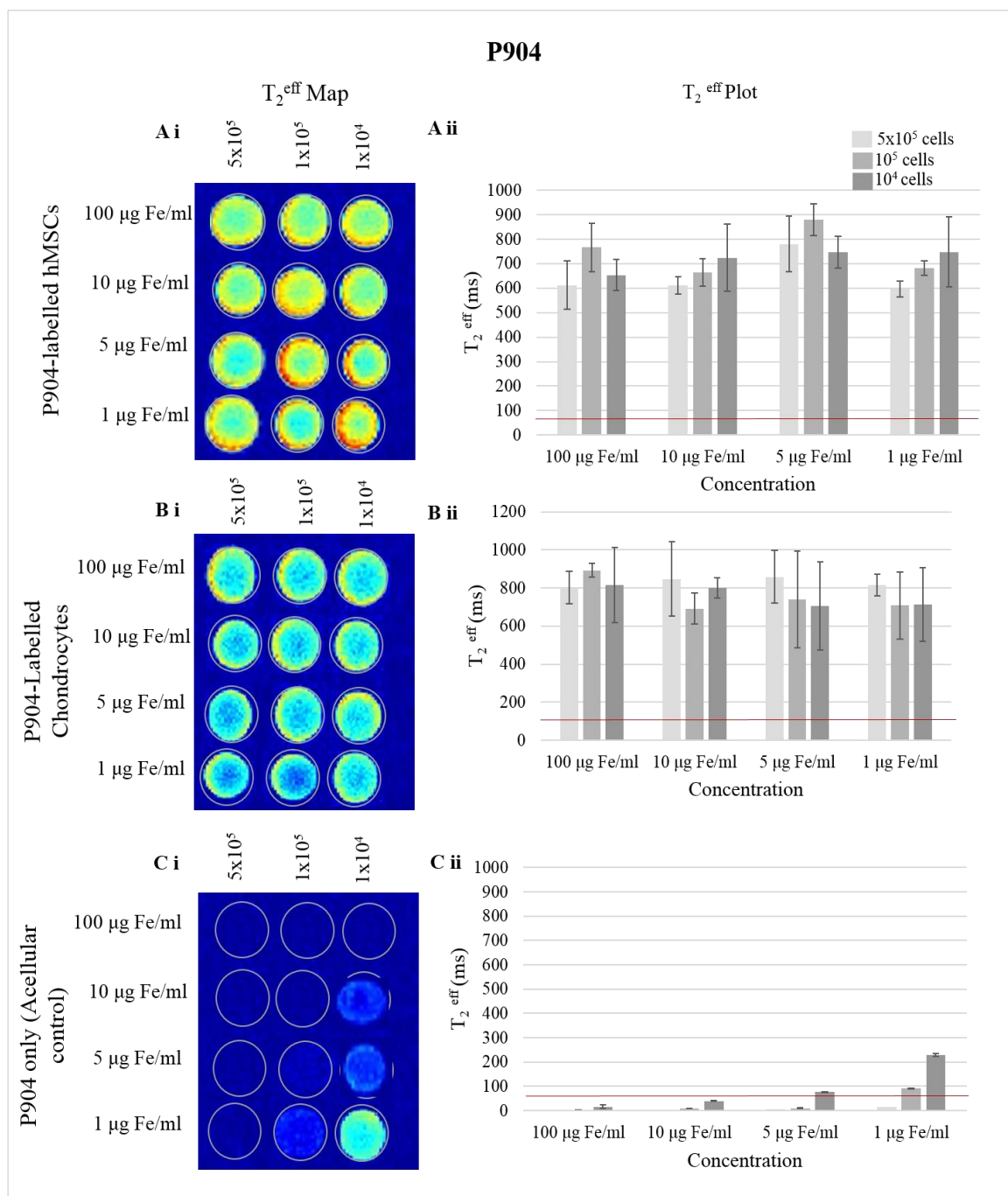
Figure 4.9. *In vitro* **dose response; P904. Investigating the relationship between SiMAG concentration (1, 5, 10 and 100 µgFe/ml) and cell dose (10^4, 10^5, $5x10^5$) on the MR visibility threshold for 2 cell types A) hMSCs and B) Chondrocytes while C) represents the acellular control. Data is presented as i) T_2^{eff} map and ii) corresponding T_2^{eff} plot. Red line indicated visibility threshold 75 ms.**

From the above set of data (section 4.4.2.2) it is clear that only SiMAG is internalised by hMSCs and chondrocytes to a degree to significantly influence T_2^{eff} (particle and cell dose dependant). For this reason, only SiMAG was carried forward from here onwards.

4.4.2 *Ex vivo* MRI dose response

The ability to create contrast within a tissue and the effect of tissue type on the perceived contrast of SiMAG-labelled cells was investigated. Muscle and fat specimens were isolate from the knee joint of a pig, and injected with hMSCs and chondrocytes labelled with 0, 1, 5, and 10 μgFe/ml at varying cell doses ($1x10^4$, $1x10^5$, and $5x10^5$). Ligament was only investigated for SIMAG-labelled hMSCs. Specimens were then MR imaged using MSME sequences (n=3). In this set of experiments, hypointense areas of signal void (implying the presence of SiMAG) are represented by black areas. Comparing the MR images of untreated samples of ligament, muscle and fat (Figure 4.10 C) clear differences are noticed in the appearance of ligament when compared to that of muscle and fat. Ligament appeared be completely black in form creating significant contrast with the surround water in the wells of the plate. Conversely, fat and muscle were brighter in appearance, with fat being brighter than muscle (similar to that of the surrounding water). No contrast was detected between SiMAG-labelled hMSCs and ligament specimens (Figure 4.10 A). The same result is expected for SiMAG-labelled chondrocytes when MR imaged against ligament tissue. Further to this, implantation of SiMAG-labelled hMSCs and chondrocytes appeared to create contrast against both muscle and fat in particular when 10^5 and $5x10^5$ cells labelled with 5 and 10 μgFe/ml. The minimum visibility threshold is set at 10^5 labelled with 5 μgFe/ml (Figure 4.10 A & B). These results are summarised in Table 4.2.
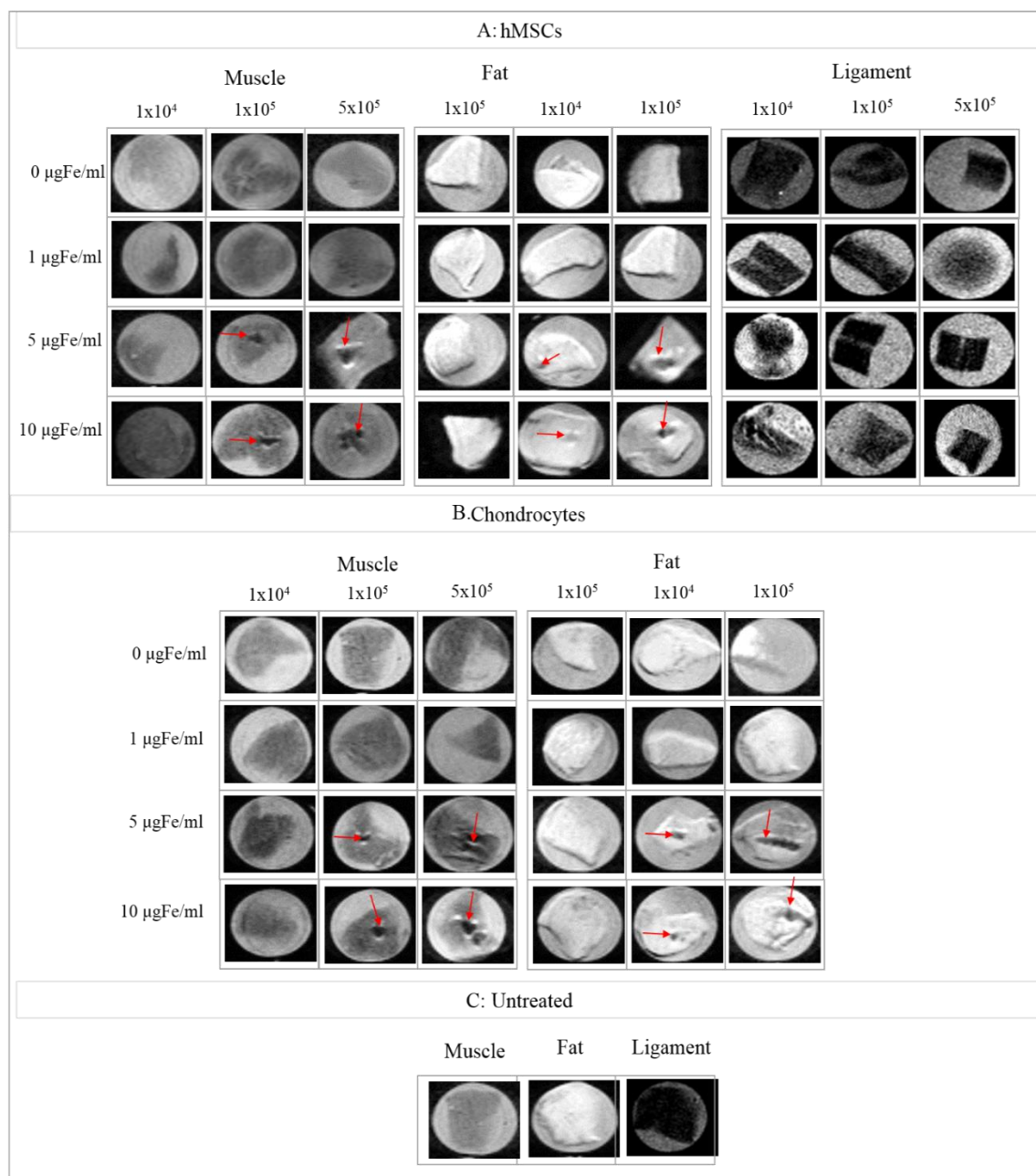
Figure 4.10. Ex vivo MR images of ligament, muscle and fat injected with A) hMSCs and B) chondrocytes when labelled with 1, 5, and 10 µgFe/ml SiMAG at varying cell doses (10⁴, 10⁵, and 5x10⁵). C) Represent specimens of untreated samples. Red arrows represent hypointense regions.

Table 4.2. Table summarising results obtained from *ex vivo* visibility threshold investigation emphasising conditions where contrast was created between tissue and SiMAG-labelled cells.

	SiMAG Concentration	hMSCs			Chondrocytes		
Cell Number		10^4	10^5	5×10^5	10^4	10^5	5×10^5
Ligament	0 µg Fe/ml	🔴	🔴	🔴	🔴	🔴	🔴
	1 µg Fe/ml	🔴	🔴	🔴	🔴	🔴	🔴
	5 µg Fe/ml	🔴	🔴	🔴	🔴	🔴	🔴
	10 µg Fe/ml	🔴	🔴	🔴	🔴	🔴	🔴
Muscle	0 µg Fe/ml	🔴	🔴	🔴	🔴	🔴	🔴
	1 µg Fe/ml	🔴	🔴	🔴	🔴	🔴	🔴
	5 µg Fe/ml	🔴	🟢	🟢	🔴	🟢	🟢
	10 µg Fe/ml	🔴	🟢	🟢	🔴	🟢	🟢
Fat	0 µg Fe/ml	🔴	🔴	🔴	🔴	🔴	🔴
	1 µg Fe/ml	🔴	🔴	🔴	🔴	🔴	🔴
	5 µg Fe/ml	🔴	🟢	🟢	🔴	🟢	🟢
	10 µg Fe/ml	🔴	🟢	🟢	🔴	🟢	🟢

🔴 No Contrast   🟢 Contrast

4.4.3 Porcine Knee Model

A cadaveric model of cartilage damage in a pigs knees was established with the primary aim of translating the established labelling protocol to a clinically relevant scenario. Knees were MR imaged using the Symphony 1.5 T clinical canner with a T_2/T_1 DESS (double echo steady state) imaging sequence as this is commonly used for looking at knee cartilage in humans to differentiate between cartilage and synovial fluid. It also has a strong T_2 weighting which is preferential for identifying the presences of particle labelled cells.

4.4.3.1 Porcine Knee Model optimisation

A preliminary study was performed to assess the suitability of the cadaveric model in this context. Figure 4.11 highlights the key features of the porcine knee when MR imaged. In the first instance, a cartilage flap was created on the upper left condyle while another piece of articular cartilage was completely removed in the upper right condyles of the same knee (Figure 4.12 i). Figure 4.12 ii demonstrates the coronal MRI view of the knee highlighting the appearance of full cartilage thickness in the left condyle (A). The small black marks are significant of the cuts made to create the cartilage flap and is more clearly shown in Figure 4.12 iii). The cartilage of the right condyle is shown to not be intact with a disturbance in the articular cartilage (Figure 4.12 i B & iv)
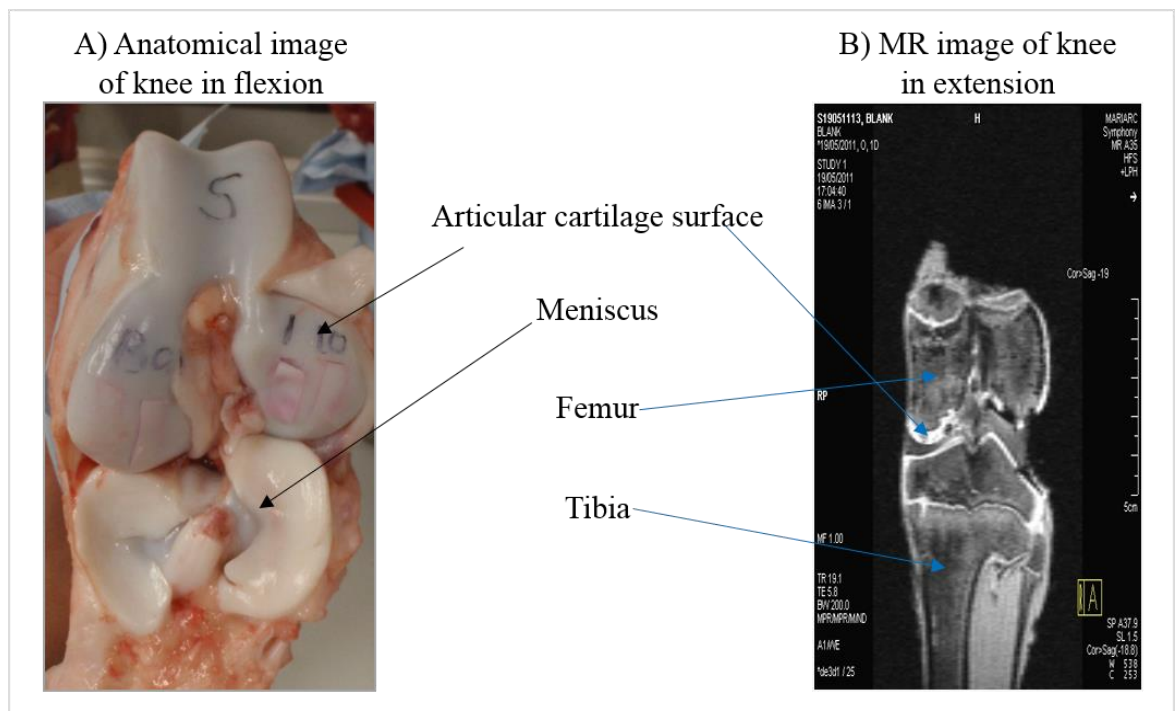
Figure 4.11. Diagram highlighting key anatomical structures of the knee when in A) flexion and B) in extension.

Front anatomical view	Front MRI view (Coronal)	Side view (Sagittal): A	Side view (Sagittal) : B

A Cartilage flap intact and filled with collagen gel
B Cartilage completely removed
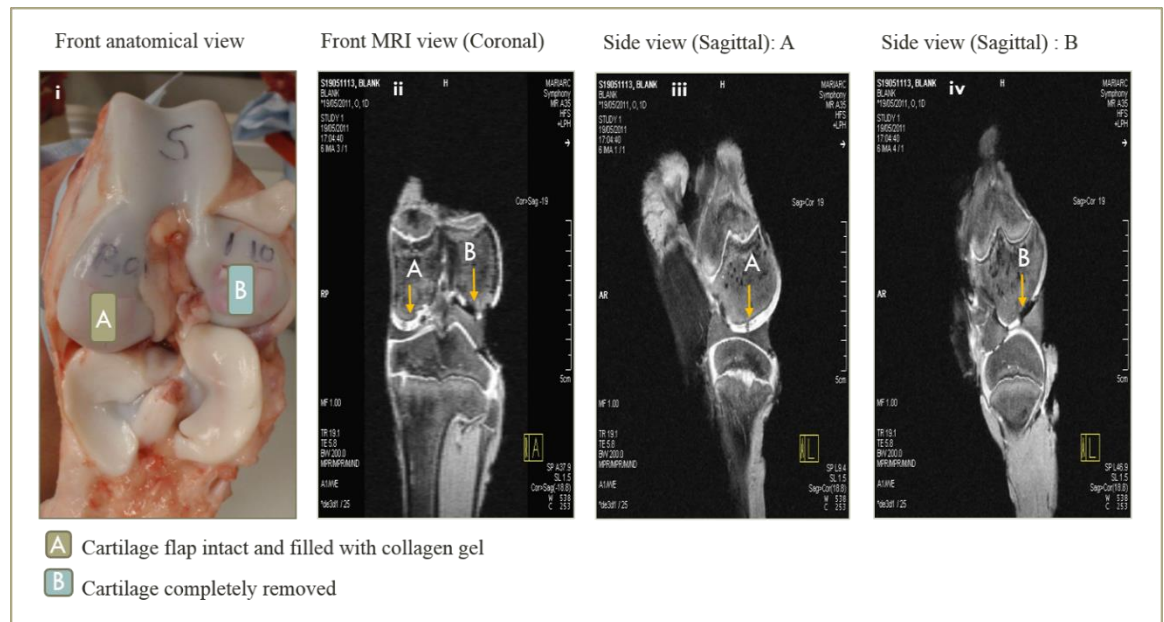
Figure 4.12. Assessing the suitability of the cadaveric porcine model. From left to right, (i) Anatomical schematic highlighting defect sites A) Flap B) Excision ii) DESS MR image coronal view highlighting both sites (A & B) of the defect on each of the upper condyle iii) Sagittal view highlighting defect site A iv) Sagittal view highlighting defect site B

To validate the use of the DESS sequence and its applicability in assessing knee anatomy in conjunction with identifying the presence of the labelled cells, 3 million chondrocytes labelled with SiMAG in excess were implanted within a cartilage defect and scanned using the Symphony 1.5T. Exaggerated hypointensity are observed in areas corresponding to the implantation site (upper left condyle) implying that the presence of particle labelled cells can be detected with this system (Figure 4.13).
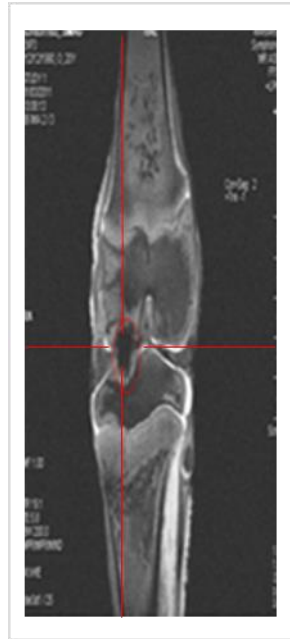
Figure 4.13. Hypointense areas of signal void corresponding to implantation of 3 million chondrocytes implanted on the upper left condyle of each knee, imaged with Siemens Symphony 1.5T (double steady state image; DESS). Region of interest (ROI), highlighted by cross hairs (red lines).

4.4.3.2 Particle Concentration Investigation

Here, 5×10^5 SiMAG-labelled (0.1 µgFe/ml, 1 µgFe/ml and 10 µgFe/ml) were implanted in series across the upper condyles within the same knee, as illustrated in Figure 4.14 A. Hypointense areas of signal loss are observed only in areas corresponding to the implantation site of 10 µgFe/ml SiMAG. All anatomical features of the knee are clearly visible in particular the bright white articular cartilage with the implanted cells.
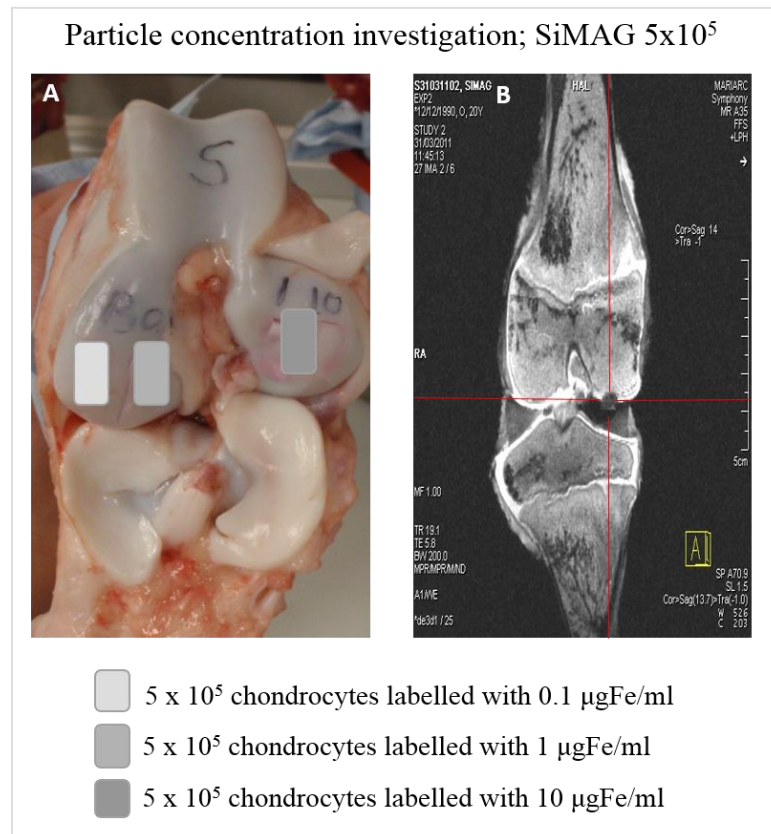
Figure 4.14. Particle concentration assessment: A) Schematic highlighting implantation sites of 5x10^5 chondrocytes labelled with 0.1, 1 and 10 µgFe/ml SiMAG B) Corresponding coronal DESS image when imaged with Siemens Symphony 1.5T. Region of interest (ROI), highlighted by cross-hairs (red lines).

4.4.3.3 Cell dose investigation

In a similar study chondrocytes labelled with 5 and 10 µgFe/ml SiMAG were implanted at varying cell doses (10^4, 10^5 and 5x10^5) in series across the upper condyles within the same knee, as illustrated in Figure 4.15 A. Hypointense regions of signal loss were only observed in the location corresponding to the implantation site of 5x10^5 chondrocytes labelled with 5 µgFe/ml SiMAG (upper right condyle) (Figure 4.15 Bii) with no hypointense regions are observed in the left condyle corresponding to the implantation site of 10^4, 10^5. chondrocytes labelled with 5 µgFe/ml (Figure 4.15 Bii). While hypointense regions are observed (Figure 4.15 Ci) and ii) in both the right and the left condyles when varying cell doses of

chondrocytes labelled with 10 µgFe/ml are implanted. This corresponds to 5×10^5 and 1×10^4 cells.
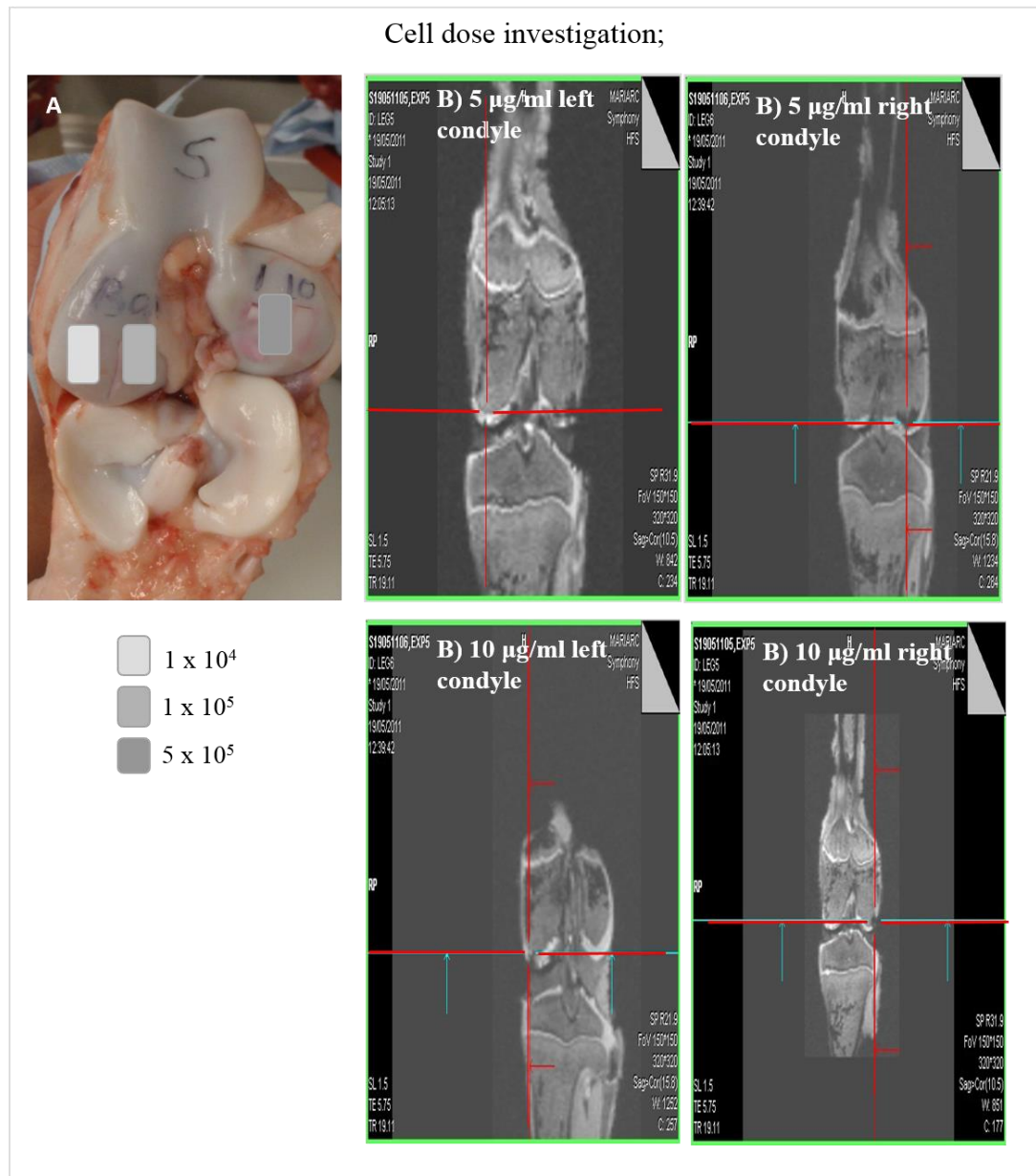
Figure 4.15. Cell dose investigation: A) Schematic highlighting implantation sites of 10^4, 10^5 and 5×10^5 SiMAG-labelled chondrocytes B) Corresponding coronal DESS image (Siemens Symphony 1.5 T MRI Scanner) for each particle concentration i) 5 µgFe/ml ii) 10 µgFe/ml SiMAG. Region of interest (ROI), highlighted by cross-hairs (red lines).

4.5 Discussion

SPIONs form a group of negative MRI contrast agents designed to overcome the inherent low sensitivity associated with MRI (97, 130, 164). They are particularly beneficial in the identification of implanted cell populations, *in vivo* (84, 93, 183). The Fe component of these particles disrupts the local magnetic field causing a shortening of T_2, therefore allowing for SPION-labelled cells to be visualised as signal voids or hypointense areas when imaged with T_2 weighted MRI pulse sequences. T_1 weighed MRI pulse sequences typically have a reduced sensitivity to SPIONs (159, 164). This is because T_1 is a parameter determined by the physical and chemical structure of the sample whilst T_2 is strongly affected by local changes in the magnetic field such as those caused by the presence of SPIONs. Therefore a SPIONs ability to create contrast is dependent on the interactions or communication of the magnetic moments associated with the particle and those associated with the neighbouring water protons and is appropriately governed by the magnetization of the particles, strength of the MRI scanner and proton density of the tissue (97)(14).

Based on this principle, the ability to detect implanted cell populations (detection limits) by MRI is dependent on a number of interconnected factors. These include; a) the relaxivity properties of the particles (contrast forming ability) (97), b) concentration of contrast agent (130) (in the case of *in vivo* MRI imaging and tracking, this refers to the cumulative Fe, which is the intracellular Fe content and cell dose relationship), c) magnet strength, d) diffusivity of protons within the sample and finally e) MRI pulse sequences.

For cell imaging and tracking applications, particles with high relaxivity properties are extremely beneficial as this implies that relatively lower labelling concentration are required to generate contrast in comparison to particles with lower relaxivity properties. However,

this would only prove beneficial with the ability to be internalised by cells in appropriate doses. An ideal scenario would be the application of a particle with high particle relaxivity potential and high cell uptake efficiency. It is equally important to optimise these parameters to clinical systems to encourage clinical adoption of such techniques.

The relaxivity of a SPION is a measure of contrast efficiency and is governed by the physiochemical properties of the particles such as: core material, coating thickness and crystallinity (91, 162, 201). Furthermore, it is important to understand that relaxivities are field dependant and therefore it is difficult to directly compare values between systems. This is clearly shown by Hinds *et al* where the R_2 of Feridex was found to be 240 mM^{-1}s^{-1} when measured using a 4.7 T with this value increasing to 498 mM^{-1}s^{-1}when measured using a 11.7 T (186). As a general indication, particles with large magnetization and stronger magnetic field enhances this effect and so creates better contrast with increased sensitivity in tissues. However, this is often at the expense of obscuring underlying pathology at the higher range of values (known as blooming) (97). The properties of the coating (material and thickness) have been reported to further affect relaxivity. Yu *et al* successfully demonstrated the ability to tune particle relaxivity by maintaining core properties but altering the thickness of the monodisperse mesoporous silica coating (162). Preliminary relaxivity data (Chapter 3 section 3.4.2.3) for particles used in this study (SiMAG, Lumirem, Nanomag and P904) indicate greatest transverse relaxivity (R2) for Lumirem closely followed by SiMAG, Nanomag and P904. This is not unexpected given that Lumirem is purposely designed to be an MRI contrast agent and therefore should have high contrast potential.

Despite the high potential of Lumirem to generate contrast (highest R2 in comparison to the other particles), little contrast was observed by Lumirem labelled hMSC and chondrocyte populations. This could be attributed to the limited uptake of Lumirem by hMSCs and chondrocytes, which resulted in far less intracellular Fe than SIMAG. It has been reported

that as little as 1.4-3.0 pgFe/cell is capable of generating contrast when MR imaged (97, 202). The intracellular iron values measured by ICP-OES (chapter 3) were significantly greater for SiMAG-labelled cell types (hMSCs and chondrocytes; $\pm$ 20 pgFe/cell) when compared to Lumirem, Nanomag and P904 which ranged from 1.05 pg/cell (Nanomag; hMSCs) to a maximum of 4.8 pg/cell (Lumirem; hMSCs). This implies that although these values were lower than SiMAG, contrast could still be generated. However, this was not the case with these MRI parameter. The discrepancies observed between the reported data in this chapter and literature may be accounted for by considering that MRI pulse sequences can influence potential contrast (97)(134). The effect of MRI pulse sequences on the contrast potential and *in vitro* visibility threshold was demonstrated by Li *et al*, where 1×10^6 labelled cells (25 pgFe/cell) demonstrated significant contrast with the application of $GRET_2$*W (Gradient Echo T_2* weighted sequence), whilst the use of FSET2W (Fast Spin Echo T_2 weighted sequence) failed to generate any contrast at these cell doses with the same strength MRI scanner (1.5 T). This demonstrates how the chosen parameters of the MRI sequences can influence contrast potential (83, 97, 134) and may account for the lack of contrast observed by hMSCs and chondrocytes labelled with Lumirem, Nanomag and P904 at these Fe doses and MRI parameters (2.35 T; MSME sequences) in comparison to published studies (3 T; FIESTA sequences). This also highlights the difficulty in making direct comparisons between studies and the need to optimise visibility threshold in a case by case manner.

By considering conditions mimicking 100 % particle uptake (Lumirem, Nanomag and P904), significant shortening of T_2 was observed at each condition. Therefore, it can be deduced that the lack of contrast generated by these SPION-labelled cell populations is likely to be due to the limited intracellular Fe content either as a result of limited uptake or low labelling concentrations. Labelling protocols could therefore benefit from increased labelling concentrations or perhaps the application of transfection agents to facilitate better particle

uptake. This highlights the importance of designing a SPION-based labelling agent with specific physiochemical properties to not only generate contrast but also be efficiently internalised.

It is essential to establish MRI visibility thresholds in terms of particle concentration and cell number *in vitro* and to understand the limits of the tracking study. Labelled cell populations were re-suspended in a collagen type I gel (a substrate highly applicable in cartilage tissue engineering) (203) and MR imaged using specific T_2 weighted sequences. This study demonstrated the ability of only SiMAG-labelled hMSCs and chondrocytes to form significant dose dependant contrast when MR imaged. As expected, T_2^{eff} was seen to decrease with increasing cell numbers and particle concentrations corresponding to the increasing Fe content. A minimum *in vitro* visibility threshold of 5 µgFe/ml (5×10^5 labelled cells) in terms of minimum particle concentration and 10^5 cells (10 µgFe/ml) in terms of cells dose for SiMAG-labelled hMSCs and chondrocytes was set with this system as it is believed that these conditions can potentially generate contrast with a host tissue. These values are considered to be highly acceptable as similar published studies have reported values ranging from a single cell when labelled with micron sized particles (11.7T) (97, 183) to 1×10^6 labelled with 12 µg/ml (3T) (101).

The ability to detect a single cell *in vivo* may be a highly attractive prospect in specific clinical applications especially those focused on the imaging and tracking of implanted cells within soft tissue such as liver and brain. However, the availability of high field strength scanners in a clinical setting is not realistic as 1.5 and 3 T scanners are primarily found in clinical practise today. High strength scanner (4.7 T, 7 T and 11.7 T) are currently limited to research application (130, 135, 199). This implies the use of this technology to track a single cell in the clinical evaluation of cell based therapies, is not translatable to clinic as yet and is thus limited to research application. It is therefore important to design and optimise

imaging and tracking protocols in terms of cell number and particle concentration to clinically relevant scanners 1.5 and 3 T (130) justifying the use of the 2.35 T scanner in this study.

The knee is a complex structure made up of a variety of interconnected tissues such as ligaments, adipose tissues, articular cartilage and bone all interacting with synovial fluid. It is therefore not unreasonable to question the contrast created with SPION-labelled cell populations against these tissues given the migratory ability of especially hMSCs in terms of injectable therapies (non-scaffold assisted approaches) and the tissue integration potential. For this reason, the visibility threshold established *in vitro* for SiMAG were further evaluated *ex vivo* within relevant tissue associated with the knee; ligament, adipose tissue in addition to skeletal muscle. To our knowledge this has not been evaluated in other similar studies before.

MRI imaging is sensitive to the hydration of the tissue (proton density) and the structure of the tissue (204). These factors govern the magnetic susceptibility (extent to which a tissue becomes magnetized) of each tissue and is affected by tissue microstructure, relative blood volume and the range of induced magnetization (97). Tissues are categorised by their magnetic susceptibility and appropriately referred to as; a) fluids e.g. cerebrospinal fluid, synovial fluid and oedema, b) fat-based tissues e.g. fat and bone marrow and c) water-based tissues e.g. muscle, brain, cartilage and ligaments. Fat is considered to have high magnetic susceptibility, (accounting for the high water and lipid content) followed by water based tissue. On the other hand, bone has the lowest of all susceptibility generating similar contrast to air, in MRI images (130). Tissues of high magnetic susceptibility appear to be brightest associated with highest signal intensity where brightness is then observed to decrease with decreasing magnetic susceptibility characteristic of low signal intensity such as that seen in

bone (dark) (130). The images generated of the native untreated tissues follow this theory where adipose tissue appeared to be brighter than muscles under the same scanning parameters. Despite ligament being a water based tissue, the characteristic bright "high signal" image was not observed, instead the ligament appeared to be dark (low signal intensity). This is a common problem associated with the imaging of tendons and ligamnets and is as a consequence of the anisotropic diffusion of water within the tightly packed fibre structure. Under routine MRI scans, the ligament is commonly positioned parallel to the main magnetic field instead of perpendicular due to human physiology. However, by adjusting the ligaments to be positioned at the magic angle of 54.7° ligaments appear as bright areas of high signal which can be useful diagnostically (205, 206).

The *in vitro* visibility threshold of SiMAG labelled cells was found to create contrast against muscle and fat with the visibility threshold being slightly different. The *in vitro* visibility threshold for hMSCs and chondrocytes labelled with SiMAG re-suspended within a collagen gel was set at a minimum concentration of 5 μgFe/ml ($5x10^5$ cells) and a minimal cell dose of 10^5 (when labelled with 10 μgFe/ml) (100 μgFe/ml SiMAG excluded). Within the environment of a tissue, this threshold changes to a minimum of 10^5 cells labelled with 5 μgFe/ml with no variations observed between adipose tissue and muscle. This implies that within these tissues there is increased sensitivity which could be beneficial as less concentration is needed to create contrast. No contrast was generated with SiMAG-labelled cell population and the ligament tissue.

The use of MRI in the imaging and tracking of implanted cell population for arthritic cell based therapies bares a dual purpose. Not only can it be used to image and track implanted cells, but its ability to distinguish between cartilage and bone (99) can be used to assess the defect and determine the extent of cartilage repair. The amount of fill in the image could

reflect the extent of repair while comparing the signal of the new graft with surrounding tissue could indicate the maturity of the graft (207). For this reason, it was important to develop a realistic model of articular damage to assess the clinical potential of this imaging and tracking protocol. This goes further to analyse the extent to which implanted cell population could be detected within a clinical system in relation to the anatomical structures. The clinical system applied in this study was a Siemens 1.5 T Symphony Scanner, a knee extremity coil and DESS pulse sequences. This is common practise in the diagnosis of pathology in the knee. The application of a porcine knee is significant in that the dimensions of the knee are similar to that of a human. In addition, the visibility threshold of SiMAG-labelled cells was further assessed using this system (Siemens 1.5 T Symphony scanner) and found to be similar to the *ex vivo* thresholds established (10^5 cells labelled with 5 or 10 μgFe/ml). The implantation of SiMAG-labelled cells generated significant contrast within this system and could be clearly detected against anatomical structure. This study encourages the clinical translation in therapies such as ACI of the tracking protocol with confidence that implanted cell populations can be detected and the extent of tissue repair could be evaluated.

4.6 Conclusion

This study has demonstrated the ability of SiMAG-labelled hMSCs and chondrocytes to create particle and cell dose dependant contrast *in vitro* when MR imaged using T_2 specific MRI sequences (Bruker 2.35 T animal scanner). No significant contrast was generated for either cell type when labelled with Lumirem, Nanomag and P904. Enhanced MRI contrast efficiency of SiMAG was related to the superior cell uptake intracellular Fe content.

Minimal *in vitro* visibility thresholds were set at 5 µgFe/ml (5×10^5 labelled cells) in terms of minimum SiMAG concentration and 10^5 cells (10 µgFe/ml) in terms of minimal cell dose. *In vitro* visibility threshold was found to be influenced by the presence of fat muscle and ligament tissue resulting in a shift in visibility thresholds to 10^5 cells labelled with 5 µgFe/ml with no variation between fat and muscle tissue, whilst no contrast was generated in ligament tissue. The development of a clinically relevant cadaveric porcine model of articular cartilage damage allowed all anatomical features of the knee to be detected simultaneously with the implanted labelled cells when MR imaged using Siemens 1.5 T MRI scanner whilst maintaining visibility *ex vivo* threshold. This study further confirms the applicability of SiMAG as a potential tracking agent.

This study suggests the potential application of SiMAG as a possible tracking agent will therefore be implemented in small animal tracking studies.

Chapter 5

In vivo Imaging and Tracking of SiMAG - Labelled mMSCs in Arthritic Animal Models

5.1 Introduction

Arthritis can be defined as a set of musculoskeletal disorders responsible for the inflammation and destruction of the synovial joint (24). It can be classed as either degenerative/mechanical arthritis in the case of OA (osteoarthritis) or as inflammatory/autoimmune arthritis in the case of RA (rheumatoid arthritis) (30). The names offer some insight as to the broad mechanism of damage with OA generally being classified as a wear and tear disease, and affects approximately 8 million people in the UK. RA is considered an autoimmune disease and is known to affect approximately 400 000 people in the UK every year (30). In both cases, the quality of life for patients is greatly reduced due to pain and loss of join function with disease progression (24).

Regardless of the mechanism of destruction, arthritis treatments involve a combination of drug regiments to alleviate symptoms such as pain and inflammation to maintain quality of life for the patient. Pain killers such as paracetamol, and non-steroidal anti-inflammatory (NSAIDs) drugs are typically prescribed. These approaches however do not target the disease process itself (6, 24, 208) thus allowing the disease to progress in severity with most individuals continuing to experience pain even at rest (209). In fact, pain is often considered the worst symptom by patients, often having severe implications on simple every day activities. Therefore, pain relief is clearly of clinically importance and currently is an unmet need (210). Current pain treatments have limited efficacies, hence alternative means of treating pain have to be investigated (40, 211). Arthroplasty (joint replacement) is often recommended in extreme cases of OA (24). However, this technique is not suitable for patients under the age of 55 due to the limited life span of the prosthesis (24).

In recent years, cell therapy approaches have been applied in an effort to regenerate damaged joint tissues (articular cartilage) in order to restore function, ultimately improving quality of life (24). These approaches aim to produce a tissue comparable to that of native cartilage, which would act to replace and or repair the damaged cartilage (13). Microfracture, Mosaicplasty, and Autologous Chondrocyte Implantation (ACI) are examples of cartilage regeneration techniques and have shown varying degrees of success (44). The chronic inflammatory environment of the rheumatic arthritic joint renders these techniques ineffective, as similarly to original native cartilage, newly formed cartilage would again undergo destruction within the hostile environment (6). Therefore the above mentioned approaches are limited to the damage caused by osteoarthritis and trauma (6).

Mesenchymal stem cells (MSCs) have been identified as suitable candidates in treating both OA and RA (6, 78, 79, 184). They can be implemented to address not only structural destruction but also the inflammatory aspects of the disease (24). This potential is a direct result of the properties demonstrated by MSCs; these include the ability to home to the site of tissue injury and their immunosuppressive and immune-privileged properties. Therefore cell therapy approaches involving the implantation of MSCs either encompassed within a biodegradable scaffold or simply injected directly into the synovial cavity have been investigated (31). The use of small and large animal models are primarily implemented to gather data related to the *in vivo* events occurring post transplantation. This is a vital step in understanding and optimising any therapy. Animal models closely resembling the human form of RA and OA have been established (212). These models allow for the progressive degeneration of articular cartilage with histopathologically accurate features and bare significant importance in understanding pathogenesis and evaluating potential treatments for these diseases (213, 214). Studies have investigated the effects of MSCs within AIA (Antigen Induced Arthritis) models of RA in mice. Here, Kehoe *et al* demonstrated the

significant reduction in inflammation, joint swelling and cartilage destruction in response to MSC delivery (article under review). Other studies have demonstrated the significant reduction of OA progression and improved healing capacity in both the MIA (Monosodium Iodoacetate) (215) and the MXN (Meniscal Transection) (31) models of OA when treated with MSCs.

To investigate aspects linked to the mechanisms of repair (cell migration, tissue integration and rate of repair) *in vivo*, histological analysis has traditionally been performed on the animal models. This tends to be very labour intensive and highly invasive as it requires the euthanization of the test animal and the processing of all tissues. For these reasons, the recent initiative proposed by the NC3R (National Centre for the Replacement Refinement and Reduction of Animals in Research) further aims to reduce, refine and replace the number of animal models used in scientific experiments today. This initiative has driven the development of alternative, non-invasive techniques to evaluate *in vivo* experiments. Having a practical and non-invasive means of identifying and subsequently optimising key parameters linked to the therapeutic potential of implanted cells (cell migration, tissue integration, rate of repair and mechanism of action) is an extremely powerful tool to have and will contribute to the optimisation and eventual clinical adoption of such therapies.

The combined use of SPIONs and MRI has been proposed as one such technique. Extensive *in vitro* work has been carried out to demonstrate the feasibility of using SPIONs to label various cell populations. A range of cell types (fibroblasts, stem cells, lung cells, liver cells, kidney cells, macrophages, nerve cells, endothelial cells and various cancer cells lines) have been labelled with a wide variety of SPIONs (Endorem, Feraheme) and optimised towards different strength MRI scanners (1.5 T, 4 T, 11.7 T) (109). In recent years these strategies have been applied to *in vivo* animal models of disease processes. Song *et al* demonstrated the ability to track human neural stem cells labelled with Endorem (150 nm particle size)

within a rat model of focal cerebral brain ischemia over a period of 4 weeks using a 1.5 T scanner (216). Jackon *et al* implemented a 9.7 T MR scanner to track USPION labelled MSCs within a preclinical rat modal of Parkinson's for six weeks while studying the functional recovery of the rats with behavioural soring methods (217). Furthermore, MRI allows for real time correlation of cell localisation with corresponding, measurable physiological outcomes (141).

More relevantly, studies have focused on the development of strategies to image and track stem cells within the articular joint for articular cartilage regeneration cell-based therapies. Henning *et al* compared the use of transfection agents to label hMSCs with Endorem. Labelled cells were seeded onto agarose scaffolds and implanted within a surgically induced osteochondral defect within the distal femur (rats knee) to mimic the MASI approach of articular cartilage regeneration. Animals were monitored for 12 weeks using a 3T MR scanner. However, Endorem has recently been taken off the market and replaced with Feraheme (20-30 nm) instead (184). The study was repeated by the same group later using Feraheme, (187). Here, adipose derived MSC labelled with Feraheme (with a transfection agent) transfection agent) were seeded within an agarose and gel implanted within an osteochondral defect. These cells were monitored *in vivo* for 4 weeks using a 7 T MR scanner (187). Further studies can be found in Table 5.1 which have also demonstrated the ability to track particles within animal models.

Table 5.1. Tracking studies in arthritic animal models

Cell type	Animal model	Particles	MRI scanner	Transfection agents	Scaffold	Tracking period	Ref
Chondrocytes	Osteochondral defects. Mini pigs	Ferric oxide nano-composites (79nm)	3 T	None	Collagen type II gel	12 weeks	(101)
MSCs	Trochlear cartilage defects. Rabbits	Endorem 150nm	1.5 T	Protamine sulphate	CGP gel	12 weeks	(83)
Rabbit MSC	*Ex vivo* knee model OA. Bovine	Commercial 1.63μm	3T	None	Puramatric	None	(103)

From these studies, it is evident that SPION based tracking studies have focused on the use of scaffold driven approaches to tackle articular cartilage damage in small animal models such as in the case of OA. It is evident that SPIONs ranging in size between 30- 150 nm (diameter) have primarily been implemented for *in vivo* studies. It is fair to mention that the application of micron sized particles in small animal models such as articular cartilage defects has not been widely investigated. Finally, the end point of these studies (Table 5.1) assessed the extent and quality of cartilage regeneration while no studies were found which investigated any functional outcomes as a result of these approaches.

To our knowledge, the following gaps have been identified in the literature:

1. There are no published studies which have adopted the rheumatoid arthritis model to track cells in this manner.

2. There are no studies which inject cells within the joint cavity without the aid of a scaffold in order to localise cells within a specific area to be tracked.

3. Micron sized SPIONs have not been used in the live tracking of cells in arthritic cell based therapies.

4. Clinically relevant functional outcomes are yet to be assessed in conjunction with tracking studies aimed at cartilage regeneration focused cell based therapies. In particular the effect of MSC treatment on pain outcomes in OA models.

5.2 Aims and Objectives

The work presented in previous chapters suggests the use of SiMAG (a micron sized particle) to be implemented to image and track murine mesenchymal stem cells (mMSCs) within two separate animal models (RA and OA) to monitor the long and short term bio-distribution of implanted stem cells *in vivo.* In addition, clinically relevant functional outcomes of the disease models will also be assessed. Specifically, this chapter aims to investigate the relationship between the location of implanted mMSCs and:

- Joint swelling and inflammation to histopathological features of RA.

- Pain and histopathological features of OA.

5.2 Materials and Methods

5.2.1 Overall Experimental Plan

A mouse model of RA and a rat model of OA have been selected to evaluate the feasibility of the devised protocol (SiMAG, 24hr incubation, SFM) for *in vivo* tracking of cell populations for the treatment of arthritis (OA and RA). Therefore, the protocol will initially be optimized to assess the *in vitro* and *in vivo* visibility thresholds for SiMAG-labelled mMSCs within a mouse and rat model prior to the tracking study. Details of the optimizing stages are shown in Figure 5.1.

| Assessment of SiMAG uptake |
| Prussian blue staining and ICP-OES, mMSCs labelled with 10 µgFe/ml SiMAG under passive incubation period of 24 hrs in SFM |

| *In vitro* assessment; cell viability proliferation |
| Live dead assay and MTT assay |

| Characterisation of cells pre and post SiMAG-labelling |
| mMSCs ; multi-lineage differentiation, cell surface markers (FACS) |

| *In vitro* minimal visibility threshold assessment of SiMAG - labelled cells by MRI |
| SiMAG labelled mMSCs (1, 5, 10 µgFe/ml) re-suspended in 2 mg /ml collagen gel at varying cell doses (10^3, 10^4, 10^5, 3×10^5, 5×10^5) and MRI Imaged. |

| *In vivo* minimal visibility threshold assessment of SiMAG - labelled cells by MRI |
| Mouse; injection of 3×10^6 SiMAG labelled mMSCs (1, 5, 10 µgFe/ml) re-suspended 10 µl SFM in mouse knee joint and MRI Imaged. Rat; injection of 1×10^6 2×10^6 SiMAG labelled mMSCs (1, 5, 10 µgFe/ml) re-suspended 10 µl SFM in rat knee joint and MRI Imaged. |

| *Tracking Studies* |

Figure 5.1. Optimisation and adaption of established labelling protocol for applications in tracking.

5.2.2 Animal Model Experimental Plan.

Murine mesenchymal stem cells (mMSCs) were tracked for a total time period of 7 days when applied in a RA mouse model and 29 days when applied to an OA model. Figure 5.2 highlights the general schema applied in the animal studies. In general, experimental groups consisted of animals treated either with; SiMAG-labelled mMSCs, unlabeled mMSCs or serum free media (Table 5.2 & 5.3). All cells were pre-labeled with a fluorescent tracker; CM-DiI prior to implantation. This allows for the therapeutic potential of MSCs to be evaluated post SiMAG-labelling but also offers the opportunity to correlate the location of implanted cells as deciphered by MRI to histological assessment.
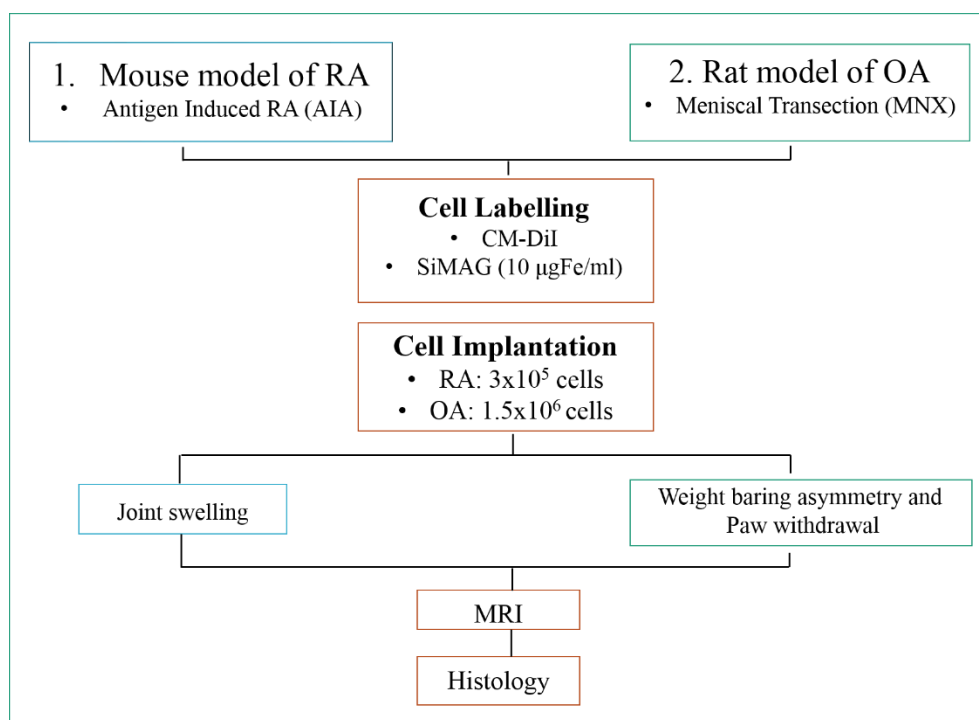
Figure 5.2. Overall experimental plan for the two animal studies: (1) Mouse model of RA and (2) Rat model of OA.

Rheumatoid Arthritis

The short term bio-distribution of implanted mMSCs population (SiMAG-labelled and unlabelled mMSCs) was assessed over 7 days in a mouse model of RA by MRI. In addition the effects of mMSC administration on the progression of RA was assessed in parallel to the tracking aspects of the study. Upon RA induction, 3×10^5 CM-DiI labelled mMSCs (SiMAG-labelled or unlabelled) were implanted within the joint of arthritic mice and joint swelling monitored throughout the experiment. Upon termination of the experiment, animals were sacrificed and MR imaged (Days 3 and 7 post implantation). A description of the experimental groups is shown in Table 5.2 while key experimental time points are shown in Figure 5.3.

Table 5.2. Description of experimental groups; RA.

Group	Description	Tracking period	Study
1 (n=6)	SiMAG-labelled mMSCs	3 days	MRI tracking study
2 (n=5)	SiMAG-labelled mMSCs	7 days	MRI tracking study
3 (n=6)	Unlabelled mMSCs	3 days	MRI tracking study
4 (n=5)	Unlabelled mMSCs	7 days	Pilot mMSCs study
5 (n=6)	No cells + No Particles (control)	3 days	Pilot mMSCs study
6 (n=5)	No cells + No Particles (control)	7 days	MRI tracking study
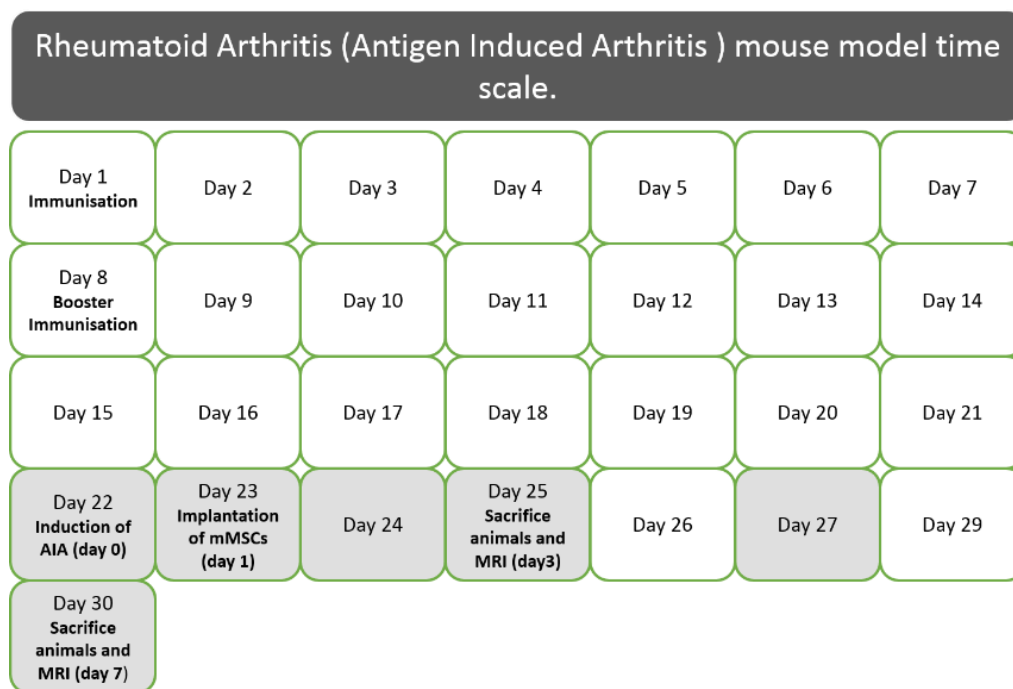
Figure 5.3. Experimental timeline for the RA tracking study. Coloured boxes highlight days where joint swelling was measured.

Osteoarthritis

A MNX model of OA was implemented to evaluate the long term tracking of SiMAG-labelled and unlabelled mMSCs in a rat model of OA. This experiment further serves as a short pilot study to investigate the effect of MSC administration and the potential antinoceptive abilities of MSCs. To our knowledge, this is the first study of its kind where the potential of mMSCs to influence pain are assessed. This has implication in MSC therapies for both OA and RA. In this study, 1.5×10^6 CM-DII-labelled mMSCs (SiMAG-labelled or unlabelled) were implanted via intra-articular injection within diseased joints and pain behavioural assessment (paw withdrawal threshold and weight bearing asymmetry) performed throughout the study. Animals were sacrificed and MR imaged 29 days post implantation. A description of the experimental groups is shown in Table 5.3 while key

experimental time points are shown in Figure 5.4 Description of experimental groups for OA

Table 5.3. Description of experimental groups for OA

Group	*Description*	*Tracking period*	*Study*
1 (n=3)	SiMAG-labelled mMSCs	29 days	MRI tracking study
2 (n=4)	Unlabelled mMSCs	29 days	MRI tracking study
3 (n=4)	Serum free media	29 days	MRI tracking study
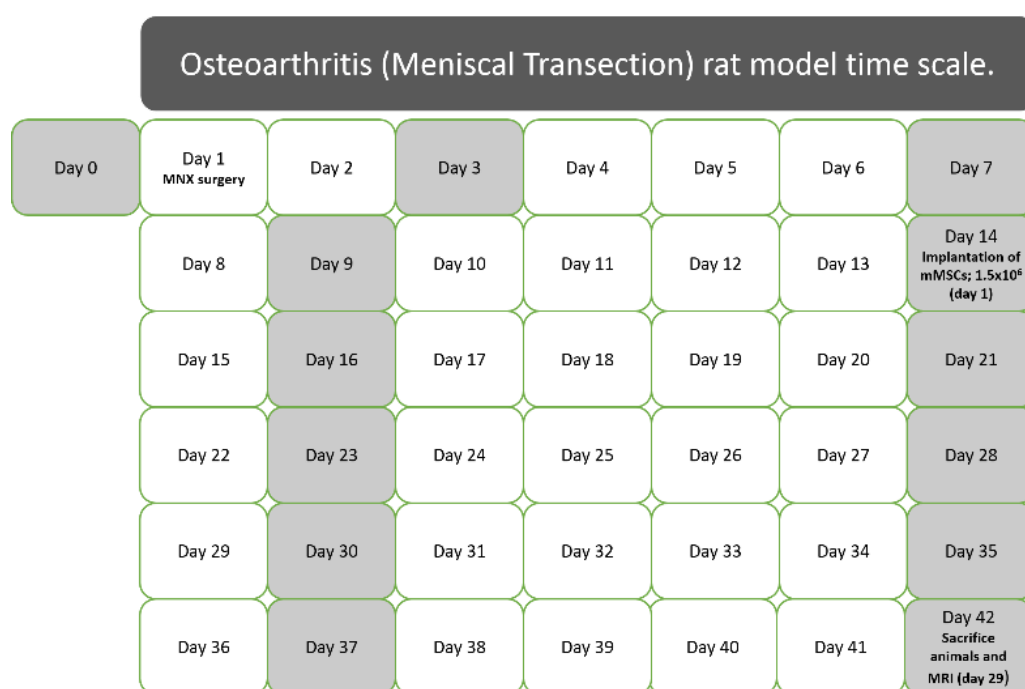
Figure 5.4. Experimental timeline for the OA tracking study. Coloured boxes highlight days where behavioural outcomes were assessed in terms of weight baring asymmetry and hind paw withdrawal threshold.

5.3 Results

5.3.1 *In vitro* Assessment.

5.3.1.1 Particle uptake

Particle uptake following a 24 hr passive incubation period of SiMAG (10 μgFe/ml) with mMSCs was confirmed by Prussian blue staining (Figure 5.5). Internalised particles were stained blue and were visible within the cell. Intracellular Fe content was measured by ICP as 20.64 ± 1.34 pg/cell. Cells retained morphology post labelling
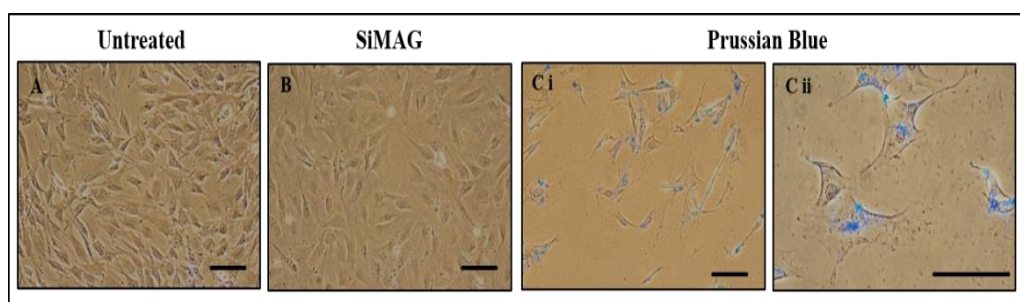
Figure 5.5. Particle uptake and cell morphology evaluation post 24 hr SiMAG-labelling of mMSCs. (A) Unlabelled mMSCs, B) SiMAG-labelled mMSCs, C) Prussian blue stain of SiMAG-labelled cells; (i) x 20 magnification, (ii) x 40 magnification. Scale bar = 100μm.

5.3.1.2 Viability and Proliferation.

Live dead (Figure 5.6) and MTT (Figure 5.7) analysis revealed no diminished viability and proliferation capacity for SiMAG-labelled mMSCs (10 μgFe/ml) when compared to unlabelled mMSCs. Figure 5.6 visually highlights the relative increase in the number of live cells (stained green) from 24 hrs to 7 days in culture with no obvious differences observed between SiMAG-labelled and unlabelled groups either at 24 hrs or day 7.

Live dead results were further validated quantitatively by MTT analysis demonstrating a significantly higher OD (Optical density; $p < 0.001$) (function of metabolic activity) between SiMAG-labelled and unlabelled groups at either time point (24 hrs and day 7) when compared to the negative control (dead). Additionally, no significant differences in OD was observed between SiMAG-labelled and unlabelled groups at either 24 hrs or day 7. The significant increase ($p < 0.001$) in metabolic activity from 24 hrs to 7 days as exhibited by both groups highlights the proliferative capabilities of SiMAG-labelled and unlabelled mMSCs. These results suggest that mMSCs are able to tolerate the internalisation of SiMAG (10 µgFe/ml) with no measured impairment to viability and proliferation.
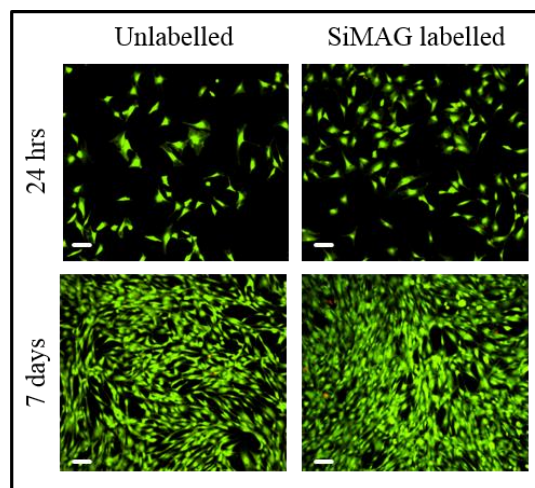
Figure 5.6. Cell viability analysis. Live/dead staining of SiMAG-labelled (10 µgFe/ml) and unlabelled mMSCs characterised at 24 hrs and 7 days. Scale bar = 100 µm.
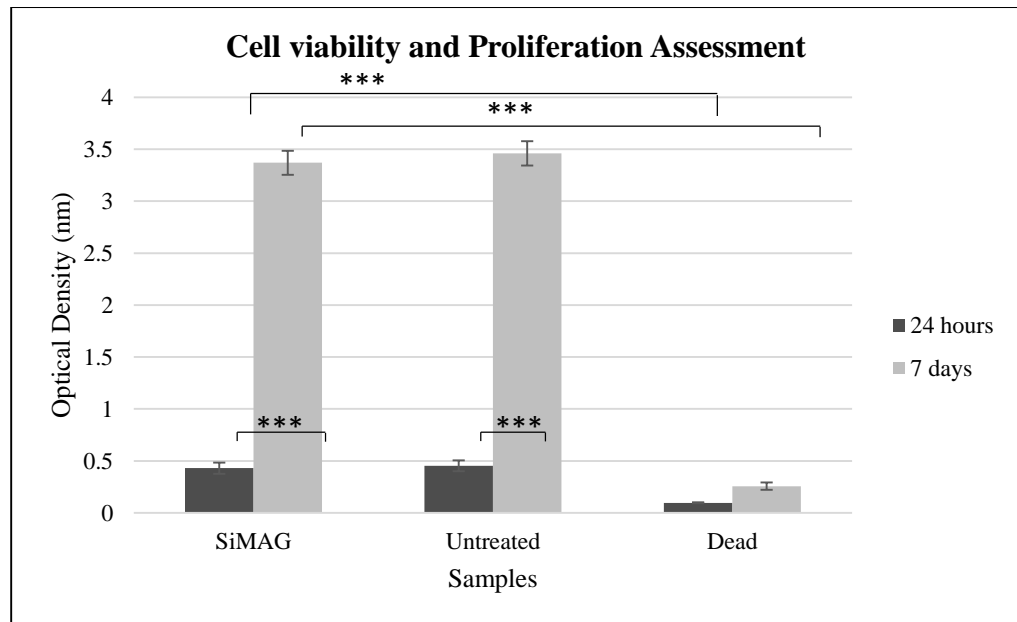
Figure 5.7. MTT analysis. SiMAG-labelled (10 µgFe/ml) and unlabelled mMSCs characterised at 24 hrs and 7 days. Data expressed as mean ± SD * Indicates p <0.001.**

5.3.1.3 Expression of mMSC Surface Markers pre and post SiMAG-labelling.

Flow cytometry (Fluorescence activated cell sorting; FACS) analysis was implemented to validate the expression of specific cell surface markers associated with mMSCs and then to further confirm the retention of these markers post SiMAG-labelling (10 µgFe/ml). FACS analysis revealed the lack of hematopoietic markers CD 11b and CD 45 and endothelial cell marker CD 31 (PECAM) on both SiMAG-labelled and unlabelled mMSCs (Figure 5.8). Furthermore, positive expression was revealed of key mesenchymal markers (CD44 and CD 105), including the stem cell marker Sca-1 for SiMAG-labelled and unlabelled mMSCs. PI (Propidium Iodine) staining confirmed a cell viability of >95 % for both SiMAG-labelled and unlabelled cell populations. Similar profiles are observed for SiMAG-labelled and unlabelled mMSCs with no significant differences in the percentage of positive expression of each of these cell markers (Table 5.4). This data confirmed that the labelling of mMSCs with SiMAG did not affect the immunophenotype profile of mMSCs.
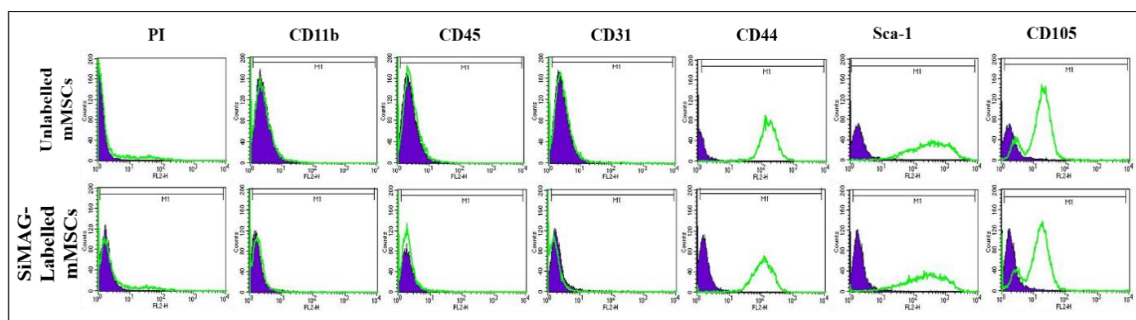
Figure 5.8. Characterisation of mMSC Surface Markers. SiMAG-labelled (10 µgFe/ml) and unlabelled mMSCs showed no variation in immunopheotypical markers profiles.

Table 5.3. Positive Expression of key mMSC Surface Markers.

Cell Surface Markers	Positive (%)	
	Unlabelled mMSCs	SiMAG-labelled mMSCs
CD11b	7.71	5.53
CD31	7.71	1.47
CD34	22.36	25.38
CD44	99.47	98.75
CD45	6.75	5.98
CD105	88.14	83.57
SCA -1	99.42	97.87

5.3.1.4 Multi-lineage Differentiation Capacity of mMSCs pre and post SiMAG-labelling.

SiMAG-labelled (10 µgFe/ml) and unlabelled mMSCs were assessed for their ability to undergo differentiation down the mesenchymal lineage (osteogeneic, adipogenic and chondrogenic lineages). Both SiMAG-labelled (10 µgFe/ml) and unlabelled mMSCs demonstrated successful differentiation towards osteogenic and adipogenic lineages after 21 days in culture with relevant differentiation media. Calcium deposition was stained positive by alizarin red in both labelled and unlabelled cells receiving osteogenic differentiation

media confirming osteogenesis (Figure 5.9). Adipogenesis was confirmed by the presence

of lipid and triglyceride droplets stained positive with oil red O after 21 days for SiMAG-

labelled and unlabelled cells treated with adipogenic differentiation media (Figure 5.10). No

staining was observed in control groups receiving basic expansion media and at day 0.

mMSCs (either labelled with or without SiMAG) were unable to undergo chondrogenic

differentiation when performed in 2D monolayer or in 3D micro mass pellet form (data not

available). This study confirms that the internalisation of SiMAG does not hinder the ability

of mMSCs to differentiate towards osteogenic and adipogenic lineages.
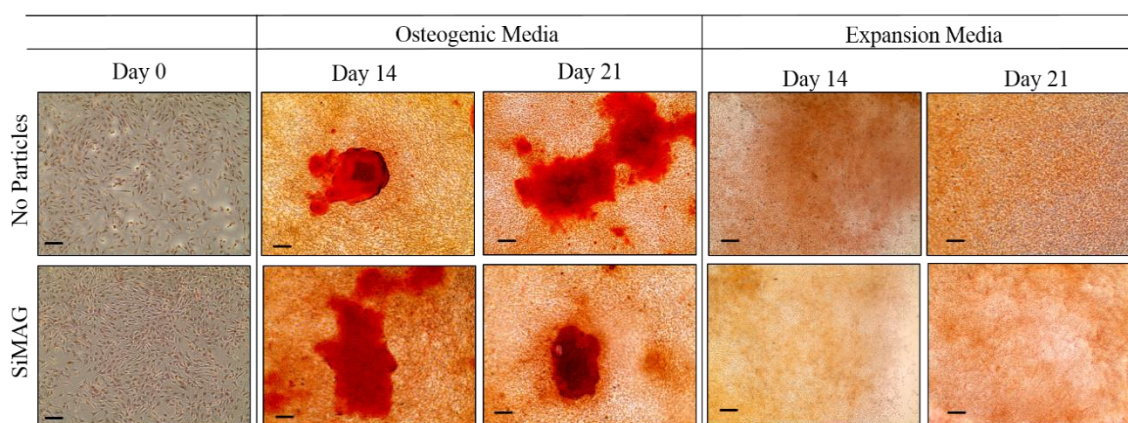
Figure 5.9. Osteogenic differentiation. SiMAG-labelled mMSCs (10 µgFe/ml) and unlabelled mMSCs cultured in osteogenic media for 21 days. Successful differentiation demonstrated by alizarin red stained calcium deposits (red). Scale Bar = 100µm
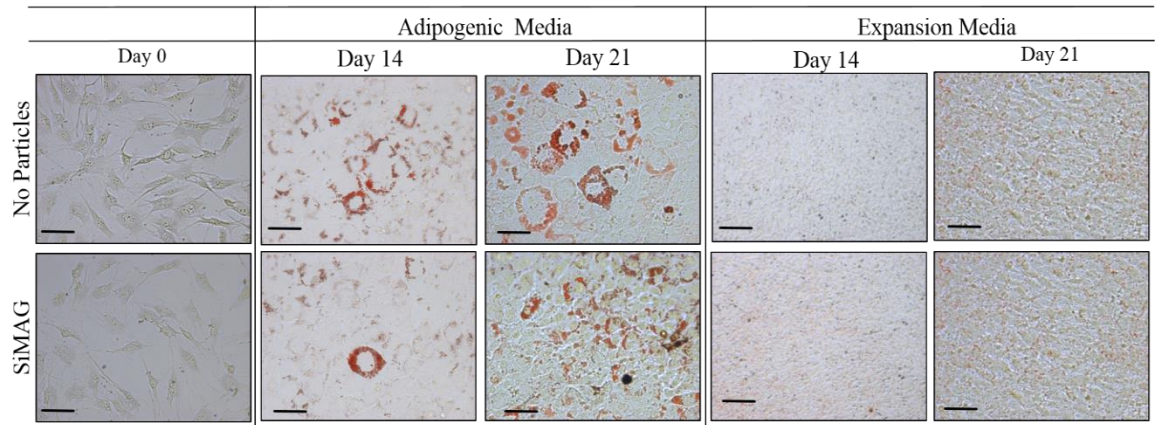
Figure 5.10. Adipogenic differentiation. SiMAG-labelled mMSCs (10 μgFe/ml) and unlabelled mMSCs cultured in adipogenic media for 21 days. Successful differentiation demonstrated by oil red "O" stained oil droplets (red). Scale bar = 100μm

5.3.1.5 Evaluating Minimum Visibility Threshold by MRI

Figure 5.11 demonstrates the relationship between SiMAG concentration and cell number (mMSCs) in terms of MRI signal loss or hypointensity (highlighted by blue areas). Hypointense regions of signal loss highlight the presence of SiMAG-labelled cells. As expected, hypointensity increases with cell number and SiMAG concentration (Figure 5.11A). T_2^{eff} was found to be shorter for higher numbers of labelled cells with this further decreasing with increasing SiMAG concentration from 1 μgFe/ml to 10 μgFe/ml (Figure 5.11B). MRI detection thresholds correspond to a minimum SiMAG concentration of 5 μgFe/ml (3×10^5 cells) ($T_2^{eff} = 69.38$ms) and a minimum cell dose of 10^5 cells (10 μgFe/ml) ($T_2^{eff} = 75.81$ms). In essence, any cell:particle combination that results in a T_2^{eff} value of 75 ms or below would be visible by MRI.
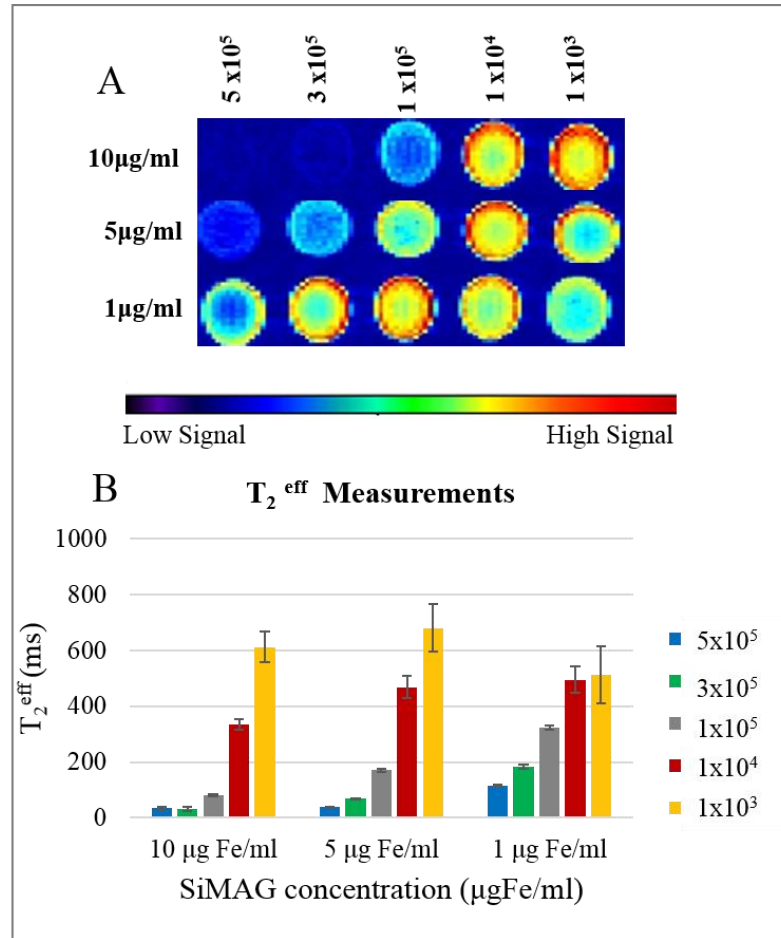
Figure 5.11. *In vitro* **dose response: (A) T$_2$^{eff} map for 10^3, 10^4, 10^5, 3x10^5, 5x10^5 mMSCs labelled with 1, 5 and 10 µgFe/ml SiMAG, re-suspended in collagen gels (2 mg/ml) and MR imaged using MSME sequences. Hypointense areas of low signal (Blue) highlight the presence of SiMAG-labelled cells. (B) Corresponding T$_2$^{eff} measurements at each particle concentration (1-10 µgFe/ml) and cell dose (10^3, 10^4, 10^5, 3x10^5, 5x10^5). Red line indicates visibility threshold (75ms). Data = mean T$_2$^{eff} $\pm$ SD (n=6).**

5.3.2 Rheumatoid Arthritis Model

5.3.2.1 *In vivo* Dose Response

In vivo dose response was assessed by intra-articular delivery of 3x10^5 SiMAG-labelled mMSCs (0, 1, 5 and 10 µgFe/ml) into each knee (left and right) of a mouse (n=2). Mice were MR imaged immediately post-delivery and signal profiles across treated knees compared.

Figure 5.12 indicates the key features of a mouse when MR imaged. MR images demonstrate good contrast (visualised as hypointense regions of signal losses or black areas over right knees, shown by the white arrow in Figure 5.13) in mice receiving mMSCs labelled with 10 µgFe/ml (Figure 5.13 iii) and 5 µgFe/ml (Figure 5.13 iv) SiMAG in both knees. This was not the case for mice receiving doses of 1 µgFe/ml SiMAG (Figure 5.13 ii) and the untreated mouse (Figure 5.13 i) where no hypointense regions could be visualised over the treated knees. Similar results are seen for the left knee however data is not shown here.

This was further validated by evaluating and comparing the signal intensity (SI) across the treated knees in all groups (Figure 5.14). A greater loss in signal over a greater area was observed in mice injected with 5 and 10 µgFe/ml SiMAG in both knees (Figure 5.14 A&B (i), A&B (ii)) whilst a less obvious drop in SI was observed for mice injected with 1µgFe/ml (SiMAG) (Figure 5.14 A&B (iii)) when compared to the control mouse (untreated) (Figure 5.14 A&B (iv)). The comparative signal profile clearly highlights differences in signal intensities between groups (Figure 5.15).
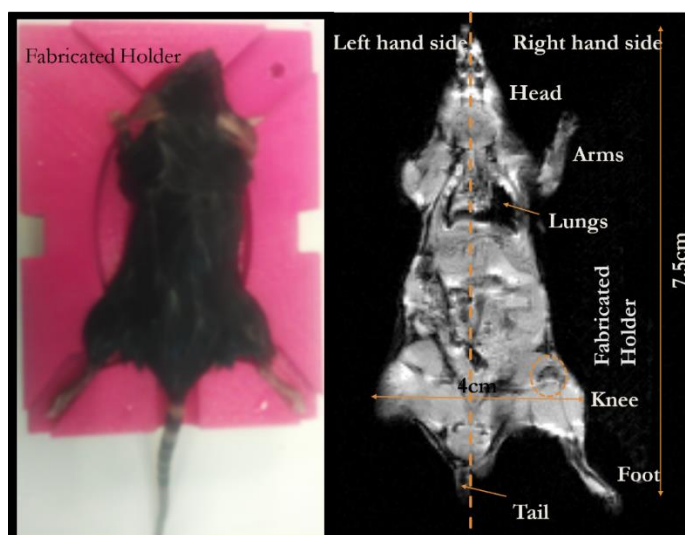
Figure 5.12. Diagram of a mouse: (A) within the customised holder and (B) corresponding GEFI MR Image depicting the key structural features of the mouse and the relative dimensions.
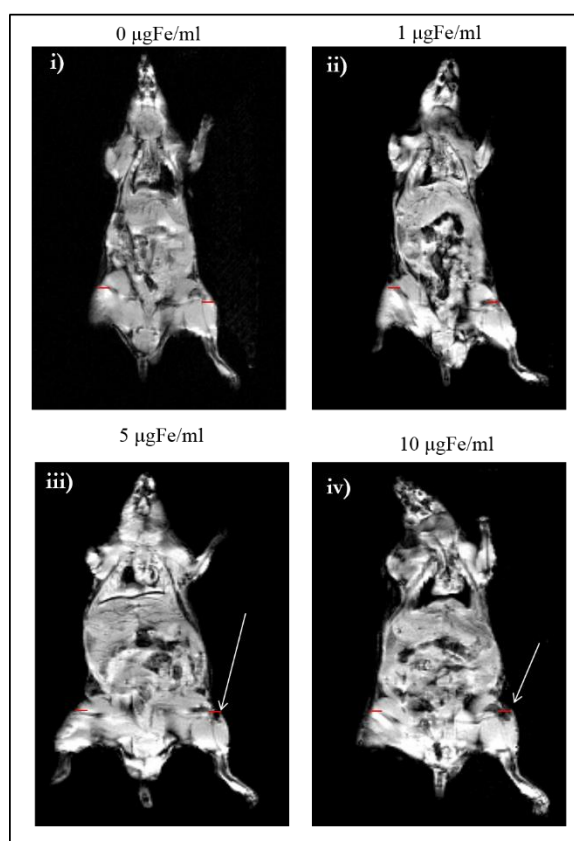
Figure 5.13. *In vivo* **dose response. GEFI MR Images relating to mMSCs labelled with (i) 0 µgFe/ml, (ii) 1 µgFe/ml, (iii) 5 µgFe/ml & (iv) 10 µgFe/ml of SiMAG and implanted within the right knee of each mouse. Red line highlights area across which SI was measured.**
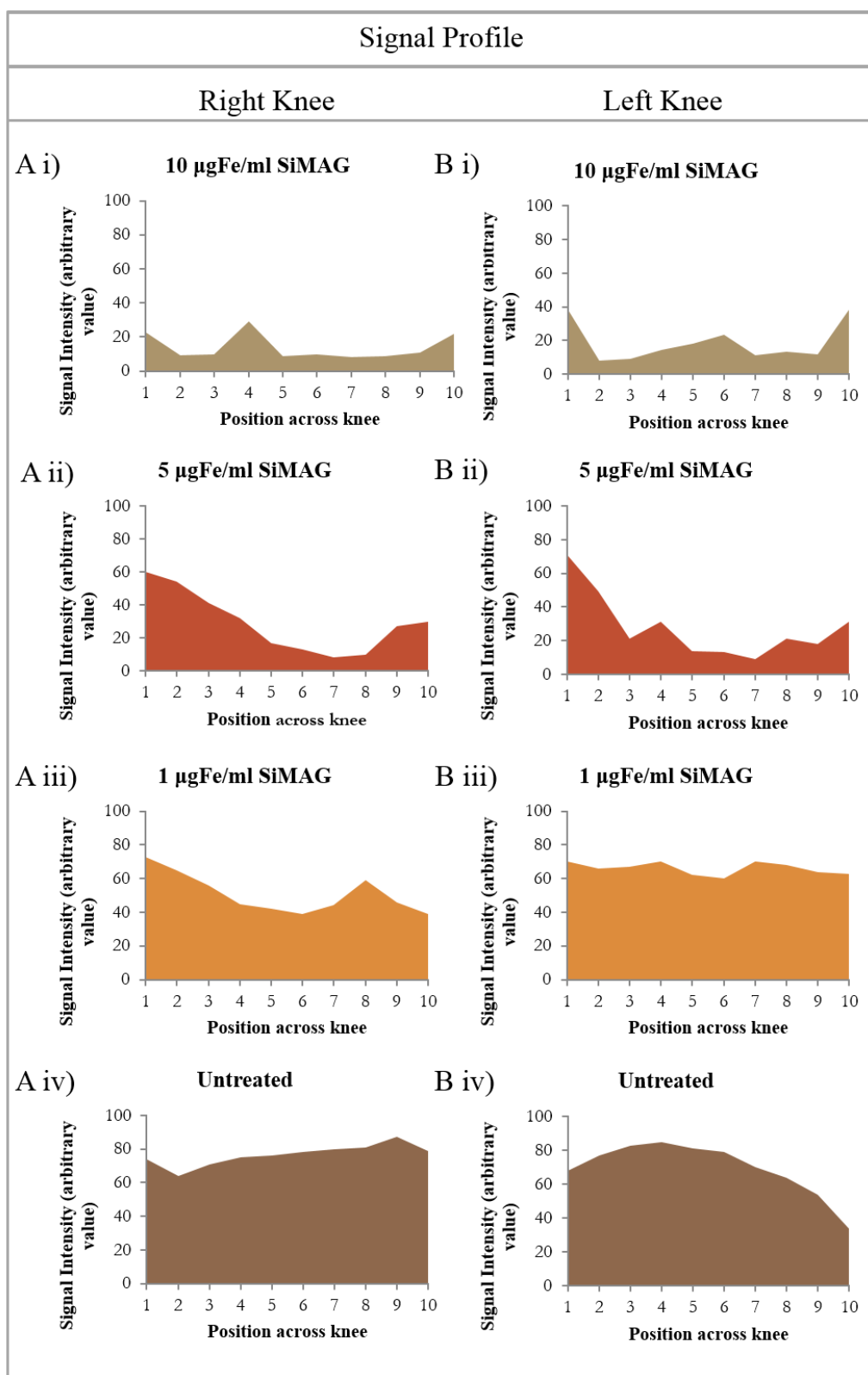
Figure 5.14. *In vivo* **dose response. Signal intensity of 10 points measured across both the (A) right and (B) left knees relating to delivery of mMSCs labelled with (i) 10 µgFe/ml, (ii) 5 µgFe /ml, (iii) 1 µgFe/ml & (iv) untreated knees to give a signal profile.**

Comparative Signal Profile
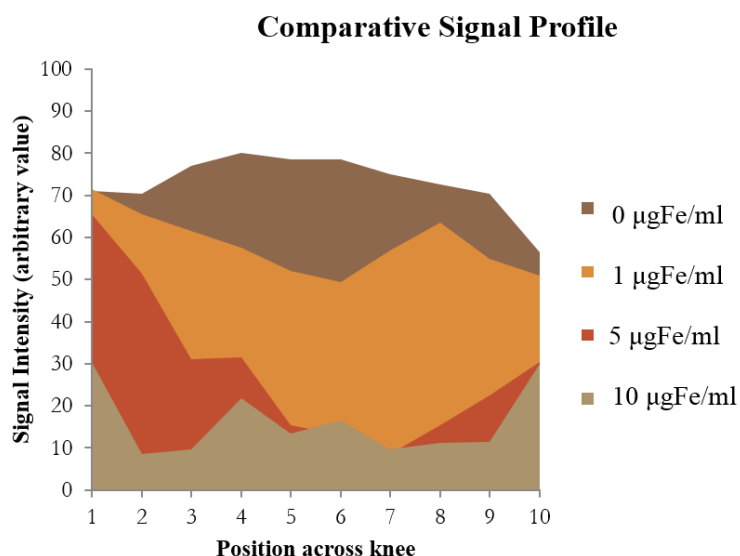
Figure 5.15. Comparative signal profile. Comparing the averaged SI of the left and right knees as measured over 10 points across the knee for mice treated with 10 μgFe/ml, 5 μgFe /ml, 1 μgFe/ml & 0 μgFe/ml (untreated knees) SiMAG. Data = average of left and right knee.

5.3.2.2 RA Progression (Joint Swelling)

A model of antigen induced arthritis (AIA) was applied to investigate the therapeutic effects of mMSCs in arthritic mice by measuring joint swelling (mm) as a clinical indication of joint inflammation. Upon RA induction (day 0), knee swelling increased approximately 1.5 (3 day study) and 1.1 (7 day study) times that of the control knee (left). Intra-articular administration of mMSCs (SiMAG labelled and unlabelled) on day 1 resulted in an immediate decrease in joint swelling in both studies. A significant drop in swelling measured on day 2, in the 3 day study (Figure 5.16 A) (SiMAG-labelled; 0.8± 0.09 mm , unlabelled mMSCs; 0.8 ± 0.05 mm vs. control group; 1.23 ± 0.07mm p=0.0104) and day 3 of the 7 day study (Figure 5.16 B) (SiMAG-labelled; 0.46 ± 0.06 mm p=0.040, unlabelled mMSCs; 0.45 ±0.07mm p=0.026 vs control group; 0.78±0.07mm). This trend continued in the 3 day study (SiMAG-labelled; 0.6± 0.11mm, p=0.044 unlabelled mMSCs; 0.5 ± 0.07mm p= 0.0309 vs. control group; 0.9 ± 0.08mm) and ultimately in the 7 day study (SiMAG-labelled;

0.12 $\pm$ 0.05 mm p= 0.0064, unlabelled mMSCs; 0.18 $\pm$ 0.07 mm p= 0.0342 vs. control group; 0.45 $\pm$ 0.08mm). The joint swelling in the control groups of the 7 day study was seen to increase in from 0.3$\pm$ 0.085 mm on day 5 to 0.45$\pm$ 0.08mm on day 7 (Figure 5.16).
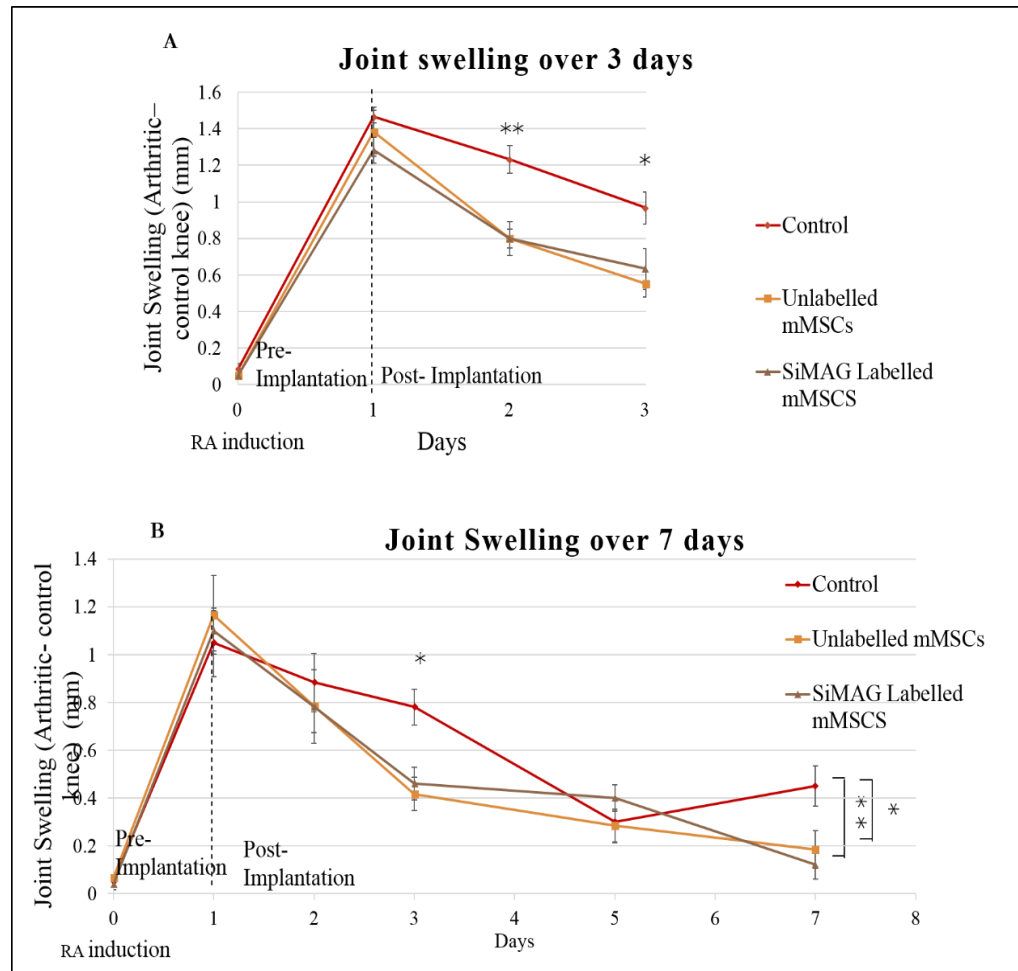
Figure 5.16. Joint swelling measurements (mm) as an indication of inflammation and RA progression. Comparing joint swelling between SiMAG-labelled mMSCs, unlabelled mMSCs and control groups (SFM) over A) 3 days and B) 7 days. Data expressed as mean ± SEM Significant levels ** Indicates p<0.01 and * indicates p<0.05.

5.3.2.3 *In vivo* tracking - MRI

Sacrificed mice were MR imaged at day 3 and 7 using FLASH and GEFI sequences respectively. Hypointense areas of signal voids were observed over the diseased knee (right) of every mouse in group 1 (+ mMSCs, + SiMAG; day 3; Figure 5.17 A) and group 2 (+ mMSCs, + SiMAG; day 7; Figure 5.17 C). This is attributed to the presence of intracellular Fe as a result of SiMAG-labelled mMSCs. No signal voids or hypointense regions could be detected over the diseased knee in group 3 (+ mMSCs, − SiMAG; day 3; Figure 5.17 B) and group 6 (- mMSCs, +SiMAG; day 7; Figure 5.17 D) nor in any of the untreated knees (Left knees; Groups 1, 2, 3, 6) as expected.

This was further validated graphically by plotting signal loss profiles across each knee and comparing the signal of the right (diseased and treated joint) (Figure 5.18 i & Figure 5.19 i) to the corresponding left (healthy and untreated joint) (Figure 5.18 ii & Figure 5.19 ii). Comparative signal loss profiles demonstrated a drop in signal over SiMAG-labelled mMSCs treated knees (groups 1 and 2) when compared to untreated knees (Figure 5.18 A iii and Figure 5.19 A iii). Similar high-signal profiles are shown for both the right (diseased joint) and left (untreated joint) in (groups 3 and 6) (Figure 5.18 B iii and Figure 5.19 B iii). These results confirm the ability to identify the presence of SiMAG-labelled cells up to day 7 post implantation using MRI.
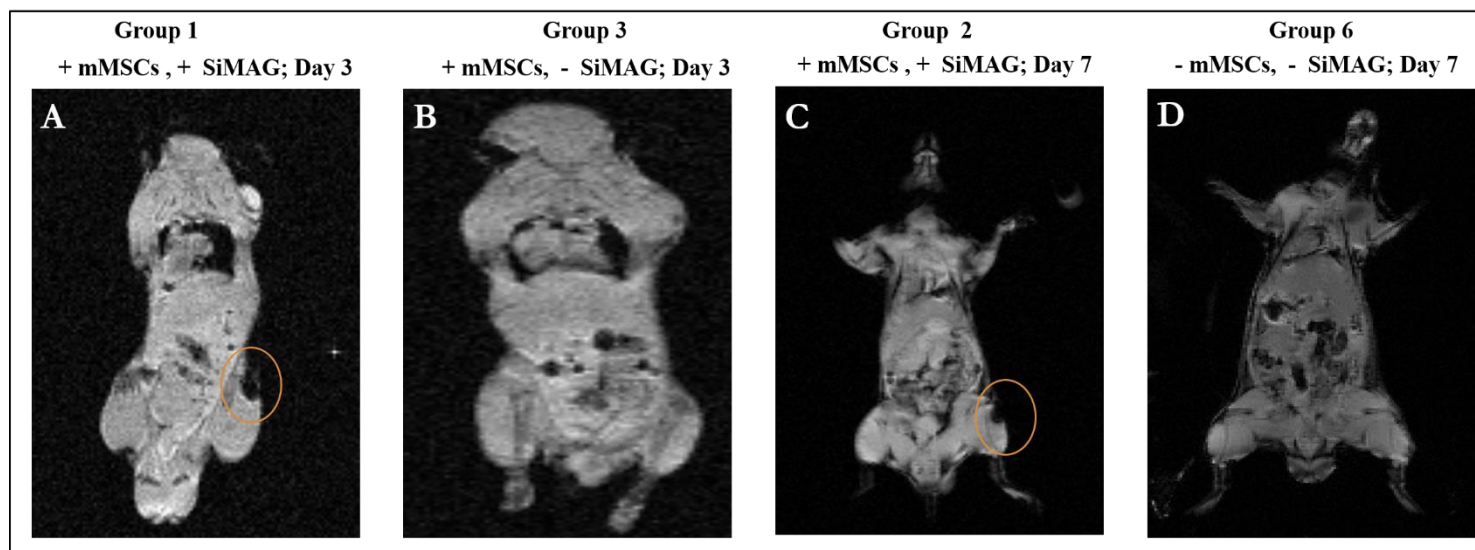
Figure 5.17. Whole body coronal MRI images for RA tracking study. (A) Group 1 (+ mMSCs, + SiMAG, Day 3, GEFI sequence), (B) Group 3 (+ mMSCs, - SiMAG, Day 3, Flash Sequence), (C) Group 2 (+ mMSCs, + SiMAG, Day 7, GEFI sequence), (D) Group 6 (- mMSCs, - SiMAG, Day 7, FLASH sequence). Orange ring represents hypointense areas of signal void highlighting location of SiMAG labelled cells.
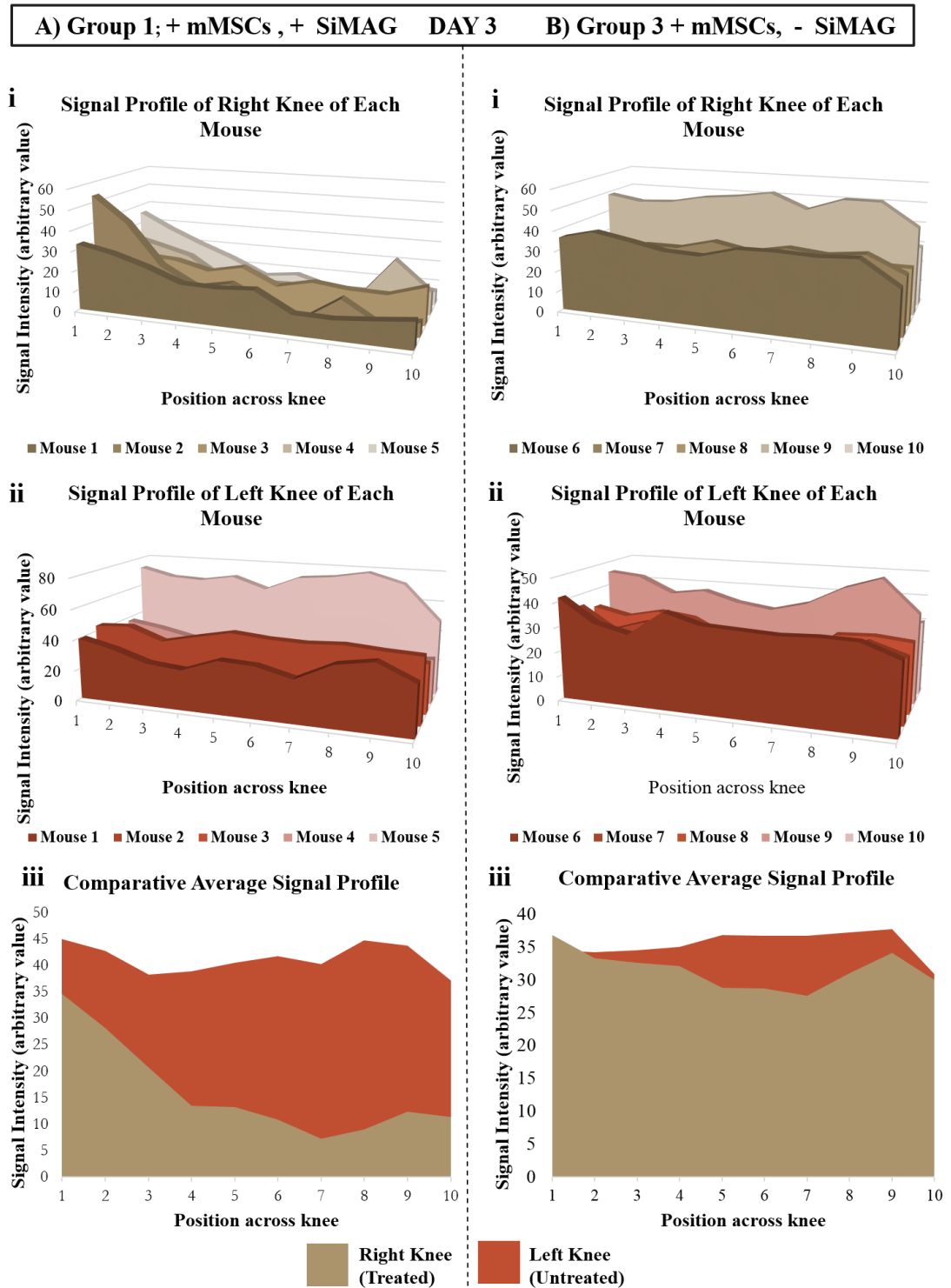
Figure 5.18. Signal loss profiles for RA tracking study. (A) group 1 (+ mMSCs, + SiMAG, n=6), (B) group 3 (+ mMSCs, - SiMAG, n=6) where: (i) treated knee (right), (ii) untreated knee (left) and (iii) average comparative signal profile.
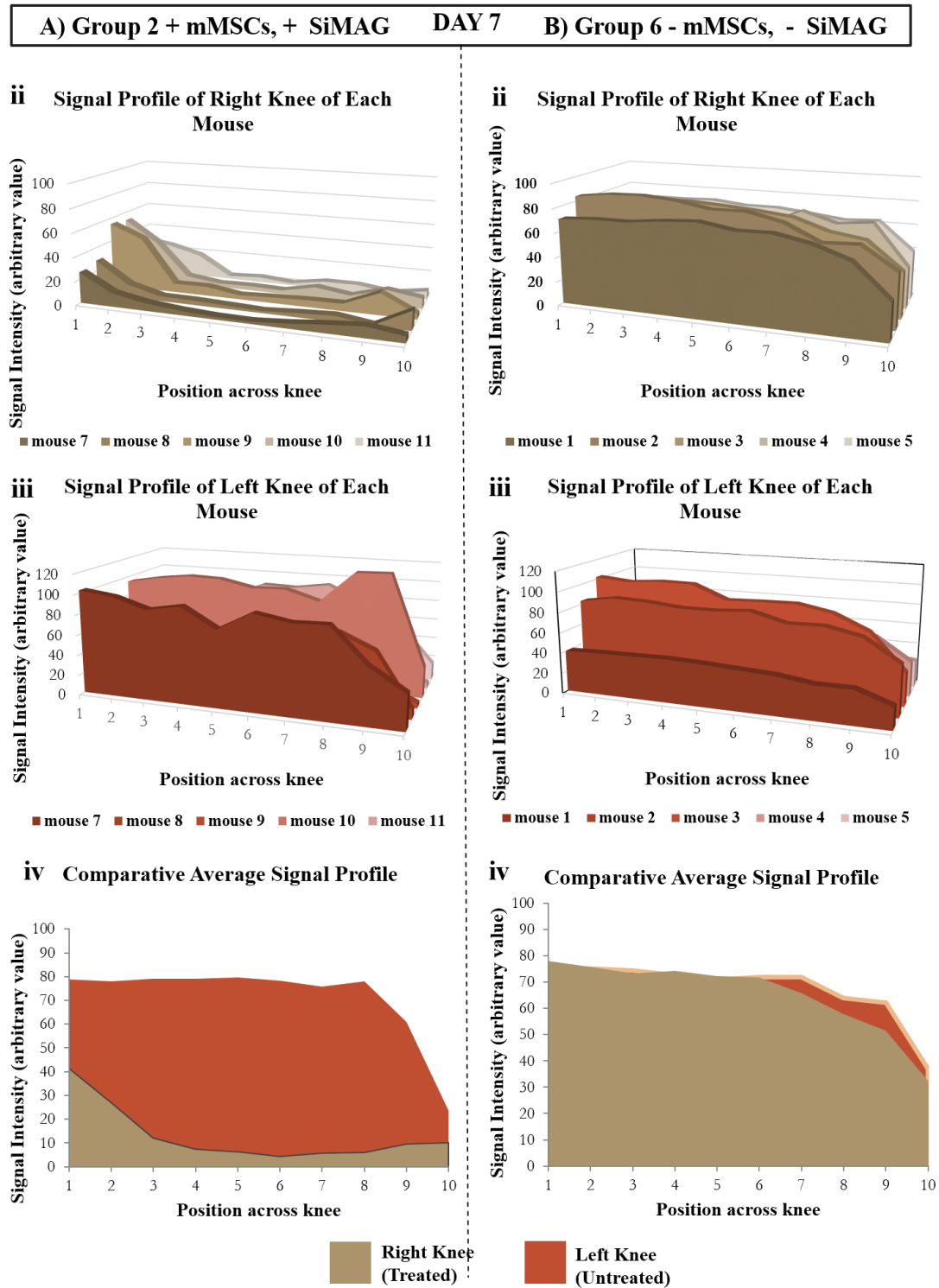
Figure 5.19. Signal loss profiles for RA tracking study. (A) group 2 (+ mMSCs, + SiMAG; n=5), (B) group 6 (-mMSCs, -SiMAG; n=5) where: (i) treated knee (right), (ii) untreated knee (left) and (iii) average comparative signal profile.

5.3.2.4 Histological Evaluation

Hematoxylin and Eosin Stain (H&E)

H&E staining was used to identify key structural features of the mouse knee joint shown in Figure 5.20. Nuclear material was stained dark purple (hematoxylin) whilst the cytoplasmic material, connective tissue and collagen was stained pink (Eosin) (16). H&E staining offers a qualitative means of analysing the cellular content within the synovial joint. A greater number of cells were noticed within the synovial cavity of the right knee (AIA induced joint) of all groups (Figure 5.21 A i, B i, C i, D i, E i, F i) when compared to the left control joint knee (Figure 5.21 A ii, B ii, C ii, D ii, E ii, F ii). This was likely due to the influx of immune cells (macrophages, neutrophils) as a result of RA induction. No obvious differences between days 3 and day 7 studies can be observed.
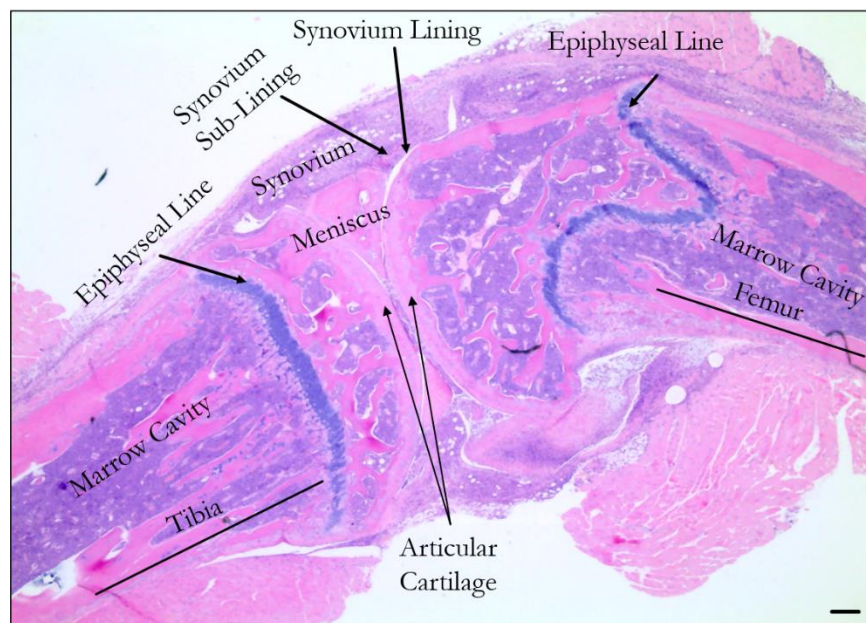
Figure 5.20. Sagittal H&E section of mouse knee joint (post RA induction) highlighting the key structures of the joint. The curvy epiphyseal line denotes the femur while the straighter epiphyseal line highlights the tibia. Nuclear material is stained purple while connective tissue such as collagen is shown as pink. Scale bar =100µm
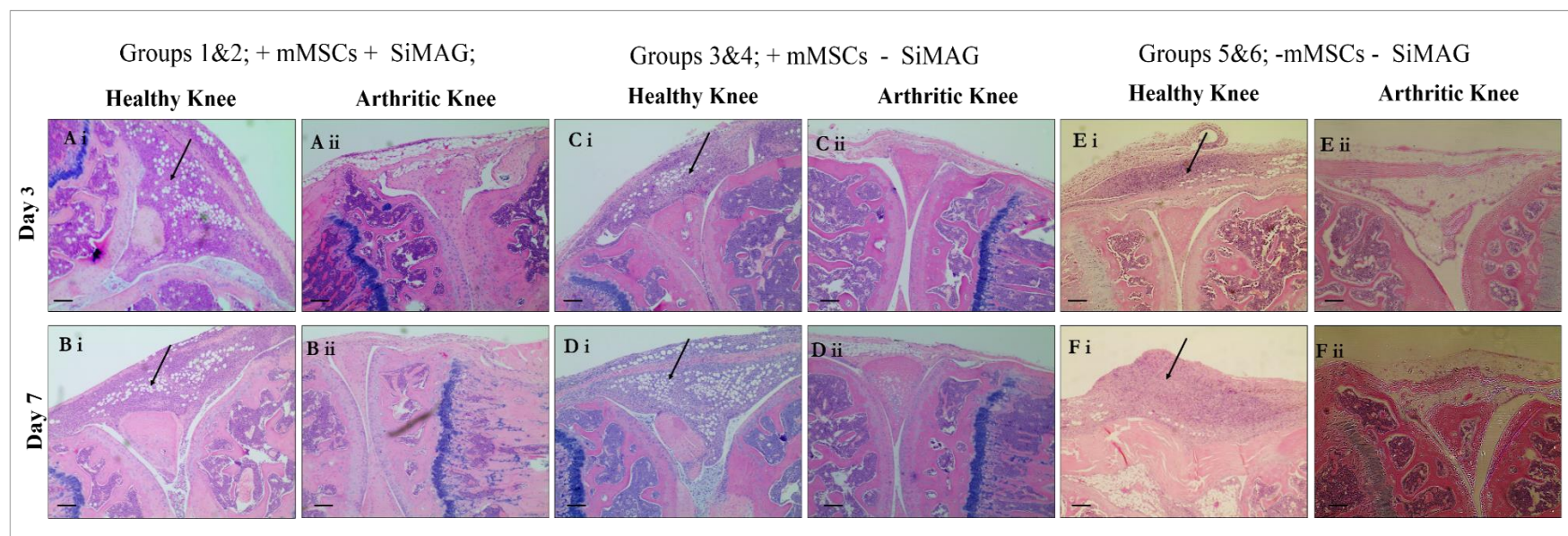
Figure 5.21. H&E stained sagittal sections of mice synovial joints: (A) group 1 (+mMSCs + SiMAG; day 3; n=6), (B) group 2 (+mMSCs + SiMAG; day 7; n=5), (C) group 3 (+mMSCs – SiMAG; day 3; n=6), (D) group 4 (+mMSCs, – SiMAG; day 7; n=5), (E) group 5 (-mMSCs, – SiMAG; day 3 ; n=6) and (F) group 6 (- mMSCs, - SiMAG; day 7; n=5). Nuclear material stained dark purple whilst connective tissue is stained pink. Increase in cellular content in the right knees of groups 1-6 is shown by arrow. Scale bar = 100 μm.

Fluorescence

Both SiMAG-labelled and unlabelled mMSCs were stained with a cell tracking dye (CM-DiI), prior to intra-articular delivery to allow the identification of implanted cells post implantation. All sections were counterstained with DAPI (a fluorescent nuclear marker; blue) and analysed using fluorescent microscopy under the TRITC and DAPI filter. CM-DiI labelled cells (indicated in red) were clearly visible within the synovium (seen in the x4 images) up to 7 days post implantation in the right joint of groups receiving mMSC treatments (groups 1, 2, 3 and 4) as shown in Figure 5.22 A-D (i,iii). No CM-DiI labelled cells could be detected in the untreated joints (left) Figure 5.22 A-D (ii, iv) and in either acellular control joints Figure 5.22 E&F (i,- iv).
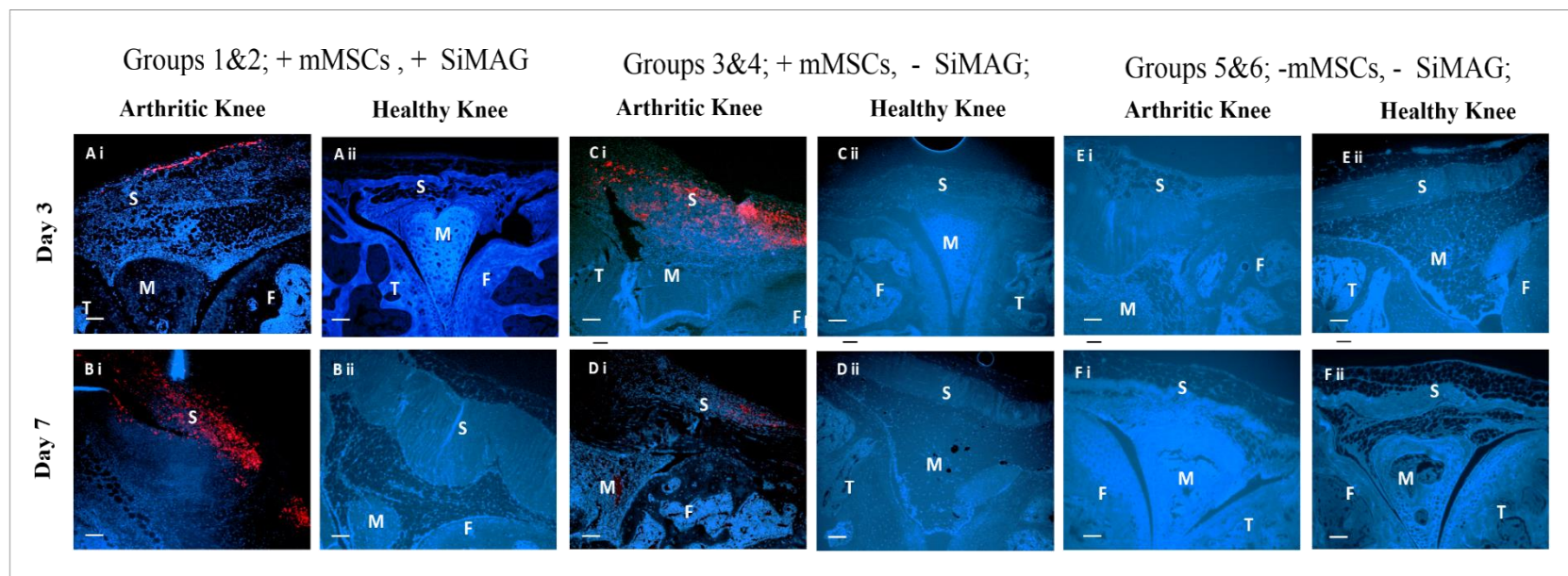
Figure 5. 22. Fluorescent evaluation of the synovial joint (CM-DiI (red) and DAPI (blue). CM- DiI labelled cells visualised in the synovium of the right (treated) joints of: (A) group 1 (+mMSCs, + SiMAG; day 3), (B) group 2 (+mMSCs, + SiMAG; day 7), group 3 (+mMSCs, – SiMAG; day 3) and group 4 (+ mMSCs, - SiMAG; day 7). No CM-DiI labelled cells were detected in the control (left) joints and groups 5 and 6 (-mMSCs, – SiMAG; days 3 and 7 respectively). Key anatomical structures are labelled in each image namely the meniscus (M), Femur (F), Synovium (S) and the Tibia (T) . Scale bar = 100μm.

Prussian Blue

Prussian blue staining was performed on joint sections to identify the location of SiMAG - labelled mMSCs. Prussian blue staining successfully revealed the presence of iron oxide particles (stained blue) within the synovium (marked x on the accompanying H&E section; Figure 5.23). These areas were found to overlap with the location of CM-DiI labelled mMSCs in the treated joints (right) of groups 1 (+ mMSCs, + SiMAG; day 3; Figure 5.23 Ai, ii) and 2 (+ mMSCs, + SiMAG; day 7; Figure 5.23 Bi, ii). Conversely, no blue staining was observed anywhere in the treated joint of group 3 (+ mMSCs, − SiMAG; day 3; Figure 5.23 C ii) and group 4 (+ mMSCs, − SiMAG; day 7; Figure 5.23 D ii); neither in any of the control joints (left joint Figure 5.23 E) in all groups.
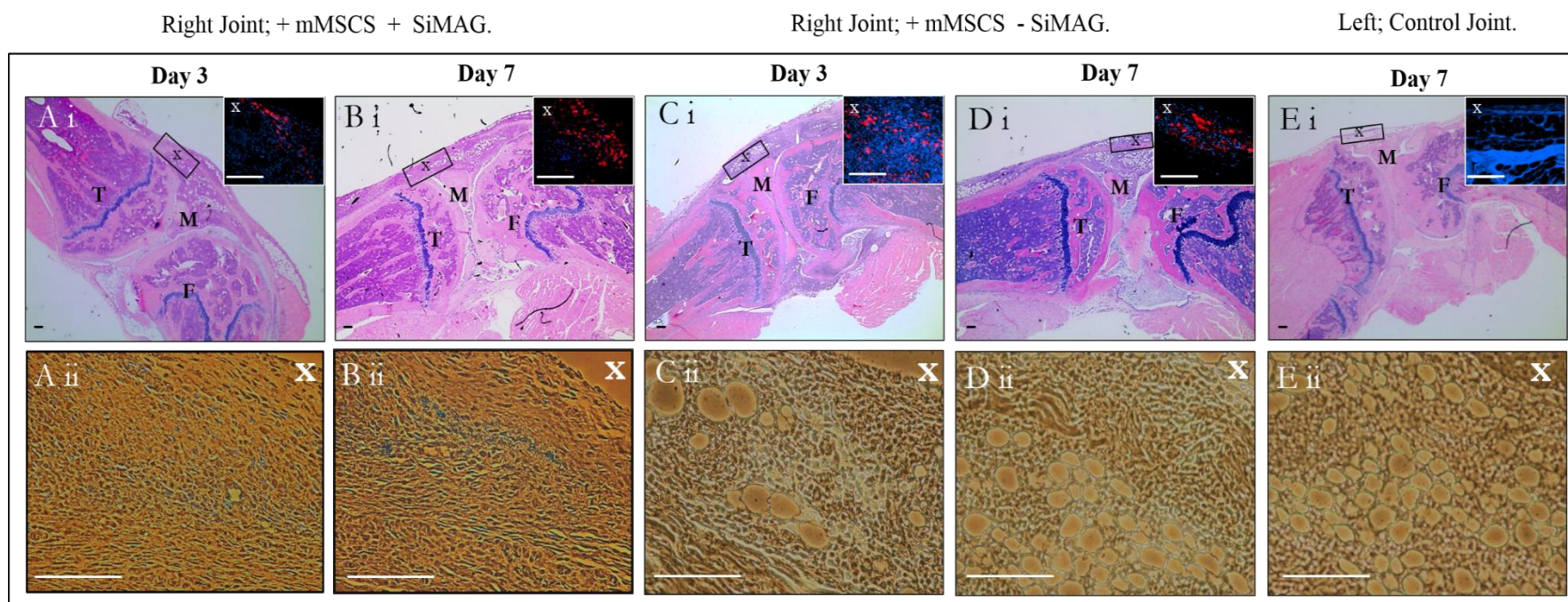
Figure 5.23. Prussian blue staining of joint sections with corresponding H&E and fluorescent sections. Blue staining highlights the presence of iron oxide particles (SiMAG) in the synovium of groups 1 (+ mMSCs, + SiMAG; day 3) and group 2 (+ mMSCs, + SiMAG; day 7) corresponding to the location of CM-DiI labelled mMSCs (X). No blue staining was detected for groups 3 (+ mMSCs, - SiMAG; day 7) and group 4 (+ mMSCs, - SiMAG; day 7), or for the control joint (left). (M) Meniscus, (T) Tibia and (F) Femur. Scale bar = 100μm

Toluidine Blue

Toluidine blue primarily stains acidic proteoglycans found in articular cartilage deep purple. Cartilage depletion is a key characteristic in the AIA model and is significant of proteoglycans losses on the articular surface. Therefore toluidine blue staining is an applicable stain to assess cartilage depletion in arthritis. Proteoglycan losses are depicted by a change in colour from a deeper blue to lighter blue. Proteoglycan loss is clearly visible in the treated (right) joint of control groups 5 and 6 receiving SFM (Figure 5.24 E, F arrow). No proteoglycan loss can be visualised in groups 1-4 receiving mMSC treatments at either day 3 or day 7 (Figure 5.24 A, B, C, D). As expected, the untreated left joint (Figure 5.24 G) for the same animals show no cartilage depletion.
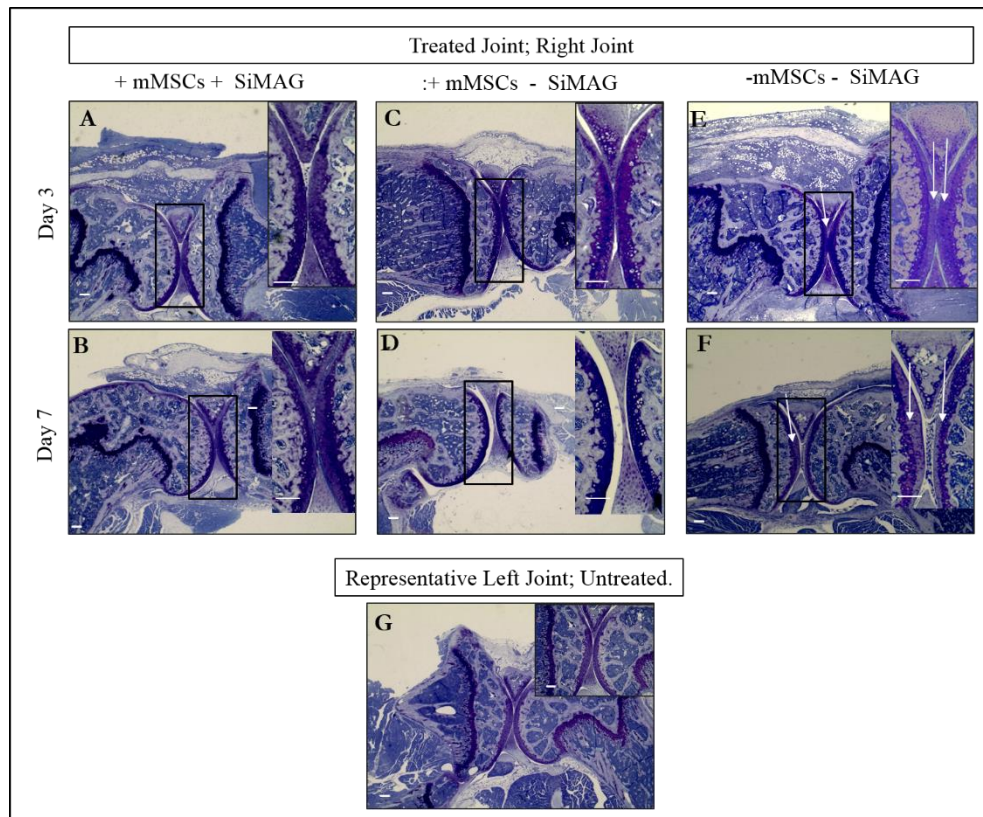
Figure 5.24. Toluidine staining to demonstrate cartilage depletion within treated joint sections for; A) group 1 (+ mMSCs, + SiMAG; day 3), B) group 2 (+ mMSCs, + SiMAG; day 7), C) group 3 (+ mMSCs, - SiMAG; day 3), D) group 4 (+ mMSCs, - SiMAG; day 7), E) group 5 (− mMSCs, - SiMAG; day 3), F) group 6 (− mMSCs, - SiMAG; day 3). G) Representative left untreated joint. Bars = 100 μm

5.3.3 OA model

5.3.3.1 *In vivo* Dose Response

Figure 5.25 illustrates the key features of a rat's hind leg when MR imaged. By comparing the sagittal MR images of the untreated (Figure 5.26 D) and the PBS treated joints (Figure 5.26 C) to all the treated joints (Figure 5.26 A (i,-iii), B (i-iii), obvious variations in hypointensities (exaggerated black marks) are clearly observed. The delivery of 1×10^6 mMSCs labelled with 5 and 10 µgFe/ml of SiMAG and 2×10^6 mMSCs labelled with 1, 5 and 10 µgFe/ml of SiMAG resulted in obvious hypointense areas of signal loss (circled in red, Figure 5.26 A (ii, iii), B (i-iii)) in the region of the synovial joint. However, less obvious areas of hypointensities could be identified in joints receiving 1×10^6 mMSCs labelled with 1 µgFe/ml of SiMAG (Figure 5.26 Ai). As expected, no hypointense regions observed in the control groups (untreated and PBS treated joints) when MR imaged (Figure 5.26 C&D). The visibility threshold in this system could therefore be set at a minimal cell dose of 1×10^6 (when labelled with 5 µgFe/ml) and minimal particle concentration of 1 µg Fe/ml (2×10^6 implanted cells).
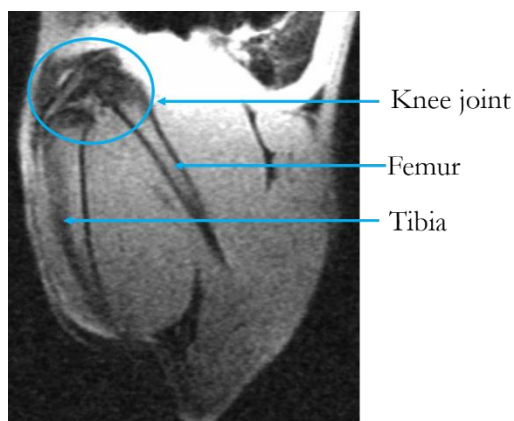
Figure 5.25. Sagittal MR image of a rat's hind leg highlighting key structural features.
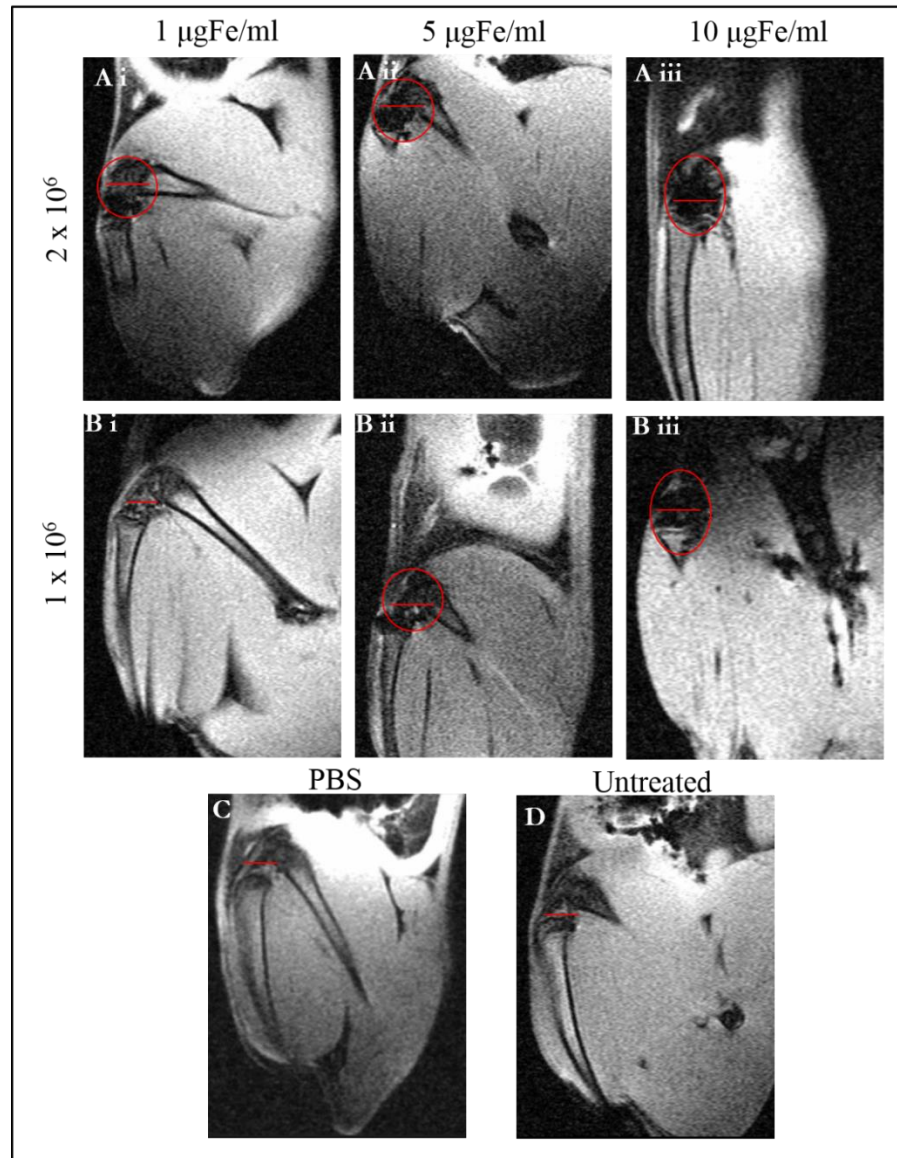
Figure 5.26. *In vivo* **dose response: Sagittal GEFI MR images relating to the implantation of: (A) 1x10^6 and (B) 2x10^6 mMSCs when labelled with: (i) 1 µgFe/ml, (ii) 5 µgFe/ml and (iii) 10 µgFe/ml SiMAG. Red circles highlight hypointense areas of signal loss. (C) PBS treated (D) Untreated. Red line highlights area across which SI was measured.**

Further assessment of the *in vivo* dose response was performed by analysing the signal profiles produced when 1x10^6 and 2x10^6 mMSCs labelled with 0, 1, 5 and 10 µgFe/ml SiMAG were injected within the synovial cavity of a rat (Figure 5.27). Similar signal profiles were generated for groups receiving 1x10^6 mMSCs labelled with 5 and 10 µgFe/ml SiMAG

(Figure 5.27 Bi, ii) and $2x10^6$ mMSCs labelled with 1, 5 and 10 µgFe/ml SiMAG (Figure 5.27 A (i-iii)) with no obvious variations between these groups. The signal profile generated when $1x10^6$ mMSCs were labelled with 1 µgFe/ml (Figure 5.27 B iii) was overall greater and similar to the control groups (Figure 5.27 C&D).
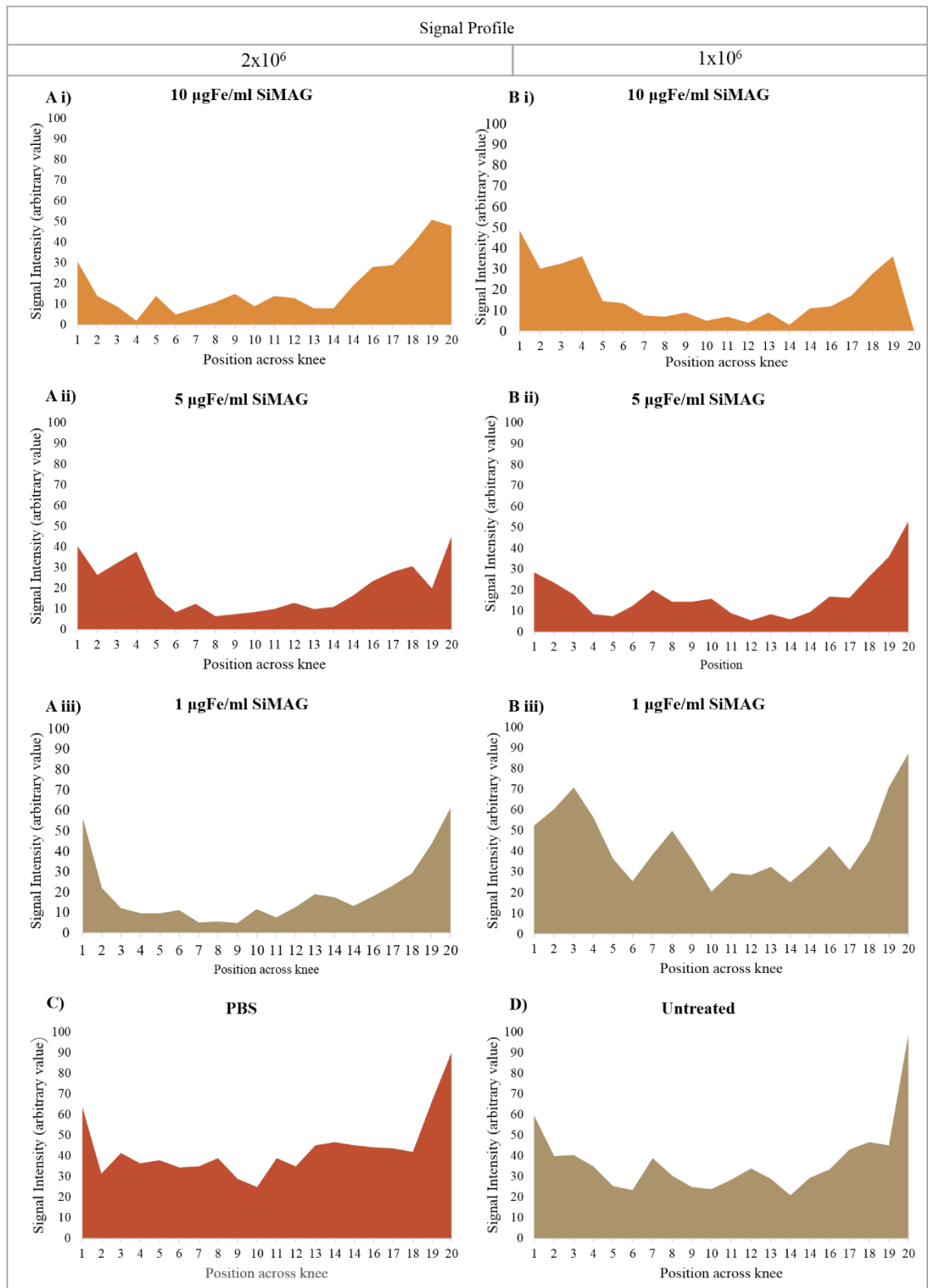
Figure 5.27. *In vivo* **dose response: Signal profiles generated by measuring signal intensity across 20 points of the rats knee when injected with: (A) 2x10^6 and (B) 1x10^6 mMSCs labelled with: (i) 10 µgF /ml, (ii) 5 µgFe/ml and (iii) 1 µgFe/ml SiMAG C) PBS and D) Untreated.**

5.3.3.2 Pain Perception

The perception of pain by osteoarthritic rats was assessed by monitoring the weight-bearing asymmetry (Figure 5.28 A) and the paw withdrawal threshold (as a measure of mechanical allodia) (Figure 5.28 B) for each rat. Following MNX surgery, rats developed a 16 % increase in weight-bearing asymmetry from the pre-surgery assessment on day 0 (pre-surgery) (+mMSCs, + SiMAG; 0.26 ± 2.89 %, +mMSCs, - SiMAG; 2.2 ± 2.30 %, -mMSCs, - SiMAG; -0.2 ± 1.84 %) to the pre implantation measurements on day 14 (+mMSCs, + SiMAG; 16.3 ± 5.70 %, + mMSCs, - SiMAG; 16.3 ± 1.17 % -mMSCs, - SiMAG; 16.29 ± 3.08 %) in all experimental groups 1-3. Rats receiving an intra-articular injection of SFM showed a gradual increase in weight-bearing asymmetry over the 29 days resulting in a final measurement of 19.50 ± 0.59 % (at day 42). Intra-articular injection of mMSCs (labelled with or without SiMAG) prevented any further increase in weight-bearing asymmetry resulting in a significant decrease in the weight-bearing asymmetry of SiMAG-labelled mMSC treated animals (group 1; 4.8 % decrease to 12.60 ± 4.80 % $p<0.05$) and unlabelled mMSCs (group 2; 8.7 % decrease, to 7.23 ± 4.25 % $p <0.001$) by day 29 when compared to SFM treated animals (19.50 ± 0.59 %).

Rats developed a decrease in paw withdrawal threshold in treated (L-left) (Figure 5.28 B) paws over 3 days directly following MNX surgery compared to pre-surgery baseline values at day 0 (mMSCs with and without SiMAG (L) 15 ± 0 g and no mMSCs and SiMAG (L) 13.75 ± 1.15 g). These trends persisted until day 14 at which point mMSCs were implanted (+mMSCs, + SiMAG; (L) 7.35 ± 1.76 g, +mMSCs, - SiMAG; (L) 7.75 ± 2.46 g, -mMSCs - SiMAG; (L) 6.65 ± 2.06 g). Intra-articular injection of SiMAG-labelled mMSCs resulted in no significant increase in the paw withdrawal threshold over 29 days (+mMSCs, + SiMAG; (L) 7.6 ± 3.60 g,) whereas a further significant decrease in paw withdrawal for unlabelled

MSCs and SFM was measured (+mMSCs, - SiMAG; (L) 3 ±0.57 g –mMSCs, - SiMAG; (L) 2.85 ± 0.67 g p<0.005).
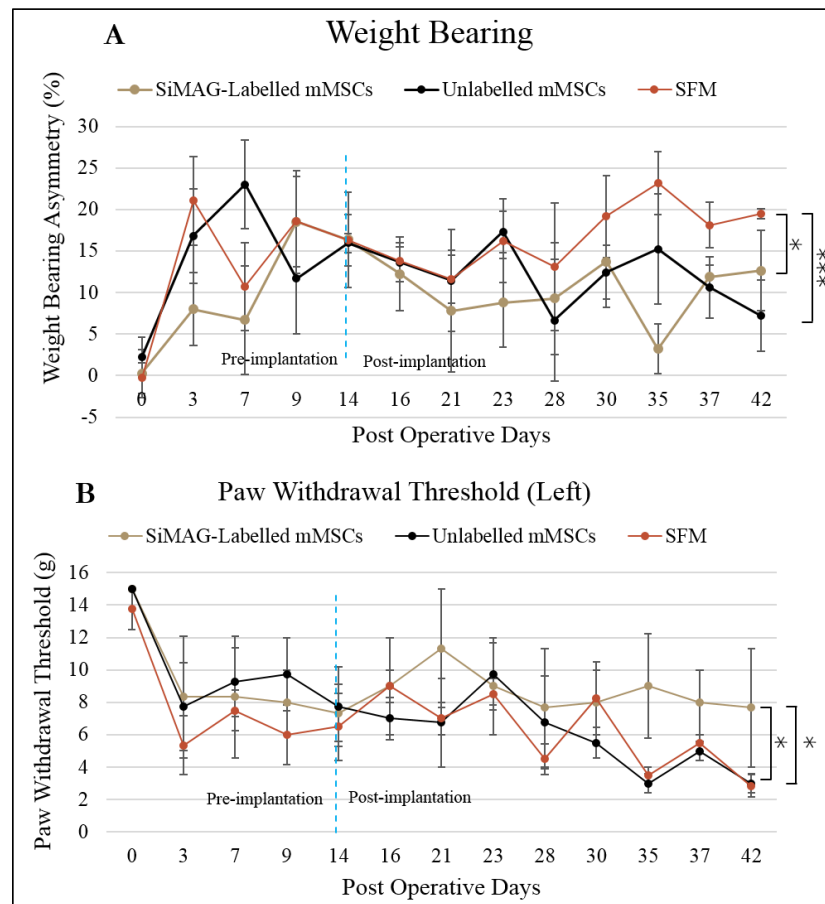
Figure 5.28. Pain assessment by monitoring the development of: (A) weight-bearing asymmetry and (B) mechanical paw withdrawal thresholds (Allodynia) in the MNX model of OA in response to the intra-articular implantation of SiMAG-labelled (10μl) (n=3) and unlabelled mMSCs (n=4) and serum free media (n=4) over 42 days. Data is expressed as mean ± SEM. Significant levels *** indicates p<0.001** Indicates p<0.01 and * indicates p<0.05.

5.3.3.3 *In vivo* Tracking – MRI

Increased areas of hypointensity are observed in the synovial cavity of each rat treated with SiMAG-labelled mMSCs (Group 1) 29 days post implantation (Figure 5.29 Bi). This

represents the presence of SiMAG and is further validated by the signal profile plots, (Figure 5.29 Ai) a significant loss in signal is detected over the synovial joint. As expected, this was not the case for rats in groups 2 (+ mMSCs, – SiMAG) & 3 (-mMSCs, –SiMAG) where MRI images (Figure 5.29 Bii & iii) and signal loss profiles (Figure 5.29 Aii and iii) generated appear to be similar in appearance to untreated joint (Figure 5.26 D) with the relatively high signal across the joint.
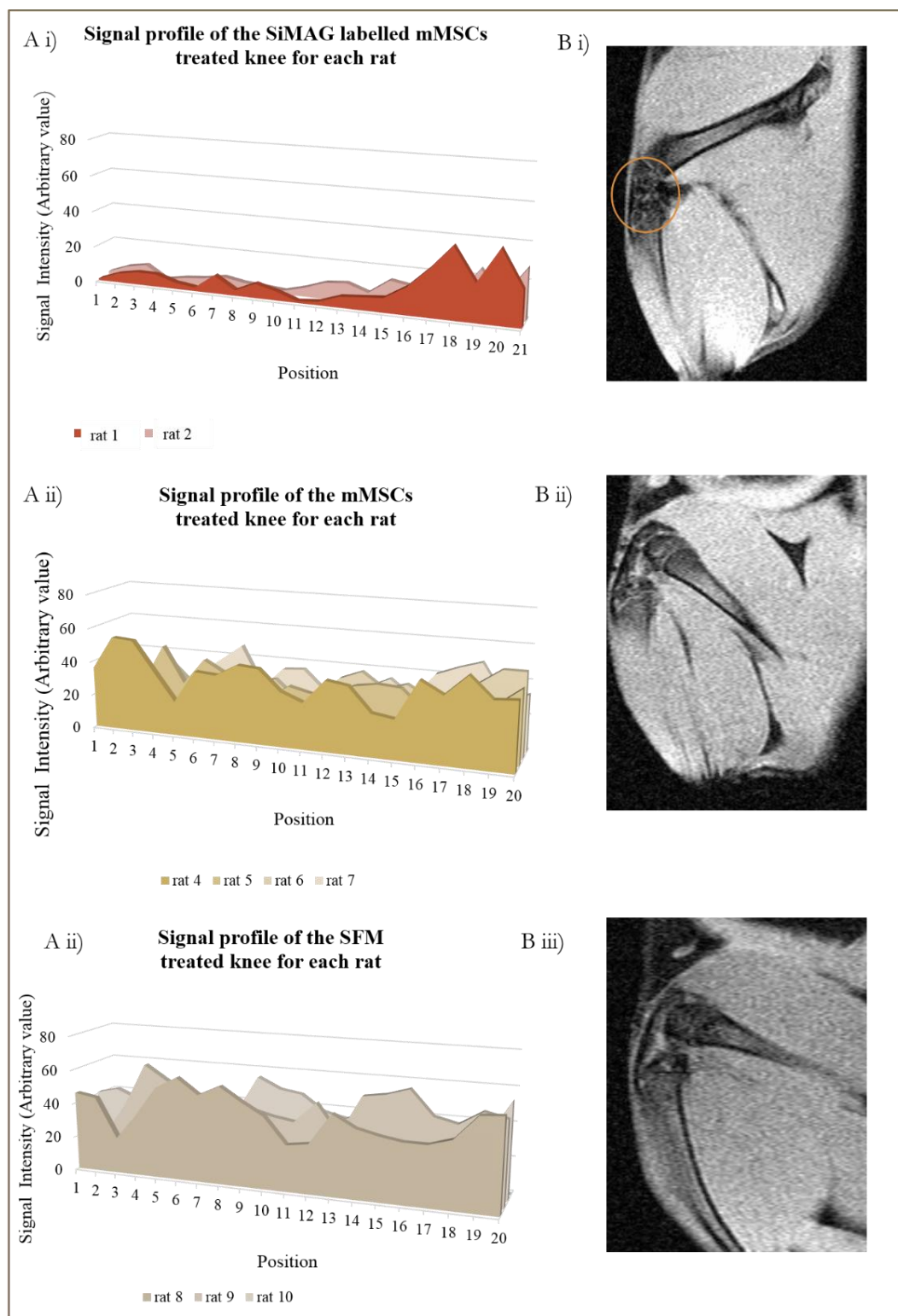
Figure 5.29. MRI tracking of mMSCs in a MNX rat model of OA 29 days post implantation. (A) Signal profile and (B) corresponding sagittal MSME MR images: (i) SiMAG-labelled mMSCs (10 μgFe/ml), (ii) unlabelled mMSCs and (iii) SFM.

5.3.3.4 Histological Evaluation

Hematoxylin and Eosin Stain (H&E) and Fluorescence (DAPI)

H&E staining was used to identify key structural features of the knee joint (rat) whilst identifying the location of fluorescent imaging (marked by X on H&E images) (Figure 5.30). DiI labelled mMSCs (stained red) were identified in the synovium in the treated (left) knee of animals in groups 1 (+mMSCs, + SiMAG) and 2 (+ mMSCs, – SiMAG), and can be seen in the fluorescent images (Figure 5.30 A & Biv) and corresponding H&E image (Figure 5.30 A & Bii, Marked as X). No labelled cells were visible in any of the untreated knees (right) (Figure 5.30 A, B & C iii) or in the treated knee of group 3 (+ mMSCs, + SiMAG) (Figure 5.30 C iv).
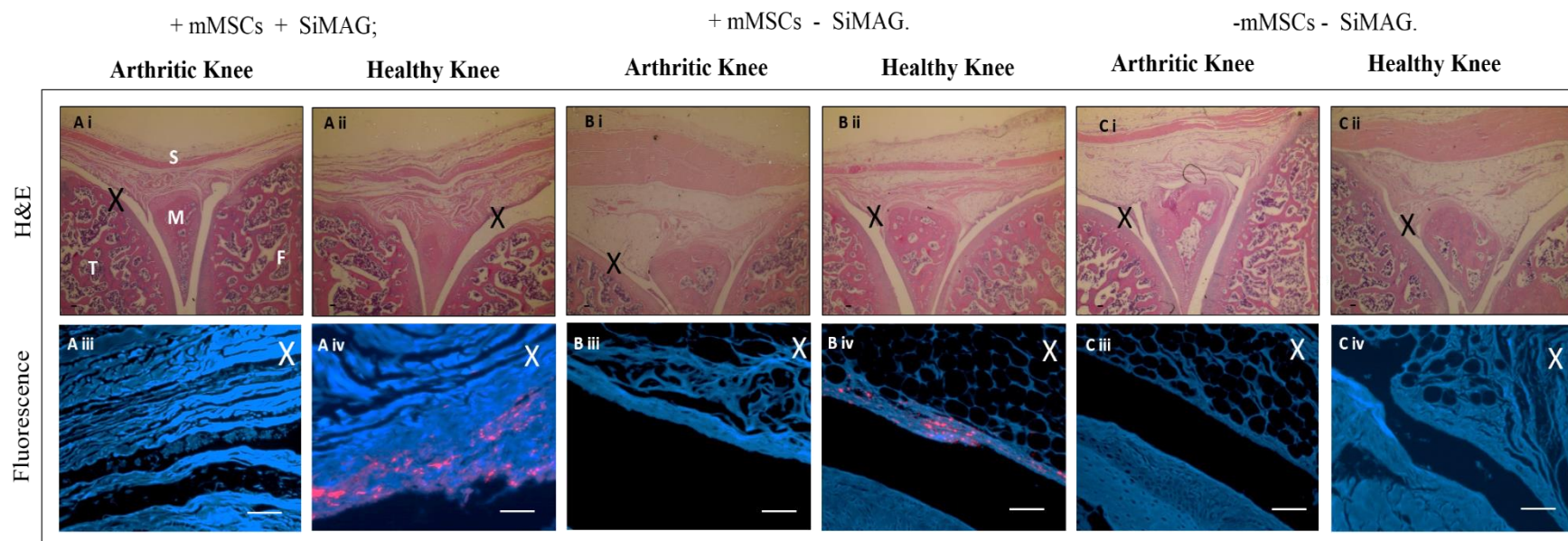
Figure 5.30. H&E and fluorescent stained sagittal sections of rat synovial joints for: (A) group 1 (+ mMSCs, + SiMAG; 3 days. n=3), B) group 2 (+ mMSCs, + SiMAG; 7 days. n=4), C) group 3 (+ mMSCs, - SiMAG; 3 days. n=4). Fluorescent images correspond to location marked X on H&E images. Nuclear material such as cells is depicted by dark purple staining while connective tissue such as collagen is stained pink in H&E staining. CM- DiI (red) and DAPI (blue). Left knees are the treated knees while the right knee was used as a control. Bars = 100μm

5.4 Discussion

Despite the extraordinary medical advances made to tackle RA and OA, these disease remain to be a significant burden on society today. Medicine has reached the point where pain and inflammation can be treated effectively. However, till now no cures for OA and RA have been developed where the damage made to the synovial joint can be reversed giving patients full function of their joint. The development of stem cell-based therapies however, aim to address this need and has the potential to challenge current gold standard treatments. MSCs in particular hold the most promise in achieving this goal. The use of enabling technologies such as those described in this thesis may be used to evaluate such therapies to assess risks and successes thereby enabling the clinical translation of such therapies. This chapter therefore aims to implement the established labelling protocol (1-10 µgFe/ml SiMAG, 24 hr passive incubation, serum free media) to track implanted murine MSCs in a mouse model of RA and also a rat model of OA with time whilst also assessing clinically relevant functional outcomes.

Previous chapters (chapter 3 and 4) have clearly demonstrated the ability of hMSCs and chondrocytes to passively and efficiently internalising SiMAG, (a commercially available 1 µm silica coated SPION) with labelled populations successfully creating dose dependant contrast when MR imaged using a Bruker 2.35 T animal scanner. This data has encouraged the progression from *in vitro* experiments to small animal *in vivo* tracking studies in order to explore the potential application of this strategy to track implanted cell populations in arthritic cell-based therapies.

The implementation of any SPION and MRI based tracking protocol to a new system (cell type and animal model), calls for the interaction between the cell type and the tracking agent (in this case SiMAG) to be evaluated. It is necessary to assess the effect of cell type on the labelling efficiency and consequent visibility threshold for the particular system as well as the effect of labelling on the cellular function (viability, proliferation and potency). Failing to run these preliminary experiments can impact on the full potential of the established imaging protocol and limit the therapeutic efficiency of the cells. Hence, a series of *in vitro* experiments were performed to assess the uptake of SiMAG by mMSCs and the subsequent effect of internalisation on hMSCs (cell viability, proliferation and potency).

Prussian blue staining successfully revealed the presence of SiMAG (stained blue) within the cell membrane of mMSCs labelled with 10 µgFe/ml (SiMAG), thus positively confirming internalisation with a total iron content of 20.64 ± 1.34 pg/cell. This value is comparable to the values detected for hMSC (21.8 ± 0.4 pg) and chondrocytes (20 ± 0.3 pg of Fe) in chapter 3 when labelled under similar conditions.

Toxicity and safety is a major concern in the implementation of nano-materials in any cell based therapy and can be a major hurdle in the adoption of SPION based tracking protocol (117). The application of SPIONs should in no way inhibit the therapeutic potential of the cells or should the SPIONs trigger any toxic events either on the cells during the labelling stage or evoke an immune response once implanted within the body (198). *In vitro* cell viability assays revealed no diminished cell viability and proliferation capacity on SiMAG-labelled mMSC populations implying the optimised dose and exposure period was not harmful. The *in vivo* toxicity of SiMAG was not investigated at this time but no abnormal behavioural or immune reactions were observed by any of the animals receiving SiMAG-labelled mMSCs over the duration of either studies. However, the *in vivo* toxicity should be strategically tested in longer term studies.

Currently, there is a debate regarding the differentiation ability of MSCs once they have been labelled with SPIONs (199). Generally, studies have found that the osteogenic and apidogenic potential of MSCs was maintained post SPION labelling whilst there are conflicting reviews reported for the differentiation of SPION labelled MSCs to chondrocytes (147, 199). Studies have shown that stem cells labelled with Feridex (an FDA approved contrast agent), inhibited their differentiation towards the chondrogenic lineage but not for osteogenic and adipogenic lineages (105, 143, 199). Kostura *et al* found that the presence of Feridex interfered with the signalling pathways responsible for driving chondrogenic differentiation (143). In contrast, Jasmin *et al* reported that MCSs labelled with Feridex underwent successful differentiation down all three lineages (adipogenesis, chondrogenesis and osteogenesis) (136). In a study by Henning *et al*, it was revealed that the differentiation of SPION-labelled MSCs to chondrocytes was dependant of the dose of the particle which may explain the contrasting results (147). Henning *et al*, also suggested that the use of a transfection agent could mitigate this effect by encouraging the internalisation of particles via alternative mechanism and further compartmentalization which might cause less interaction with differentiation associated intracellular substrates (147). In this study, it was not possible to demonstrate the differentiation of BALB/c mMSCs to chondrocytes labelled either with or without SiMAG. In a study by Chamberlain *et al*. BALB/c derived mMSCs were shown to differentiate down osteogenic and adipogenic, but not chondrogenic, lineages (175). It may therefore be the case that a lack of chondrogenic potential does not stem from the presence of SiMAG but to properties of the cells themselves. Importantly, we have shown that mMSCs labelled with 10 μgFe/ml of SiMAG retain their capability to successfully differentiate down osteogenic and adipogenic lineages.

A key aspect of using SPIONs in this context involves establishing and optimising minimal doses which achieve best resolution and contrast. Investigating the minimal *in vitro* MRI

visibility thresholds in terms of particle concentration and cell number offers some insight as to the optimal doses to be used in subsequent tracking studies. *In vitro* MRI threshold assessment resulted in a minimal cell dose of 10^5 mMSCs when labelled with 10 μgFe/ml SiMAG and a minimal SiMAG concentration of 5 μgFe/ml with $3x10^5$ labelled mMSCs. These are considered highly acceptable values as similar studies by Jing *et al* reported a minimal cell dose ($5x10^5$) MSCs when labelled with 25 μgFe/ml of Feridex aided by the transfection agent protamine sulphate (83). This implies that SiMAG labelling offers potentially greater resolution and higher sensitivity in tracking studies. Based on this set of results and supported by current literature where therapeutic doses of MSCs ranging from $3x10^5 - 10^6$ have been implemented with successful outcomes in similar RA studies (218, 219), $3x10^5$ SiMAG-labelled MSCs were carried forward to the RA mouse tracking study. With regards to the OA model, positive therapeutic effects have previously been reported with much higher MSC doses ranging from $1x10^6$ to $10 x10^6$ (31, 215, 220). Therefore, cell doses at the lower end of this range ($1x10^6$ and $2x10^6$) were chosen for the OA study in an effort to mitigate the effects of excessive accumulated Fe content associated with higher cell doses in MR imaging such as the blooming effect. The magnetic susceptibility of an individual particle results in a blooming artefact which extends beyond the size of the individual particles allowing for small injections of particles to be amplified beyond the actual location. This makes for practical identification of implanted cells but consequently becomes challenging to assess anatomical features in that vicinity (152, 155).

Detection thresholds and cell doses were consequently validated *in vivo* for both the mouse model and rat model. In this study, $3x10^5$ mMSCs labelled with 1, 5, 10 μgFe/ml SiMAG were implanted within mouse joints, whereas $1x10^6$ and $2x10^6$ mMSCs labelled with 1, 5, 10 μgFe/ml SiMAG were implanted within a rat joint. To my knowledge similar studies have not assessed the effect of the *in vivo* biological environment on the MRI visibility threshold

prior to *in vivo* tracking studies. It is important to understand that the surrounding tissues can affect the MR contrast and therefore influence the visibility threshold. Unfortunately, relaxivity measurements could not be taken due to the inhomogeneities associated with biological tissue and for this reason, the signal intensity across the hypointense regions of the knee were read, plotted and compared to each other and untreated joints. Mice injected with mMSCs labelled with SiMAG (5 and 10 μgFe/ml) revealed a significant loss in signal over a substantial area; however, this signal loss was experienced over a greater area in the mice injected with 10 μgFe/ml than in 5 μgFe/ml. A less obvious drop in signal intensity was observed for mice injected with 1 μgFe/ml when compared to the control mouse. This revealed that the minimal visibility threshold for the mouse model was therefore $3x10^5$ cells labelled with 5 μgFe/ml. Resultant signal loss profiles of the rat assessment appeared similar in form with a significant signal loss (attributed to the presence of SiMAG) when $1x10^6$ SiMAG-labelled mMSCs (5 & 10 μgFe/ml) and $2x10^6$ SiMAG-labelled mMSCs (1, 5 & 10 μgFe/ml of SiMAG) were implanted within the synovial cavity of a rat. This implied that either one of the mentioned conditions would be suitable for implementation in the OA tracking study.

SiMAG concentration appeared to have a greater influence on the signal profiles created within the mouse model as opposed to the rat model where less variations was detected in the signal profiles in response to varying cell dose and SiMAG concentration. This is likely due to overall greater accumulated Fe content in the rat model causing the blooming to saturate at $1x10^6$ mMSCs (5 μgFe/ml). Given the prolonged duration of the OA rat study and the unknown *in vivo* dilution rate of SiMAG-labelled mMSCs, it was decided that $1.5x10^6$ mMSCs labelled with 10 μgFe/ml would be implemented. This assumes that particle labelled cells would still be visible even after a hypothetical 10 fold dilution which is a reasonable rate after 4 weeks (97).

Generally, MRI images associated with the rat study resulted in greater anatomical details of the area of interest (knee) in comparison to the mouse where only whole body images were possible. This was expected and is a direct consequence of the overall larger size of the rat in comparison to the mouse; an observation also made by Burtea *et al* highlighting the general preferential use of rats in small animal MRI tracking studies for this reason (159). As mentioned earlier, the presence of a SPION are amplified beyond their exact location, a phenomenon known as the blooming effect. Although the blooming effect can be a useful means of identifying the general location of implanted cells, it makes it difficult to specifically identify the exact location of the cells with relation to the rest of the anatomical features of the knee. This was particularly evident in this study and in tracking within the knee in general given the complexity of the knee joint. The application of a purposely designed MRI knee transmitter coil (similar to those routinely used clinically in the diagnosis of knee pathology (130) in this system would have allowed for better resolution and sensitivity allowing for greater anatomical features in conjunction with particle location particularly in the rat (130, 158). Alternatively higher field strength MRI scanners (4.7, 7, 11.7T) could have also improve image resolution (159) however these scanners are limited to research applications and therefore do not translate well into clinic.

The chosen OA and RA animal models have been shown to develop similar pathology to human disease and is thus suitable for predicating the efficacy and appropriateness of MSC therapy in humans (213). It must be noted that the rodent version of this disease progresses at a faster rate than that of the human version (212). The chosen duration of the RA tracking study is significant in terms of the acute nature of joint swelling. Based on unpublished studies by Kehoe *et al*, MSC treatment was found to have the greatest effect on joint swelling in the first 3-7 days in a study monitoring joint swelling over 28 days. This suggests that cells are most active within this time frame and for this reason implemented in this short

term tracking study. These time points comply with the current literature where SPION – labelled cells could be detect with similar arthritic cell based MR tracking studies as long as 12 weeks post implantation (101, 184).

MR imaging revealed the presence of SiMAG-labelled cells which were identified within the synovial joint up to 7 days post implantation in the mouse model of RA and 29 days post implantation in the rat model of OA. The exact location of SiMAG-labelled and unlabelled cells was further verified via histological analysis where Dill-labelled cells were clearly identified along the synovial lining in both studies at the final time point (7 day; mouse RA, 29 days; rat OA) in the treated knees of all groups receiving MSC treatment. No integration with the articular cartilage was observed. Henning *et al* successfully detected the transplanted hMSCs (SPION labelled and unlabelled) within the defect site over 12 weeks by MRI (184). Similar results were found in the study by Chen *et al* where the implantation of autologous chondrocyte seeded onto a collagen II hydrogel into a surgically induced defect (mini-pig) resulted in the persistence of hypointense signal voids up to 12 week post-surgery within the defect. This implies that the cells had remained within the defect and was later confirmed by histology (101). The use of biological scaffolds may account for the conflicting engraftment sites of the cells with the scaffold acting to localise transplanted cells within the defect site. This theory is supported by work carried by Murphy *et al* where evidence of cell engraftment in several tissues (synovial capsule, fat pad, and lateral meniscus) in the joint were observed while no cell engraftment in the cartilage was observed post intra-articular implantation of MSCs (scaffold free) in an MNX model of OA in goats (31).

This study was able to link the presence of mMSCs (SiMAG-labelled and unlabelled) within the synovium to the various clinically relevant functional outcomes; pain and inflammation. Pain is caused by multiple mechanisms and results in increased nociceptive inputs via

various pain processing pathways linked to the peripheral or central nervous system (40, 211). In this study, progression in pain was monitored by weight bearing asymmetry and paw withdrawal evaluations and are commonly implemented the evaluation of pharmaceutical interventions in pain research. Weight bearing asymmetry is a standard behavioural correlate of hyperalgesia (increased sensitivity to pain) and is believed be initiated from the peripheral system (40). Paw withdrawal threshold on the other hand is indicative of mechanical allodeniya (pain due to a stimulus which does not normally provoke pain) and is associated with pain stemming from the central nervous system (40)

Prior to OA induction, animals are able to place equal force on each hind leg when standing i.e it can be said that animal have little variation their weight bearing asymmetry. With OA induction in one leg, more force will naturally be place on the healthy leg as opposed to the injured leg which is experiencing pain. therefore there is an increase in the difference in force placed between each leg i.e increase in weight bearing asymmetry. This trend was clearly observed in this study where weight bearing asymmetry significantly increased upon OA induction and is indicative of pain. The administration of mMSCs (SiMAG labelled and unlabelled) was seen to mitigate the development of weight bearing asymmetry in rats with established OA. This implies that upon MSCs administration, rats were able to more evenly distribute their weight over both legs, significant of alleviated pain.

Mechanical allodynia describes a scenario whereby pain is initiated by a stimulus what would not normally provoke pain. In healthy animals (Pre-OA induction) a large localised force would need to be implemented on the hind leg of the rat to provoke the withdrawal of their paw as a result of the stimulus. Upon OA induction, rats become more sensitive to this pain and therefore, low forces are required to generate a result. There was no effect of unlabelled mMSC (unlabelled) on the development of mechanical Allodynia while the

administration of SiMAG labelled mMSCs appeared to significantly influence the progression of mechanical allodynia.

Collectively, this set of data indicates that the administration of MSCs may be able to alter peripherally-driven pain, but possibly not centrally-mediated pain in established OA. Finally, this data may offer insights into the mechanisms of underlying pain in OA.

The effects of MSC treatment on inflammation in RA were monitored by assessing acute inflammation (macrophage, lymphocyte and neutrophil infiltration) in terms of joint swelling (99, 213). As expected, a significant decrease in joint swelling was measured upon mMSC administration. In a similar way the administration of SiMAG-labelled mMSC also resulted in a significant decrease in joint swelling with no statistical difference between mMSC groups. This suggests that the immunomodulating properties of mMSC labelled with SiMAG was maintained. Biological variation between mice within groups accounted for the conflicting rates of joint swelling progression between the two studies where a significant drop in joint swelling found on day 2 for the 3 day study, but only on day 3 for the 7 day study.

Toluidine blue staining demonstrated far less cartilage depletion in groups receiving either SiMAG-labelled or unlabelled mMSC when compared to control groups. This suggests that the therapeutic potential of mMSCs is not affected by SiMAG-labelling. Although the mechanism of action is unknown, it can be hypothesised that the implanted cells are not differentiating into chondrocytes and repopulating the damaged area as no fluorescently labelled cells could be detected within the articular cartilage (corroborating findings by *Kehoe et al).* This suggests that mechanism of repair is attributed to a paracrine effect whereby the early MSC treatment acts to prevent proteoglycan loss possibly via the secretion

of factors influencing the activity of ADAMTS enzyme, an enzyme responsible for the cleaving of aggrecan (an abundant proteoglycan in articular cartilage) (221)

The presence of SiMAG particles within the synovial lining was identified via Prussian blue staining at 7 days in the RA study. It is difficult to ascertain whether this staining was related to internalised SiMAG-labelled cells or to the particle dilution effect at this point. Particle dilution refers to the loss of particle from labelled cells as a result of either exocytosis or the division and proliferation of implanted cells. Released particles may then either be removed by the reticuloendothelial system (159) or taken up neighbouring cells (97). This effectively limits the extent of tracking introducing the concerns of false positive where particles are being tracked instead of the cells. This becomes an increasing concern with longer tracking studies as is the case rat OA and warrants further investigations. (97).

5.5 Conclusion

This chapter confirms the potential application of SiMAG as a feasible tracking agent in cell based therapies. *In vivo* MRI scans demonstrated good contrast and the identification of SiMAG-labelled populations within the synovial joint up to 7 days (mouse study) and 29 days (rat OA) post implantation. Furthermore, it has been demonstrated that the presence of SiMAG does not affect the therapeutic potential of mMSCs when applied in small animal *in vivo* studies. The presence of mMSCs (SiMAG-labelled or unlabelled) resulted in a marked decrease joint swelling over 7 days in the RA tracking study implying that SiMAG-labelled mMSCs maintained their anti-inflammatory and immunosuppressive property. Finally for the first time we demonstrate the potential antinociceptive properties of mMSCs as shown in the rat OA study.

Chapter 6

Discussion, Future Work and

Concluding Remarks

6.1 Overriding Discussion

In response to the lack of effective osteoarthritis and rheumatoid arthritis treatments, cell-therapies have been developed offering new opportunities in tackling these diseases. Mesenchymal stem cells have been identified as ideal candidates in the development of arthritic cell-based therapies. Their specific self-renewal, multipotent differentiation ability, migratory, anti-inflammatory and immunosuppresssive properties are all key characteristics linked to their success in stem cell based therapies (6, 68, 76, 79, 222). Animal models are a vital aspect in the development of these cell-based therapies and are implemented to investigate the safety and efficacy of such therapies. The need to rapidly, practically and reproducibly assess optimal delivery routes, cell doses, tissue engraftment and cellular bio-distribution patterns whilst also minimising the number of animals implemented has driven the need for non-invasive techniques of monitoring *in vivo* cell fate. The combined use of Magnetic Resonance Imaging (MRI) and superparamagnetic iron oxide nanoparticles (SPIONs) have been proposed as one such non-invasive strategy. Therefore, this project has sought to develop a MRI and SPION based imaging strategy to potentially evaluate the success and risks of arthritic cell-based therapies whilst monitoring clinically relevant functional outcomes (pain and inflammation). This thesis is the first to report the use of SPIONs and MRI to track implanted MSCs within an AIA mouse model while monitoring joint swelling as an indication of inflammation. Furthermore, this thesis is the first to investigate the antinociceptive properties of MSCs in addition to tracking implanted cells within an MNX rat model of OA.

Four commercially available SPIONs ranging in size from 25 nm-1000 nm (P904, Nanomag, Lumirem and SiMAG) were investigated as potential labelling agents for the application of

hMSCs and chondrocytes, in arthritic cell based therapies. Although, it is understood that passive incubation methods are limited to cells with a high degree of phagocytosis (a property not generally exhibited by stem cells), this technique was preferred over transfection agent (TA) mediated labelling due to the complications associated with TA labelling and limited clinical prospects. Following a passive incubation period of 24 hrs, greatest intracellular Fe content was detected for SiMAG (the largest particle; 1000 nm) when internalised by hMSCs or chondrocyte under serum free conditions, specifically. In comparison, significantly lower amount of Fe was detected for Lumirem, Nanomag and P904. By analysing this data one could assume a size dependant uptake of SPION by hMSCs, in particular with the following trend which was revealed (SiMAG; 1000 nm 21.8 pg/cell > Lumirem; 300 nm, 4.8 pg/cell > Nanomag; 50 nm 1.05 pg/cell > P904; 25nm 0.65 pg/cell). However, it cannot be assumed that these results follow a size dependant uptake relationship when assessing the uptake of particles of varying sizes by Fe quantification, due to variation in the Fe content of a single particle with varying particle size. Generally, the Fe content of a particle increases with increasing size (103, 161). This justifies the significantly higher Fe content of SiMAG–labelled cells (hMSCs and chondrocytes) in comparison to other SPIONs (Lumirem, Nanomag and P904) suggesting that this result is not related to the size dependant uptake of SPION.

Despite the extensive number of cell labelling studies that have been performed with SPIONs of varying sizes, it is still unclear as to which particle size facilitates most efficient internalisation by stem cells. This is partially attributed to the limited particle configurations investigated in studies where contributing factors such as surface coating, surface charge and cell type are not taken into account. Further complications include data generated by using TA where the effect is seen to be dose dependant in addition to TA type dependant. Few studies have systematically investigated the size dependant uptake of particles as

demonstrated by Thorek and colleagues (194). In their study, the cellular uptake of SPIONs of varying sizes (33 nm - 1.5 μm) by non-phagocytic T cells was systematically evaluated. Efficient labelling of cells was observed for particles up to 300 nm; however, micron-sized particle uptake was limited (194). A review by Li *et al* further suggested that particles sizes less than 100 nm were generally preferred for cell uptake, whilst positively charged surfaces further encouraged internalisation. This may be due to the electrostatic interactions between the positively charged particles and the negatively charged cell membrane (8). In summary, it can be deciphered that particle uptake by cells must be evaluated in a case to case manner and according to the desired application. For applications in cell imaging and tracking there is an interest in particles that can be internalised in sufficient quantities, generating significant contrast when MR imaged.

The ideal particle size range for cell tracking purposes has further been debated (97, 160, 194). Contrast is dependent on total intracellular Fe content post labelling. The Fe content of a single particle is thought to increase with increasing particle size, subsequently causing an increase in magnetic moment (103, 161). Although reports have highlighted the efficient uptake of nano-sized particles (< 300 nm), particle of this size range often have relatively low Fe content in comparison to their larger (micron-sized) counterparts. This in turn, demands the internalisation of many more nanometre sized particles than would be required of larger micron-size particles. This calls for a highly efficient and robust labelling protocol with higher particle concentrations often requiring the use of TA for the labelling of stem cells with nano-sized particles in order to achieve quantities that will generate *in vivo* contrast by MRI (160). On the other hand, larger micro-sized particles may not necessarily facilitate better uptake (194) in non-phagocytic cells but the higher Fe content of each particle implies that few particles would need to be taken up (ideal for cells with a low degree of phagocytosis) in order to generate contrast by MRI. This argument is clearly demonstrated in literature.

Passive incubation methods have not demonstrated the significant *in vitro* internalisation of popular FDA approved particles; Endorem, Resovist and Feraheme (20 nm-150 nm) by non-phagocytic stem cells in sufficient quantities to generate satisfactory *in vivo* contrast, thus relying on the use of TA. This has been observed repeatedly through a wide range of studies (107, 188, 223). In comparison, studies by Hinds *et al* , Shapiro *et al* and Saldanha *et al* for example have all demonstrated the non-transfection mediated uptake of micron-sized particles at realistic doses to generate significant contrast *in vivo* (103, 160, 186). Understandably, the clinical approval of FDA approved particles is highly attractive. However, the need for transfection agents in my opinion questions the potential clinical applicability of using such labelling strategies.

Our findings have demonstrated that exclusively SiMAG (a micron sized particle) was internalised in significant quantities by both hMSCs and chondrocytes to develop dose dependant contrast when MR imaged using a 2.35T MRI scanner under these labelling conditions. It is essential to establish MRI visibility thresholds in terms of particle concentration and cell number, both *in vitro* and *in vivo* and to appreciate that the detection threshold is affected by magnetic field strength and MRI acquisition parameters (152). The overall detection threshold of a population of cells is dependent on the combination of intracellular Fe content and the number of cells. The detection thresholds of SiMAG-labelled cells within this system was set at 5 μgFe/ml (5×10^5 labelled cells) in terms of minimum particle concentration and 10^5 cells (10 μgFe/ml) in terms of cell dose. This demonstrates the relationship between labelling concentration and cell dose. The lower the labelling concentration, the more cells are required for detection.

MRI scanner strength significantly influences resolution and contrast, not only defining MRI detection threshold but also defining the quality of images and the extent to which information can be gathered. In general, higher strength scanners (similar to those used in

research; 4.7, 7 and 11.7 T) offer better contrast, resolution and specificity (130). These are all highly attractive qualities in the evaluation of cellular therapies *in vivo*. For example, single hepatocytes have been reportedly to be imaged by Shapiro *et al* and could be detected in the liver one month post implantation using a 7 T scanner (161). Hinds *et al* also successfully managed to image a single cell labelled with 900 nm SPION with 11.7 T scanner (186). However, it is difficult to achieve such resolution on clinical grade scanners (1.5 T, 3 T). To my knowledge, only one group has succeeded in achieving single SPION-labelled cell detection on clinical systems (1.5 and 3 T). In achieving this, elaborate theoretical models were applied pre-imaging, in order to extensively modify standard pulse sequences in addition to building customised gradients and RF coils required to achieve such resolution (202, 224). Therefore, it is unrealistic to design pre-clinical tracking approaches to high strength scanners knowing that such resolution will not be achieved under standard conditions. To this end, we have optimised towards current clinical MRI modalities commonly found in hospitals which are 1.5 T and 3 T scanners.

We have adopted two relevant models of arthritis to evaluate the feasibility of the developed labelling and tracking strategy (SiMAG; Bruker 2.35T MRI) to evaluate arthritic cell based therapies in the future. In addition, we sought to assess the effects of mMSC administration on the clinically relevant functional outcomes (pain and inflammation) and ensure that SiMAG-labelling of mMSCs does not impair their therapeutic potential *in vivo*. MRI and SPION based technologies offer a practical and non-invasive means of gathering data linked to the success and risks of cell based therapies. Although most published studies remain as proof-of concept studies, mainly optimising *in vitro* labelling and detection threshold; few cell based tracking studies have managed to offer conclusive data of migratory patterns and tissue integration within the knee over time, with reliance on histology. In particular, a successful case of cell tracking within an osteoarthritic joint was demonstrated by Jing *et al*,

where serial MRI imaging over 12 weeks highlighted hypointensity associated with MSC implantation within synovial fluid (one hour) post implantation using T_2 weighted sequences. Hypointensity persisted within the synovial fluid for 2 weeks until significant signal changes were detected within the defect and intensified over the next 4 weeks, implying that the implanted SPION-labelled cells had migrated towards the defect site and repopulated the defect. This data was further cross-validated by histological evaluation (83), which highlighted the potential of such tracking techniques in non-invasively monitoring cell migration *in vivo*. A key aspect of gathering information on the cellular bio-distribution and tissue integration is serial and longitudinal imaging of the same animal. This requires access to an MRI suite linked to the animal house to allow for animals to be anesthetised prior to being MR imaged facilitating imaging at multiple time points throughout the study. Unfortunately, this was not possible in our studies as the MRI suite and the animal houses were situated in different universities (MRI; Nottingham Trent University, Mice; Liverpool John Moors University; Rat; Nottingham University). Consequently, serial imaging could not be performed. This is a significant limitation of the studies presented in this thesis as migratory patterns and tissue integration with time could not be assessed.

Good contrast of implanted cell population was demonstrated for both models over 7 days in the RA mouse model and 29 days in the OA rat model when MR imaged. The intracellular Fe disturbs the local magnetic field thus allowing cells to be visualised as negative contrast or lack of signal when MR imaged (103, 104, 106, 152, 155, 199, 225). The generation of negative contrast by SPIONs is particularly hindering in cell tracking as it becomes difficult to discriminate between labelled cells presented as dark exaggerated marks and artefacts such as air. In addition, it is also difficult to quantify the effect of particle concentration on the extent of signal loss as the signal cannot be quantified below 0, where particles cannot be unambiguously distinguished from background (97, 135). Bulte *et al* suggested the

application of a specific "white marker" pulse sequence which would allow SPIONs to be detected and quantified as a positive contrast (97).

The question of particle dilution becomes a concern particularly in the long term OA model. Particle dilution is an inherent limitation of all SPION and MRI based tracking in cell-based therapies. This defines the loss of the particle labelled cells by either exocytosis or by cell division beyond detectable levels. Released particles may be taken up by neighbouring cells or phagocytosed by macrophages. In general, small particles are thought to be exocytosed more efficiently than larger micro-sized particles. However, larger particles are more efficiently taken up by macrophages and removed (159). This may introduce false positives where released particles (either taken up my neighbouring cells, macrophages or freely moving) are tracked instead of the cells, further limiting the reliability of long term tracking studies. In an *in vivo* study by Baligand *et al* , the label was visible in tissues for 3 months apparently overestimating cell survival by more than 1 week (226). Berman *et al* suggested that particle dilution was an indication of viable cells, as non-viable cells retained the particle due to the inability to actively exocytose (227). However, distinguishing between live cells, pre-particle loss, released particles and non-viable cells retaining particles is impossible at this stage. Furthermore, gathering conclusive data on cell viability, cell activity and the differentiation state of cells post labelling is impossible highlighting an additional limitation of applying such tracking techniques (95). Overcoming such limitations may require the development and implementation of novel particles. Nonetheless, cell viability may be indirectly assessed by evaluating the effects of implanted cells in terms of functional outcomes over time as presented in this thesis. The positive joint swelling and weight bearing asymmetry results imply that cells are active in their role of secreting biological factors responsible for reducing joint swelling and minimising pain. Importantly, SiMAG labelling did not influence the effects of MSCs on joint swelling or weight bearing asymmetry.

6.2 Future Work

This thesis has investigated the potential of four commercially available superparamagnetic iron oxide nanoparticles as likely labelling agents in MRI mediated cell tracking. Of the four particles, only SiMAG was deemed suitable given the potential to be internalised under passive incubation conditions, generate contrast at relevant cell doses on clinical MRI systems over a 29 day period with no impaired biological functions. Given the opportunity, the potential of the other three particles would be more closely evaluated to determine if higher particle concentrations would have facilitated better contrast when MR imaged. Furthermore, in terms of tracking studies, pre-implantation images would be taken of every animal and subsequently imaged at multiple time points to allow not only the migratory patterns and tissue integration to be evaluated, but to more closely link the location of cells with measurable functional outcomes such as pain and inflammation. For this to be possible it is necessary to fabricate a knee coil for all subsequent experiment. This ensures that images of better resolution would be obtained allowing the location of cells to be more precisely evaluated in relation to anatomical structures whilst analysing tissue repair. This has been difficult to achieve in this particular study due to the anatomical dimension of rats and in particular mice. Ideally, future experiments would be performed on larger animals such as pigs or goats where the larger joint dimension would facilitate greater anatomical detail. Furthermore, greater emphasis would be placed on the clinical success of MSC administration in terms of disease progression and tissue repair. Finally, the *in vitro* and *in vivo* degradation rates of SiMAG would be closely evaluated to assess important aspect such as long term tracking potential, physicochemical properties and toxicity.

6.3 Concluding Remarks

The data presented in this thesis introduces the application of SiMAG (a 1 μm superparamagnetic iron oxide nanoparticle) as a possible tracking agent in arthritic cell-based therapies. The labelling protocol has been established as the passive incubation of 1-10 μgFe/ml SiMAG under serum free conditions for 24 hrs and has been validated for hMSCs and chondrocytes. Referring to the list presented in Chapter 3 (Figure 3.2) defining the pre-perquisites for an *in vivo* cell tracking agent, we can conclude that SiMAG largely meets these criteria. Furthermore, the application of a mouse model of RA and a rat model of OA demonstrates the potential to detect implanted cell population over a 29 day period using a 2.35T animal MRI scanner. Overall, the proposed labelling and imaging strategy lays the foundation for further developments and holds great potential in monitoring the success and risks not only arthritic cell-based therapies but cell-therapies in general.

References

1.   Mason C, Dunnill P. A brief definition of regenerative medicine. Regenerative Medicine. 2008 Jan;3(1):1-5. PubMed PMID: WOS:000252370900001.

2.   Takahashi K, Yamanaka S. Induction of Pluripotent Stem Cells from Mouse Embryonic and Adult Fibroblast Cultures by Defined Factors. Cell. 2006;126(4):663-76.

3.   Macchiarini P, Jungebluth P, Go T, Asnaghi MA, Rees LE, Cogan TA, et al. Clinical transplantation of a tissue-engineered airway. Lancet. 2008 Dec 13;372(9655):2023-30. PubMed PMID: 19022496. Epub 2008/11/22. eng.

4.   Brittberg M, Lindahl A, Nilsson A, Ohlsson C, Isaksson O, Peterson L. Treatment of deep cartilage defects in the knee with autologous chondrocyte transplantation. N Engl J Med. 1994;331:889 - 95. PubMed PMID: doi:10.1056/NEJM199410063311401.

5.   Information VGH. Arthritis & musculoskeletal disorders National Health Priority Areas background paper [http://www.health.vic.gov.au/nhpa/arthritis.htm]. 2006 [09/10/2013].

6.   Ringe J, Sittinger M. Tissue engineering in the rheumatic diseases. Arthritis Research & Therapy. 2009;11(1):211. PubMed PMID: doi:10.1186/ar2572.

7.   Schulze-Tanzil G. Activation and dedifferentiation of chondrocytes: implications in cartilage injury and repair. Annals of anatomy = Anatomischer Anzeiger : official organ of the Anatomische Gesellschaft. 2009 Oct;191(4):325-38. PubMed PMID: 19541465. Epub 2009/06/23. eng.

8.   Campaign AR. An Information Booklet, Osteoarthritis. 2004. [21].

9.   Philip G Conaghan LS. Fast Facts: Osteoarthritis. Oxford UK: Health Press Limited; 2009.

10.   Eckstein F, Cicuttini F, Raynauld JP, Waterton JC, Peterfy C. Magnetic resonance imaging (MRI) of articular cartilage in knee osteoarthritis (OA): morphological assessment. Osteoarthritis Cartilage. 2006;14 Suppl A:A46-75. PubMed PMID: 16713720. Epub 2006/05/23. eng.

11.   David J. Dandy DJE. Essential Orthopaedics and Trauma. 3 ed. London, UK: Churchill Livingstone; 1999. 475 p.

12.   Gillian Hosie JD. Managing Osteoarthritis in Primary Care. Oxford: Blackwell Science; 2000.

13.   Kyriacos Athanasiou ED, Jerry Hu Articular Cartilage Tissue Engineering: Morgan and Claypool Publishers; 2010. 168 p.

14.   Meisel AD, Bullough PG. Atlas of osteoarthritis: Lea & Febiger; 1984.

15.   Knudson CB, Knudson W. Cartilage proteoglycans. Seminars in cell & developmental biology. 2001 Apr;12(2):69-78. PubMed PMID: 11292372. Epub 2001/04/09. eng.

16.   Ross MH, Kaye GI, Pawlina W. Histology: A Text and Atlas: Lippincott Williams & Wilkins; 2003.

17.   Naumann A, Dennis JE, Awadallah A, Carrino DA, Mansour JM, Kastenbauer E, et al. Immunochemical and mechanical characterization of cartilage subtypes in rabbit. The journal of histochemistry and cytochemistry : official journal of the Histochemistry Society. 2002 Aug;50(8):1049-58. PubMed PMID: 12133908. Epub 2002/07/23. eng.

18.   Bakbak S, Kayacan R, Akkuş O. Effect of collagen fiber orientation on mechanical properties of cortical bone. Journal of biomechanics. 2011;44:11.

19.   Freemont AJ, Hoyland J. Lineage plasticity and cell biology of fibrocartilage and hyaline cartilage: its significance in cartilage repair and replacement. Eur J Radiol. 2006 Jan;57(1):32-6. PubMed PMID: 16182502. Epub 2005/09/27. eng.

20.   Mouw JK, Case ND, Guldberg RE, Plaas AH, Levenston ME. Variations in matrix composition and GAG fine structure among scaffolds for cartilage tissue engineering.

Osteoarthritis Cartilage. 2005 Sep;13(9):828-36. PubMed PMID: 16006153. Epub 2005/07/12. eng.

21.   LIU H-C, LIN F-H, KUO T-F, CHANG C-H. CARTILAGE TISSUE ENGINEERING. Biomedical Engineering: Applications, Basis and Communications. 2005;17(02):61-71.

22.   Goldberg AJ, Lee DA, Bader DL, Bentley G. Autologous chondrocyte implantation - Culture in a TGF-beta-containing medium enhances the reexpression of a chondrocytic phenotype in passaged human chondrocytes in pellet culture. Journal of Bone and Joint Surgery-British Volume. 2005 Jan;87B(1):128-34. PubMed PMID: WOS:000226535500026.

23.   Hayman DM, Blumberg TJ, Scott CC, Athanasiou KA. The effects of isolation on chondrocyte gene expression. Tissue Eng. 2006 Sep;12(9):2573-81. PubMed PMID: 16995790. Epub 2006/09/26. eng.

24.   Roberts S, Genever P, McCaskie A, De Bari C. Prospects of stem cell therapy in osteoarthritis. Regenerative Medicine. 2011 May;6(3):351-66. PubMed PMID: WOS:000290835900012.

25.   Pereira D, Peleteiro B, Araujo J, Branco J, Santos RA, Ramos E. The effect of osteoarthritis definition on prevalence and incidence estimates: a systematic review. Osteoarthritis Cartilage. 2011 Nov;19(11):1270-85. PubMed PMID: 21907813. Epub 2011/09/13. eng.

26.   Blumenkrantz G, Majumdar S. Quantitative magnetic resonance imaging of articular cartilage in osteoarthritis. European cells & materials. 2007;13:76-86. PubMed PMID: 17506024. Epub 2007/05/17. eng.

27.   Evangelou E, Valdes AM, Kerkhof HJ, Styrkarsdottir U, Zhu Y, Meulenbelt I, et al. Meta-analysis of genome-wide association studies confirms a susceptibility locus for knee osteoarthritis on chromosome 7q22. Ann Rheum Dis. 2011 Feb;70(2):349-55. PubMed PMID: 21068099. Pubmed Central PMCID: PMC3615180. Epub 2010/11/12. eng.

28.   Teichtahl AJ, Wluka AE, Davies-Tuck ML, Cicuttini FM. Imaging of knee osteoarthritis. Best Pract Res Clin Rheumatol. 2008 Dec;22(6):1061-74. PubMed PMID: 19041077. Epub 2008/12/02. eng.

29.   Vavken P, Samartzis D. Effectiveness of autologous chondrocyte implantation in cartilage repair of the knee: a systematic review of controlled trials. Osteoarthritis Cartilage. 2010 Jun;18(6):857-63. PubMed PMID: 20346400. Epub 2010/03/30. eng.

30.   UK AR. Conditions What is arthritis. In: UK AR, editor. 2012.

31.   Murphy J, Fink D, Hunziker E, Barry F. Stem cell therapy in a caprine model of osteoarthritis. Arthritis Rheum. 2003;48:3464 - 74. PubMed PMID: doi:10.1002/art.11365.

32.   Avouac J, Gossec L, Dougados M. Diagnostic and predictive value of anti-cyclic citrullinated protein antibodies in rheumatoid arthritis: a systematic literature review. Ann Rheum Dis. 2006 Jul;65(7):845-51. PubMed PMID: 16606649. Pubmed Central PMCID: PMC1798205. Epub 2006/04/12. eng.

33.   Blumberg SN, Fox DA. Rheumatoid arthritis: guidelines for emerging therapies. The American journal of managed care. 2001 Jun;7(6):617-26. PubMed PMID: 11439735. Epub 2001/07/07. eng.

34.   Clements JN. Treatment of rheumatoid arthritis: A review of recommendations and emerging therapy. 2011.

35.   Myouzen K, Kochi Y, Okada Y, Terao C, Suzuki A, Ikari K, et al. Functional Variants in <italic>NFKBIE</italic> and <italic>RTKN2</italic> Involved in Activation of the NF-κB Pathway Are Associated with Rheumatoid Arthritis in Japanese. PLoS Genet. 2012;8(9):e1002949.

36.   Asquith DL, Miller AM, McInnes IB, Liew FY. Animal models of rheumatoid arthritis. European Journal of Immunology. 2009;39(8):2040-4.

37.   Cesaro A, Anceriz N, Plante A, Pagé N, Tardif MR, Tessier PA. An Inflammation Loop Orchestrated by S100A9 and Calprotectin Is Critical for Development of Arthritis. Plos One. 2012;7(9):e45478.

38.   Chang L-H, Huang H-S, Wu P-T, Jou IM, Pan M-H, Chang W-C, et al. Role of Macrophage CCAAT/Enhancer Binding Protein Delta in the Pathogenesis of Rheumatoid Arthritis in Collagen-Induced Arthritic Mice. Plos One. 2012;7(9):e45378.

39.   Endres M, Neumann K, Haupl T, Erggelet C, Ringe J, Sittinger M, et al. Synovial fluid recruits human mesenchymal progenitors from subchondral spongious bone marrow. J Orthop Res. 2007;25:1299 - 307. PubMed PMID: doi:10.1002/jor.20394.

40.   Sagar DR, Ashraf S, Xu L, Burston JJ, Menhinick MR, Poulter CL, et al. Osteoprotegerin reduces the development of pain behaviour and joint pathology in a model of osteoarthritis. Annals of the Rheumatic Diseases. 2013 May 30, 2013.

41.   Tew SR, Murdoch AD, Rauchenberg RP, Hardingham TE. Cellular methods in cartilage research: primary human chondrocytes in culture and chondrogenesis in human bone marrow stem cells. Methods (San Diego, Calif). 2008 May;45(1):2-9. PubMed PMID: 18442700. Epub 2008/04/30. eng.

42.   Berthiaume F, Maguire TJ, Yarmush ML. Tissue engineering and regenerative medicine: history, progress, and challenges. Annual review of chemical and biomolecular engineering. 2011;2:403-30. PubMed PMID: 22432625. Epub 2011/01/01. eng.

43.   Robert H. Chondral repair of the knee joint using mosaicplasty. Orthopaedics & Traumatology: Surgery & Research. 2011 6//;97(4):418-29.

44.   Kedage VV, Sanghavi SY, Badnre A, Desai NS. Autologous chondrocyte implantation (ACI): an innovative technique for articular cartilage defects. Journal of Clinical Orthopaedics & Trauma. 2010;1(1):33-6.

45.   Institute PTBS. Cell Therapy and Regenerative Medicine Glossary. London: BSI Standards Limited 2012; 2012.

46.   Boeuf S, Richter W. Chondrogenesis of mesenchymal stem cells: role of tissue source and inducing factors. Stem Cell Res Ther. 2010;1(4):31. PubMed PMID: 20959030. Pubmed Central PMCID: PMC2983444. Epub 2010/10/21. eng.

47.   Brittberg M, Lindahl A, Nilsson A, Ohlsson C, Isaksson O, Peterson L. Treatment of Deep Cartilage Defects in the Knee with Autologous Chondrocyte Transplantation. New England Journal of Medicine. 1994;331(14):889-95. PubMed PMID: 8078550.

48.   Yang KG, Saris DB, Geuze RE, van Rijen MH, van der Helm YJ, Verbout AJ, et al. Altered *in vitro* chondrogenic properties of chondrocytes harvested from unaffected cartilage in osteoarthritic joints. Osteoarthritis Cartilage. 2006 Jun;14(6):561-70. PubMed PMID: 16735197. Epub 2006/06/01. eng.

49.   Knutsen G, Drogset J, Engebretsen L, Grontvedt T, Isaksen V, Ludvigsen T, et al. A randomized trial comparing autologous chondrocyte implantation with microfracture. Findings at five years. J Bone Joint Surg Am. 2007;89:2105 - 12. PubMed PMID: doi:10.2106/JBJS.G.00003.

50.   Bosnakovski D, Mizuno M, Kim G, Takagi S, Okumura M, Fujinaga T. Chondrogenic differentiation of bovine bone marrow mesenchymal stem cells (MSCs) in different hydrogels: influence of collagen type II extracellular matrix on MSC chondrogenesis. Biotechnology and bioengineering. 2006 Apr 20;93(6):1152-63. PubMed PMID: 16470881. Epub 2006/02/14. eng.

51.   Feely MG. New and emerging therapies for the treatment of rheumatoid arthritis. Rheumatology: Research and Revies. 2010;2:35-43.

52.   Katz SJ, Russell AS. Palindromic rheumatism: a pre-rheumatoid arthritis state? J Rheumatol. 2012;39(10):1912-3.

53.   Wolfe F, Zwillich SH. The long-term outcomes of rheumatoid arthritis: a 23-year prospective, longitudinal study of total joint replacement and its predictors in 1,600 patients with rheumatoid arthritis. Arthritis Rheum. 1998 Jun;41(6):1072-82. PubMed PMID: 9627017. Epub 1998/06/17. eng.

54.   Bentley G, Biant LC, Carrington RWJ, Akmal M, Goldberg A, Williams AM, et al. A prospective, randomised comparison of autologous chondrocyte implantation versus mosaicplasty for osteochondral defects in the knee. Journal of Bone & Joint Surgery, British Volume. 2003 March 1, 2003;85-B(2):223-30.

55.   Chiang H, Kuo TF, Tsai CC, Lin MC, She BR, Huang YY, et al. Repair of porcine articular cartilage defect with autologous chondrocyte transplantation. J Orthop Res. 2005;23(3):584-93.

56.   Catapult CT. Cell Therapy Definition and Scope [Web site]. 2013 [cited 2013 05/12/2013]. Available from: www.ct.catapult.org.uk.

57.   Mason C, Brindley DA, Culme-Seymour EJ, Davie NL. Cell therapy industry: billion dollar global business with unlimited potential. Regen Med. 2011 May;6(3):265-72. PubMed PMID: 21548728. Epub 2011/05/10. eng.

58.   Cancedda R, Dozin B, Giannoni P, Quarto R. Tissue engineering and cell therapy of cartilage and bone. Matrix biology : journal of the International Society for Matrix Biology. 2003 Mar;22(1):81-91. PubMed PMID: 12714045. Epub 2003/04/26. eng.

59.   Dua H. Transplantation of Limbal Stem Cells. In: Reinhard T, Larkin DFP, editors. Cornea and External Eye Disease. Essentials in Ophthalmology: Springer Berlin Heidelberg; 2006. p. 35-56.

60.   Risbud MV, Sittinger M. Tissue engineering: advances in *in vitro* cartilage generation. Trends in Biotechnology. 2002;20(8):351-6.

61.   Atala A, Bauer SB, Soker S, Yoo JJ, Retik AB. Tissue-engineered autologous bladders for patients needing cystoplasty. Lancet. 2006 Apr 15;367(9518):1241-6. PubMed PMID: 16631879. Epub 2006/04/25. eng.

62.   Naderi H, Matin MM, Bahrami AR. Review paper: critical issues in tissue engineering: biomaterials, cell sources, angiogenesis, and drug delivery systems. Journal of biomaterials applications. 2011 Nov;26(4):383-417. PubMed PMID: 21926148. Epub 2011/09/20. eng.

63.   Hwang N, Varghese S, Elisseeff J. Cartilage Tissue Engineering. In: Vemuri M, editor. Stem Cell Assays. Methods in Molecular Biology™. 407: Humana Press; 2007. p. 351-73.

64.   Kock L, van Donkelaar CC, Ito K. Tissue engineering of functional articular cartilage: the current status. Cell and tissue research. 2012 Mar;347(3):613-27. PubMed PMID: 22030892. Pubmed Central PMCID: PMC3306561. Epub 2011/10/28. eng.

65.   Weiner LP. Definitions and criteria for stem cells. Methods in molecular biology (Clifton, NJ). 2008;438:3-8. PubMed PMID: 18369744. Epub 2008/03/29. eng.

66.   Wagers AJ, Weissman IL. Plasticity of adult stem cells. Cell. 2004 Mar 5;116(5):639-48. PubMed PMID: 15006347. Epub 2004/03/10. eng.

67.   Körbling M, Estrov Z. Adult Stem Cells for Tissue Repair — A New Therapeutic Concept? New England Journal of Medicine. 2003;349(6):570-82. PubMed PMID: 12904523.

68.   Chamberlain G, Fox J, Ashton B, Middleton J. Concise Review: Mesenchymal Stem Cells: Their Phenotype, Differentiation Capacity, Immunological Features, and Potential for Homing. Stem Cells. 2007;25(11):2739-49.

69.   Docheva D, Haasters F, Schieker M. Mesenchymal Stem Cells and Their Cell Surface Receptors. Current Rheumatology Reviews. 2008 //;4(3):155-60.

70.   Meirelles Lda S, Fontes AM, Covas DT, Caplan AI. Mechanisms involved in the therapeutic properties of mesenchymal stem cells. Cytokine & growth factor reviews. 2009 Oct-Dec;20(5-6):419-27. PubMed PMID: 19926330. Epub 2009/11/21. eng.

71.   Pittenger M, Mackay A, Beck S, Jaiswal R, Douglas R, Mosca J, et al. Multilineage potential of adult human mesenchymal stem cells. Science. 1999;284:143 - 7. PubMed PMID: doi:10.1126/science.284.5411.143.

72.   Krampera M, Pizzolo G, Aprili G, Franchini M. Mesenchymal stem cells for bone, cartilage, tendon and skeletal muscle repair. Bone. 2006 Oct;39(4):678-83. PubMed PMID: 16765663. Epub 2006/06/13. eng.

73.   Jorgensen C, Djouad F, Bouffi C, Mrugala D, Noel D. Multipotent mesenchymal stromal cells in articular diseases. Best Pract Res Clin Rheumatol. 2008;22:269 - 84. PubMed PMID: doi:10.1016/j.berh.2008.01.005.

74.   Baksh D, Song L, Tuan RS. Adult mesenchymal stem cells: characterization, differentiation, and application in cell and gene therapy. Journal of cellular and molecular medicine. 2004 Jul-Sep;8(3):301-16. PubMed PMID: 15491506. Epub 2004/10/20. eng.

75.   Dominici M, Le Blanc K, Mueller I, Slaper-Cortenbach I, Marini F, Krause D, et al. Minimal criteria for defining multipotent mesenchymal stromal cells. The International Society for Cellular Therapy position statement. Cytotherapy. 2006;8(4):315-7. PubMed PMID: 16923606. Epub 2006/08/23. eng.

76.   Chen Y, Shao J-Z, Xiang L-X, Dong X-J, Zhang G-R. Mesenchymal stem cells: A promising candidate in regenerative medicine. The International Journal of Biochemistry & Cell Biology. 2008;40(5):815-20.

77.   Jones BJ, McTaggart SJ. Immunosuppression by mesenchymal stromal cells: From culture to clinic. Exp Hematol. 2008 Jun;36(6):733-41. PubMed PMID: WOS:000256167800010. English.

78.   Bouffi C, Djouad F, Mathieu M, Noël D, Jorgensen C. Multipotent mesenchymal stromal cells and rheumatoid arthritis: risk or benefit? Rheumatology. 2009 October 1, 2009;48(10):1185-9.

79.   Kastrinaki MC, Sidiropoulos P, Roche S, Ringe J, Lehmann S, Kritikos H, et al. Functional, molecular and proteomic characterisation of bone marrow mesenchymal stem cells in rheumatoid arthritis. Ann Rheum Dis. 2008;67(6):741-9.

80.   Halme DG, Kessler DA. FDA Regulation of Stem-Cell–Based Therapies. New England Journal of Medicine. 2006;355(16):1730-5. PubMed PMID: 17050899.

81.   Liu W, Frank JA. Detection and quantification of magnetically labeled cells by cellular MRI. European Journal of Radiology. 2009;70(2):258-64.

82.   Berman SMC, Walczak P, Bulte JWM. Tracking stem cells using magnetic nanoparticles. Wiley Interdiscip Rev-Nanomed Nanobiotechnol. 2011 Jul-Aug;3(4):343-55. PubMed PMID: WOS:000291593300002. English.

83.   Jing X-h, Yang L, Duan X-j, Xie B, Chen W, Li Z, et al. *In vivo* MR imaging tracking of magnetic iron oxide nanoparticle labeled, engineered, autologous bone marrow mesenchymal stem cells following intra-articular injection. Joint Bone Spine. 2008;75(4):432-8.

84.   Himmelreich U, Dresselaers T. Cell labeling and tracking for experimental models using Magnetic Resonance Imaging. Methods (San Diego, Calif). 2009;48(2):112-24.

85.   Athiraman H, Jiang Q, Ding GL, Zhang L, Zhang ZG, Wang L, et al. Investigation of Relationships Between Transverse Relaxation Rate, Diffusion Coefficient, and Labeled Cell Concentration in Ischemic Rat Brain Using MRI. Magnetic Resonance in Medicine. 2009 Mar;61(3):587-94. PubMed PMID: WOS:000263608300011.

86.   Ferreira L. Nanoparticles as tools to study and control stem cells. J Cell Biochem. 2009;108(4):746-52.

87.   Tran LA, Krishnamurthy R, Muthupillai R, da Graca Cabreira-Hansen M, Willerson JT, Perin EC, et al. Gadonanotubes as magnetic nanolabels for stem cell detection. Biomaterials. 2010;31(36):9482-91.

88.   Ju S, Teng G, Zhang Y, Ma M, Chen F, Ni Y. *In vitro* labeling and MRI of mesenchymal stem cells from human umbilical cord blood. Magn Reson Imaging. 2006;24(5):611-7.

89.   Wu YL, Ye Q, Foley LM, Hitchens TK, Sato K, Williams JB, et al. In situ labeling of immune cells with iron oxide particles: An approach to detect organ rejection by cellular MRI. Proceedings of the National Academy of Sciences of the United States of America. 2006;103(6):1852-7.

90.   Massoud TF, Gambhir SS. Molecular imaging in living subjects: seeing fundamental biological processes in a new light. Genes & Development. 2003;17(5):545-80.

91.   Li Li WJ, Kui Luo, Hongmei Song, Fang Lan, Yao Wu and Zhongwei Gu. Superparamagnetic Iron Oxide Nanoparticles as MRI contrast agents for Non-invasive Stem Cell Labeling and Tracking. Theranostics. 2013;3(8):595-615.

92.   Castaneda RT, Boddington S, Henning TD, Wendland M, Mandrussow L, Liu S, et al. Labeling human embryonic stem-cell-derived cardiomyocytes for tracking with MR imaging. Pediatric Radiology. 2011 Nov;41(11):1384-92. PubMed PMID: WOS:000296005400006.

93.   Crabbe A, Vandeputte C, Dresselaers T, Sacido AA, Verdugo JM, Eyckmans J, et al. Effects of MRI contrast agents on the stem cell phenotype. Cell Transplant. 2010;19(8):919-36. PubMed PMID: 20350351. Epub 2010/03/31. eng.

94.   Engberink RDO, van der Pol SMA, Walczak P, van der Toorn A, Viergever MA, Dijkstra CD, et al. Magnetic Resonance Imaging of Monocytes Labeled with Ultrasmall Superparamagnetic Particles of Iron Oxide Using Magnetoelectroporation in an Animal Model of Multiple Sclerosis. Molecular imaging. 2010 Sep-Oct;9(5):268-77. PubMed PMID: WOS:000283457200004.

95.   Ferreira L, Karp JM, Nobre L, Langer R. New Opportunities: The Use of Nanotechnologies to Manipulate and Track Stem Cells. Cell Stem Cell. 2008;3(2):136-46.

96.   Ramaswamy S, Greco JB, Uluer MC, Zhang Z, Zhang Z, Fishbein KW, et al. Magnetic Resonance Imaging of Chondrocytes Labeled with Superparamagnetic Iron Oxide Nanoparticles in Tissue-Engineered Cartilage. Tissue Engineering Part A. 2009 Dec;15(12):3899-910. PubMed PMID: WOS:000272528400021.

97.   Bulte JW, Kraitchman DL. Iron oxide MR contrast agents for molecular and cellular imaging. NMR Biomed. 2004 Nov;17(7):484-99. PubMed PMID: 15526347. Epub 2004/11/05. eng.

98.   Bulte JWM. *In vivo* MRI Cell Tracking: Clinical Studies. American Journal of Roentgenology. 2009 Aug;193(2):314-25. PubMed PMID: WOS:000268148600007.

99.   Beckmann N, Falk R, Zurbrugg S, Dawson J, Engelhardt P. Macrophage infiltration into the rat knee detected by MRI in a model of antigen-induced arthritis. Magn Reson Med. 2003;49(6):1047-55.

100.   Beckmann N, Cannet C, Fringeli-Tanner M, Baumann D, Pally C, Bruns C, et al. Macrophage labeling by SPIO as an early marker of allograft chronic rejection in a rat model of kidney transplantation. Magn Reson Med. 2003 Mar;49(3):459-67. PubMed PMID: 12594748. Epub 2003/02/21. eng.

101.   Chen J, Wang F, Zhang Y, Jin X, Zhang L, Feng Y, et al. *In vivo* Tracking of Superparamagnetic Iron Oxide Nanoparticle Labeled Chondrocytes in Large Animal Model. Ann Biomed Eng. 2012;19:19.

102.   Loebinger MR, Kyrtatos PG, Turmaine M, Price AN, Pankhurst Q, Lythgoe MF, et al. Magnetic resonance imaging of mesenchymal stem cells homing to pulmonary metastases using biocompatible magnetic nanoparticles. Cancer research. 2009 Dec 1;69(23):8862-7. PubMed PMID: 19920196. Pubmed Central PMCID: PMC2833408. Epub 2009/11/19. eng.

103.   Saldanha KJ, Doan RP, Ainslie KM, Desai TA, Majumdar S. Micrometer-sized iron oxide particle labeling of mesenchymal stem cells for magnetic resonance imaging-based monitoring of cartilage tissue engineering. Magn Reson Imaging. 2011 Jan;29(1):40-9. PubMed PMID: WOS:000285570100006.

104.   He G, Zhang H, Wei H, Wang Y, Zhang X, Tang Y, et al. *In vivo* imaging of bone marrow mesenchymal stem cells transplanted into myocardium using magnetic resonance imaging: A novel method to the transplanted cells. International Journal of Cardiology. 2007 Jan 2;114(1):4-10. PubMed PMID: WOS:000243051900002.

105.   Kim HS, Oh SY, Joo HJ, Son K-R, Song I-C, Moon WK. The effects of clinically used MRI contrast agents on the biological properties of human mesenchymal stem cells. NMR in Biomedicine. 2010;23(5):514-22.

106.   Kim TH, Kim JK, Shim W, Kim SY, Park TJ, Jung JY. Tracking of transplanted mesenchymal stem cells labeled with fluorescent magnetic nanoparticle in liver cirrhosis rat model with 3-T MRI. Magn Reson Imaging. 2010 Sep;28(7):1004-13. PubMed PMID: WOS:000281046100011. English.

107.   Farrell E, Wielopolski P, Pavljasevic P, Kops N, Weinans H, Bernsen MR, et al. Cell labelling with superparamagnetic iron oxide has no effect on chondrocyte behaviour. Osteoarthritis and Cartilage. 2009;17(7):961-7.

108.   Riehemann K, Schneider SW, Luger TA, Godin B, Ferrari M, Fuchs H. Nanomedicine-Challenge and Perspectives. Angew Chem-Int Edit. 2009;48(5):872-97. PubMed PMID: WOS:000263082200005. English.

109.   Morteza Mahmoudi HH, Barbara Rothen-Rutishauser, Alke Petri-Fink. Assessing the *In vitro* and *In vivo* Toxicity of Superparamagnetic Iron Oxide Nanoparticles. American Chemical Society. 2011.

110.   Krishnan KM. Biomedical Nanomagnetics: A Spin Through Possibilities in Imaging, Diagnostics, and Therapy. Magnetics, IEEE Transactions on. 2010;46(7):2523-58.

111.   Pankhurst QA, Connolly J, Jones SK, Dobson J. Applications of magnetic nanoparticles in biomedicine. Journal of Physics D: Applied Physics. 2003;36(13):R167.

112.   Banerjee R, Katsenovich Y, Lagos L, McIintosh M, Zhang X, Li CZ. Nanomedicine: Magnetic Nanoparticles and their Biomedical Applications. Current Medicinal Chemistry. 2010;17(27):3120-41.

113.   Jin Y, Jia C, Huang S-W, O'Donnell M, Gao X. Multifunctional nanoparticles as coupled contrast agents. Nat Commun. 2010;1:41.

114.   Yildirimer L, Thanh NTK, Loizidou M, Seifalian AM. Toxicology and clinical potential of nanoparticles. Nano Today. 2011;6(6):585-607.

115.   Markides H, Kehoe O, Morris R, El Haj A. Whole body tracking of superparamagnetic iron oxide nanoparticle-labelled cells -- a rheumatoid arthritis mouse model. Stem Cell Research & Therapy. 2013;4(5):126. PubMed PMID: doi:10.1186/scrt337.

116.   Cartmell SH, Dobson J, Verschueren S, El Haj AJ. Development of Magnetic Particle Techniques for Long-Term Culture of Bone Cells With Intermittent Mechanical Activation. Transaction on Nanobioscience. 2002;1:92-7.

117.   Markides H, Rotherham M, El Haj AJ. Biocompatibility and Toxicity of Magnetic Nanoparticles in Regenerative Medicine. Journal of Nanomaterials. 2012;2012:11.

118.   Hughes S, El Haj AJ, Dobson J. Magnetic micro- and nanoparticle mediated activation of mechanosensitive ion channels. Medical Engineering & Physics. 2005;27(9):754-62.

119.   Hofmann-Amtenbrink M, Hofmann H, Montet X. Superparamagnetic nanoparticles - a tool for early diagnostics. Swiss Medical Weekly. 2010 Dec 11;140:7-13. PubMed PMID: WOS:000286015600002.

120.   Berry CC. Possible exploitation of magnetic nanoparticle-cell interaction for biomedical applications. Journal of Materials Chemistry. 2005;15(5):543-7.

121.   Mahmoudi M, Simchi A, Imani M, Shokrgozard MA, Milani AS, Haefeli UO, et al. A new approach for the *in vitro* identification of the cytotoxicity of superparamagnetic iron oxide nanoparticles. Colloids and Surfaces B-Biointerfaces. 2010 Jan 1;75(1):300-9. PubMed PMID: WOS:000278695300040.

122.   Lin M, Kim D, El Haj A, Dobson J. Development of superparamagnetic iron oxide nanoparticles (SPIONS) for translation to clinical applications. IEEE Trans Nanobioscience. 2008;7(4):298-305.

123.   Solanki A, Kim JD, Lee K-B. Nanotechnology for regenerative medicine: nanomaterials for stem cell imaging. Nanomedicine. 2008 2011/08/11;3(4):567-78.

124.   Lin MM, Kim do K, El Haj AJ, Dobson J. Development of superparamagnetic iron oxide nanoparticles (SPIONS) for translation to clinical applications. IEEE Trans Nanobioscience. 2008 Dec;7(4):298-305. PubMed PMID: 19203873.

125.   Stacey M Cromer Bermen PW, Jeff W.M.Bulte. Tracking stem cells using magnetic nanoparticles. Nanomadicine and Nanobiotechnology. 2011;3:343-55.

126.   Faraji M, Yamini Y, Rezaee M. Magnetic nanoparticles: Synthesis, stabilization, functionalization, characterization, and applications. JICS. 2010 2010/03/01;7(1):1-37. English.

127.   Bean CP. Hysteresis Loops of Mixtures of Ferromagnetic Micropowders. Journal of Applied Physics. 1955;26(11):1381-3.

128.   Mahmoudi M, Amiri H, Shokrgozar MA, Sasanpour P, Rashidian B, Laurent S, et al. Raman active jagged-shaped gold-coated magnetic particles as a novel multimodal nanoprobe. Chemical Communications. 2011;47(37):10404-6.

129.   Getzlaff M. Fundamentals of Magnetism. New York: Springer; 2008.

130.   Donald W. McRobbie EAM, Martin J. Graves, Martin, R. Prince. MRI From Picture to Proton: Cambridge university press; 2003.

131.   Gupta AK, Gupta M. Synthesis and surface engineering of iron oxide nanoparticles for biomedical applications. Biomaterials. 2005;26(18):3995-4021.

132.   Heath Pardoe WC-a, TimothyG. St. Pierre, Jon Dobson. Structural and magnetic properties of nanoscale iron oxide particles synthesized in the presence of dextran or polyvinyl alcoho. Journal of Magnetism and Magnetic Materials. 2001; 22: 41}4.

133.   Mahmoudi M, Sant S, Wang B, Laurent S, Sen T. Superparamagnetic iron oxide nanoparticles (SPIONs): Development, surface modification and applications in chemotherapy. Advanced Drug Delivery Reviews. 2011 Jan-Feb;63(1-2):24-46. PubMed PMID: WOS:000290353900003.

134.   Na HB, Song IC, Hyeon T. Inorganic Nanoparticles for MRI Contrast Agents. Advanced Materials. 2009;21(21):2133-48.

135.   Zabow G, Dodd SJ, Shapiro E, Moreland J, Koretsky AP. Microfabricated high-moment micrometer-sized MRI contrast agents. Magn Reson Med. 2011 Mar;65(3):645-55. PubMed PMID: 20928829. Pubmed Central PMCID: PMC3065941. Epub 2010/10/12. eng.

136.   Jasmin, Torres ALM, Nunes HMP, Passipieri JA, Jelicks LA, Gasparetto EL, et al. Optimized labeling of bone marrow mesenchymal cells with superparamagnetic iron oxide

nanoparticles and *in vivo* visualization by magnetic resonance imaging. Journal of Nanobiotechnology. 2011 Feb 9;9. PubMed PMID: WOS:000288089800001.

137.   Zhou R, Acton PD, Ferrari VA. Imaging Stem Cells Implanted in Infarcted Myocardium. Journal of the American College of Cardiology. 2006;48(10):2094-106.

138.   Lu C-W, Hung Y, Hsiao J-K, Yao M, Chung T-H, Lin Y-S, et al. Bifunctional Magnetic Silica Nanoparticles for Highly Efficient Human Stem Cell Labeling. Nano Letters. 2006;7(1):149-54.

139.   Sung C, Hong K, Lin S, Lee Y, Cha J, Lee J, et al. Dual-Modal Nanoprobes for Imaging of Mesenchymal Stem Cell Transplant by MRI and Fluorescence Imaging. Korean J Radiol. 2009;10(6):613-22.

140.   Dousset V, Tourdias T, Brochet B, Boiziau C, Petry KG. How to trace stem cells for MRI evaluation? Journal of the Neurological Sciences. 2008;265(1-2):122-6.

141.   Walczak P, Ruiz-Cabello J, Kedziorek DA, Gilad AA, Lin S, Barnett B, et al. Magnetoelectroporation: improved labeling of neural stem cells and leukocytes for cellular magnetic resonance imaging using a single FDA-approved agent. Nanomedicine: Nanotechnology, Biology and Medicine. 2006;2(2):89-94.

142.   Arbab AS, Yocum GT, Rad AM, Khakoo AY, Fellowes V, Read EJ, et al. Labeling of cells with ferumoxides–protamine sulfate complexes does not inhibit function or differentiation capacity of hematopoietic or mesenchymal stem cells. NMR in Biomedicine. 2005;18(8):553-9.

143.   Kostura L, Kraitchman DL, Mackay AM, Pittenger MF, Bulte JWM. Feridex labeling of mesenchymal stem cells inhibits chondrogenesis but not adipogenesis or osteogenesis. NMR in Biomedicine. 2004;17(7):513-7.

144.   Yiu HHP, Maple MJ, Lees MR, Palona I, El Haj AJ, Dobson J. Preparation and Characterization of Iron Oxide-Silica Composite Particles Using Mesoporous SBA-15 Silica as Template and Their Internalization Into Mesenchymal Stem Cell and Human Bone Cell Lines. IEEE Trans Nanobioscience. 2010;9(3):165-70.

145.   Weissleder R, Stark DD, Engelstad BL, Bacon BR, Compton CC, White DL, et al. Superparamagnetic iron oxide: pharmacokinetics and toxicity. American Journal of Roentgenology. 1989;152(1):167-73.

146.   Chen Y-C, Hsiao J-K, Liu H-M, Lai IY, Yao M, Hsu S-C, et al. The inhibitory effect of superparamagnetic iron oxide nanoparticle (Ferucarbotran) on osteogenic differentiation and its signaling mechanism in human mesenchymal stem cells. Toxicology and Applied Pharmacology. 2010;245(2):272-9.

147.   Henning TD, Sutton EJ, Kim A, Golovko D, Horvai A, Ackerman L, et al. The influence of ferucarbotran on the chondrogenesis of human mesenchymal stem cells. Contrast Media & Molecular Imaging. 2009 Jul-Aug;4(4):165-73. PubMed PMID: WOS:000269597900002.

148.   Dong-Ming Huang T-HC, Yann Hung, Fang Lu, Si-Han Wu,Chung-Yuan Mou, Ming Yao, Yao-Chang Che. Internalization of mesoporous silica nanoparticles induces transient but not sufficient osteogenic signals in human mesenchymal stem cells. Toxicology and Applied Pharmacolog. 2008; 231: 208-15.

149.   Yang C-Y, Hsiao J-K, Tai M-F, Chen S-T, Cheng H-Y, Wang J-L, et al. Direct Labeling of hMSC with SPIO: the Long-Term Influence on Toxicity, Chondrogenic Differentiation Capacity, and Intracellular Distribution. Molecular Imaging and Biology. 2011 Jun;13(3):443-51. PubMed PMID: WOS:000290277300006.

150.   Chamnongpol S, Dodson W, Cromie MJ, Harris ZL, Groisman EA. Fe(III)-mediated cellular toxicity. Molecular microbiology. 2002 Aug;45(3):711-9. PubMed PMID: 12139617. Epub 2002/07/26. eng.

151.   The dose makes the poison. Nat Nano. 2011;6(6):329-.

152.   Budde MD, Frank JA. Magnetic Tagging of Therapeutic Cells for MRI. J Nucl Med. 2009;50(2):171-4.

153.   Balakumaran A, Pawelczyk E, Ren J, Sworder B, Chaudhry A, Sabatino M, et al. Superparamagnetic Iron Oxide Nanoparticles Labeling of Bone Marrow Stromal (Mesenchymal) Cells Does Not Affect Their "Stemness". PLoS ONE. 2010;5(7):e11462.

154.   Omidkhoda A, Mozdarani H, Movasaghpoor A, Fatholah AAP. Study of apoptosis in labeled mesenchymal stem cells with superparamagnetic iron oxide using neutral comet assay. Toxicol Vitro. 2007;21(6):1191-6.

155.   Hill JM, Dick AJ, Raman VK, Thompson RB, Yu ZX, Hinds KA, et al. Serial cardiac magnetic resonance imaging of injected mesenchymal stem cells. Circulation. 2003 Aug;108(8):1009-14. PubMed PMID: WOS:000184954900020. English.

156.   Kim T, Momin E, Choi J, Yuan K, Zaidi H, Kim J, et al. Mesoporous Silica-Coated Hollow Manganese Oxide Nanoparticles as Positive T(1) Contrast Agents for Labeling and MRI Tracking of Adipose-Derived Mesenchyrnal Stem Cells. Journal of the American Chemical Society. 2011 Mar 9;133(9):2955-61. PubMed PMID: WOS:000289455200032.

157.   Delcroix GJR, Jacquart M, Lemaire L, Sindji L, Franconi F, Le Jeune J-J, et al. Mesenchymal and neural stem cells labeled with HEDP-coated SPIO nanoparticles: *In vitro* characterization and migration potential in rat brain. Brain Research. 2009;1255(0):18-31.

158.   Schild H. MRI made easy. Berlin Germany: Schering AG; 1990. 105 p.

159.   Burtea C, Laurent S, Vander Elst L, Muller RN. Contrast agents: magnetic resonance. Handbook of experimental pharmacology. 2008 (185 Pt 1):135-65. PubMed PMID: 18626802. Epub 2008/07/16. eng.

160.   Shapiro EM, Skrtic S, Koretsky AP. Sizing it up: cellular MRI using micron-sized iron oxide particles. Magn Reson Med. 2005 Feb;53(2):329-38. PubMed PMID: 15678543. Epub 2005/01/29. eng.

161.   Shapiro EM, Sharer K, Skrtic S, Koretsky AP. *In vivo* detection of single cells by MRI. Magn Reson Med. 2006 Feb;55(2):242-9. PubMed PMID: 16416426. Epub 2006/01/18. eng.

162.   Ye F, Laurent S, Fornara A, Astolfi L, Qin J, Roch A, et al. Uniform mesoporous silica coated iron oxide nanoparticles as a highly efficient, nontoxic MRI T(2) contrast agent with tunable proton relaxivities. Contrast Media Mol Imaging. 2012 Sep-Oct;7(5):460-8. PubMed PMID: 22821880. Epub 2012/07/24. eng.

163.   Bjornerud A, Johansson L. The utility of superparamagnetic contrast agents in MRI: theoretical consideration and applications in the cardiovascular system. NMR Biomed. 2004 Nov;17(7):465-77. PubMed PMID: 15526351. Epub 2004/11/05. eng.

164.   Pooley RA. AAPM/RSNA physics tutorial for residents: fundamental physics of MR imaging. Radiographics : a review publication of the Radiological Society of North America, Inc. 2005 Jul-Aug;25(4):1087-99. PubMed PMID: 16009826. Epub 2005/07/13. eng.

165.   Kyrtatos PG, Lehtolainen P, Junemann-Ramirez M, Garcia-Prieto A, Price AN, Martin JF, et al. Magnetic Tagging Increases Delivery of Circulating Progenitors in Vascular Injury. J Am Coll Cardiol Intv. 2009 August 1, 2009;2(8):794-802.

166.   Ho VHB, Barcza A, Chen R, Müller KH, Darton NJ, Slater NKH. The precise control of cell labelling with streptavidin paramagnetic particles. Biomaterials. 2009;30(33):6548-55.

167.   Kim J, Lee H, Kang H-J, Park T. The targeting of endothelial progenitor cells to a specific location within a microfluidic channel using magnetic nanoparticles. Biomedical Microdevices. 2009;11(1):287-96-96.

168.   Hsiao J-K, Tai M-F, Chu H-H, Chen S-T, Li H, Lai D-M, et al. Magnetic nanoparticle labeling of mesenchymal stem cells without transfection agent: Cellular behavior and

capability of detection with clinical 1.5 T magnetic resonance at the single cell level. Magnetic Resonance in Medicine. 2007;58(4):717-24.

169.   Wilhelm C, Bal L, Smirnov P, Galy-Fauroux I, Clément O, Gazeau F, et al. Magnetic control of vascular network formation with magnetically labeled endothelial progenitor cells. Biomaterials. 2007;28(26):3797-806.

170.   Sniadecki NJ. Minireview: A Tiny Touch: Activation of Cell Signaling Pathways with Magnetic Nanoparticles. Endocrinology. 2010;151(2):451-7.

171.   Ingber DE. Cellular mechanotransduction: putting all the pieces together again. 2006. p. 811-27.

172.   Kirkham GR, Elliot KJ, Keramane A, Salter DM, Dobson JP, El Haj AJ, et al. Hyperpolarization of human mesenchymal stem cells in response to magnetic force. IEEE Trans Nanobioscience. 2010;9(1):71-4.

173.   Janos M. Kanczler HSS, Julia Magnay, David Green, Richard O.C. Oreffo, Jon P. Dobson, and Alicia J. El Haj. Controlled Differentiation of Human Bone Marrow Stromal Cells Using Magnetic Nanoparticle Technology. Tissue Engineering Part A. 2010;16 (10):3241-50.

174.   Cartmell SH, Dobson J, Verschueren SB, El Haj AJ. Development of magnetic particle techniques for long-term culture of bone cells with intermittent mechanical activation. IEEE transactions on nanobioscience. 2002 2002-Jun;1(2):92-7. PubMed PMID: MEDLINE:16689213.

175.   Chamberlain G, Wright K, Rot A, Ashton B, Middleton J. Murine Mesenchymal Stem Cells Exhibit a Restricted Repertoire of Functional Chemokine Receptors: Comparison with Human. Plos One. 2008;3(8):e2934.

176.   Mackay AM, Beck SC, Murphy JM, Barry FP, Chichester CO, Pittenger MF. Chondrogenic differentiation of cultured human mesenchymal stem cells from marrow. Tissue Eng. 1998 Winter;4(4):415-28. PubMed PMID: 9916173. Epub 1999/01/23. eng.

177.   Jaiswal N, Haynesworth SE, Caplan AI, Bruder SP. Osteogenic differentiation of purified, culture-expanded human mesenchymal stem cells *in vitro*. J Cell Biochem. 1997 Feb;64(2):295-312. PubMed PMID: 9027589. Epub 1997/02/01. eng.

178.   Luciani A, Dechoux S, Deveaux V, Poirier-Quinot M, Luciani N, Levy M, et al. Adipose tissue macrophages: MR tracking to monitor obesity-associated inflammation. Radiology. 2012 Jun;263(3):786-93. PubMed PMID: 22523321. Epub 2012/04/24. eng.

179.   López Pérez JA, López Quintela MA, Mira J, Rivas J, Charles SW. Advances in the Preparation of Magnetic Nanoparticles by the Microemulsion Method. The Journal of Physical Chemistry B. 1997 1997/10/01;101(41):8045-7.

180.   Nowell MA, Richards PJ, Horiuchi S, Yamamoto N, Rose-John S, Topley N, et al. Soluble IL-6 receptor governs IL-6 activity in experimental arthritis: Blockade of arthritis severity by soluble glycoprotein 130. Journal of Immunology. 2003 Sep 15;171(6):3202-9. PubMed PMID: WOS:000185247300059.

181.   Clayton NM, Oakley I, Thompson S, Wheeldon A, Sargent B, Bountra C. Validation of the dual channel averager as an instrument of the measure of clincally relevant pain. British Journal of Pharmacology. 1997 Winter 2006;120 supplement:219P.

182.   Elmes SJ, Winyard LA, Medhurst SJ, Clayton NM, Wilson AW, Kendall DA, et al. Activation of CB1 and CB2 receptors attenuates the induction and maintenance of inflammatory pain in the rat. Pain. 2005 Dec 5;118(3):327-35. PubMed PMID: 16289798.

183.   Li Calzi S, Kent DL, Chang KH, Padgett KR, Afzal A, Chandra SB, et al. Labeling of stem cells with monocrystalline iron oxide for tracking and localization by magnetic resonance imaging. Microvascular research. 2009 Jun;78(1):132-9. PubMed PMID: 19345699. Pubmed Central PMCID: PMC3755588. Epub 2009/04/07. eng.

184.   Henning TD, Gawande R, Khurana A, Tavri S, Mandrussow L, Golovko D, et al. Magnetic Resonance Imaging of Ferumoxide-Labeled Mesenchymal Stem Cells in Cartilage Defects: *In vitro* and *In vivo* Investigations. Molecular imaging. 2011 Sep 28. PubMed PMID: 21955668. Epub 2011/10/01. Eng.

185.   Amiri H, Bordonali L, Lascialfari A, Wan S, Monopoli MP, Lynch I, et al. Protein corona affects the relaxivity and MRI contrast efficiency of magnetic nanoparticles. Nanoscale. 2013 Jul 30. PubMed PMID: 23896964. Epub 2013/07/31. Eng.

186.   Hinds KA, Hill JM, Shapiro EM, Laukkanen MO, Silva AC, Combs CA, et al. Highly efficient endosomal labeling of progenitor and stem cells with large magnetic particles allows magnetic resonance imaging of single cells. Blood. 2003 Aug 1;102(3):867-72. PubMed PMID: 12676779. Epub 2003/04/05. eng.

187.   Khurana A, Nejadnik H, Chapelin F, Lenkov O, Gawande R, Lee S, et al. Ferumoxytol: a new, clinically applicable label for stem-cell tracking in arthritic joints with MRI. Nanomedicine (London, England). 2013 Mar 27. PubMed PMID: 23534832. Epub 2013/03/29. Eng.

188.   Reimer P, Balzer T. Ferucarbotran (Resovist): a new clinically approved RES-specific contrast agent for contrast-enhanced MRI of the liver: properties, clinical development, and applications. Eur Radiol. 2003 Jun;13(6):1266-76. PubMed PMID: 12764641. Epub 2003/05/24. eng.

189.   Dardzinski BJ, Schmithorst VJ, Holland SK, Boivin GP, Imagawa T, Watanabe S, et al. MR imaging of murine arthritis using ultrasmall superparamagnetic iron oxide particles☆. Magn Reson Imaging. 2001 11//;19(9):1209-16.

190.   Mahmoudi M, Lynch I, Ejtehadi MR, Monopoli MP, Bombelli FB, Laurent S. Protein−Nanoparticle Interactions: Opportunities and Challenges. Chemical Reviews. 2011 2011/09/14;111(9):5610-37.

191.   Maiorano G, Sabella S, Sorce B, Brunetti V, Malvindi MA, Cingolani R, et al. Effects of Cell Culture Media on the Dynamic Formation of Protein−Nanoparticle Complexes and Influence on the Cellular Response. ACS Nano. 2010 2010/12/28;4(12):7481-91.

192.   Clift MJD, Bhattacharjee S, Brown DM, Stone V. The effects of serum on the toxicity of manufactured nanoparticles. Toxicology Letters. 2010;198(3):358-65.

193.   Lundqvist M, Stigler J, Cedervall T, Berggård T, Flanagan MB, Lynch I, et al. The Evolution of the Protein Corona around Nanoparticles: A Test Study. ACS Nano. 2011 2011/09/27;5(9):7503-9.

194.   Thorek DL, Tsourkas A. Size, charge and concentration dependent uptake of iron oxide particles by non-phagocytic cells. Biomaterials. 2008 Sep;29(26):3583-90. PubMed PMID: 18533252. Pubmed Central PMCID: PMC2518173. Epub 2008/06/06. eng.

195.   Osiris Therapeutics, Inc. homepage.

196.   Laurent S, Burtea C, Thirifays C, Häfeli UO, Mahmoudi M. Crucial Ignored Parameters on Nanotoxicology: The Importance of Toxicity Assay Modifications and "Cell Vision". Plos One. 2012;7(1):e29997.

197.   Mahmoudi M, Laurent S, Shokrgozar MA, Hosseinkhani M. Toxicity Evaluations of Superparamagnetic Iron Oxide Nanoparticles: Cell "Vision" versus Physicochemical Properties of Nanoparticles. ACS Nano. 2011 2011/09/27;5(9):7263-76.

198.   Rivera-Gil P, Jimenez de Aberasturi D, Wulf V, Pelaz B, del Pino P, Zhao Y, et al. The challenge to relate the physicochemical properties of colloidal nanoparticles to their cytotoxicity. Accounts of chemical research. 2013 Mar 19;46(3):743-9. PubMed PMID: 22786674. Epub 2012/07/13. eng.

199.   Heymer A, Haddad D, Weber M, Gbureck U, Jakob PM, Eulert J, et al. Iron oxide labelling of human mesenchymal stem cells in collagen hydrogels for articular cartilage repair. Biomaterials. 2008;29(10):1473-83.

200.   Khaing Oo MK, Yang Y, Hu Y, Gomez M, Du H, Wang H. Gold Nanoparticle-Enhanced and Size-Dependent Generation of Reactive Oxygen Species from Protoporphyrin IX. ACS Nano. 2012 2012/03/27;6(3):1939-47.

201.   Smolensky ED, Park HY, Zhou Y, Rolla GA, Marjanska M, Botta M, et al. Scaling Laws at the Nano Size: The Effect of Particle Size and Shape on the Magnetism and Relaxivity of Iron Oxide Nanoparticle Contrast Agents. Journal of materials chemistry B, Materials for biology and medicine. 2013 Jun 14;1(22):2818-28. PubMed PMID: 23819021. Pubmed Central PMCID: PMC3695630. Epub 2013/07/03. Eng.

202.   Heyn C, Bowen CV, Rutt BK, Foster PJ. Detection threshold of single SPIO-labeled cells with FIESTA. Magn Reson Med. 2005 Feb;53(2):312-20. PubMed PMID: 15678551. Epub 2005/01/29. eng.

203.   Deponti D, Di Giancamillo A, Gervaso F, Domenicucci M, Domeneghini C, Sannino A, et al. Collagen scaffold for cartilage tissue engineering: the benefit of fibrin glue and the proper culture time in an infant cartilage model. Tissue Eng Part A. 2013 Oct 23. PubMed PMID: 24152291. Epub 2013/10/25. Eng.

204.   Richard S, Querleux B, Bittoun J, Jolivet O, Idy-Peretti I, de Lacharriere O, et al. Characterization of the skin *in vivo* by high resolution magnetic resonance imaging: water behavior and age-related effects. The Journal of investigative dermatology. 1993 May;100(5):705-9. PubMed PMID: 8388010. Epub 1993/05/01. eng.

205.   Yang Y, Zhang J, Qian Y, Dong S, Huang H, Boada FE, et al. Superparamagnetic iron oxide is suitable to label tendon stem cells and track them *in vivo* with MR imaging. Ann Biomed Eng. 2013 Oct;41(10):2109-19. PubMed PMID: 23549900. Pubmed Central PMCID: PMC3766440. Epub 2013/04/04. eng.

206.   Bydder M, Rahal A, Fullerton GD, Bydder GM. The magic angle effect: a source of artifact, determinant of image contrast, and technique for imaging. Journal of magnetic resonance imaging : JMRI. 2007 Feb;25(2):290-300. PubMed PMID: 17260400. Epub 2007/01/30. eng.

207.   Henderson IJ, Tuy B, Connell D, Oakes B, Hettwer WH. Prospective clinical study of autologous chondrocyte implantation and correlation with MRI at three and 12 months. J Bone Joint Surg Br. 2003;85(7):1060-6.

208.   Rindfleisch JA, Muller D. Diagnosis and management of rheumatoid arthritis. Am Fam Physician. 2005;72(6):1037-47.

209.   Zhang RX, Ren K, Dubner R. Osteoarthritis pain mechanisms: basic studies in animal models. Osteoarthritis Cartilage. 2013 Sep;21(9):1308-15. PubMed PMID: 23973145. Pubmed Central PMCID: PMC3771690. Epub 2013/08/27. eng.

210.   Fernihough J, Gentry C, Malcangio M, Fox A, Rediske J, Pellas T, et al. Pain related behaviour in two models of osteoarthritis in the rat knee. Pain. 2004 11//;112(1–2):83-93.

211.   Ashraf S, Mapp PI, Burston J, Bennett AJ, Chapman V, Walsh DA. Augmented pain behavioural responses to intra-articular injection of nerve growth factor in two animal models of osteoarthritis. Annals of the Rheumatic Diseases. 2013 July 13, 2013.

212.   Bendele A, Mccomb J, Gould T, Mcabee T, Sennello G, Chlipala E, et al. Animal Models of Arthritis: Relevance to Human Disease. Toxicologic Pathology. 1999 January 1, 1999;27(1):134-42.

213.   Bendele A. Animal models of rheumatoid arthritis. J Musculoskelet Neuronal Interact. 2001;1(4):377-85.

214.   Bendele AM. Animal models of osteoarthritis. J Musculoskelet Neuronal Interact. 2001;1(4):363-76.

215.   Suhaeb AM, Naveen S, Mansor A, Kamarul T. Hyaluronic acid with or without bone marrow derived-mesenchymal stem cells improves osteoarthritic knee changes in rat model:

a preliminary report. Indian journal of experimental biology. 2012 Jun;50(6):383-90. PubMed PMID: 22734248. Epub 2012/06/28. eng.

216.   Song M, Kim Y, Kim Y, Ryu S, Song I, Kim SU, et al. MRI tracking of intravenously transplanted human neural stem cells in rat focal ischemia model. Neuroscience Research. 2009 6//;64(2):235-9.

217.   Jackson J, Chapon C, Jones W, Hirani E, Qassim A, Bhakoo K. *In vivo* multimodal imaging of stem cell transplantation in a rodent model of Parkinson's disease. Journal of Neuroscience Methods. 2009;183(2):141-8.

218.   Santos JM, Barcia RN, Simoes SI, Gaspar MM, Calado S, Agua-Doce A, et al. The role of human umbilical cord tissue-derived mesenchymal stromal cells (UCX(R)) in the treatment of inflammatory arthritis. Journal of translational medicine. 2013;11:18. PubMed PMID: 23324136. Pubmed Central PMCID: PMC3561123. Epub 2013/01/18. eng.

219.   Gonzalez MA, Gonzalez-Rey E, Rico L, Buscher D, Delgado M. Treatment of experimental arthritis by inducing immune tolerance with human adipose-derived mesenchymal stem cells. Arthritis Rheum. 2009 Apr;60(4):1006-19. PubMed PMID: 19333946. Epub 2009/04/01. eng.

220.   Desando G, Cavallo C, Sartoni F, Martini L, Parrilli A, Veronesi F, et al. Intra-articular delivery of adipose derived stromal cells attenuates osteoarthritis progression in an experimental rabbit model. Arthritis Research & Therapy. 2013;15(1):R22. PubMed PMID: doi:10.1186/ar4156.

221.   Stanton H, Rogerson FM, East CJ, Golub SB, Lawlor KE, Meeker CT, et al. ADAMTS5 is the major aggrecanase in mouse cartilage *in vivo* and *in vitro*. Nature. 2005 Mar 31;434(7033):648-52. PubMed PMID: 15800625. Epub 2005/04/01. eng.

222.   Ito A, Hibino E, Honda H, Hata K-i, Kagami H, Ueda M, et al. A new methodology of mesenchymal stem cell expansion using magnetic nanoparticles. Biochemical Engineering Journal. 2004;20(2-3):119-25.

223.   Arbab AS, Yocum GT, Rad AM, Khakoo AY, Fellowes V, Read EJ, et al. Labeling of cells with ferumoxides-protamine sulfate complexes does not inhibit function or differentiation capacity of hematopoietic or mesenchymal stem cells. NMR Biomed. 2005 Dec;18(8):553-9. PubMed PMID: 16229060. Epub 2005/10/18. eng.

224.   Foster-Gareau P, Heyn C, Alejski A, Rutt BK. Imaging single mammalian cells with a 1.5 T clinical MRI scanner. Magn Reson Med. 2003 May;49(5):968-71. PubMed PMID: 12704781. Epub 2003/04/22. eng.

225.   Golovko DM, Henning T, Bauer JS, Settles M, Frenzel T, Mayerhofer A, et al. Accelerated stem cell labeling with ferucarbotran and protamine. European Radiology. 2010 Mar;20(3):640-8. PubMed PMID: WOS:000274544800015.

226.   Baligand C, Vauchez K, Fiszman M, Vilquin JT, Carlier PG. Discrepancies between the fate of myoblast xenograft in mouse leg muscle and NMR label persistency after loading with Gd-DTPA or SPIOs. Gene Ther. 2009 Jun;16(6):734-45. PubMed PMID: 19282845. Epub 2009/03/14. eng.

227.   Berman SC, Galpoththawela C, Gilad AA, Bulte JW, Walczak P. Long-term MR cell tracking of neural stem cells grafted in immunocompetent versus immunodeficient mice reveals distinct differences in contrast between live and dead cells. Magn Reson Med. 2011 Feb;65(2):564-74. PubMed PMID: 20928883. Pubmed Central PMCID: PMC3031985. Epub 2010/10/12. eng.

Appendix

A 1. Equations

A 1.1 SPION labelling of cells.

Equation A.1.1 Example calculation for the labelling of 1x10^6 cells with 100 µgFe/ml of Nanomag

For the labelling of 1×10^6 cells with Nanomag at an iron concentration of 100 µgFe/ml

Equation 1: $\dfrac{Fe\ concentration}{Stock\ Fe\ concentration} = A$

➔ $\dfrac{100}{2400} = 0.041 ml$

Equation 2: $A\ x\ \dfrac{number\ of\ cells\ to\ be\ labelled}{200000} = B$

➔ $0.041 ml\ x\ \dfrac{1000,000}{200,000} = 0.2 ml$

Therefore; add 0.2ml of stock Nanomag to the required volume of media for the specific flask size.

A 1.2 Collagen Gels

Equation A.1.2. Equations to make up collagen gel.

$Amount\ of\ 10\ X\ \textbf{DMEM}\ to\ be\ added\ (ml) = \dfrac{A}{10} = D$

$Amount\ of\ stock\ \textbf{collagen}\ (ml) = \dfrac{A\ x\ B}{C} = E$

$Amount\ of\ \textbf{NaOH}\ to\ be\ added\ (ml) = E\ x\ 0.023 = F$

$Amount\ of\ \textbf{water}\ to\ be\ added\ (ml) = A - D - F$

Where **A**: Total gel volume required, **B**: Required collagen concentration, **C**: Stock collagen concentration

A 2 Iron Content Validation (ICP-OES).

The Fe content (as reported by the manufacturer, shown in Table A 2.1) of each particle was validated using ICP-OES. This technique allows the accurate evaluation of Fe within a sample. The Fe content of SiMAG was not supplied by the manufactured and for this reason was quantified by ICP-OES as 15 mg/ml and validated in the same way. Based on the values in Table A 2.1, a range of particle concentration (0.001, 0.01, 0.1, 1, 5, 10 µgFe/ml) were made up in dH_2O, digested, analysed and compared to an ICP-OES Fe standard curve. The unit of measurement of the ICP-OES instrument is PPM (1 PPM = 1 µg/ml). The Fe content of SiMAG and P904 has been confirmed in this system to be similar to the reported values (Figure A 2.1 and Table A 2.1); whilst Lumirem and Nanomag seemed to be 58 % and 70 % respectively of the reported value.

Table A 2.1 Fe quantification of each of the four particles: SiMAG, Lumirem, Nanomag and P904 as reported by the supplier where appropriate.

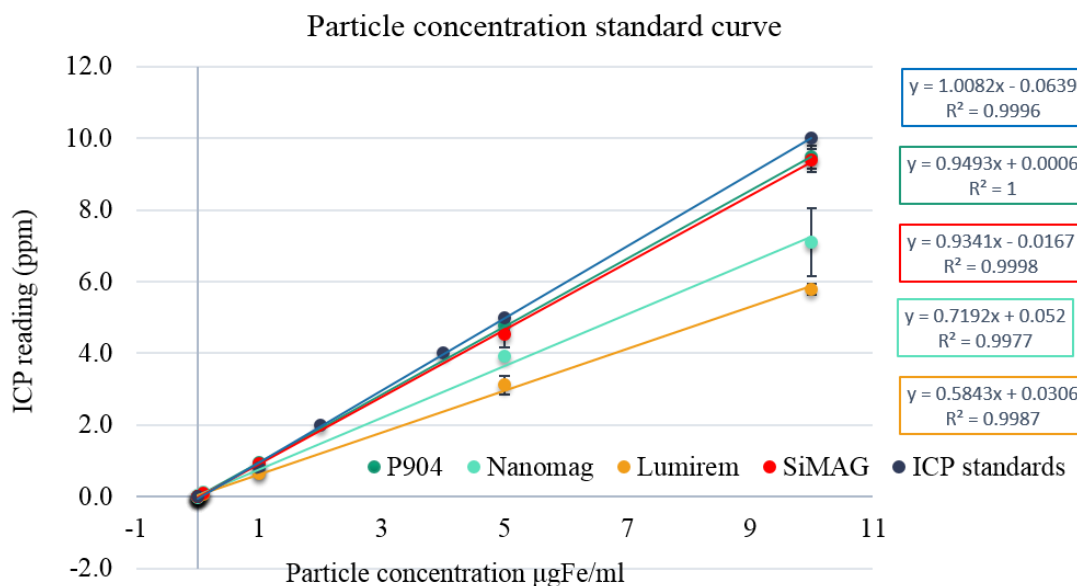| Particle	Fe content (µgFe/ml)
SiMAG	15000
Lumirem	175
Nanomag	2400
P904	22000

Figure A 2.1. Particle concentration curve for each particle (SiMAG, Lumirem, Nanomag and P904) against an ICP-OES Fe standard (1-10 µgFe/ml) as a validation of the Fe content of each particle as reported by the manufacturer. Data = mean Fe (n=3) ± SD.

In addition, the detection limits of ICP-OES have been determined as 0.1 PPM. The ICP-OES handbook states that the detection threshold of ICP-OES in terms of Fe to be 0.001 PPM. However as can be seen in Table A 2.2, accuracy is lost below the 0.01 PPM mark and for this reason, 0.1 PPM will be considered the detection threshold in this system and not 0.001PPM.

Table A 2.2. ICP-OES values for SiMAG, Lumirem, Nanomag and P904 ranging in concentration from 0.0001 μgFe/ml to 10 μgFe/ml. Red line indicates detection levels (0.1 PPM)

	SiMAG (15mg/ml)	Lumirem (175 mg/ml)	Nanomag (2.4 mg/ml)	P904 (22mg/ml)
10 μg/ml	9.383 ±0.33	5.786±0.15	7.101±0.95	9.479±0.32
5 μg/ml	4.537±0.38	3.119±0.26	3.931±0.06	4.775±0.12
1 μg/ml	0.915±0.07	0.654±0.05	0.755±0.01	0.945±0.04
0.1 μg/ml	0.088±0.007	0.065±0.007	0.117±0.01	0.096±0.042
0.01 μg/ml	0.007	0.002	0.044	0.015
0.001 μg/ml	0.000	0.008	-0.002	-0.007
0.0001 μg/ml	0.002	-0.006	-0.010	-0.005